INNOVATION IN CEMENTS FOR SUSTAINABILITY

EDITED BY: John L. Provis, Maria Juenger and Miroslav Komljenovic
PUBLISHED IN: Frontiers in Materials

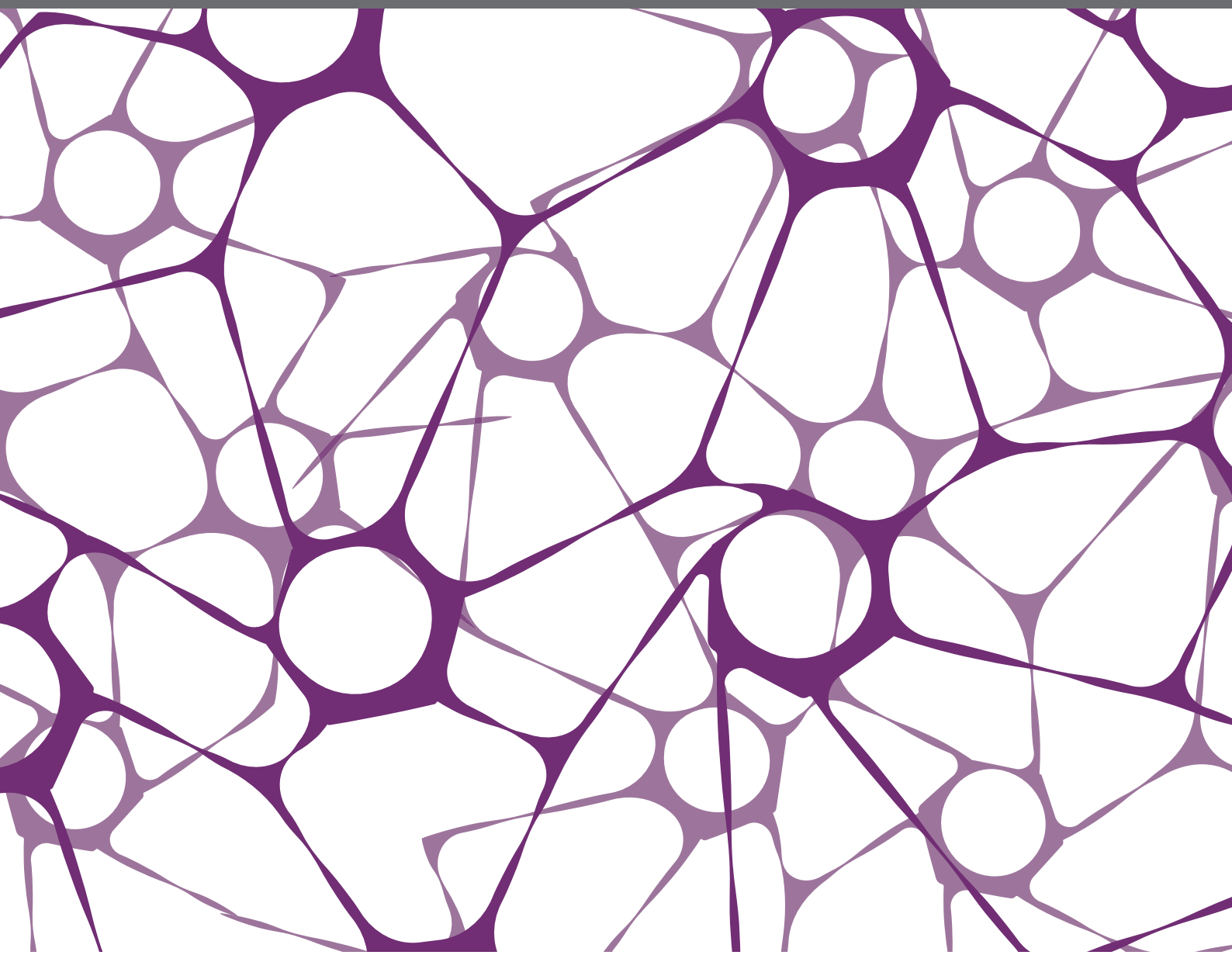

frontiers Research Topics

frontiers

ISSN 1664-8714
ISBN 978-2-88963-346-3
DOI 10.3389/978-2-88963-346-3

About Frontiers

Frontiers is more than just an open-access publisher of scholarly articles: it is a pioneering approach to the world of academia, radically improving the way scholarly research is managed. The grand vision of Frontiers is a world where all people have an equal opportunity to seek, share and generate knowledge. Frontiers provides immediate and permanent online open access to all its publications, but this alone is not enough to realize our grand goals.

Frontiers Journal Series

The Frontiers Journal Series is a multi-tier and interdisciplinary set of open-access, online journals, promising a paradigm shift from the current review, selection and dissemination processes in academic publishing. All Frontiers journals are driven by researchers for researchers; therefore, they constitute a service to the scholarly community. At the same time, the Frontiers Journal Series operates on a revolutionary invention, the tiered publishing system, initially addressing specific communities of scholars, and gradually climbing up to broader public understanding, thus serving the interests of the lay society, too.

Dedication to Quality

Each Frontiers article is a landmark of the highest quality, thanks to genuinely collaborative interactions between authors and review editors, who include some of the world's best academicians. Research must be certified by peers before entering a stream of knowledge that may eventually reach the public - and shape society; therefore, Frontiers only applies the most rigorous and unbiased reviews.
Frontiers revolutionizes research publishing by freely delivering the most outstanding research, evaluated with no bias from both the academic and social point of view. By applying the most advanced information technologies, Frontiers is catapulting scholarly publishing into a new generation.

What are Frontiers Research Topics?

Frontiers Research Topics are very popular trademarks of the Frontiers Journals Series: they are collections of at least ten articles, all centered on a particular subject. With their unique mix of varied contributions from Original Research to Review Articles, Frontiers Research Topics unify the most influential researchers, the latest key findings and historical advances in a hot research area! Find out more on how to host your own Frontiers Research Topic or contribute to one as an author by contacting the Frontiers Editorial Office: researchtopics@frontiersin.org

INNOVATION IN CEMENTS FOR SUSTAINABILITY

Topic Editors:
John L. Provis, University of Sheffield, United Kingdom
Maria Juenger, University of Texas at Austin, United States
Miroslav Komljenovic, University of Belgrade, Serbia

Citation: Provis, J. L., Juenger, M., Komljenovic, M., eds. (2020). Innovation in Cements for Sustainability. Lausanne: Frontiers Media SA. doi: 10.3389/978-2-88963-346-3

Table of Contents

frontiers in Materials

EDITORIAL
published: 19 November 2019
doi: 10.3389/fmats.2019.00298

Editorial: Innovation in Cements for Sustainability

John L. Provis[1]*, *Miroslav Komljenovic*[2] *and Maria C. G. Juenger*[3]

[1] *Department of Materials Science and Engineering, University of Sheffield, Sheffield, United Kingdom,* [2] *Department of Materials Science, Institute for Multidisciplinary Research, University of Belgrade, Belgrade, Serbia,* [3] *Department of Civil, Architectural and Environmental Engineering, University of Texas at Austin, Austin, TX, United States*

Keywords: cement, sustainability, construction, concrete, alkali-activated (AA) cement

Editorial on the Research Topic

Innovation in Cements for Sustainability

Sustainability is trying to balance economic growth, environmental protection and social progress with future technologies, while supporting innovation, and not compromising the way of life for present and future generations. The idea of sustainability should bring people together to foster the biosphere for the benefit of all living beings on our planet Earth.

It is with great pleasure that we present this Research Topic on *Innovation in Cements for Sustainability*. The collection of 10 articles in this Research Topic represent some very exciting advances in how we design, use, and analyse cementitious materials, and we expect that this work will lead to further advances along the pathway toward sustainability for the construction materials sector.

The work presented here related to Portland cement includes a pioneering study of tricalcium silicate hydration under microgravity conditions (Moraes Neves et al.), and important work on reducing Portland cement production temperatures using increased iron content in the clinker (Elakneswaran et al.). Portland-blended cements are highlighted through work on improving metakaolin dispersion in mortars (Geng et al.), and on the use of nano-alumina to improve the strength and microstructure of high-volume blended cements (Shaikh and Hosan). Hybrid alkaline-belite cements, which involve aspects of both conventional cement and alkali-activation chemistry, are also presented (Sánchez-Herrero et al.).

The development of innovative approaches to the activation of aluminosilicates to produce non-Portland cements is also addressed, using phosphate activators (Wang et al.) and also alkaline waste soda residues (Song et al.) as pathways to produce cements with novel characteristics. The combination of mechanical and chemical activation of fly ash was demonstrated as a way to unlock the potential to produce high-performing binders from ashes of various quality levels (Fernández-Jiménez et al.). The use of new precursors to produce alkali-activated binders has also shown exciting results in materials designed for key applications: heat-resistant porous cementitious materials produced from a combination of wastes from different industries (Bajare et al.), and also innovative mixed-valence ferrosilicate/ferrisilicate binders from synthetic iron-rich slags (Peys et al.).

The Guest Editorial team is confident that this collection of papers will be of benefit to the broader community in research and application of cementitious materials.

OPEN ACCESS

Edited and reviewed by:
Zuhua Zhang,
University of Southern Queensland, Australia

***Correspondence:**
John L. Provis
j.provis@sheffield.ac.uk

Specialty section:
This article was submitted to Structural Materials, a section of the journal Frontiers in Materials

Received: *24 October 2019*
Accepted: *06 November 2019*
Published: *19 November 2019*

Citation:
Provis JL, Komljenovic M and Juenger MCG (2019) Editorial: Innovation in Cements for Sustainability. Front. Mater. 6:298. doi: 10.3389/fmats.2019.00298

AUTHOR CONTRIBUTIONS

All authors participated in drafting and approving this Editorial.

Conflict of Interest: The authors declare that the research was conducted in the absence of any commercial or financial relationships that could be construed as a potential conflict of interest.

frontiers in Materials

ORIGINAL RESEARCH
published: 04 April 2019
doi: 10.3389/fmats.2019.00051

Mechanical-Chemical Activation of Coal Fly Ashes: An Effective Way for Recycling and Make Cementitious Materials

Ana Fernández-Jiménez, Ines Garcia-Lodeiro, Olga Maltseva and Angel Palomo*

Department of Materials, Eduardo Torroja Institute, Consejo Superior de Investigaciones Cientificas (CSIC), Madrid, Spain

This paper is wholly committed to resource efficiency through the valorization of waste from other industries, and more specifically fly ash as a raw material to produce concrete-like geopolymers. In particular, this study aimed to determine the effect of the physical and chemical characteristics of recycled coal fly ash used to manufacture alkaline cement on reaction kinetics and product microstructure and performance. The ash was mixed with 8 M NaOH and cured for 20 h at 85°C and RH > 90% to form a compact paste, after which mechanical strength was determined and the reaction rate was calculated using isothermal conduction calorimetry. The findings showed that vitreous content (SiO_2/Al_2O_3), reactive and (especially) fineness play a very important role in both the development of cement mechanical strength and the composition and structure of the reaction products formed.

Keywords: recycling, fly ash, alkaline activation, geopolymer, mechanical-chemical activation, NMR

OPEN ACCESS

Edited by:
Maria Juenger,
University of Texas at Austin,
United States

Reviewed by:
Prinya Chindaprasirt,
Khon Kaen University, Thailand
Jae Eun Oh,
Ulsan National Institute of Science and Technology, South Korea

****Correspondence:***
Ines Garcia-Lodeiro
iglodeiro@ietcc.csic.es

Specialty section:
This article was submitted to Structural Materials, a section of the journal Frontiers in Materials

Received: *08 January 2019*
Accepted: *11 March 2019*
Published: *04 April 2019*

Citation:
Fernández-Jiménez A, Garcia-Lodeiro I, Maltseva O and Palomo A (2019) Mechanical-Chemical Activation of Coal Fly Ashes: An Effective Way for Recycling and Make Cementitious Materials. Front. Mater. 6:51. doi: 10.3389/fmats.2019.00051

INTRODUCTION

Portland cement manufacture consumes around 4 GJ of energy per ton and accounts for approximately 8% of worldwide CO_2 emissions, or 2.981 $GtCO_{2eq}$ in 2014 (CSI/ECRA—Cement Sustainability Initiative/ European Cement Research., 2017).

The Roadmap for a resource-efficient Europe (COM, 2011) 0571 describes industrial strategies to mitigate the effects of industrial activity and ensure that by 2050 Europe will have a sustainable economy, in which "resources are not simply extracted, used and thrown away, but are put back in the loop so they can stay in use for longer."

Cross-cutting concerns such as the need for more long-term, innovative thinking are also being addressed. The research supporting this paper is wholly committed to resource efficiency through the valorization of waste from other industries, and more specifically, fly ash as a raw material to produce concrete-like "geopolymers," which contain a drastically reduced proportion of portland cement.

Worldwide production of combustion products (CCPs), including fly ash, amounted to 780 Mt in 2011 and nearly 1 Gt in 2015. Whilst the rate of re-use varies widely from country to country (10.6–96.4%), overall 47% of the fly ash generated is presently landfilled (Thomas, 2007). Options for reusing CCPs, which have been under study around the world for the last 70 years, can be classified as non-beneficial, simply transformed manufactures (STM) or elaborately transformed manufactures (ETM). Like other industrial waste such as blast furnace slag or red mud, fly ash can be activated in alkaline media, setting and hardening to acquire properties similar to

those characteristics of portland cement. Such materials, known as "alkali-activated cements" or "geopolymers," constitute optimal vehicles for valorizing and recycling coal fly ash (Palomo et al., 2014; Zhuang et al., 2016; Bai and Colombo, 2018).

The 500 Mt/year of coal fly ash presently landfilled could be reused to manufacture cement or concrete (Chindaprasirt et al., 2005; Duvallet et al., 2015; Hemalatha and Ramaswamy, 2017) if ash particle reactivity could be significantly enhanced. Such valorization would also help mitigate global warming by reducing the CO_2 emitted by the building materials industry. The primary objective of the present study was consequently to devise processing methods that would heighten fly ash reactivity.

The main reaction product formed in the alkali activation of fly ash is an amorphous, three-dimensional alkaline inorganic polymer generically known as N-A-S-H (Na_2O-Al_2O_3-SiO_2-H_2O) gel (Fernández-Jiménez et al., 2005; Provis and van Deventer, 2014). Secondary reaction products may include zeolites such as Na-chabazite, zeolites A and P, and faujasite (Fernández-Jiménez et al., 2005; Panias et al., 2007).

Earlier studies have shown an intrinsic relationship between the composition and structure of N-A-S-H gel and its physical and mechanical properties (Fernández-Jiménez et al., 2006; De Silva et al., 2007). Given similar degrees of reaction, the formation of N-A-S-H gels with an Si/Al ratio of ≈1 (type 1 gels) yields materials with lower mechanical strength than when the gel formed has an Si/Al ratio of ≈2 (type 2 gels) (Fernández-Jiménez et al., 2006; Hajimohammadi et al., 2010; Nikolic et al., 2015). Further studies by a number of authors (Sagoe-Crentsil et al., 2005; Kovalchuk et al., 2007; Fernández-Jiménez et al., 2017) optimal Si/Al ranges from 2 to 4. Such findings attest to the importance of the reactive silica and alumina content in the starting materials, which largely conditions the ultimate composition of the gel formed. In high calcium based systems (such as type C fly ashes), the initial setting process is governed by the formation of C-S-H or C-A-S-H-like phases rather than pure N-A-S-H. Fast dissolution of highly active Al_2O_3 and SiO_2 sources in high pH medium provides high initial concentrations of silicate species and aluminate to react with Ca forming C-A-S-H phase in the early reaction stages (Chindaprasirt et al., 2012). Other works developed in the field of hybrid alkaline cements (systems with small OPC contents + high content of an aluminosilicate source) point out the co-precipitation of both C-A-S-H+ (N,C)-A-S-H gels during the early reaction stages, which would evolve with time to a C-A-S-H gel (Garcia-Lodeiro et al., 2011, 2013).

In addition to the chemical composition of the ash, the vitreous phase content and the $(SiO_2/Al_2O_3)_{reactive}$ ratio, particle size is a factor to be borne in mind when determining a material's reactive potential. A number of studies mention the effect of fly ash particle size when used either as a supplementary cementitious material to lower the clinker factor (Paya et al., 1997; Chindaprasirt et al., 2005; Hemalatha and Ramaswamy, 2017) or as a precursor in the preparation of alkaline (OPC-less) cements (Fernández-Jiménez et al., 2005; Marjanovic et al., 2014; Duvallet et al., 2015).

Many authors (Rakesh et al., 2007; Temuujin et al., 2009; Kumar and Kumar, 2011; Kumar et al., 2015; Shekhovtsova et al., 2018) have broached the effect of fineness on ash reactivity, separating the material either by sieving (particles under 45 μm (Duvallet et al., 2015) or electrostatic precipitation (Kumar et al., 2015). Their findings have consistently shown that mechanical strength rises substantially with ash fractions of under 45 μm. Particle size separation normally prompts an increase in the proportion of vitreous phase, for the particles eliminated (the largest) consist essentially in scantly reactive crystalline phases such as quartz, unburnt carbon, and hematite. The discards generated by such processes would, naturally, need to be managed.

Kumar et al. have published a host of papers on the mechanical activation of fly ash (Kumar and Kumar, 2011; Kumar et al., 2015). They observed that milling fly ash raised the mechanical strength of the resulting cements, which they attributed both to the stimulation of ash reactivity by the smaller particle size (particularly at early ages) and to physical changes in porosity and the pore size distribution of the end product. Temuujin et al. (2009), however, observed no clear correlation between the rise in strength and changes in material porosity and density. The general consensus in the literature to date (Kumar and Kumar, 2011; Kumar et al., 2015) is that the mechanical activation of fly ash enhances the mechanical strength of the end product because the changes in particle morphology along with size hasten dissolution-precipitation reactions, raising reactivity. That in turn yields more compact microstructures, with a larger amount of gel and smaller fraction of unreacted particle (Zhang et al., 2016).

Most papers published on the effect of the mechanical activation of ash focus on a single material, with very few comparing the effect in ash from different sources (Marjanovic et al., 2014; Kumar et al., 2015). In a recent article proposing an equation to assess the suitability of fly ash for the production of a high-strength geopolymer, Zhang et al. (2016) reported that physical properties (density, specific surface, and fineness) may have a greater effect on ash reactivity than its vitreous phase content.

In light of the foregoing, the present study aimed to determine the effect of the mechanical activation of ash (by milling) on strength development, reaction kinetics and micro- and nanostructure of the reaction products.

The materials used had different vitreous phase contents and $(SiO_2/Al_2O_3)_{reactive}$ fractions. Their initial particle size also differed, although they were ground for a sufficient time to substantially modify the specific surface of the original ash. The three ashes were ground and alkali-activated, after which their mechanical strength was determined and the reaction products were characterized by using XRD, SEM/EDX, and NMR.

EXPERIMENTAL

Materials

The three fly ashes used in this study, sourced from different Chinese steam plants, had different chemical and mineralogical compositions. Their chemical composition (% of oxides by mass), found with a PHILIPS PW 2400 X-ray fluorescence spectrometer fitted with a PW 2540 VTC sample changer, is given in **Table 1**.

TABLE 1 | Bulk chemical composition of the coal fly ash studied.

	F1	F2	F3
SiO_2	58.02	45.18	42.68
Al_2O_3	18.7	33.59	49.36
CaO	9.82	9.36	2.21
Fe_2O_3	4.10	4.54	1.45
K_2O	3.10	1.13	0.32
Na_2O	1.59	1.07	–
MgO	1.36	0.83	–
SO_3	0.50	0.74	0.12
TiO_2	0.79	1.26	1.67
CrO	0.13	0.18	0.07
MnO	0.11	0.11	/
Other	1.03	0.29	0.26
LoI	0.79	1.72	1.86
Total	100	100	100
SiO_2/Al_2O_3	3.10	1.34	0.86
Minor crystalline phases	Quartz caO	Quartz corundum mullite caO	Corundum mullite

The table also shows the XRD-detected minority crystalline phases in each ash. The significant differences in aluminum content prompted a fairly wide-ranging initial SiO_2/Al_2O_3 ratio, from 3.10 to 0.86.

Experimental

Particle size distribution was determined on a COULTER LS 130 laser sizer with a measuring range of 0.1–900 μm. The ash was ground in a laboratory ball grinder for 4 h (regarded as sufficient time to ensure similar particle size distributions in all three varieties of ash), using the same number of balls and loading the grinder with the same weight of sample throughout.

The materials were exposed to an acid attack (continuously stirring 1 g of ash in 100.00 mL of a 1% HF solution for 5 h (Ruiz-Santaquiteria et al., 2013) to quantify the potential reactivity of both the unground original (F1, F2, and F3) and ground (GF1, GF2 and GF3) ash. The resulting solution was then filtered, the residue was rinsed with distilled water to a neutral pH and the amount of dissolved (=potentially reactive) silica and alumina in the leachate was quantified by ICP on a Varian 725-ES optical ICP atomic emission spectrometer with the following settings: power, 1.40 kW; plasma gas flow, 15.00 L/min; nebulizer gas flow, 0.85 L/min; read time, 5 s. The findings were used to calculate the $(SiO_2/Al_2O_3)_{reactive}$ ratio for each ash.

The ground and unground ashes were mixed with an 8 M NaOH solution and the resulting pastes molded into prismatic specimens measuring 1 × 1 × 6 cm^3 to determine whether these materials were susceptible to alkali activation and able to yield a product with good mechanical properties. The alkaline solution/ash ratio varied depending on the ash (see **Table 2**), yet was the same for the ground and unground versions of each. The samples were cured for 20 h in an oven at 85°C and a relative humidity of ≥90%. These conditions usually guarantee a proper FA reactivity (Fernández-Jiménez and Palomo, 2007; Zhou et al., 2016). The compressive strength of the specimens was found on an Ibertest Autotest 200/10-SW frame 24 h after mixing. Ten specimens of each composition were tested.

TABLE 2 | Mechanical strength of alkali-activated paste prepared with ground or unground coal fly ash and cured for 20 h at 85°C.

Fly ash	8 M NaOH /FA ratio (wt)	Compressive strength (MPa) in 1 day pastes		Δ Strength (est., %)
		Original	Ground	
F1Na	0.35	17.04 ± 0.96	29.26 ± 2.17	41.8
F2Na	0.35	27.29 ± 1.74	46.39 ± 2.63	41.2
F3Na	0.4	1.33 ± 0.20	18.13 ± 1.82	92.66

The starting ashes and reaction products were characterized by XRD, scanning electron microscopy (SEM/EDX) and NMR. X-ray diffraction (XRD) was conducted on a Bruker AXS D8 ADVANCE diffractometer. The scanning spectrum ranged from 2Θ angles 5 to 60° with a nominal step size of 0.0119736° at a rate of 0.5 s/step. Powder samples were exposed to Cu-Kα1, α2 X-ray radiation.

Fly ash morphology and cured specimen microstructure were examined under a JEOL 5400 scanning electron microscope fitted with an OXFORD LINK-ISIS EDX (energy dispersive X-ray) system. EDS analyses (on spots) were done with accelerating voltage of 20 kV, working distance of 15 mm and beam current of 20 μA and acquiring for 60 s per spot analysis. An average of 50 analys were taken per sample.

The NMR scans were recorded on a BRUKER AVANCE-400 spectrometer. All the samples were spun at 10 kHz. For ^{27}Al MAS-NMR, the settings were: frequency, 104.3 MHz; 2 ms single pulse MAS; 5 s relaxation delay; external standard, $Al(H_2O)_6$. For ^{23}Na MAS-NMR they were: frequency, 105.8 MHz; 2 ms single pulse MAS; 5 s relaxation delay; external standard, NaCl. For ^{29}Si MAS-NMR the data were: frequency 79.5 MHz; 5 ms single pulse MAS; 10 s relaxation delay; external standard, TMS.

Ash reaction rate was determined in terms of heat flow calculated using isothermal conduction calorimetry. Pastes were prepared by adding 5 g of fly ash to 2.5 g of alkaline solution to ensure satisfactory mixing. The paste was mixed manually for 3 min *ex-situ* in a sample cell, which was subsequently sealed and then immediately placed in a TAM Air Thermometric calorimeter where heat flow was recorded at a constant external temperature of 85 ± 1°C.

RESULTS AND DISCUSSION

Effect of Grinding on Ash Physical and Chemical Characteristics

Figure 1 shows the particle size distribution of the fly ash as received from the steam-fired power plants and after grinding. Ash F1 initially had a median particle size, d_{50}, of 9 μm; ash F2 of around 20 μm; and F3, the coarsest, a value of approximately 34 μm. After grinding, these differences narrowed substantially, with all three types of ash exhibiting d_{50} values of 5 μm to 7 μm.

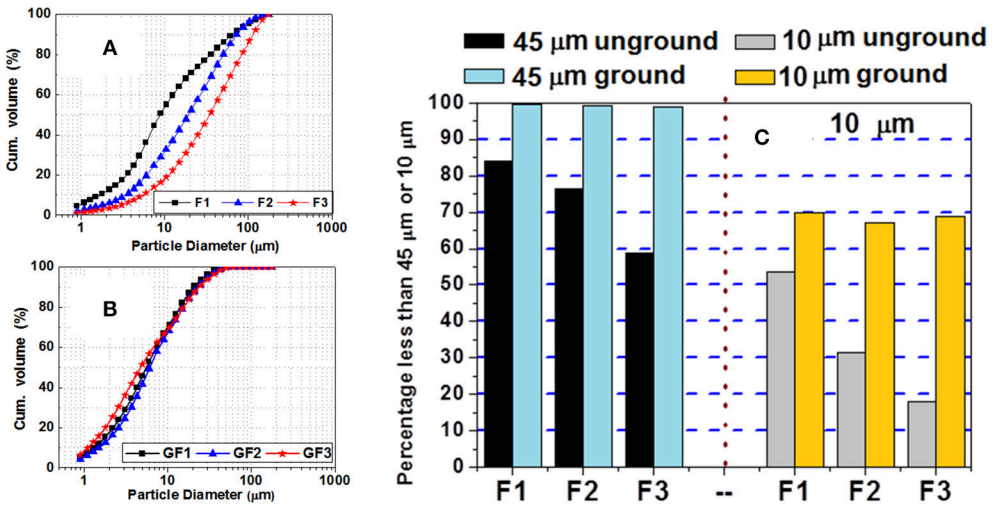

FIGURE 1 | Cumulative volume of **(A)** initial and **(B)** ground ash, and **(C)** percentage of particles under 45 and 10 μm before and after grinding.

The effect of grinding is graphically illustrated in **Figure 1C**, which shows the percentage of particles under 45 and 10 μm before and after milling. Grinding clearly yielded a more uniform particle size in all three varieties of ash, with 98% of the particles under 45 and 67% under 10 μm. The most significant change was observed in F3, the ash with the initially largest particle size. The data in **Figure 1** show that ashes with initially different particle sizes exhibited fairly similar distributions after grinding. The inference appears to be that below a given threshold particle size, the grinding system used was ineffective.

Based on their chemical composition (**Table 1**: $SiO_2 + Al_2O_3 + Fe_2O_3 \geq 70\%$; $CaO < 10\%$), F1, F2, and F3 constituted what is regarded by European standard EN 450-1 and ASTM standard C 618 as class F fly ash, i.e., pozzolanic ash resulting from the combustion of anthracite or bituminous coal. Further, to Canadian standard CSA A3001, however, which classifies fly ash in three groups depending on CaO content, only ash F3 would qualify as class F: silicoaluminous, low calcium fly ash with <8% CaO, consisting predominantly in aluminosilicate glass with varying amounts of crystalline quartz, mullite, hematite and magnetite. In the Canadian system, both F1 and F2 would be class C1 (8–20% CaO) ash, with an intermediate proportion of calcium oxide.

The results of the acid attack conducted to determine ash reactivity are compared in **Figure 2** to the overall silica and alumina contents found with chemical analysis. As the sum of the reactive silica and alumina was not over 70% in any of the materials studied, all three could be defined as Canadian standard class C1 ash.

Figure 2 shows that grinding-based mechanical activation barely modified the potentially reactive silica and alumina identified in the starting ash. In other words, particle size would not initially appear to have any significant effect on the reactive potential of the ash. The figure also reveals the clearly smaller reactive than bulk aluminum content in ground and unground ashes F2 and F3. In these two materials, bulk alumina was on the order of 30–50% whilst the potentially reactive compound accounted for no more than 10%.

The SEM micrographs (see **Figure S1**) showed that the ashes with coarser particle sizes (F2 and F3) prior to grinding exhibited a more heterogeneous morphology, whereas the finer ash (F1) was more uniform and had a higher proportion of spherical particles.

The diffractograms for the original ash contained a hump at 2Θ values of 20–35° associated with the vitreous content of the ash. The intensity of this hump is usually related to the amorphous content. The minority crystalline phases identified were quartz, mullite, hematite, corundum and traces of CaO. The corundum and mullite contents were high in ashes F2 and F3, which justify the lower intensity of the hump in these two with respect to F1. No significant mineral differences were observed between the pre-and post-ground ash diffractograms. The sole visible changes included a slight decline in the intensity of the quartz diffraction line, which might explain the slight increase in the soluble SiO_2 content in the ground ash (see **Figure 2**), and a rise in the diffraction line for hematite, possibly attributable to the use of iron grinding balls.

The ^{27}Al NMR spectra (see **Figure 3**) for the original ash contained an aluminum signal at around 58 to 60 ppm associated with tetrahedral aluminum (Al_T), present primarily in the vitreous phases of fly ash. Ash F1 clearly contained no octahedral aluminum (Al_O), a finding consistent with the HF chemical attack results (see **Figure 2**), according to which nearly all the alumina present in this ash was reactive. In varieties, F2 and F3 mullite were detected as a shoulder at ∼2.5 ppm, associated with Al(VI), while resonances observed at ∼60 and 45 ppm were attributed to Al(IV). The intense signal at 45 ppm on the spectra for fly ash F3 was attributed to the tetrahedral aluminum in mullite, where three shares one oxygen atom surrounding Al tetrahedral (Sanz et al., 1988; Merwin et al., 1991). Ashes

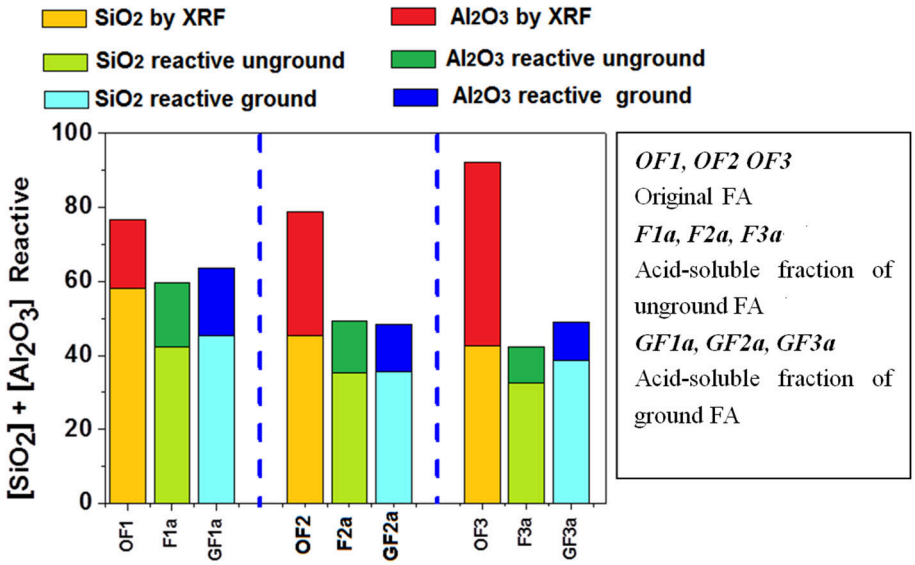

FIGURE 2 | Initial and potentially reactive silica and alumina in ground and unground ash.

F2 and F3 also exhibited a very intense signal at around 12 ppm, generated by the octahedral aluminum in corundum. This octahedral aluminum would explain the findings shown in **Figure 2**, according to which although the bulk aluminum content (∼33–50%) was high in these materials, less than half (14–15%) was dissolved by the acid. Hence the intensity of the Al_O signals on the spectra for these two ashes.

The ^{27}Al spectra for F2 and F3 after grinding, also shown in **Figure 3** by way of example, were practically identical to those for the unground ash. The sole difference, the slightly lower post-grinding intensity of the shoulder at 2.5 ppm associated with mullite, may have been the result of the reduction in mullite crystal size, together with surface amorphisation of the mineral. In a study on the mechanical amorphisation of mullite drew similar conclusions (Schmucker et al., 1998). After grinding mullite for 240 h, they observed that the signal at 45 ppm was gradually replaced by one at 30 ppm, which appeared to grow at the expense of the resonances for both the tetrahedral and octahedral aluminum. In this study, whilst the intensity of the Al(VI) shoulder clearly declined, no signal was detected at 30 ppm. The apparent thrust of these findings was that mechanical activation did not significantly alter the coordination of the aluminum present in the ash: i.e., the tetrahedral and octahedral environments were the same in the ground and initial materials.

The ^{29}Si MAS-NMR spectra for the original ash (see **Figure 4**) exhibited a wide, poorly defined signal that actually enveloped a series of overlapping resonances. The area of the spectrum with absolute values greater than−108 ppm was attributed to the presence of crystal phases with Q^4(0Al) environments, such as quartz (-108 to−109 ppm) and cristobalite (-113 to−114 ppm) (Engelhardt and Michel, 1987). The area between−80 and−104 ppm was primarily identified with Q^4(mAl) units in the vitreous component of the ash (Criado et al., 2008). The signal at around−87 to−88 ppm, clearly visible on the F3, and as a shoulder on the F2 spectrum, was attributed to the presence of a less polymerized (more reactive) glassy component. This area may also contain a signal attributed to the Q^3(3Al) units in crystalline mullite. The ash F1 spectrum exhibited a small peak at−71 ppm. Also observed but less clearly on the spectra for the other materials, that resonance may be due to the presence of scantly crystalline calcium silicate, which would partly explain the CaO content present in this ash (∼10%).

Figure 4 also reproduces ^{29}Si spectra for F2 and F3 after grinding (GF2 and GF3), by way of example. Analogously to the Al spectra, the Si spectra showed no significant variations in the Si atoms after mechanical activation. In short, milling fly ash had a substantial effect on fineness and its distribution, but a much lesser impact on its potentially reactive silica and alumina content. A slight variation in the aluminum environments was nonetheless observed, possibly due to surface amorphisation of minority crystalline particles such as mullite. This effect was more visible in the ashes with a higher percentage of such minority crystalline phases, namely F2 and F3, despite the rather shorter ("medium" intensity) grinding time than applied in other studies (Marjanovic et al., 2014).

Alkali Activation of Fly Ash

Table 2 gives the compressive strength of the pastes obtained by activating the unground and ground ashes with 8 M NaOH. All the ground ash pastes exhibited strength values at least 40–50% higher than their unground counterparts. The most striking difference was observed for ash F3. When mixed with 8 M NaOH, the unground ash hardened but was scantly compact and broke readily. Such an indication of poor quality might lead to the rejection of this ash. When the ash was ground, however, the resulting paste reached a strength of 18 MPa, a value comparable to those observed for the other materials before grinding. These findings attest to the significant role played by fineness in the

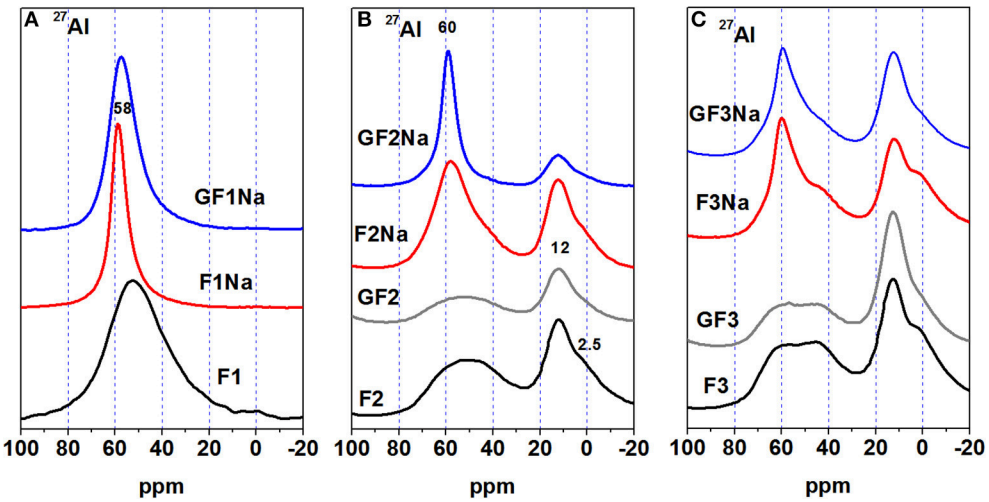

FIGURE 3 | ^{27}Al MAS-NMR spectra for ash **(A)** F1 **(B)** F2, and **(C)** F3.

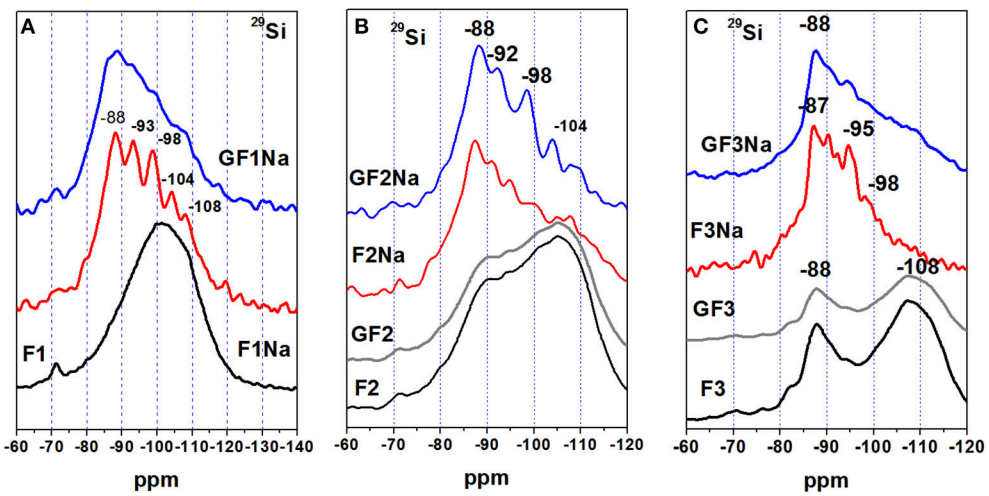

FIGURE 4 | ^{29}Si MAS-NMR spectra for ash **(A)** F1 **(B)** F2, and **(C)** F3.

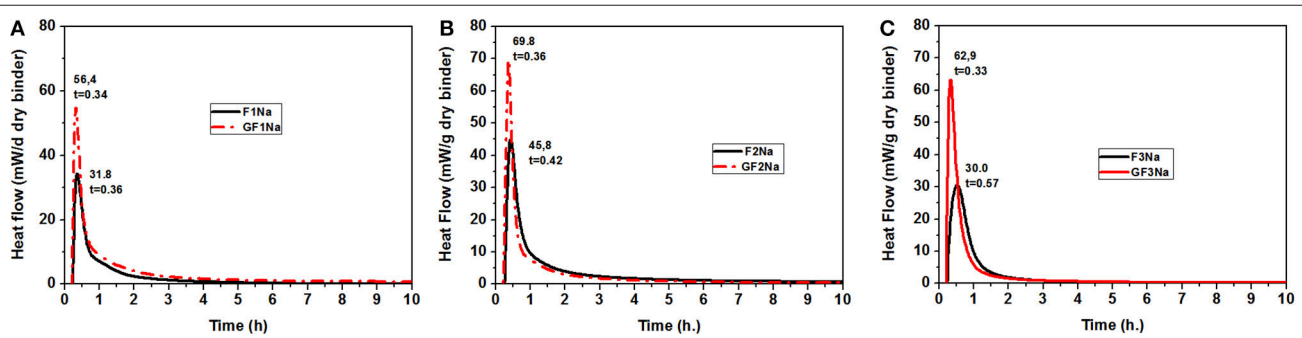

FIGURE 5 | Rate of Heat release for the different coal fly ashes activated with an 8 M NaOH solution at 85°C **(A)** F1Na (unground) and GF1Na (ground) **(B)** F2Na (unground) and GF2Na (ground) **(C)** F3Na (unground) and GF3Na (ground).

development of mechanical strength in cements made with alkali-activated fly ash.

Figure 5 shows the heat curves for the ground and unground fly ash pastes activated with an 8 M solution of NaOH at 85°C. Peak intensity was nearly double and appeared slightly earlier in all the pastes made with ground ash. The latter effect was more visible in ash F3, which initially had the coarsest particle size. These findings corroborated earlier reports (Zhang et al., 2016) to the effect that reducing the mean particle size raised the early age reaction rate in the material.

The XRD patterns for the initial fly ash and the activated pastes made with both ground and unground ash are reproduced in **Figure 6**. The most prominent features of the diffractograms were:

- the persistence of the same crystalline phases in the pastes as observed in the initial ash, confirming their low reactivity in alkaline media
- a shift in the hump of the pastes to slightly higher 2Θ values (25–40°), attesting to the formation of a N-A-S-H gel (Fernández-Jiménez et al., 2005)
- the presence of diffraction lines on the patterns for the initial (unground) activated fly ash (F1Na, N2Na, and F3Na) associated with the presence of herschelite, hydroxysodalite and zeolite Y (see **Figure 6**), in contrast to the diffractograms for the activated pastes prepared with ground ash (GF1Na, GF2Na, and GF3Na), on which no zeolite phases were detected.

The ^{27}Al and ^{29}Si MAS NMR spectra for the initial ash and ground and unground activated materials are reproduced in **Figures 3**, **4**. A comparison of these spectra revealed clear differences.

The signal at +58 to +60 ppm associated with Al(IV) ($AlQ^4(4Si)$-type units) present both in the N-A-S-H gel formed and in the zeolites was narrower and more intense on the ^{27}Al spectra (**Figure 3**) for the activated pastes made with ground and unground ash than on the spectra for the respective initial ashes. Pastes F1Na and GF1Na generated no signal that could be associated with Al(VI), for which no resonance was observed in the original ash either. The pastes prepared with ashes 2 and 3 (F2Na, GF2Na, F3Na, and GF3Na), in contrast, contained an intense signal at around 12 ppm, together with a shoulder at 2 ppm associated with the presence of Al(VI) in the crystalline phases of the initial ash (corundum and mullite). The signal for Al(IV) was narrower and more intense than the Al(VI) signal on the spectra for the pastes, whereas the opposite was observed on the spectra for the initial materials. The Al(VI) signal on the spectrum for paste GF2Na was very weak. Normally the Al_O present in corundum and mullite is scantly responsive to alkaline activation. Here, however, ash grinding might be thought to have prompted a significant decline in corundum crystal size, along with surface amorphisation. As a result of the enhanced reactivity of this phase, part of the Al present would have subsequently been taken up in the matrix. That would explain the high strength values observed for the ground fly ash, despite its apparently low reactive Al content.

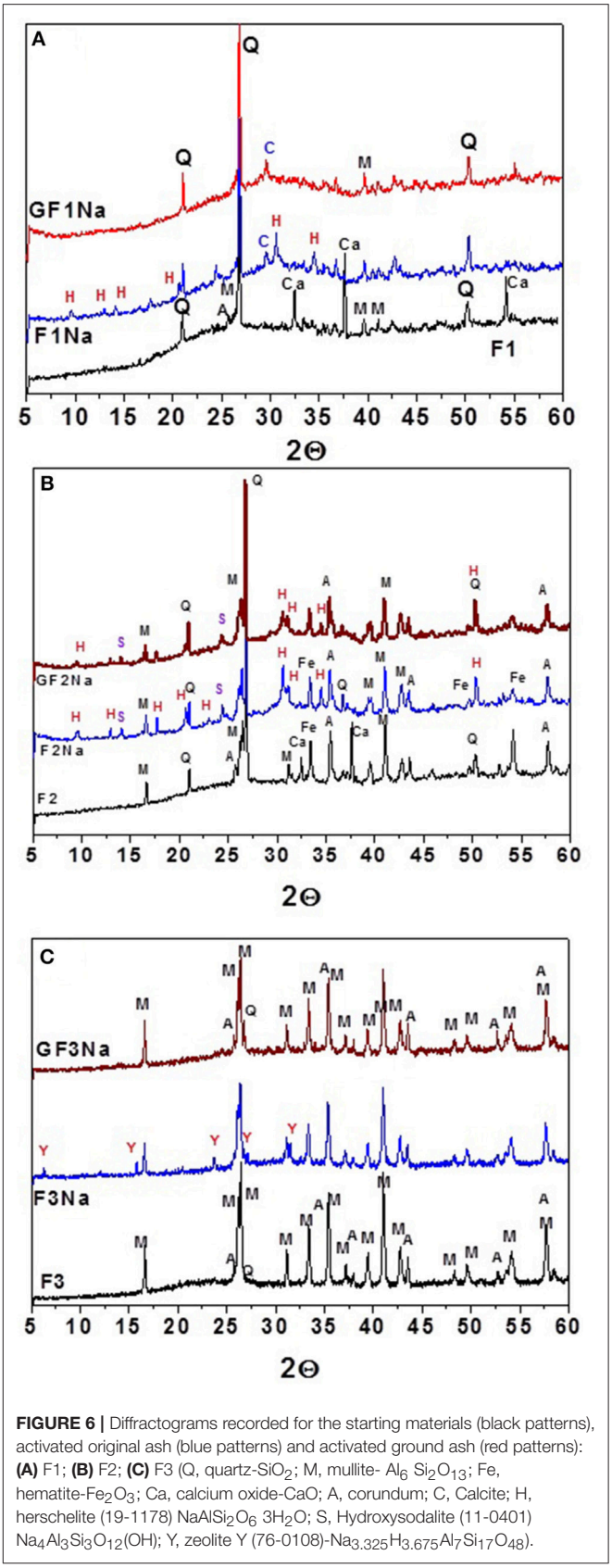

FIGURE 6 | Diffractograms recorded for the starting materials (black patterns), activated original ash (blue patterns) and activated ground ash (red patterns): **(A)** F1; **(B)** F2; **(C)** F3 (Q, quartz-SiO_2; M, mullite- Al_6 Si_2O_{13}; Fe, hematite-Fe_2O_3; Ca, calcium oxide-CaO; A, corundum; C, Calcite; H, herschelite (19-1178) $NaAlSi_2O_6$ $3H_2O$; S, Hydroxysodalite (11-0401) $Na_4Al_3Si_3O_{12}(OH)$; Y, zeolite Y (76-0108)-$Na_{3.325}H_{3.675}Al_7Si_{17}O_{48}$).

The ^{29}Si spectra for the pastes also differed substantially from the spectra for the initial ashes (see **Figure 4**). Here the spectra for the unground ash pastes had more clearly defined signals, attributed to the higher zeolite content in these pastes, as observed in the XRD findings. As zeolites are more orderly structures than gels, their spectra are characterized by higher resolution. The ^{29}Si spectra for all the pastes exhibited a broad signal that masked overlapping resonances at positions at around−88,−93,−98,−104, and−108 ppm, attributed to tetrahedral silicons, respectively, surrounded by Al_4, $SiAl_3$, Si_2Al_2, Si_3Al, and Si_4. The intensity of the signals varied with the ash (unground and ground). A signal detected at around−87 ppm, particularly intense in paste F3Na, was partly generated by the mullite present in the starting ashes (see spectra F3 and F3Na in **Figure 4C**).

The ^{23}Na spectra for the same pastes are reproduced in **Figure 7**. All contained a signal centered over−6.5 to−10 ppm, attributed to the presence of partially hydrated sodium, and needed to balance the charge in the geopolymer when silicon was replaced by aluminum in the aluminosilicate hydrate gel structure. As a rule, in aluminosilicate glass this signal shifts to more negative values when the Si/Al ratio rises and more positive values when it declines, very likely as the result of the increase in the Na-O interatomic distance or in the coordination numbers (Duxson et al., 2005; Provis et al., 2009). Paste F3Na, which exhibited the lowest strength, had two shoulders on its spectrum, one at around 3 ppm to 5 ppm associated with the Na in unbound $NaOH.nH_2O$ (Koller and Engelhardt, 1994) which is consistent with the lower degree of reaction in this paste, and the other at around−15 ppm, possibly attributable to sodium bonded with oxygen atoms only (Koller and Engelhardt, 1994; Duxson et al., 2005; Provis et al., 2009).

Figure 8 compares the microstructure of the chemically activated, ground and unground pastes made with ashes F1, F2, and F3. The pastes made with unground ash (F1Na, F2Na, and F3Na) were less compact on the whole than ground ash (GF1Na, GF2Na, and GF3Na) and contained a substantial number of unreacted glass microspheres, hollow (cenospheres) or filled with very small particles. The ground ash pastes (GF1Na, GF2Na, and GF3Na), especially GF3Na, had more compact matrices and a higher proportion of reacted ash. Zeolites were observed in the SEM micrographs of both ground and unground matrices, whereas XRD could detect them only in the pastes with unground ash. These data suggest that activation takes place so quickly in pastes with a high proportion of very fine particles that the new phases formed barely had time to develop a crystalline structure: i.e., reaction kinetics prevailed over thermodynamics.

Although qualitative, EDX analysis can approximate the compositional variability and homogeneity of the gels formed. The values in **Figure 9** are for $CaO\text{-}SiO_2\text{-}Al_2O_3$ and $Na_2O\text{-}SiO_2.Al_2O_3$ diagrams. Further to these data, very low calcium content (∼2%) ash F3 formed which what was essentially a N-A-S-H gel. Ashes F1 and F2, with calcium contents of ∼10%, exhibited greater compositional variability. The matrices containing unground ash appeared to contain a heterogeneous mix of N,C-A-S-H-like gels with variable calcium contents (Garcia-Lodeiro et al., 2011; Walkley et al., 2016). A comparison

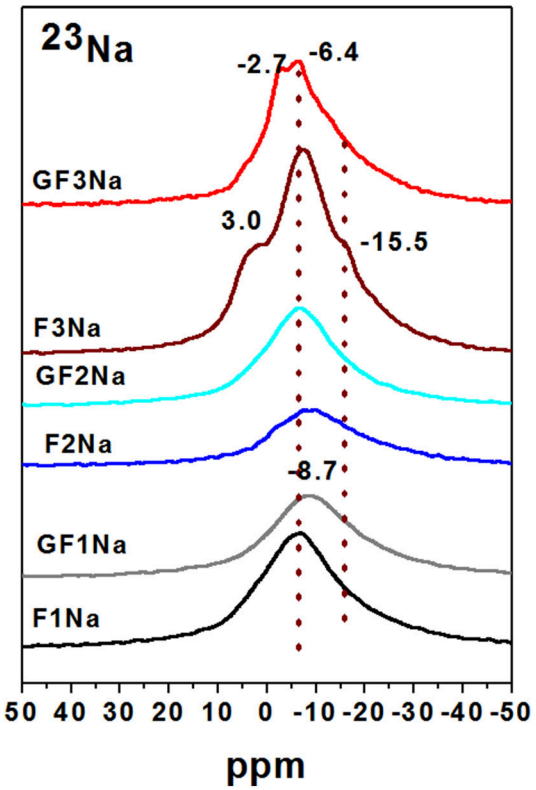

FIGURE 7 | ^{23}Na MAS-NMR spectra.

of the diagrams for F1 and F2 revealed that in the gels formed, the silicon/aluminum ratio was greater in the pastes prepared with ash F2, possibly due to the lower proportion of reactive aluminum present. When the ash was ground, the point distribution (red points) was slightly more homogeneous, indicating that mechanical activation, in addition to reducing the particle size, afforded the original ash a more uniform composition. As a result, the mean composition of the gels forming in pastes with ground ash was more homogeneous.

The findings for a given ash before and after grinding, compared here to determine the effect of fineness in materials with the same chemical composition, showed that the proportion of potentially reactive phase was only slightly modified by mechanical activation. Reaction kinetics and mechanical strength, however, rose significantly. These data are consistent with results reported by Zhang et al. (2016) suggesting that physical properties may play a more prominent role in ash reactivity than vitreous phase content or composition.

The smaller particle size in ground ash modified reaction kinetics, hastened dissolution and raised the initial degree of reaction, thereby generating higher early age strength. Smaller sized ash particles favored Al and Si dissolution in the medium as well as the precipitation of an N,C-A-S-H-like cementitious gel, which also affected material mineralogy and microstructure. The speedier reaction allowed practically no time for zeolites to crystallize or for the crystals to grow large enough to be detected by XRD. Another factor that may affect zeolite formation is the

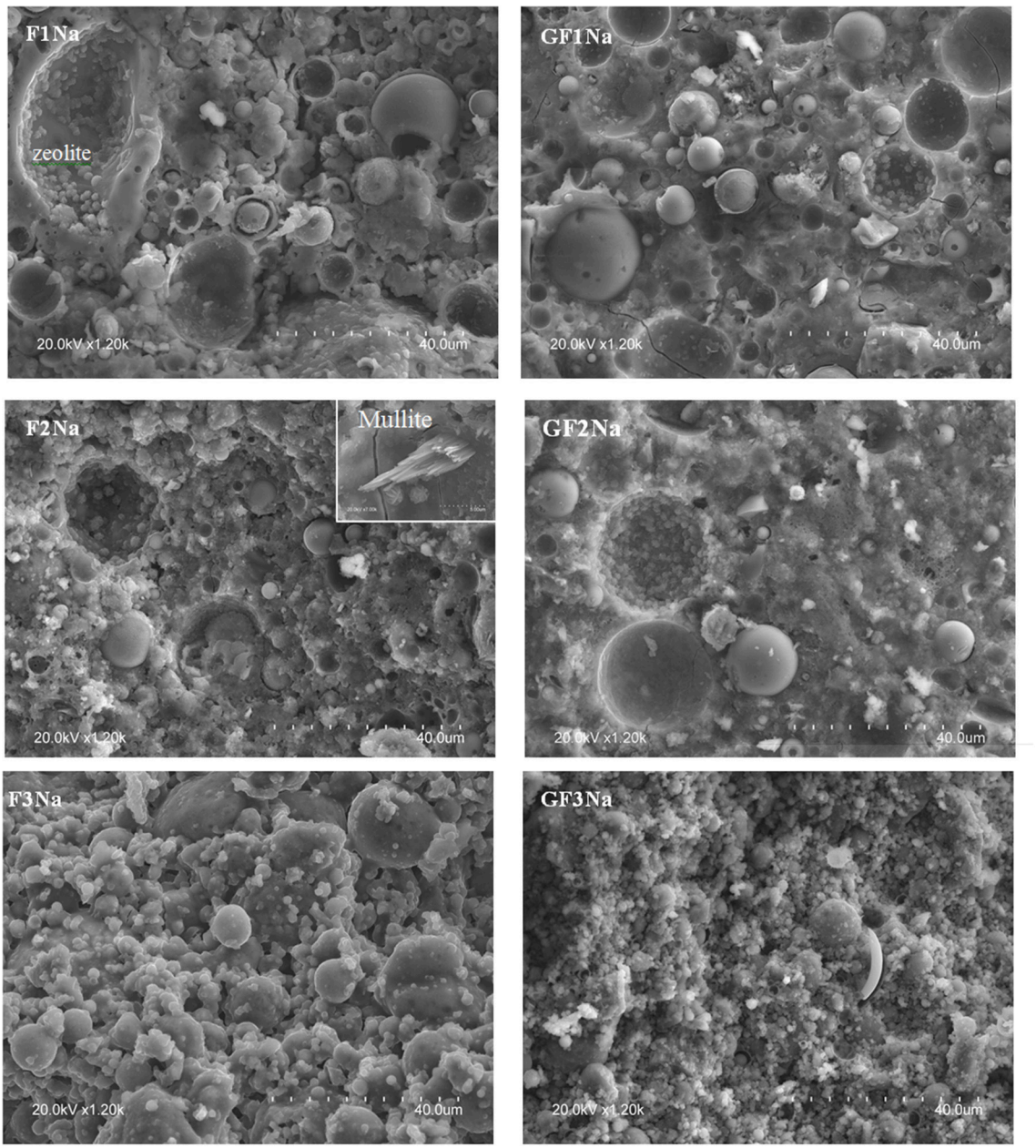

FIGURE 8 | SEM micrographs of pastes.

need for space. As **Figure 8** shows, zeolites form preferably inside cenospheres where they have sufficient space to crystallize and grow. Grinding the ash breaks these hollow particles, leaving a smaller number of voids. Fewer zeolites and more N-A-S-H gel raise mechanical strength (Panias et al., 2007; Criado et al., 2008).

Further to these data, for ash with similar vitreous phase contents, reducing the particle size substantially raises the mechanical strength that can be developed during alkaline activation. The question posed is: given a similar particle size, how does vitreous phase content affect ash reactivity? Although after grinding the three ashes had very similar particle size (d50 ranges between 5 and 7 μm), their mechanical strength values differed significantly. According to the proportion of potentially reactive phase identified by attacking the ash with acid (see **Figure 2**), the highest strength should have been recorded for ash GF1 followed by GF2 and GF3. Nonetheless, mechanical strength was the greatest in ash GF2.

Many studies have attempted to establish a criterion for assessing ash quality for the manufacture of alkaline cements (Fernández-Jiménez and Palomo, 2003; Fernández-Jiménez et al., 2005; Zhuang et al., 2016). The present authors deem that vitreous phase content, $(SiO_2/Al_2O_3)_{reactive}$ ratio and fineness are

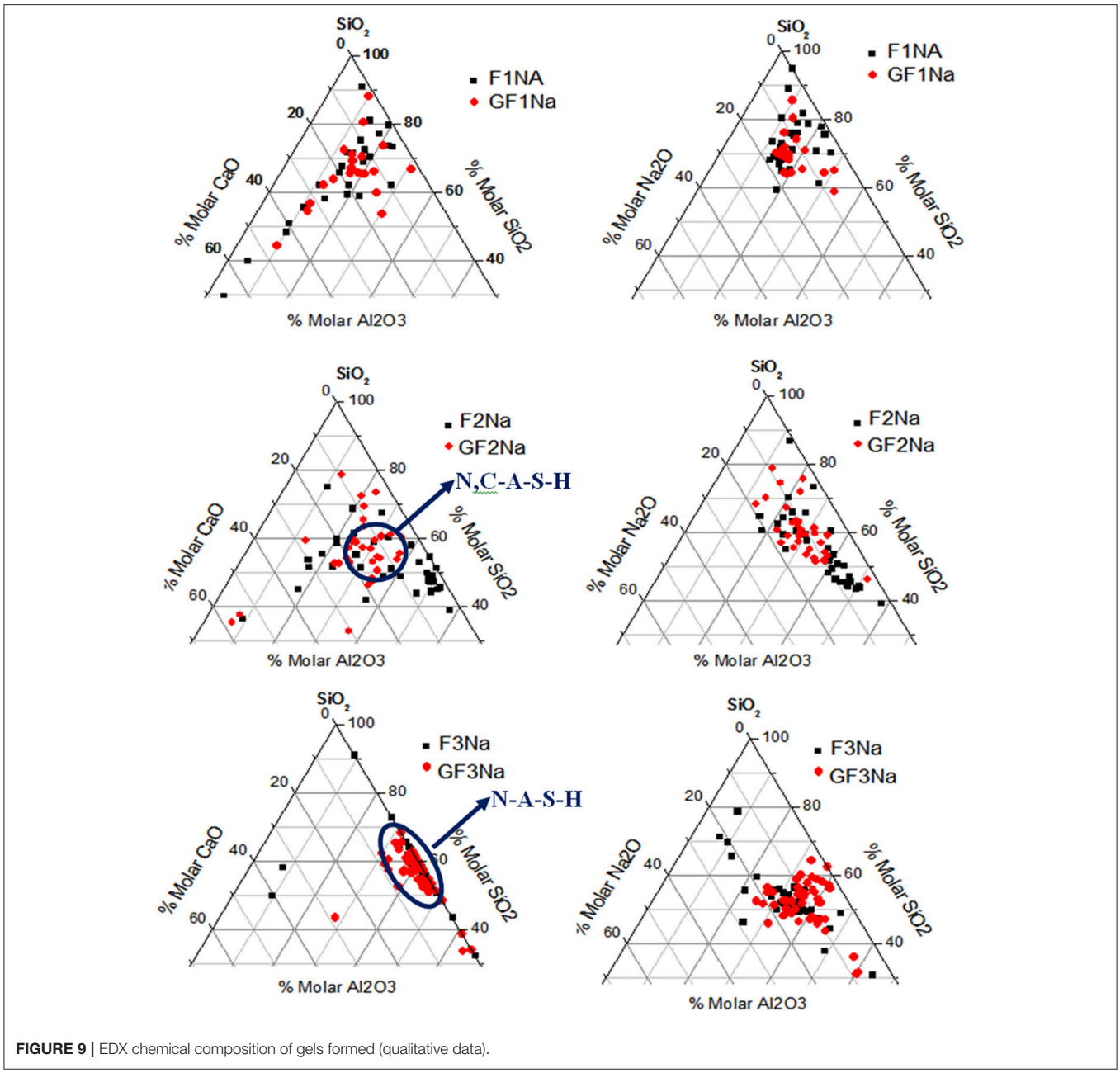

FIGURE 9 | EDX chemical composition of gels formed (qualitative data).

determinants that provide an approximate idea of the reactive potential of an ash. Nonetheless, the findings reported here suggest the existence of yet another parameter that may affect ash reactivity. The effect of minority elements in the ash (network modifiers such as alkalis, calcium, titanium, or iron) must be taken into consideration, inasmuch as their inclusion in the glass structure may modify its solubility. Presumably, the higher the concentration of such elements in the vitreous phase, the greater its glass reactivity. That hypothesis concurs partially with the one put forward by Zhang et al. (2016).

Determining the presence of network modifiers in the vitreous phase with the techniques deployed here is hardly straightforward. Comparing the ^{29}Si NMR spectra for ashes F1 and F2, however, revealed that the zone between−80 and−100 ppm was more intense in the latter than in the former. That may be indicative of a less polymerized and consequently more reactive glass, which would explain the higher strength in F2, fruit of a higher initial degree of reaction. The present authors feel, however, that the structure and composition of the gel forming as the main reaction product is another factor to be borne in mind when explaining mechanical strength. The EDX findings (see **Figure 9**) showed that as a rule the gel forming in pastes F2Na and GF2Na had a higher SiO_2/Al_2O_3 ratio, a finding consistent with the higher $(SiO_2/Al_2O_3)_{reactive}$ ratio determined

by acid attack. Reports can be found in the literature showing that more silica-rich N-A-S-H gels yield higher strength alkaline cements (Fernández-Jiménez et al., 2006; Criado et al., 2008; Provis et al., 2009).

The suitability of coal fly ash for manufacturing alkaline cements can in any event be predicted fairly precisely on the grounds of physical, mineralogical and chemical parameters (fineness, chemical composition, vitreous phase content...), which can approximate reactivity. Nonetheless, given a vitreous phase content that can be regarded as acceptable (>30%, see ash F3), fineness prevails over glass content.

This fact is promising with a view to raising fly ash reactivity. The mineralogical and chemical compositions of ash depend essentially on the coal and burning conditions used in steam-fired power plants and are consequently very difficult to control or modify. Fineness, in contrast, can be readily established and manipulated. This study shows that in ash with <80–90% of particles under 45 μm, grinding would suffice to raise reactivity substantially. Ash such as F3 that initially failed to harden into a sufficiently compact specimen when alkali-activated, after grinding yielded mechanical strength of up to 18 MPa, a value similar to that was observed for unground ash F1.

CONCLUSIONS

The conclusions drawn from the findings of this study are listed below:

- Fly ash reactivity depends essentially on fineness, vitreous phase content and chemical composition ($(SiO_2/Al_2O_3)_{reactive}$). Modifying the first parameter via mechanical activation is unquestionably the simplest way to heighten and control reactivity.
- Mechanical activation has only a minor effect on fly ash reactivity, inasmuch as the amount of potentially reactive SiO_2 and Al_2O_3 depends more on the mineralogical phases in the ash than on fineness.
- The mechanical activation of fly ash enhanced initial strength development substantially in the alkaline cements studied due to reaction kinetics: more ash reacted in less time.
- Mechanical activation of ash affects the nature of the reaction products formed: a faster reaction rate generates more N-A-S-H or N,C-A-S-H gel and fewer zeolites as secondary reaction products. A higher gel content contributes to higher mechanical strength.
- In this study, which compared ashes with different chemical compositions, mechanical activation of the materials was observed to enhance mechanical strength development substantially, partially offsetting low vitreous phase contents or scantly optimal $(SiO_2/Al_2O_3)_{reactive}$ ratios.

AUTHOR CONTRIBUTIONS

IG-L and OM conducted the experiments, data analyses and characterizations. AF-J and IG-L drafted the manuscript. AP helped with manuscript preparation and supervised the overall research. AF-J and IG-L finalized the manuscript.

ACKNOWLEDGMENTS

This research was funded by the Spanish Ministry of the Economy and Competitiveness and FEDER under research projects BIA2013-43293-R, BIA2016-76466-R, and RTC2016-4872-S.

SUPPLEMENTARY MATERIAL

The Supplementary Material for this article can be found online at: https://www.frontiersin.org/articles/10.3389/fmats.2019.00051/full#supplementary-material

Figure S1 | SEM Micrographs of the coal fly ashes before (F1, F2 and F3) and after grinding (F1G, F2G and F3G).

REFERENCES

Bai, C., and Colombo, P. (2018). Processing, properties and applications of highly porous geopolymers: a review. *Ceramics Int.* 44, 16103–16118. doi: 10.1016/j.ceramint.2018.05.219

Chindaprasirt, P., De Silva, P., Sagoe-Crentsil, K., and Hanjitsuwan, S. (2012). Effect of SiO_2 and Al_2O_3 on the setting and hardening of high calcium fly ash-based geopolymer systems. *J. Mater. Sci.* 47, 4876–4883. doi: 10.1007/s10853-012-6353-y

Chindaprasirt, P., Jaturapitakkul, C., and Sinsiri, T. (2005). Effect of fly ash fineness on compressive strength and pore size of blended cement paste. *Cem. Concr. Compos.* 27, 425–432. doi: 10.1016/j.cemconcomp.2004.07.003

Communication from the Commission to the European Parliament, the Council, the European Economic and Social Committee and the Committee of the Regions (2011). *Roadmap to a Resource Efficient Europe* (COM), 571. Available online at: http://eur-lex.europa.eu/legal-content/EN/TXT/?uri=CELEX:52011DC0571

Criado, M., Fernández-Jiménez, A., Palomo, A., Sobrados, I., and Sanz, J. (2008). Effect of the SiO_2/Na_2O ratio on the alkali activation of fly ash. Part II: ^{29}Si MAS-NMR Survey. *Micropor. Mesopor. Mater.* 109, 525–534. doi: 10.1016/j.micromeso.2007.05.062

CSI/ECRA—Cement Sustainability Initiative/ European Cement Research. (2017). *Technology Papers 2017 Development of State of the Art Techniques in Cement Manufacturing: Trying to Look Ahead, Dusseldorf, Geneva*. Available online at: www.wbcsdcement.org (Accessed December 30, 2017).

De Silva, P., Sagoe-Crenstil, K., and Sirivivatnanon, V. (2007). Kinetics of geopolymerization: role of Al_2O_3 and SiO_2. *Cem. Concr. Res.* 37, 512–518. doi: 10.1016/j.cemconres.2007.01.003

Duvallet, T., Frouin, L., and Robl, L. T. (2015). "Effect of fly ash particle packing on performance of OPC-activated GGBS slag," *Presented at the 2015 World of Coal Ash Conference* (Nashville).

Duxson, P., Lukey, G. C., Separovic, F., and van Deventer, J. S. J. (2005). Effect of alkali cations on aluminum incorporation in geopolymeric gels. *Ind. Eng. Chem. Res.* 44, 832–839. doi: 10.1021/ie0494216

Engelhardt, G., and Michel, D. (1987). *High Resolution Solid State NMR of Silicates and Zeolites*. New York, NY: John Wiley and Sons.

Fernández-Jiménez, A., Cristelo, N., Miranda, T., and Palomo, A. (2017). Sustainable alkali activated materials: precursor and activator derived from industrial wastes. *J. Cleaner Prod.* 162, 1200–1209. doi: 10.1016/j.jclepro.2017.06.151

Fernández-Jiménez, A., and Palomo, A. (2003). Characterization of fly ashes. Potential reactivity as alkaline cements. *Fuel* 82, 2259–2265. doi: 10.1016/S0016-2361(03)00194-7

Fernández-Jiménez, A., and Palomo, A. (2007). Factors affecting early compressive strength of alkali activated flys ash (OPC fee) concrete. *Mater. Construt.* 57, 7–22.

Fernández-Jiménez, A., Palomo, A., and Criado, M. (2005). Microstructure development of alkali-activated fly ash cement: a descriptive model. *Cem. Concr. Res.* 35, 1204–1209. doi: 10.1016/j.cemconres.2004.08.021

Fernández-Jiménez, A., Palomo, A., Sobrados, I., and Sanz, J. (2006). The role played by the reactive alumina content in the alkaline activation of fly ashes. *Microporous Mesoporous Mater.* 91, 111–119. doi: 10.1016/j.micromeso.2005.11.015

Garcia-Lodeiro, I., Fernández-Jiménez, A., and Palomo, A. (2013). Variation in hybrid cements over time. Alkaline activation of fly ash–portland cement blends. *Cem. Concr. Res.* 52, 112–122. doi: 10.1016/j.cemconres.2013.03.022

Garcia-Lodeiro, I., Palomo, A., Fernández-Jiménez, A., and Macphee, D. E. (2011). Compatibility studies between N-A-S-H and C-A-S-H gels. Study in the ternary diagram Na_2O–CaO–Al_2O_3-SiO_2-H_2O. *Cem. Concr. Res.* 41, 923–931. doi: 10.1016/j.cemconres.2011.05.006

Hajimohammadi, A., Provis, J. L., and van Deventer, J. S. J. (2010). Effect of alumina release rate on the mechanism of geopolymer gel formation. *Chem. Mater.* 22, 5199–5208. doi: 10.1021/cm101151n

Hemalatha, T., and Ramaswamy, A. (2017). A review on fly ash characteristics e towards promoting high volume utilization in developing sustainable concrete. *J. Cleaner Prod.* 147, 546–559. doi: 10.1016/j.jclepro.2017.01.114

Koller, H., and Engelhardt, G. (1994). ^{23}Na NMR spectroscopy of solids: interpretation of quadrupole. Interaction parameters and chemical shifts. *J. Phys. Chem.* 98, 1544–1551. doi: 10.1021/j100057a004

Kovalchuk, G., Fernández-Jiménez, A., and Palomo, A. (2007). Alkali-activated fly ash: effect of thermal curing conditions on mechanical and microstructural development—Part II. *Fuel* 86, 315–322. doi: 10.1016/j.fuel.2006.07.010

Kumar, S., Kristály, F., and Mucsi, G. (2015). Geopolymerisation behaviour of size fractioned fly ash. *Adv. Powder Technol.* 26, 24–30. doi: 10.1016/j.apt.2014.09.001

Kumar, S., and Kumar, R. (2011). Mechanical activation of fly ash: effect on reaction, structure and properties of resulting geopolymer. *Ceram. Inter.* 37, 533–541. doi: 10.1016/j.ceramint.2010.09.038

Marjanovic, N., Komljenovic, M., Bašcarevic, Z., and Nikolic, V. (2014). Improving reactivity of fly ash and properties of ensuing geopolymers through mechanical activation. *Constr. Build. Mater.* 57, 151–162. doi: 10.1016/j.conbuildmat.2014.01.095

Merwin, L. H., Sebald, A., Rager, H., and Schneider, H. (1991). ^{29}Si and ^{27}Al MAS NMR spectroscopy of mullite. *Phys. Chem. Minerals* 18, 47–52. doi: 10.1007/BF00199043

Nikolic, V., Komljenovic, M., Bašcarevic, Z., Marjanovic, N., Miladinovic, Z., and Petrovic, R. (2015). The influence of fly ash characteristics and reaction conditions on strength and structure of geopolymers. *Construct. Build. Mater.* 94, 361–370. doi: 10.1016/j.conbuildmat.2015.07.014

Palomo, A., Krivenko, P., Garcia-Lodeiro, I., Kavalerova, E., Maltseva, O., and Fernández-Jiménez, A. (2014). A review on alkaline activation : new analytical perspectives. *Mater. Construt.* 641, 23. doi: 10.3989/mc.2014.00314

Panias, D., Giannopoulou, I. P., and Perraki, T. (2007). Effect of synthesis parameters on the mechanical properties of fly ash-based geopolymers. *Colloids Surf A* 301, 246–54. doi: 10.1016/j.colsurfa.2006.12.064

Paya, J., Monzo, J., Borrachero, M. V., Peris, E., and Gonzalez-Lopez, E. (1997). Mechanical treatment of fly ashes. Part III: studies on strength development of ground fly ashes (GFA) – cement mortars. *Cem. Concr. Res.* 27, 1365–77. doi: 10.1016/S0008-8846(97)00129-4

Provis, J., and van Deventer, J. S. J. (2014). *Alkali Activated Materials: State-of-the-Art Report*. London, UK: Springer.

Provis, J. L., Yong, C. Z., Duxon, P., and van Deventer, J. S. J. (2009). Correlating mechanical and thermal properties of sodium silicate-fly ash geopolymer. *Colloids Surf. A Physicochem. Eng. Asp.* 336, 57–63. doi: 10.1016/j.colsurfa.2008.11.019

Rakesh, K., Sanjay, K., and Mehrotra, S. P. (2007). Towards sustainable solutions for fly ash through mechanical activation Resources. *Resour. Conserv. Recycl.* 52, 157–179. doi: 10.1016/j.resconrec.2007.06.007

Ruiz-Santaquiteria, C., Skibsted, J., Fernández-Jiménez, A., and Palomo, A. (2013). Clay reactivity: production of alkali activated cements. *Appl. Clay Sci.* 73, 11–16. doi: 10.1016/j.clay.2012.10.012

Sagoe-Crentsil, L. W., Brown, T., and Song, S. (2005). Effects of aluminates on the formation of geopolymers. *Mater. Sci. Eng. B* 117, 163–168. doi: 10.1016/j.mseb.2004.11.008

Sanz, J., Madani, A., Serratosa, J. M., Moya, J. S., and Aza, S. (1988). Aluminum-27 and Silicon-29 Magic-Angle Spinning Nuclear Magnetic Resonance Study of the Kaolinite-Mullite Transformation. *J. Amer. Cer. Soc.* 71, 3024–3028. doi: 10.1111/j.1151-2916.1988.tb07513.x

Schmucker, M., Schneider, H., and MacKenzie, K. J. D. (1998). Mechanical amorphization of mullite and thermal recrystallization. *J. Non-Crystalline Sol.* 226, 99–104. doi: 10.1016/S0022-3093(98)00366-4

Shekhovtsova, J., Zhernovsky, I., Kovtun, M., Kozhukhova, N., Zhernovskaya, I., and Kearsley, E. (2018). Estimation of fly ash reactivity for use in alkali activated cements step towards sustainable building material and waste utilization. *J. Cleaner Prod.* 178, 22–33. doi: 10.1016/j.jclepro.2017.12.270

Temuujin, J., Williams, R. P., and van Riessen, A. (2009). Effect of mechanical activation of fly ash on the properties of geopolymer cured at ambient temperature. *J. Mater. Process. Technol.* 209, 5276–5280. doi: 10.1016/j.jmatprotec.2009.03.016

Thomas, M. (2007). *Optimizing the Use of Fly Ash in Concrete Association*. Available online at: http://www.cement.org/docs/default-source/fc_concrete_technology/is548-optimizing-the-use-of-fly-ash-concrete.pdf (Accessed April 2, 2017).

Walkley, B., San Nicolas, R., Sani, M. A., Rees, G. J., Hanna, J. V., van Deventer, J. S. J., et al., (2016). Phase evolution of C-(N)-A-S-H/N-A-S-H gel blends investigated via alkali-activation of synthetic calcium aluminosilicate precursors. *Cem. Concr. Res.* 89, 120–135. doi: 10.1016/j.cemconres.2016.08.010

Zhang, Z., Provis, J. L., Zou, J., Reide, A., and Wang, H. (2016). Towards an indexing approach to evaluate fly ashes for geopolymer manufacture. *Cem. Concr. Res.* 85, 163–173. doi: 10.1016/j.cemconres.2016.04.007

Zhou, W., Yan, C., Duan, P., Liu, Y., Zhang, Z., Qiu, X., et al., (2016). A comparative study of high- and low-Al_2O_3 fly ash based-geopolymers: the role of mix proportion factors and curing temperature. *Mater. Des.* 95 63–74. doi: 10.1016/j.matdes.2016.01.084

Zhuang, X. Y., Chen, L., Komarneni, S., Zhou, C. H., Tong, D. S., Yang, H. M., et al., (2016). Fly ash-based geopolymer: clean production, properties and applications. *J. Cleaner Prod.* 125, 253–267. doi: 10.1016/j.jclepro.2016.03.019

Conflict of Interest Statement: The authors declare that the research was conducted in the absence of any commercial or financial relationships that could be construed as a potential conflict of interest.

frontiers in Materials

ORIGINAL RESEARCH
published: 18 April 2019
doi: 10.3389/fmats.2019.00066

Studies About the Hydration of Hybrid "Alkaline-Belite" Cement

M. J. Sánchez-Herrero, Ana Fernández-Jiménez and A. Palomo*

Department of Materials, Eduardo Torroja Institute (CSIC), Madrid, Spain

The mechanical performance of a hybrid cement containing 48% fly ash, 48% mineralized belite clinker, 1. 5% gypsum and 2.5% Na_2SO_4 was analyzed and the hydration products were identified. The findings showed that the newly designed cement met European standard EN 197-1 compositional, mechanical and setting time requirements (cement type IVB). The hydration products forming in this blended "alkaline-belite" cement (as it was determined through XRD, ^{29}Si and ^{27}Al MAS NMR and electron microscopy) consisted in a mix of cementitious gels: C-(A)-S-H and N-(C)-A-S-H, which interacted and over time evolved toward the latter with no detriment to the mechanical strength developed by the cement.

Keywords: hybrid cement, belitic cement, alkaline cement, NMR-MAS, XRD

OPEN ACCESS

Edited by:
Miroslav Komljenovic, University of Belgrade, Serbia

Reviewed by:
Yiannis Pontikes, KU Leuven, Belgium
Ionut Ovidiu Toma, Gheorghe Asachi Technical University of Iaşi, Romania

****Correspondence:***
Ana Fernández-Jiménez
anafj@ietcc.csic.es

Specialty section:
This article was submitted to Structural Materials, a section of the journal Frontiers in Materials

Received: *22 January 2019*
Accepted: *01 April 2019*
Published: *18 April 2019*

Citation:
Sánchez-Herrero MJ, Fernández-Jiménez A and Palomo A (2019) Studies About the Hydration of Hybrid "Alkaline-Belite" Cement. Front. Mater. 6:66. doi: 10.3389/fmats.2019.00066

INTRODUCTION

The CO_2 emissions due to Portland cement production are environmentally problematic mainly due to the very high volume of demand for cement in view of concrete needs in the world. Actually, Portland cement production is continuously increasing at global level and there exists a general agreement to consider Portland cement responsible of 7–8% of the total emissions of carbon dioxide in the world (Scrivener et al., 2018a). The use of alternative fuel, the addition of minerals to Portland cement, the inclusion of mineralizers and fluxes in the raw mix, along with the development of alternative binders, are some of the sustainable solutions envisaged today by the cement industry and the scientific community (Lothenbach et al., 2011; Zhang et al., 2012). Belite (Chatterjee, 1996; García-Díaz et al., 2011; Staněk and Sulovský, 2015), alkaline and hybrid alkaline cements (Deschner et al., 2012; García Lodeiro et al., 2013, 2016) are among the binders studied as alternatives to the traditional Portland cement.

The use of supplementary cementitious materials (SCMs, pozzolans, fly ash, blast furnace slag, limestone, etc.) as a partial substitute of Portland cement clinker in the so-called "blended cements" (Lothenbach et al., 2011; Zhang et al., 2012; Wa et al., 2018) represents not only a feasible solution but, for sure, the most investigated one. However, due to the low hydraulic activity of the SCMs, blended cements usually show delayed setting times and low early mechanical strength development, which is actually limiting the replacement of clinker by SCMs in the cement (Lothenbach et al., 2011). Obviously, many investigations are being focused on how to improve the reactivity of these SCMs. The main choices are: (i) Mechanical activation (Knop and Peled, 2016; Liu et al., 2018) (controlling the particle size distribution); (ii) Thermal activation (Vizcaíno-Andrés et al., 2015; Scrivener et al., 2018b) (especially for calcined clays—LC3 technology—); (iii) Chemical activation (Ruiz-Santaquiteria et al., 2013; Allahverdia and Malekia Mahinroosta, 2018) ("alkaline activated cement"). It is quite probable that future will lead to us to a combination of those options above mentioned like the most effective choice.

In this context the main goal of this work is to describe and discuss part of a research project (leaded by authors of this paper) linked with the development of some different types of "Hybrid

Alkaline Cements" (HYC). HYC are binders containing a small fraction of Portland clinker (or even blast furnace slag) as a source of calcium, a large fraction of aluminosilicate materials (from natural origin or byproducts from some industries, such as fly ashes (Deschner et al., 2012; García Lodeiro et al., 2013, 2016) as a source of Si and Al, and obviously some alkaline additive. Due to a wide compositional range and to a high technological, economical and environmental potential, HYC are the object of considerable research (Qu et al., 2016; Al-Kutti et al., 2018).

Inasmuch as the presence of alkalis in the medium affects, aluminosilicate and Portland clinker reactivity, this study undertook an in-depth analysis of calcium silicate and calcium aluminate behavior after hydration by a number of alkaline solutions of different concentrations. The findings revealed that the compressive strength of C_3A, C_3S and β-C_2S pastes rose in the presence of alkaline additives (Sánchez-Herrero et al., 2012, 2016). Most significantly, given the low initial reactivity of β-C_2S under normal hydration conditions, the presence of such alkaline additives hastened its hydration, affecting setting and hardening times substantially.

A mineralized belite clinker (with a belite content of over 50%) was first synthesized in the laboratory. In light of its good performance and given that the clinkerization temperature could be lowered considerably in the presence of the fluxing pair formed by "$CaSO_4$ and CaF_2," the clinker was subsequently manufactured on an industrial scale with satisfactory results. The industrial belite clinker was then blended with fly ash, gypsum (the setting regulator) and Na_2SO_4 as an alkaline additive to produce the "alkaline-belite" cement (some type of HYC).

This paper consequently describes and discusses the main singular characteristics (mechanical behavior and microstructural development) of this "alkaline-belite" cement initially formulated in the laboratory and successfully produced on an industrial scale. This advance in the design of an alkaline-belitic binder (reasonably sustainable one) was achieved due to a close collaboration between the scientific and industrial communities who simultaneously deployed some different technologies (different fields of knowledge within the "cement science") in order to produce and study the new "alkaline-belite" hybrid cement which was the object of the project. The different fields of knowledge simultaneously applied in this project were: the use of mineralizers and fluxes to produce low energy clinkers (Blanco-Varela et al., 1997; García-Díaz et al., 2011), the use of industrial by-products to generate blended cements with a low clinker factor (Deschner et al., 2012; García Lodeiro et al., 2013); and the use of affordable and innocuous natural mineral salts (alkaline additives with a minimal environmental impact) to stimulate the alkaline activation processes (García Lodeiro et al., 2016).

TABLE 1 | Chemical (wt% of oxides) and mineralogical composition of the materials.

Chemical composition (wt% of oxides)				Mineralogical composition (%)	
Oxide	**Ash**	**Clinker**	**Gypsum**	**Phase**	**Hybrid cement**
SiO_2	51.4	21.8	19.1	SiO_2	6.3
Al_2O_3	25.8	5.9	7.6	Mullite	4.8
Fe_2O_3	5.7	2.6	2.7	C_3S	11.4
CaO	4.6	60.5	20.5	β-C_2S	19.3
MgO	1.5	2.7	2.8	C_3A	1.3
SO_3	0.8	3.8	25.5	C_4AF	3.8
K_2O	1.7	1.7	1.5	$C_{11}A_7.CaF_2$	1.1
LoI	6.2(1)	0.0	19.7(2)	$CaSO_4.2H_2O$	1.2
Other	2.3	1.0	0.6	Na_2SO_4	2.2
Total	100	100	100	Amorphous	48

EXPERIMENTAL

Materials

A mineralized belite clinker produced in an industrial rotary kiln, a fly ash, gypsum (all supplied by the manufacturer) and 99.9% pure sodium sulfate (MERCK laboratory reagent) were

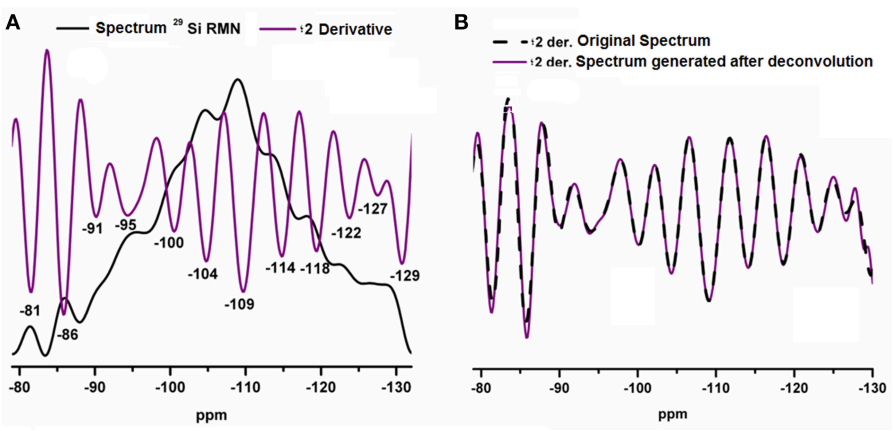

FIGURE 1 | (A) ^{29}Si MAS NMR spectrum for fly ash and second derivative of the spectrum; **(B)** second derivatives of the original ^{29}Si MAS NMR spectrum for fly ash and of the envelope generated by deconvolution.

used to prepare the hybrid cement. The respective chemical compositions are given in **Table 1**. The mineralogical phases present in the hybrid cement were identified with X-ray diffraction and quantified via Rietveld refinement of the XRD patterns (Rietveld, 1969). The software used: GSAS (General Structure Analysis System).

The fly ash used in this research was supplied by a thermal power plant located at Compostilla (Spain) and owned by Endesa (Spanish Electricity Company). This fly ash is a type F one (ASTM C 618) and is considered like a "good" fly ash. Some Spanish cement producers and concrete producers located at northern Spain are usual consumers of such a fly ash to produce their materials.

Methodology

The alkaline-belite cement or hybrid cement contained 48% fly ash, 48% mineralized belite clinker, 1.5% gypsum and 2.5% Na_2SO_4. The belite-alkaline cement was observed to have 95% of the particles are smaller than 32 μm, with a d50 of 6 μm. The smaller particle size of hybrid "belitic-alkaline" was associated by operators of the mill (at least partially) with the presence of high contents of fly ash in its composition.

The hydration reactions were explored and the hydration products analyzed on cubic ($3 \times 3 \times 3$ cm^3) paste specimens prepared with a water/cement ratio of 0.29, based on consistency (EN 196-3) testing. The setting time of the pastes was determined according to the standard EN 196-3:2017 Methods of testing cement—Part 3: Determination of setting times and soundness for a water/cement ratio of 0.29.

Mechanical strength was determined on $4 \times 4 \times 16$ cm^3 prismatic mortar specimens with a sand/cement ratio of 3:1 (EN 196-1) and a water/cement ratio of 0.45. The considerable rise in cement paste fluidity in the presence of fly ash generally translates into smaller mixing water content. Although European standard (EN 196-1 and EN 197-1) stipulates a water/cement ratio of 0.5 for mortars, here the value used was the result of slump testing, in line with the practice recommended in the ASTM standard (ASTM C230: Flow Table for Use in Tests of Hydraulic Cement).

The specimens were removed from the molds after 24 h of initial chamber curing at 21°C and 95% relative humidity and then stored in a climatic chamber until the test age (2 d, 7 d, 28 d, 90 d, or 180 d). Mortar specimens were tested for compressive and flexural strength (three for bending and six for compressive strength at each test age) on an Ibertest Autotest-200/10-SW frame (Madrid, Spain).

After the paste specimens were tested for strength they were crushed to a powder and mixed with acetone and ethanol to detain hydration and prepare the materials for mineralogical and microstructural characterization via XRD and NMR.

The XRD patterns were recorded on a Bruker D8 Avance diffractometer (Karlsruhe, Germany). The instrumental conditions were: Cu K′$\alpha_{1,2}$ radiation (1.540 Å, 1.544 Å); no monochromator; goniometer radius, 217.5 mm. The settings for the hydrated pastes were: variable 6-mm divergence slit (hydrated pastes); 2θ angle, 5° to 60°; step time, 0.5 s; step size, 0.02°. The anhydrous samples were scanned under different conditions for Rietveld quantification: divergence slit, 0.5°; 2θ scanning range, 5° to 70°; step time, 2 s; step size, 0.02°.

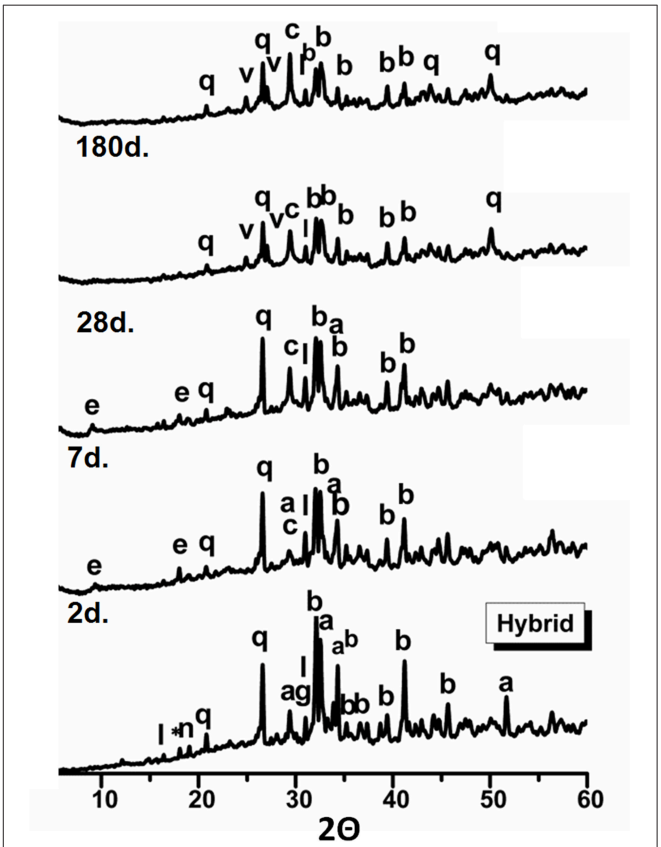

FIGURE 2 | Anhydrous and 2 d, 7 d, 28 d, and 180 d hydrated paste diffractograms *Legend:* **b,** C_2S(86-0398); **a**, C_3S(70-8632); **q**, quartz [SiO_2](46-1045); **g**, gypsum [$Ca_2SO_4.2H_2O$] (33-0311); **l,** mullite[$Al_6Si_2O_{13}$] (73-1389); **n**, Na_2SO_4 (74-2036); **e**, ettringite [$Ca_6Al_2(SO_4)_3(OH)_{12}.26H_2O$] (41-1451); **c**, calcite[$CaCO_3$] (86-0174); ***,** $C_{12}A_7$ (70-2144); **v**, vaterite [$CaCO_3$](74-1867); (in brackets, PDF codes).

TABLE 2 | Mortar strength ($4 \times 4 \times 16$ cm^3 specimens) and setting times for "alkaline-belite" hybrid cement.

Compressive strength (MPa)					Setting time (min)	
2 d	**7 d**	**28 d**	**90 d**	**180 d**	**Initial**	**Final**
10.8 ± 0.2	22.2 ± 0.5	40.0 ± 1.1	47.7 ± 1.6	51.9 ± 0.9	83	193

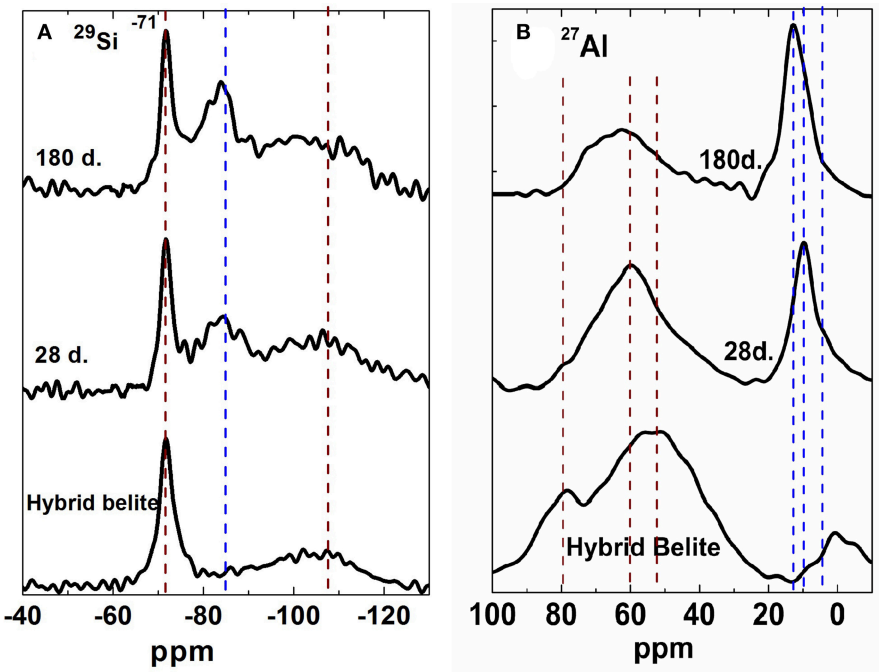

FIGURE 3 | (A) ^{29}Si MAS NMR and **(B)** ^{27}Al MAS NMR spectra for anhydrous hybrid alkaline-belite cement and 28 d and 180 d hydrated pastes.

The ^{29}Si and ^{27}Al nuclei were scanned on a Bruker MSL 400 NMR spectrometer. The conditions for ^{29}Si were: resonance frequency, 79.5 MHz; spinning rate 10 kHz; pulse sequence, single pulse (5 μs); recycle delay, 10 s; number of transients, 4912; internal standard for measuring chemical shift (in ppm), tetramethylsilane (TMS). For ^{27}Al they were: resonance frequency, 104.3 MHz; spinning rate, 10 kHz; recycle delay, 5 s; pulse sequence, single pulse (2 μs); number of transients, 400; internal standard for chemical shift measurements (in ppm), $Al(H_2O)_6^{3+}$.

The ^{29}Si NMR spectra were deconvoluted in order to determine the number and position of the signals analyzed. The second derivative criterion was used (Kucherov and Kochubei, 1983; Pérez et al., 2014). This procedure is highly useful when analyzing spectra with wide, poorly defined signals, inasmuch as it resolves closely juxtaposed resonant frequencies and determines the exact position of each. In this particular case two software applications (OriginPro 9 and MestReNova) were used with the objective of avoiding practical mistakes. The ^{29}Si MAS NMR signals exhibited a Lorentzian/Gaussian (L/G) ratio of 0.5 (independent on the software). First derivative analysis reveals the presence of peaks that appear as shoulders or weak signals on the original spectrum, whilst the second derivative furnishes more precise information in the form of minima, the value of which concurs with the peak on the main signal. The number of points taken into account during the analysis (in the zone of the spectrum between −60 and −130 ppm) was 450 approximately. **Figure 1** is an example of ^{29}Si MAS NMR spectra of our fly ash. This spectrum at **Figure 1** is an example of analysis by following the already explained procedure.

Finally some samples were vacuum dried and carbon-coated for examination under a HITACHI S-4800 (Tokyo, Japan) scanning electron microscope fitted with a Bruker energy dispersive spectroscope to confirm the working hypotheses. For BSEM analysis, the samples were embedded in epoxy resin, cut and polished with ethanol prior to vacuum drying and carbon coating.

RESULTS AND DISCUSSION

Material Properties

Material compressive strength and setting time data are given in **Table 2**. The mechanical strength development of mortars (4 × 4 × 16 cm^3 prismatic) was 10.8 MPa at 2 days 40.0 MPa at 28 days, and 51.9 MPa at 180 days. The initial setting time was t_i = 83 m. and the final t_F = 193 m; the belitic hybrid cement met European standard requirements for 32.5 type cement (EN 197-1 Cement—Part 1: Composition, specifications and conformity criteria for common cement).

As noted, this cement contained 48% mineralized belite clinker, which is characterized by low early age reactivity (Taylor, 1997). According to these findings, the constituents of the alkaline-belite cement generated synergies during hydration that contributed favorably to strength development. The heat of hydration released by the belite clinker fraction, in conjunction with the presence of the Na_2SO_4, sufficed to alkali-activate the fly ash, affording the system good initial mechanical behavior. Furthermore, as noted in prior studies (Sánchez-Herrero et al., 2017), the data appeared to indicate that the presence of the alkaline additive stimulated greater strength development in the

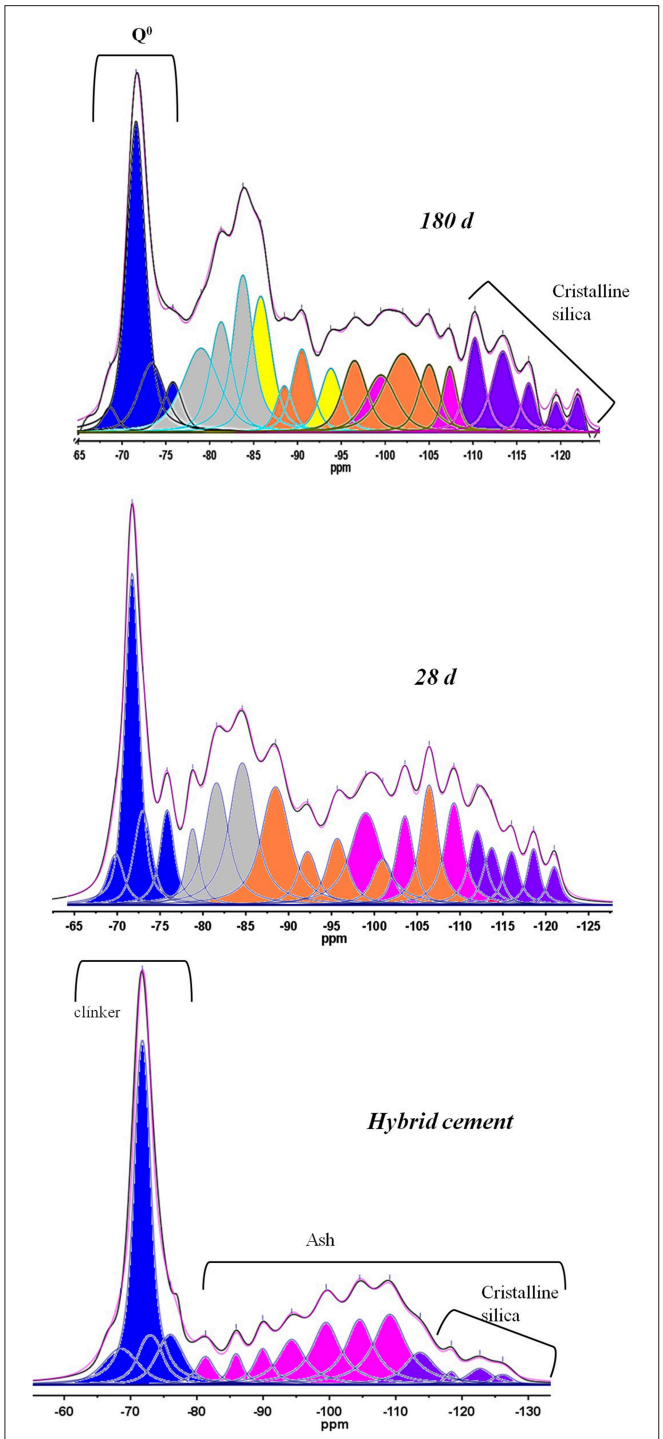

FIGURE 4 | ^{29}Si MAS NMR spectra for anhydrous and 28 d and 180 d hydrate hybrid belitic cement. Legend for hydration products: gray (Q^1, Q^2(0Al)(1Al)); orange (Q^4(0Al)(1Al)(2Al)(3Al)(4Al)); yellow (Q^3(1Al)(3Al)).

TABLE 3 | Chemical shifts (ppm) recorded after deconvolution of ^{29}Si MAS NMR spectra for hybrid cement and 28 d and 180 d cement pastes.

Attributed to	Anhydrous		28 d		180 d	
	δ (ppm)	Area (%)	δ (ppm)	Area (%)	δ (ppm)	Area (%)
Q^0 C_3S	−68.5	5.6	−69.8	2.2	−68.6	1.04
Q^0 C_2S	−71.7	27.5	−71.4	14.0	−71.6	15.0
Q^0 C_3S	−73.0	5.6	−73.0	5.1	−73.0	4.7
Q^0 C_3S	−76.0	6.0	−75.8	3.0	−75.8	2.4
Q^1 C-S-H	–	–	−78.8	3.0	−79.0	8.0
Ash/Q^2(1Al)	−81.3	2.5	−81.6	8.0	−81.3	6.2
Q^2(0Al)	–	–	−84.6	10.0	−83.8	9.0
Ash/Q^3(3Al)	−85.9	2.2	–	–	−85.8	7.7
Ash/Q^4(4Al)	−89.9	3.3	−88.5	8.7	−88.5	2.0
Q^4(3Al)	–	–	−92.2	3.2	−90.5	4.3
Ash/Q^3(1Al)	−94.3	6.6	–	–	−93.8	3.5
Q^4(2Al)	–	–	−95.7	4.4	−96.5	4.5
Ash/Q^4(mAl)	−99.4	9.6	−99.0	8.3	−99.5	4.5
Q^4(1Al)	–	–	−101.0	1.4	−102.0	7.1
Ash/Q^4(mAl)	−104.5	9.9	−103.6	5.0	–	–
Q^4(0Al)	–	–	−106.4	5.3	−105.0	3.5
Ash/Q^4(mAl)	−109.1	12.1	−109.3	5.4	−107.3	2.4
	–	–	−112.0	3.7	−110.2	4.3
Crystalline silica	−113.6	5.1	−113.7	2.8	−113.0	4.7
	–	–	−116.0	1.8	−116.3	1.8
Crystalline silica	−118.4	0.7	−118.6	2.1	−119.5	1.0
Crystalline silica	−122.7	2.1	−121.0	1.85	−121.5	1.1
Crystalline silica	−126.1	0.9	–	–	–	–

calcium silicates and aluminates present in the clinker than observed during normal water-based hydration.

In previous papers (Donatello et al., 2013) authors have already demonstrated that hybrid cements behave quite well when located in aggressive environmental conditions (sulfates, marine, acidic, etc.). Additionally, they do not undergo the ASR since alkalies are consumed in the reaction of activation of fly ashes (Malvar and Lenke, 2006).

Reaction Products

The XRD patterns for the anhydrous hybrid cement and the 2 d, 7 d, 28 d, and 180 d hydrated pastes are reproduced in **Figure 2**.

All the diffractograms exhibited a hump associated with the vitreous fraction of the fly ash and the existence of a cementitious gel precipitating during hydration. The intensity of the diffraction lines for belite was observed to decline steadily with hydration time.

All the pastes generated diffraction lines attributed to quartz and calcite. Ettringite was identified in the 2 d and 7 d patterns, whereas the 28 d and 180 d materials contained vaterite. No signals associated with portlandite were identified at any of the ages studied.

Figure 3 contains the ^{29}Si MAS NMR and ^{27}Al MAS NMR spectra for the anhydrous cement and the 28 d and 180 d pastes. Some of the signals on the hydrated paste spectra were absent on the scan for the anhydrous cement. These wide, poorly defined signals may be indicative of the presence of a mix of several components.

The ^{29}Si MAS NMR deconvoluted spectra for the hybrid cement and its hydrated pastes are reproduced in **Figure 4**, whilst

Table 3 give the chemical shifts and area for each signal identified on the spectra analyzed.

The ^{29}Si MAS NMR spectrum for the anhydrous cement exhibited a narrow signal in the clinker fraction at around −71 ppm attributed to belite, and a series of wider signals associated with the C_2S and C_3S Q^0 units in alite (Sánchez-Herrero et al., 2016, 2017). The area of the spectrum between −81 ppm and −120/−130 ppm was associated with the fly ash fraction in the cement. Deconvolution of this area of the spectrum revealed the presence of several components. The signals between −85 ppm and −108 ppm in the anhydrous cement, concurrent with the presence of the ash, were attributed to Q^4(mAl) units (**Figure 4** and **Table 3**) for, as these signals tended to disappear in the 28 d and 180 d spectra, they were associated with the vitreous phase in the fly ash (Engelhardth and Michael, 1987; Palomo et al., 2004). The signals at (absolute) values higher than −109 ppm, however, remained practically unchanged during cement hydration and were therefore associated with Q^4(0Al) units in the various crystalline forms of silica (Engelhardth and Michael, 1987). Mullite, in turn, a crystalline phase detected in this material through XRD, generated resonance frequencies at −86 ppm, −91 ppm, and −95 ppm (Merwin et al., 1991). The Q^0 and Q^4(mAl) units, respectively associated with the unreacted clinker and fly ash fractions, declined in intensity in the 28 d and 180 d pastes (García Lodeiro et al., 2013, 2016).

Attribution of the new signals appearing in the 28 d and 180 d pastes was not straightforward, for different units in the cementitious gel may overlap. In such complex systems, a single signal may be assigned to different units of the gel or gels precipitating during the reaction. The signal at −85 ppm for instance, may be attributed to a Q^2 unit in a C-S-H gel (Skibsted and Andersen, 2013), a Q^3(3Al) unit in a C-A-S-H gel (Puertas et al., 2011; Myers et al., 2015) or a Q^4(4Al) unit in an N-A-S-H gel (García-Lodeiro et al., 2010, 2011). In this study, attribution was based on the literature as well as the findings of other techniques discussed below (^{27}Al MAS NMR and BSEM/EDX).

Further to those criteria, the signals at −78.8/−79.0 ppm were associated with Q^1 units in C-S-H gel. Similarly, the signals at −81.6/−81.3 ppm and −84.6/−83.8 ppm were attributed to Q^2(1Al) and Q^2(0Al) units in C-(A)-S-H-like gels. C-S-H gel is the main reaction product that precipitates during ordinary Portland cement hydration. The uptake of aluminum in bridging tetrahedral positions in the C-S-H gel structure gives rise to Q^2(1Al) units, favoring the formation of C-(A)-S-H gels. Both gels precipitated during hydration of the mineralized belite clinker fraction of the cement.

The gels that form in cementitious systems with a very low calcium content (such as in the alkaline activation of fly ash) are alkaline aluminosilicate hydrates (N-A-S-H gels) (Fernández-Jiménez et al., 2006). Such gels, which have a three-dimensional structure consisting in Q^4(mAl) units, constitute the main hydration product of fly ash alkaline activation. Further to that criterion, the signals located at around −88.5 ppm, −92.2 ppm, −95.7 ppm, −101.0 ppm, and −106.4 ppm on the 28 d and 180 d hybrid spectra would be respectively associated with the Q^4(4Al), Q^4(3Al), Q^4(2Al), Q^4(1Al), and Q^4(04Al) units in a N-A-S-H gel (Engelhardth and Michael, 1987; Fernández-Jiménez et al., 2006).

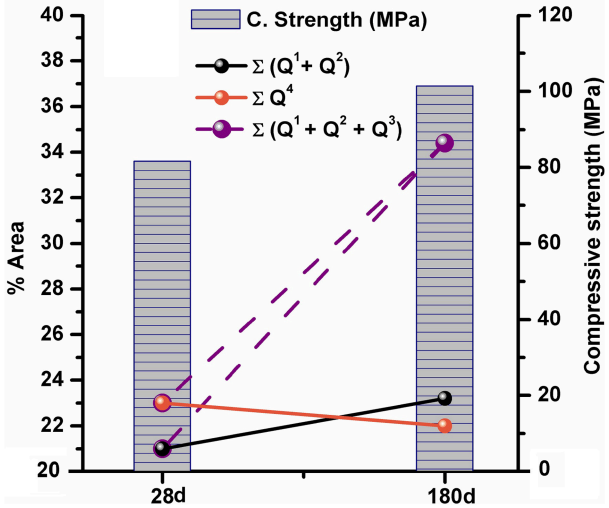

FIGURE 5 | Total areas of Q^1, Q^2, Q^3, and Q^4 units on the 28 d and 180 d ^{29}Si MAS NMR spectra and compressive strength of 3x3x3 cm paste specimens.

In these complex systems, however, the presence of calcium in the medium around the N-A-S-H gels may induce partial substitution of calcium for sodium, prompting the formation of N-(C)-A-S-H-like gels (García-Lodeiro et al., 2010, 2011) and with it slight shifts in resonance frequencies. That would explain the fluctuations observed in the positions of the signals on the 28 d and 180 d spectra, in addition to the evolution toward the precipitation of an N-(C)-A-S-H-like gel.

Two new signals were detected in the 28 d spectra at around −93.8 and −95.8 ppm, associated with Q^3(mAl) units. The presence of those signals can be explained on the grounds of the existence of phases precipitating in accordance with the following two mechanisms.

- Aluminum uptake into C-(A)-S-H gel. The presence of aluminum in a bridging tetrahedral position in the gel is known to favor sporadic connections between linear chains (Skibsted and Andersen, 2013). That induces the formation of flat (two-dimensional) laminated silicates that give rise to Q^3(1Al) units and signals at around −92/−94 ppm, indicative of a C-A-S-H-like gel. Silicon replacement by aluminum generates a charge imbalance in the gel structure, however, favoring the uptake of Na^+ ions to restore the balance and driving the precipitation of N-(C)-A-S-H-like gels (Puertas et al., 2011; Myers et al., 2015).
- De-polymerization of N-A-S-H gel. The presence of calcium in the medium tends to destabilize N-A-S-H gel, for the Si-O-Al bonds break due to the polarizing action of the Ca^{2+} ions, with the formation of Si-O-Ca bonds (García-Lodeiro et al., 2010, 2011). The outcome is a decline in the percentage of Q^4(4Al) and Q^4(3Al) units and a rise in the presence of Q^3(4Al) units. Whilst the aluminum exiting the three-dimensional structure of the N-A-S-H gel could be taken up in the C-S-H gel, it also tends to react with calcium to form secondary hydration products (García Lodeiro et al., 2016) such as AFm and

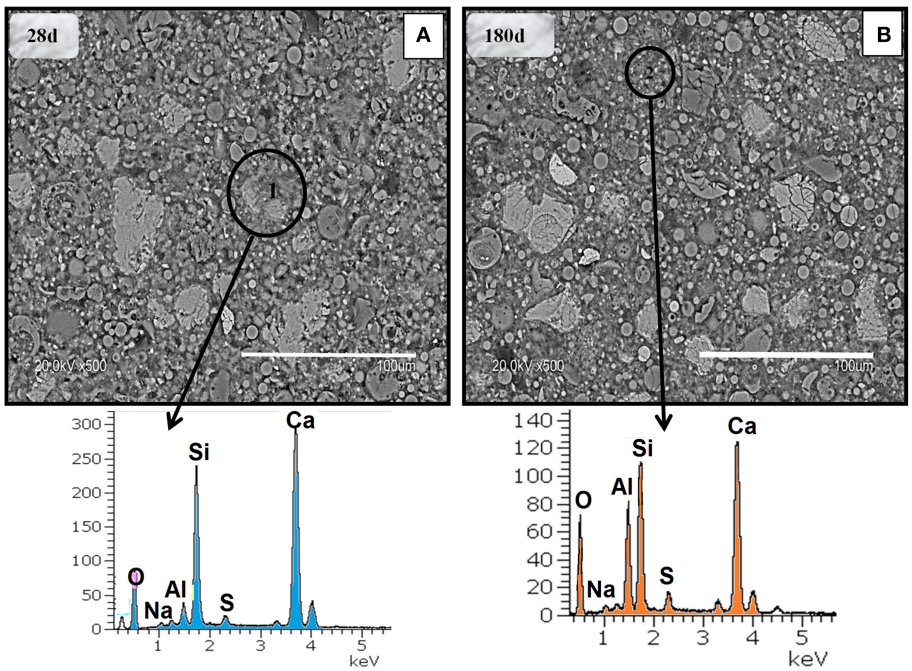

FIGURE 6 | (A) 28 d and **(B)** 180 d BSEM micrographs of hybrid cement pastes.

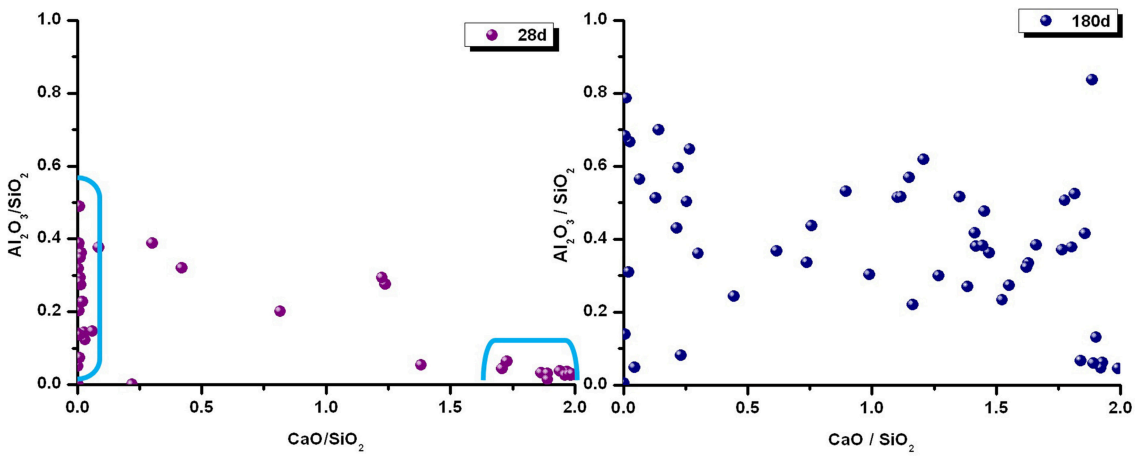

FIGURE 7 | CaO/SiO_2 and Al_2O_3/SiO_2 ratios calculated from the microanalysis of 28 d and 180 d hybrid cement pastes.

AFt. The ^{27}Al MAS NMR spectra reproduced below in **Figure 3B**, support that theory, as they contain signals for scantly crystalline AFt and AFm, phases that would not be detected with XRD.

An analysis of the tetrahedral aluminum based on the ^{27}Al MAS NMR spectra for the alkaline-belite hybrid cement and its pastes (**Figure 3B**) revealed that the intensity of the signal at +80 ppm, associated with calcium aluminates in the clinker (Baptiste d'Espinose de Lacaillerie et al., 2008; Sánchez-Herrero et al., 2012; Skibsted and Andersen, 2013), was barely perceptible in the 28 d materials and disappeared almost entirely after 180 d.

In the cement pastes, the intensity of the signal associated with the tetrahedral component of the fly ash (+52/54 ppm) declined and shifted, with the appearance of a number of signals at around +60 ppm. The inference would be that part of the aluminum was taken up into a gel or mix of gels and surrounded by two, three or four silicon atoms, providing further evidence of complex structures comprising a mix of cementitious gels of very different characteristics. According to the literature (García-Lodeiro et al., 2010, 2011; Puertas et al., 2011; Myers et al., 2015) the Al_T for N-A-S-H gel appears close to +57/+60 ppm while Al_T in C-A-S-H gel appears at +65/+68 ppm. By comparing ^{27}Al NMR spectra at 28 and 180 days, the area of the signal at around +65/+68

ppm attributed to a C-A-S-H gel rose substantially after 180 days of hydration.

The ^{27}Al NMR spectra for the 28 and 180 days pastes (see **Figure 3B**) exhibited signals at around +12 ppm, +9.4 ppm, and +4 ppm, indicative of octahedral aluminum and respectively associated with ettringite ($C_6A\hat{S}_3H_{32}$), calcium monosulfoaluminate ($C_4A\hat{S}H_{12}$) or calcium monocarboaluminate ($C_4A\hat{C}H_{11}$) and the third aluminate hydrate (TAH) (Shimada and Francis Young, 2004; Baptiste d'Espinose de Lacaillerie et al., 2008; Sánchez-Herrero et al., 2012; Skibsted and Andersen, 2013) none of these hydration products were detected with XRD. In contrast, with its high sensitivity to ^{27}Al nuclei, MAS NMR identifies compounds difficult to detect with other techniques due to the small amounts present or their low crystallinity.

Figure 5 shows the areas attributed to the Q^1, Q^2, Q^3, and Q^4 units obtained after deconvoluting the ^{29}Si MAS NMR spectra. The sum of the areas for the $Q^1 + Q^2$ units (associated with a C-(A)-S-H gel) rose in the 180 d materials, whilst the sum of the Q^4 units, corresponding to a N-A-S-H gel, declined at that age. The appearance of Q^3 units in the 180 d pastes denoted a rise in the total area of the $Q^1 + Q^2 + Q^3$ units associated with C-A-S-H gel precipitation, further supporting the evolution over time of the cementitious gels that precipitate during alkaline-belite hybrid cement hydration. These chemical and nanostructural changes in the cementitious gels did not compromise mechanical strength development in either the pastes (**Figure 5**) or the mortars (**Table 2**).

These findings corroborated the analysis of the ^{29}Si MAS NMR spectra, namely that the cementitious gel precipitating during hybrid "alkaline'-belite" cement hydration was actually a mix of interacting gels that evolved over time toward a gel with characteristics reminiscent of N-(C)-A-S-H gel. The evolution of cementitious gels toward a single product implies that part of the tetrahedral aluminum released into the medium was taken up into the secondary hydration products in the form of octahedral aluminum.

Further to the above analysis of the ^{29}Si and ^{27}Al MAS NMR findings, three types of cementitious gels precipitated during hybrid "alkaline-belite" cement hydration: C-(A)-S-H, C-(N)-A-S-H and N-(C)-A-S-H. That was possible due to system characteristics, determined by its 48% clinker, 48% fly ash, 1.5% gypsum, and 2.5% Na_2SO_4 contents. These cementitious gels interacted and their characteristics evolved over time toward those of a gel similar to C-(N)-A-S-H.

The EDX microanalyses of BSEM micrographs showed that the majority elements in paste chemical composition were calcium, silicon and aluminum, although different amounts of sulfur were also identified in most (**Figure 6**). The microanalysis conducted at point 1 on the micrograph detected the presence of a C-S-H-like gel with small amounts of aluminum (C-(A)-S-H-like gel), whereas the microanalysis at point 2 was indicative of the presence of a C-A-S-H-like gel (**Figure 6**).

The CaO/SiO_2 and Al_2O_3/SiO_2 molar ratios for the two pastes shown in **Figure 7** were calculated from the microanalyses of the BSEM micrographs. The 28 d cementitious gels were observed to precipitate primarily in two areas with very different compositional ranges. In one, low calcium N-A-S-H-like gels precipitated where some cenosphere or fly ash particle was previously located, whilst C-(A)-S-H-like gels were found in the other zones (where some particle of C_3S or C_2S was existing). The 180 d findings showed that the chemical composition of both types of gels evolved toward a single C-A-S-H-like gel.

In short, the BSEM/EDX findings for the 28 d and 180 d pastes confirmed the precipitation of different types of cementitious gels and hence the existence of a mix of gels. Due to the interaction between these gels as hydration progressed, this cementitious mix evolved toward the precipitation of a hydration product with characteristics reminiscent of C-(N)-A-S-H gel. The excellent technological behavior of the belitic-alkaline hybrid cement can only be explained by this nanostructural circumstance: two different cementitious gels being formed simultaneously. The extent to which formation of caco3 might contribute to the mechanical strength development has not been analyzed in this paper but authors consider it will be quite interesting point to analyze in the future since xrd seems to indicate that caco3 is increasing with time of curing.

CONCLUSIONS

The most prominent conclusions to be drawn from the present study are as follows.

- Hybrid belite-alkaline cement containing 48% fly ash can be prepared to the mechanical strength and setting time requirements laid down in European standard EN 197-1 for IVB type cement.
- Hydration of this hybrid alkaline-belite cement favored the simultaneous precipitation of a mix of cementitious gels that varied in nature: C-(A)-S-H and N-(C)-A-S-H. These gels interacted and over time evolved toward a C-(N)-A-S-H gel, with no detriment to the mechanical strength developed by the cement.
- Technologically speaking, this cement is comparable to most Portland cements on the market today, while from the environmental perspective, its manufacture is significantly more sustainable than traditional Portland cements.

AUTHOR CONTRIBUTIONS

MJS-H conducted the experiments, data analyses and characterizations. MJS-H and AF-J drafted the manuscript. AP helped with manuscript preparation and supervised the overall research. AF-J finalized the manuscript.

ACKNOWLEDGMENTS

This research was funded by the Spanish Ministry of the Economy and Competitiveness and FEDER under research projects BIA2016-76466-R and RTC2016-4872-S.

REFERENCES

Al-Kutti, W., Nasir, M., Azmi Megat Johari, M., Saiful Islam, A. B. M., Manda, A. A., and Blaisi, N. I. (2018). An overview and experimental study on hybrid binders containing date palm ash, fly ash, OPC and activator composites. *Construct. Build. Mater.* 159, 567–577. doi: 10.1016/j.conbuildmat.2017.11.017

Allahverdia, A., and Malekia Mahinroosta, M. (2018). Chemical activation of slag-blended Portland cement. *J. Build. Eng.* 18, 76–83. doi: 10.1016/j.jobe.2018.03.004

Baptiste d'Espinose de Lacaillerie, J., Fretigny, C., and Massiot, D. (2008). MAS NMR spectra of quadrupolar nuclei in disordered solids: the Czjzek model. *J. Magnet. Reson.* 192, 244–251. doi: 10.1016/j.jmr.2008.03.001

Blanco-Varela, M. T., Palomo, A., Puertas, F., and Vázquez, T. (1997). CaF_2 and $CaSO_4$ in white cement clinker production. *Adv. Cem. Res.* 9, 105–113. doi: 10.1680/adcr.1997.9.35.105

Chatterjee, A. K. (1996). High belite cements - present status and future technological options: part I. *Cem. Concr. Res.* 26, 1213–1225. doi: 10.1016/0008-8846(96)00099-3

Deschner, F., Winnefeld, F., Lothenbach, B., Seufert, S., Schwesig, P., Dittrich, S., et al. (2012). Hydration of Portland cement with high replacement by siliceous fly ash. *Cem. Concr. Res.* 42, 1389–1400. doi: 10.1016/j.cemconres.2012.06.009

Donatello, S., Palomo, A., and Fernández-Jiménez, A. (2013). Durability of very high volume fly ash cement pastes and mortars in aggressive solutions. *Cem. Concr. Comp.* 38, 12–20. doi: 10.1016/j.cemconcomp.2013.03.001

Engelhardth, G., and Michael, D. (1987). *High Resolution Solid State NMR of Silicates and Zeolite, Ed*. London: Wiley.

Fernández-Jiménez, A., Palomo, A., Sobrados, I., and Sanz, J. (2006). The role played by the reactive alumina content in the alkaline activation of fly ashes. *Micropor. Mesop. Mater.* 91 111–119. doi: 10.1016/j.micromeso.2005.11.015

García Lodeiro, I., Fernández-Jiménez, A., and Palomo, A. (2013). Variation in hybrid cements over time. alkaline activation of fly ash-portland cement blends. *Cem. Concr. Res.* 52, 112–122. doi: 10.1016/j.cemconres.2013.03.022

García-Díaz, I., Palomo, J. G., and Puertas, F. (2011). Belite cements obtained from ceramic wastes and the mineral pair $CaF_2/CaSO_4$. *Cem. Concr. Compos.* 33, 1063–1070. doi: 10.1016/j.cemconcomp.2011.06.003

García-Lodeiro, I., Donatello, S., Fernández-Jiménez, A., and Palomo, A. (2016). Hydration of hybrid alkaline cement containing a very large proportion of fly ash: a descriptive model. *Materials* 9:605. doi: 10.3390/ma9070605

García-Lodeiro, I., Fernández-Jiménez, A., Palomo, A., and MacPhee, D. E. (2010). Effect of calcium additions on N-A-S-H cementitious gels. *J. Am. Ceram. Soc.* 93, 1934–1940. doi: 10.1111/j.1551-2916.2010.03668.x

García-Lodeiro, I., Fernández-Jiménez, A., Palomo, A., and Macphee, D. E. (2011). Compatibility studies between N-A-S-H and C-A-S-H gels. Study in the ternary diagram Na_2O-CaO-Al_2O_3-SiO_2-H_2O. *Cem. Concr. Res.* 41, 923–931. doi: 10.1016/j.cemconres.2011.05.006

Knop, Y., and Peled, A. (2016). Packing density modeling of blended cement with limestone having different particle sizes. *Construct. Build. Mater.* 102, 44–50. doi: 10.1016/j.conbuildmat.2015.09.063

Kucherov, A. P., and Kochubei, S. M. (1983). Method for decomposition of a complex profile into elementary components using a preliminary analysis of its structure. *J. Appl. Spectrosc.* 38, 124–128. doi: 10.1007/BF00659868

Liu, C., Huang, R., Zhang, Y. S., Liu, Z. Y., and Zhang, M. Z. (2018). Modelling of irregular shaped cement particles and microstructural development of Portland cement. *Construct. Build. Mater.* 115, 362–378. doi: 10.1016/j.conbuildmat.2018.02.142

Lothenbach, B., Scrivener, K., and Hooton, R. D. (2011). Supplementary cementitious materials. *Cem. Concr. Res.* 41, 1244–1256. doi: 10.1016/j.cemconres.2010.12.001

Malvar, L. J., and Lenke, L. R. (2006). Efficiency of fly ash in mitigating alkali silica reaction based on chemical composition. *ACI Mater. J.* 103, 319–326. doi: 10.14359/18153

Merwin, L. H., Sebald, A., Rager, H., and Schneider, H. (1991). ^{29}Si and ^{27}Al MAS NMR spectroscopy of mullite. *Phys. Chem. Min.* 18, 47–52.

Myers, R. J., Bernal, S. A., Gehman, J. D., van Deventer, J. S. J., and Provis, J. L. (2015). The role of Al in cross-linking of alkali-activated slag cements. *J. Am. Ceram. Soc.* 98, 996–1004. doi: 10.1111/jace.13360

Palomo, A., Alonso, S., and Fernández-Jiménez, A. (2004). Alkaline activation of fly ashes: NMR study of the reaction products. *J. Am. Ceram. Soc.* 87, 1141–1145. doi: 10.1111/j.1551-2916.2004.01141.x

Pérez, G., Guerrero, A., Gaitero, J. J., and Goñi, S. (2014). Structural characterization of C-S-H gel through an improved deconvolution analysis of NMR spectra. *J. Mater. Sci.* 49, 142–152. doi: 10.1007/s10853-013-7688-8

Puertas, F., Palacios, M., Manzano, H., Dolado, J. S., Rico, A., and Rodríguez, J. (2011). A model for the C-A-S-H gel formed in alkali-activated slag cements. *J. Eur. Ceram. Soc.* 31, 2043–2056. doi: 10.1016/j.jeurceramsoc.2011.04.036

Qu, B., Martin, A., Pastor, J. Y., Palomo, A., and Fernandez-Jimenez, A. (2016). Characterisation of pre-industrial hybrid cement and effect of pre-curing temperature. *Cem. Concr. Compos.* 73, 281–288. doi: 10.1016/j.cemconcomp.2016.07.019

Rietveld, H. M. (1969). A profile refinement method for nuclear and magnetics structures. *J. Appl. Crystallogr.* 2, 65–71. doi: 10.1107/S0021889869006558

Ruiz-Santaquiteria, C., Skibsted, J., Fernández-Jiménez, A., and Palomo, A. (2013). Clay reactivity: production of alkali activated cements. *Appl. Clay Sci.* 73, 11–16. doi: 10.1016/j.clay.2012.10.012

Sánchez-Herrero, M. J., Fernández-Jiménez, A., and Palomo, A. (2012). Alkaline hydration of tricalcium aluminate. *J. Am. Ceram. Soc.* 95, 3317–3324. doi: 10.1111/j.1551-2916.2012.05348.x

Sánchez-Herrero, M. J., Fernández-Jiménez, A., and Palomo, A. (2016). Alkaline hydration of C_2S and C_3S. *J. Am. Ceram. Soc.* 99, 604–611. doi: 10.1111/jace.13985

Sánchez-Herrero, M. J., Fernández-Jiménez, A., and Palomo, A. (2017). C_3S and C_2S hydration in the presence of Na_2CO_3 and Na_2SO_4. *J. Am. Ceram. Soc.* 100, 3188–3198. doi: 10.1111/jace.14855

Scrivener, K., Martirena, F., Bishnoi, S., and Maity, S. (2018b). Calcined clay limestone cements (LC3). *Cem. Concr. Res.* 114, 49–56. doi: 10.1016/j.cemconres.2017.08.017

Scrivener, K. L., Vanderley, M. J., and Gartner, E. M. (2018a). Eco-efficient cements: potential economically viable solutions for a low-CO_2 cement-based materials industry. *Cem. Concr. Res.* 114, 2–26. doi: 10.1016/j.cemconres.2018.03.015

Shimada, Y., and Francis Young, J. (2004). Thermal stability of ettringite in alkaline solutions at 80°C. *Cem. Concr. Res.* 34, 2261–2268. doi: 10.1016/j.cemconres.2004.04.008

Skibsted, J., and Andersen, M. D. (2013). The effect of alkali ions on the incorporation of aluminium in the calcium silicate hydrate (C-S-H) phase resulting from Portland cement hydration studied by ^{29}Si MAS NMR. *J. Am. Ceram. Soc.* 96, 651–656. doi: 10.1111/jace.12024

Staněk, T., and Sulovský, P. (2015). Active low-energy belite cement. *Cem. Concr. Res.* 68, 203–210. doi: 10.1016/j.cemconres.2014.11.004

Taylor, H. F. W. (1997). *Cement Chemistry*, *2nd Ed.* London: ISBN

Vizcaíno-Andrés, L., Sánchez-Berriel, S., Damas-Carrera, S., Pérez-Hernández, A., Scrivener, K., and Fernando, M.-H. (2015). Industrial trial to produce a low clinker, low carbon cement. *Mater. Constr.* 65:e045. doi: 10.3989/mc.2015.00614

Wa, M., Zhang, Y., Ji, Y., Liu, G., Liu, C., She, W., et al. (2018). Reducing environmental impacts and carbon emissions: study of effects of superfine cement particles on blended cement containing high volume mineral admixtures. *J. Clean. Product.* 196, 358–369. doi: 10.1016/j.jclepro.2018.06.079

Zhang, T. S., Yu, Q. J., Wei, J. X., and Zhang, P. P. (2012). Efficient utilization of cementitious materials to produce sustainable blended cement. *Cem. Concr. Compos.* 34, 692–699. doi: 10.1016/j.cemconcomp.2012.02.004

Conflict of Interest Statement: The authors declare that the research was conducted in the absence of any commercial or financial relationships that could be construed as a potential conflict of interest.

frontiers in Materials

ORIGINAL RESEARCH
published: 24 April 2019
doi: 10.3389/fmats.2019.00083

Microgravity Effect on Microstructural Development of Tri-calcium Silicate (C_3S) Paste

Juliana Moraes Neves[1]*, *Peter J. Collins*[1], *Ryan P. Wilkerson*[2], *Richard N. Grugel*[2] and *Aleksandra Radlińska*[1]

[1] Department of Civil and Environmental Engineering, The Pennsylvania State University, University Park, PA, United States, [2] Marshall Space Flight Center-NASA, Huntsville, AL, United States

For the first time, tricalcium silicate (C_3S) and an aqueous solution were mixed and allowed to hydrate in the microgravity environment aboard the International Space Station (ISS). The research hypothesis states that minimizing gravity-driven transport phenomena, such as buoyancy, sedimentation, and thermosolutal convection ensures diffusion-controlled crystal growth and, consequently, lead to unique microstructures. Results from SEM micrographs, image analysis, mercury intrusion porosimetry, thermogravimetry, and x-ray diffraction revealed that the primary differences in μg hydrated C_3S paste are increased porosity and a lower aspect ratio of portlandite crystals, likely due to a more uniform phase distribution. Relevant observations led by the presence or absence of gravity, including bleeding effect, density, and crystallography are also presented and discussed.

Keywords: microgravity, C_3S hydration, microstructure, porosity, portlandite CH, sedimentation, bleeding, phase distribution

OPEN ACCESS

Edited by:
Maria Juenger, University of Texas at Austin, United States

Reviewed by:
Jinrui Zhang, Tianjin University, China
Hongyan Ma, Missouri University of Science and Technology, United States

***Correspondence:**
Juliana Moraes Neves
jmn273@psu.edu

Specialty section:
This article was submitted to Structural Materials, a section of the journal Frontiers in Materials

Received: *19 January 2019*
Accepted: *08 April 2019*
Published: *24 April 2019*

Citation:
Moraes Neves J, Collins PJ, Wilkerson RP, Grugel RN and Radlińska A (2019) Microgravity Effect on Microstructural Development of Tri-calcium Silicate (C_3S) Paste. Front. Mater. 6:83. doi: 10.3389/fmats.2019.00083

INTRODUCTION

Exploration of extraterrestrial bodies, such as the moon, can be facilitated by extended stays, which will require fabrication of habitats and other supporting infrastructure. Given the cost of transporting materials into space, it is envisioned that *in situ* materials, e.g., lunar regolith, would be required in such construction and a cement-like binder would be needed for creating resilient habitats. Solidification of cement in a microgravity (10^{-6} *g* or μ*g*) environment, however, is not well-understood. As a first step, the primary objective of this research is to experimentally document microgravity influence on the microstructure development of a tricalcium silicate (C_3S) paste.

The Microgravity Investigation of Cement Solidification (MICS) research project is in strong alignment with NASA's human and space exploration needs. The experiment directly addresses two objectives identified by NASA Space Technology Roadmaps and Priorities (National Research Council, 2012), listed as (1) exploring the evolution of the solar system and the potential for life elsewhere and (2) expanding the understanding of the Earth and the universe. Furthermore, it is possible that indigenous materials can be used to manufacture a binder to make concrete on the surface of the Moon, which would enable a cost-effective solution for long-duration human missions (Khoshnevis, 2004). The role the extreme environment would have on life has been researched (Isson-Francis et al., 2018), and the extraterrestrial building material would have to help combat these challenges.

Cement has been studied for over a century with pioneering research conducted by Bogue, T. C. Powers, and T. L. Brownyard. Together they remarkably contributed to the science of cement and concrete materials (Powers and Brownyard, 1946; Bogue, 1947; Powers et al., 1954; Powers, 1958), including characterization of basic fresh and hardened properties. Since then, understanding the complex hydration of portland cement has improved substantially, but is not yet fully understood. One example is the insufficient comprehension of the mechanism controlling the main heat evolution peak of cement hydration (Bullard et al., 2011; Scrivener et al., 2015), which hampers development of accurate prediction models (Bullard et al., 2010). The need for improved methods of studying cement hydration has been noted (Provis, 2015) and MICS contributes by providing a novel approach to understanding how gravity affects materials processing. Moreover, this novel insight will promote our understanding of Earth-based cementitious science, and advance development of binders for use on extraterrestrial bodies.

It should be noted that the work described here is part of the on-going MICS research project and focuses on the microstructural development of high water-to-cement ratio tricalcium silicate (C_3S) paste mixed and cured in a microgravity environment. C_3S is the main mineral component of typical commercially available portland cement and dictates most of the kinetics and early properties (Taylor, 1990; Mindess et al., 2003; Scrivener, 2004; Thomas et al., 2009). In principle, investigating pure compounds, such as C_3S, constitutes elementary research, which eases and enhances the analysis of more complex systems such as portland cement mixtures. In portland cement systems, the presence of aluminates, sulfates, alkalis, and other impurities affects pH and supersaturation of the solvent (i.e., pore solution), which makes interpretation of results and the conclusion-drawing process more complicated. As such, a thorough understanding of pure phases is necessary before more complex systems can be analyzed. To date, pure C_3S and its hydration products (C-S-H and CH[1]) have been extensively studied theoretically (Young and Hansen, 1987; Bentz and Garboczi, 1991; Joseph et al., 2017) and experimentally (Thomas et al., 2009; Bazzoni, 2014; Hu et al., 2016a,b).

As of now, no experiments have fully documented the effect of microgravity on the microstructural development of portland cement or any of its compounds. There have been cement hydration studies performed aboard a parabolic flight path, which allows for ∼20 s of a 10^{-2}-10^{-3} gravity environment (Meier et al., 2015; Lei et al., 2016; Meier and Plank, 2016). The short time duration limited the experiments to investigating instantaneous ettringite precipitation. The authors reported that the microgravity environment generally leads to increase in the amount of ettringite precipitated. However, the change in gravity has only a minor effect on the aspect ratios of ettringite formed from a neat cement by a slight reduction. The most notable changes occur in the presence of PCE polymers as the aspect ratio of the ettringite was significantly changed depending on the anionicity of the polymer. Outside of the cementitious materials realm, one experiment documenting the effects of microgravity on the growth of an inorganic crystal (sodium chloride) was conducted aboard the ISS (Fontana et al., 2011). The authors reported morphological differences between crystals precipitated in μg and typical NaCl precipitated on Earth (Fontana et al., 2011). Qi et al. (2017) modeled how settling motion could affect the morphology of a growing dendritic crystal. These studies (Fontana et al., 2011; Meier et al., 2015; Lei et al., 2016; Meier and Plank, 2016; Qi et al., 2017) advocate that gravitational forces impact crystal growth and can provide ground for interpreting the results of the present research.

[1]The usual cement chemistry notation is used throughout this manuscript, where C=CaO, S=SiO_2, and H=H_2O for both the anhydrous and hydrated phases.

TABLE 1 | Percentages (10, 50, and 90) of C_3S particles with a diameter equal to or smaller than the indicated values.

	D10	D50	D90
Average diameter (μm)	1.60	5.22	12.88
Standard deviation	0.14	0.16	0.77

For example, 10 percent of the C_3S particles are smaller than 1.60 μm. Results obtained from laser diffraction.

MATERIALS AND EXPERIMENTAL SETUP

Characterization of Anhydrous Materials: Tri-calcium Silicate (C_3S) and Hydrated Lime

Pure compound C_3S, hydrated lime, and distilled water were used in this work. High purity triclinic C_3S with a surface area of 3,500 cm^2/gram was obtained from Mineral Research Processing (Meyzieu, France). Calcium hydroxide (Alfa-Aesar) was added to the mixing water, which is explained in detail in Mixture Proportions. The present study refers to the calcium hydroxide used in the mixing water as hydrated lime, so it can be easily differentiated from the calcium hydroxide precipitated during the C_3S hydration process, which is referred to as portlandite.

The evaluation of the anhydrous powder of C_3S and hydrated lime was first conducted to characterize their size and morphology. Dry-dispersion laser diffraction (Malvern Mastersizer 3000) was employed to determine the particle size distribution of C_3S. Approximately 100 mg of powder was dispersed by an Aero S dry dispersion unit using a standard venturi at 4 bar air pressure and a 25% feed rate. The refractive index and adsorption were assumed to be, respectively, 1.68 and 0.1. **Table 1** shows diameters D10, D50, and D90. Determining the particle size distribution of hydrated lime was not performed as most of the powder was expected to dissolve once added to water.

Scanning electron microscope (SEM) images of the anhydrous C_3S and hydrated lime powders were also taken (**Figures 1**, **2**). In the specific case of hydrated lime, the images prove that it differs from the hydrated materials, which are shown and discussed in the results section. The samples were prepared by sprinkling the powders over carbon tape and placing them in an SEM at low vacuum mode. It can be seen that the C_3S particles are consistent with the results obtained through laser diffraction, as most of the particles are smaller than the 10 μm scale bar.

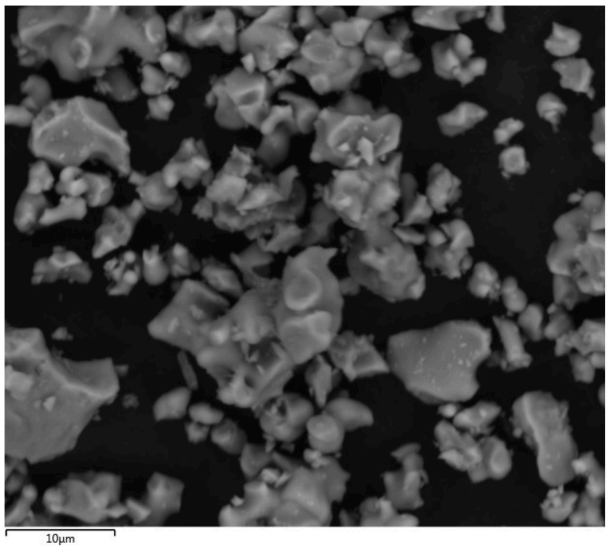

FIGURE 1 | SEM image of anhydrous C_3S particles showing irregular morphology, smooth surface, and sizes often smaller than the 10 μm (scale bar), in agreement with laser diffraction results.

Mixture Proportions

The mixture evaluated in this research consisted of C_3S mixed with lime-water at a water-to-cement ratio (w/c) of 2.0 by mass (5 grams of C_3S and 10 grams of lime-water). The lime-water consisted of a 15 mmol/liter solution of calcium hydroxide, where 1.12 grams of hydrated lime was added to 1,000 g (1 liter) of distilled water, sealed, and continuously stirred for 24 h at room temperature to ensure stabilization of the solution.

In addition to enhancing the degree of hydration, a high w/c (2.0) enhances crystal growth through coarsening the porosity of the paste (Scrivener, 1989; Taylor, 1990; Mindess et al., 2003; Thomas and Jennings, 2019). Magnifying the overall microstructural development also nourishes the μg effects and aids in their identification. Moreover, the high w/c allowed for the easiness of the manual mixing process (discussed in Experimental Setup) without need for chemical admixtures. If pure water was used rather than lime-water in this high w/c system, the initial reaction rate would be too rapid and as such, unrealistic. Using lime-water mimics the supersaturation degree with respect to portlandite in the pore solution of cement [pH of 12.5 ± 0.1(Rajabipour et al., 2015)], controls the initial reaction rate (Hu et al., 2016a,b), and still enhances nucleation and crystal growth (Bazzoni, 2014).

Experimental Setup

Commercially available plastic bags (Burst Pouches®) were used as mixing containers (**Figure 3**). A total of 12 identical pouches were prepared; 6 were sent to the ISS on the OA-9 resupply mission and 6 remained on the ground as control samples. The pouches entailed two separate compartments divided by an internal, burstable seal which allowed mixing materials under sealed conditions. Individual compartments of the pouches were filled with C_3S and aqueous solutions under laboratory conditions on Earth. This setup allowed the first contact between the C_3S and lime-water to take place while aboard the ISS. Space and ground samples were mixed simultaneously and at the same conditions (temperature of 20 ± 2°C). The pressure and relative humidity conditions (1 ATM and 35% RH) were also constant, since they are characteristics of the air confined in the sealed pouches during the preparation. As such, gravity is considered the only variable between the space and ground experiments.

The mixing procedure consisted of exerting pressure on the lime-water by rolling the pouch and effectively pushing the solution forward until the internal seal was broken, after which the solution came in contact with the anhydrous C_3S. The hydrating C_3S paste was then manually mixed with a rubberized spatula for ∼3 min, or until homogeneity was achieved. Finally, a clamp was used to assure consolidation of the paste, as shown in **Figure 3**. The processed ground and space samples remained within the sealed pouch for the entire hydration period at undisturbed, controlled temperature (20 ± 2°C) conditions. The space samples were allowed to hydrate for 42 days aboard the ISS until returning to Earth for analysis. Samples were retrieved after splash down and immediately transported in insulated containers to Marshall Space Flight Center in Huntsville, AL, where the initial analysis took place.

Both the experimental setup and mixing procedure were kept simple to meet two major requirements: (1) to reduce the volume of materials and shipping cost, which is estimated to be at least $10,000 per pound (0.454 kg) of material (Futron Corporation., 2002), and (2) to meet NASA safety requirements that consider cement and its compounds to be hazardous. To address this issue, the pouches were tested for pressure, temperature, and long-term storage of high pH materials. In addition, the samples had to be triple-contained while the experiments were executed by the astronauts on the ISS. The first containment level was the pouch itself, the second was a plastic bag seen in **Figure 3**, and the third was a portable glovebag which was fixed on top of the Maintenance Workbench Area (MWA). Note that the hardened samples were given the lowest toxicity level (0 rating).

METHODS

Scanning Electron Microscopy (SEM)

Shortly after returning to Earth, the space samples underwent a visual comparison with the ground samples. This assisted in identifying the most pronounced differences and subsequently selecting the series of most relevant tests. The fractured surfaces of samples were examined using a Hitachi S-3700N SEM immediately after their removal from the pouch, at day 56 from the initial hydration. The microscope operated under variable pressure conditions (10 to 20 Pa) with an accelerating voltage of 10 or 15 keV. In the variable pressure mode, the capability of the instrument is limited to backscattered electron (BSE) micrographs. A probe current of 25 μA and an aperture of 4 were used to maximize image resolution.

Additionally, polished cross sections were prepared at day 152 after initial hydration. The sample preparation consisted of immersing the samples in 200 ml of isopropyl alcohol for 48 h,

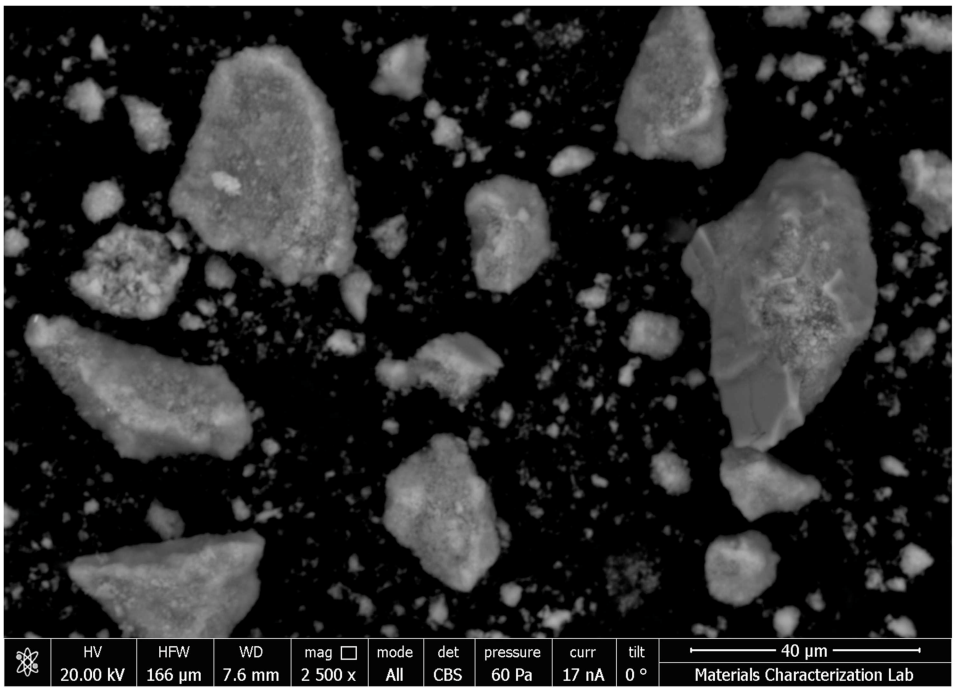

FIGURE 2 | SEM image of lime particles before being added to the mixing water.

followed by 30 h of drying under vacuum and room temperature (22°C). Subsequently, the samples were mounted in medium grade acrylic resin, ground through a series of SiC papers, and finally polish using 0.25 μm diamond paste. The polished cross-sections were examined in a FEI Q250 and BSE images were taken. The operating conditions are specified at the bottom of each micrograph presented in the results section.

Image Analysis

Analysis of the porosity through the BSE images taken of the polished samples was done by creating a binary image separating the pores from all other phases. The greyscale value to determine the upper boundary of the pores was done using the overflow method (Wong et al., 2006). There were 20 images captured for the space samples and 30 images for the ground samples at a magnification of 500x. A statistical analysis was done ensuring the number of images acquired for each sample was enough to be 95% confident that the true mean is within 10% of the sample mean. The images captured were 1,536 × 1,024 pixels with each pixel representing 0.27 × 0.27 μm. The brightness and contrast settings were adjusted to ensure a greyscale histogram with a broad range of values for the present phases. The images showed a large amount of porosity, C-S-H, and portlandite with minimal anhydrous C_3S being visible.

After creating the binary image using the greyscale value obtained from the overflow method for thresholding, the area fraction of porosity was calculated. Regions with <10 pixels were regarded as noise and not included in the porosity calculation, which is consistent with the Wong et al. study (Wong et al., 2006). As such, the smallest pore size that was detected and counted in this method had diameter of 0.96 microns. As will later be discussed in more detail, the ground sample exhibits a layered structure due to sedimentation. Each layer of the ground sample was individually analyzed. Multiple size measurements were taken and averaged to calculate the corresponding fraction of each layer. The values obtained were used to calculate a weighted average of porosity.

Mercury Intrusion Porosimetry (MIP)

Prior to the MIP test, ground and space samples were immersed individually in 200 ml of isopropyl alcohol for 48 h for solvent exchange, which was followed by 34 h of drying under vacuum at room temperature. Subsequently, a Micromeritics AutoPore V 9620 MIP mercury penetrometer was used to assess the porosity, pore size distribution, bulk density, and skeletal density of the pastes. The mercury temperature during testing of ground and space samples was 19°C.

Thermogravimetric Analysis (TGA)

Prior to TGA analysis, the space samples underwent 42 days of hydration under μ*g* condition, followed by at 109 of hydration under 1 *g*, totaling 151 days of hydration. Unopened ground and space samples of same age were removed from the pouches and stored for 10 days in a nitrogen-purged chamber, at 32°C and 65% relative humidity. Subsequently, the partially dried samples were finely ground with mortar and pestle immediately before the TGA measurement. SDT Q600 (TA Instruments) was then used to estimate the degree of hydration and to quantify the amount of portlandite in the pastes. Approximately 20 grams of

FIGURE 3 | A typical processed pouch containing hydrating cement paste and a clamp.

ground material was placed in the nitrogen purged chamber of the instrument and heated to 110°C. This temperature was held for 20 min to eliminate any remaining free water and then raised in increments of 10°C per minute until 800°C or higher.

X-Ray Diffraction (XRD)

Samples of 151 days of age were taken from the pouch immediately before the analysis and, without additional preparation, were crushed using a mortar and pestle for approximately 3 min. Due to the high water-to-cement ratio, the crushed material was somewhat wet when back-filled into a zero-background sample holder for x-ray diffraction. XRD data was collected using a PANalytical X'Pert PRO MPD diffractometer in a conventional Bragg–Brentano θ-θ configuration. CuKα X-ray ($\lambda = 1.5418$ Å) was generated using 40 mA and 45 kV operating conditions. The optics setup included incident divergence slit fixed at 0.25°, 0.04 soller slits, incident/diffracted anti-scatter slits and a nickel filter. The samples were scanned continuously between 5° and 65° 2θ at a step size of 0.013°, and spinning at 60 rpm to maximize the intensity (counts).

RESULTS AND DISCUSSION

SEM

The micrographs obtained at different magnifications provided a wide range of detail, revealing information ranging from the overall distribution of phases to the micron-scale crystal morphology. As it can be seen in **Figures 4**, **5**, the pastes cured in μg differ from the control samples cured in 1 g in several aspects. First (**Figure 4**), is the greater number of trapped air bubbles found in the space specimens, which is attributed to the lack of buoyancy in a μg environment. Buoyancy is a gravity-driven phenomenon that results from differences in specific gravities among components comprising a given system (Turner, 1979). Under the influence of gravity, air bubbles, for example, are expected to move upwards through the initial watery cement paste due to their lower density [$\approx$1.2 kg/m^3 (Cavcar, 2000)], while also promoting fluid flow (Barge et al., 2015).

The 1g micrograph in **Figure 5** clearly shows that layering and "bleeding" effects can manifest even in a paste that is merely 3 mm high, as is the case for the ground samples. Bleeding occurs at very early stages of cement hydration and generates a gradient water-to-cement ratio across the sample height, which results in a porosity gradient (Han and Wang, 2016). The physical explanation behind the commonly seen phenomenon is the gravity-driven sedimentation. Sedimentation promotes sinking of anhydrous C_3S, as well as of C-S-H, and portlandite [specific gravities of 3.15, 2.3–2.6, and 2.24, respectively (Mindess et al., 2003)], while raising the calcium-saturated pore solution (specific gravity of $\approx$1) to the surface. The film of supersaturated solution promotes unimpeded growth of portlandite at the specimen's top surface, as seen in **Figure 6**. As expected, the sedimentation layering or bleeding effects do not take place in space; rather, the pastes hydrated in μg develop a more uniform density, as shown in the μg micrograph (**Figure 5**). Gravity-driven sedimentation also seems to affect the consolidation process of cementitious materials. **Figure 7** suggests that C_3S hydrated in microgravity generates a more porous paste in comparison to the ground control. It also appears that, in 1g, the self-weight of the hydrating paste generates sufficient compaction to reduce the overall spacing between the hydrating phases. In μg, the lack of a directional gravitational force allows the anhydrous C_3S to float in the solution, enhancing the porosity.

The size, shape and distribution of portlandite crystals also differs substantially between 1g and μg samples, in agreement with the ISS NaCl experiment (Fontana et al., 2011). The different morphologies of portlandite seen in **Figure 7** can also be justified by differences in phase distribution. When hydrated in 1g, the severe bleeding caused by the high w/c reduces the availability of calcium in the pore solution, as well as reduces room for crystal growth. As a result, portlandite is more frequently distributed throughout the matrix and grows filling up the tortuous pore space (Gallucci and Scrivener, 2007). In μg, the crystals have a rather elongated, plate-like morphology, which is in line with the preferential crystal growth found by Harutyunyan and coworkers (Harutyunyan et al., 2009). The higher effective w/c and the larger porosity provide the dissolved species with more freedom to develop a purely chemical diffusion-driven microstructure, without complications from the physical effects of gravity. Also shown by Harutyunyan et al. (2009), portlandite has very specific crystallographic growth preferences that are accordant with the crystals shown in the μg image, **Figure 7**.

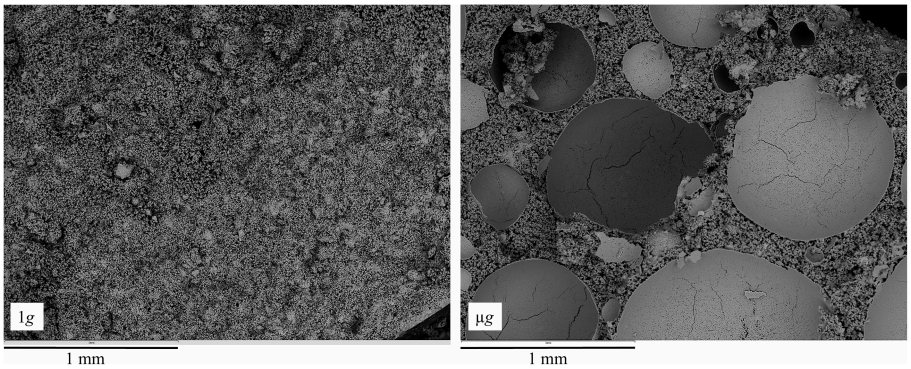

FIGURE 4 | Fractured surface of 56 days old C_3S pastes hydrated at 1 *g* (left) and μ*g* (right). The large, round, shell-like structures seen on the μ*g* sample are the trapped air bubbles. Higher porosity can also be seen on the μ*g* sample.

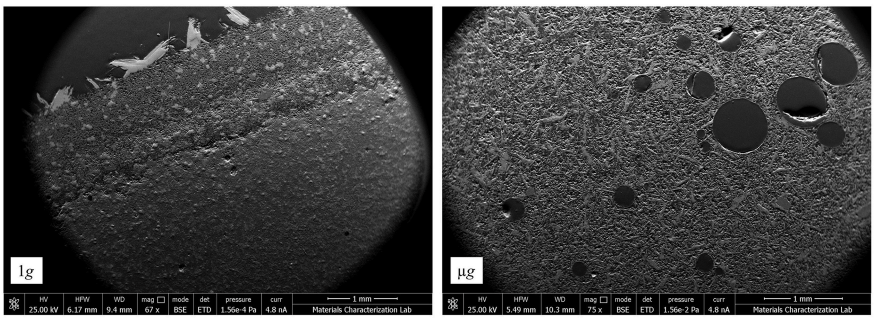

FIGURE 5 | Polished surface of C_3S pastes hydrated at 1 *g* (left) and μ*g* (right). The 1 *g* sample shows a porosity gradient and the cross-section of large portlandite crystals at the surface as a result of buoyancy. The μ*g* sample is remarked by the presence of large air bubbles and uniform porosity.

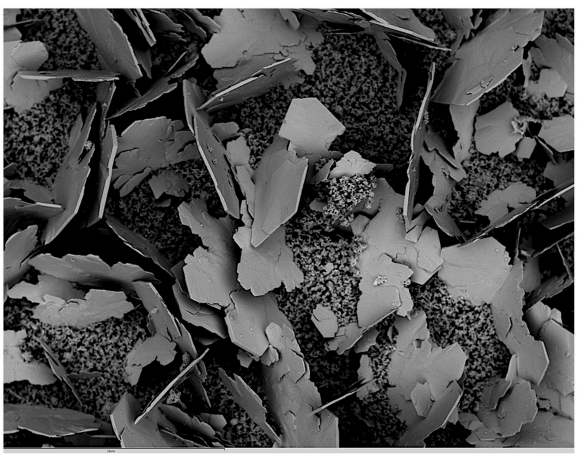

FIGURE 6 | SEM image taken from the top surface of a C_3S paste hydrated under 1 *g* environment for 56 days. The large, plate-like portlandite crystals sitting on the C-S-H matrix can reach over 1 mm of diameter and result from bleeding effect. The scale bar at the bottom of the micrograph shows 1 mm.

Smaller crystallites of well-defined hexagonal shape, and covered by C-S-H, were also found in pastes hydrated in ground and space (**Figures 8**, **9**). Characterized by the hexagonal basal plane, the euhedral crystallites are smaller in size than typical portlandite. Their smaller size indicates that they likely precipitate at later stages of the hydration period (Boistelle and Astier, 1988; Glasser, 2001) after the skeleton of the paste is formed. Prismatic crystallites were oftentimes found in samples hydrated in μ*g*, whereas plate-like crystallites of similar basal plane size were rarely found in 1*g* samples (**Figure 8**).

Image Analysis

The typical greyscale histogram seen throughout the images taken of the samples is seen on the left side of **Figure 10**. There is minimal anhydrous material observed both visually and in the greyscale histogram of polished samples images. This is indicative of advanced degree of hydration as the samples age was 152 days. The slight bump around the greyscale value of 200 would be the minimal anhydrous material. The right side of **Figure 10** shows the cumulative greyscale histogram used with the overflow method to determine the greyscale value for thresholding.

As previously discussed, there is a visual difference between the porosity of the ground and space samples (**Figure 7**) that was confirmed by the image analysis. The calculated porosity by the area fraction shows porosities for the ground and space samples of 48.1 and 71.7 percent, respectively (**Table 2**). These

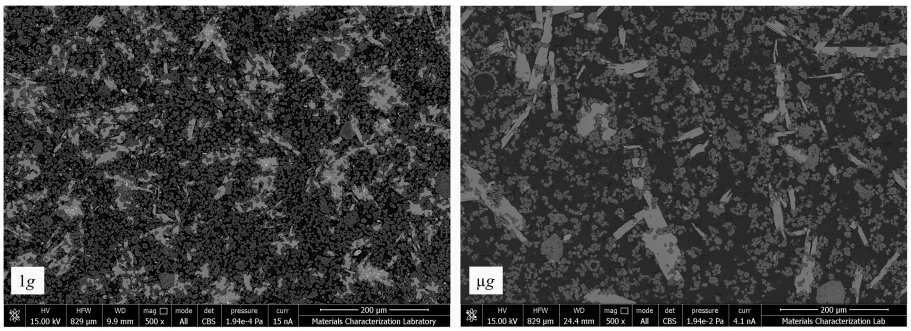

FIGURE 7 | The polished surface of C_3S paste hydrated at 1 *g* (left) implies lower porosity than the paste hydrated in μ*g* (right). The 1 *g* sample shows a larger number of small portlandite crystals distributed in higher amount throughout the C-S-H matrix. Contrarily, the μ*g* sample has a less frequent distribution of larger and fewer portlandite crystals, remarked by the lightest gray scale.

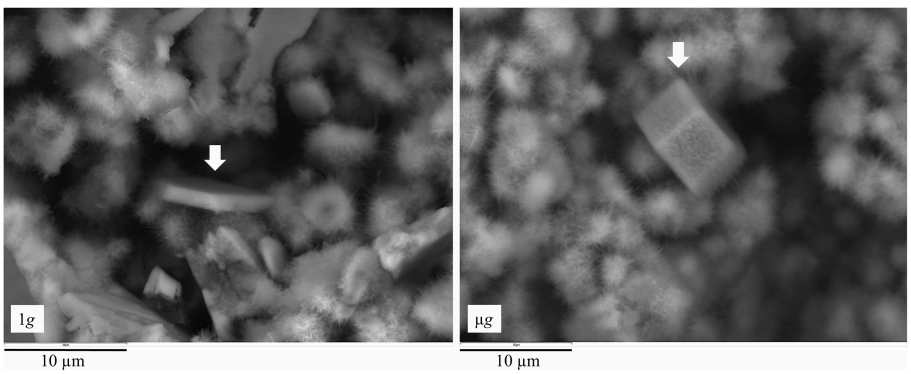

FIGURE 8 | SEM images of fractured surface of C_3S pastes, with white arrow pointing to a small, secondary CH crystallite. The crystallite formed under 1 *g* (left) presents dish-like morphology, while that formed under μ*g* (right) is more prismatic. The different morphologies are attributed to differences in the effective w/c containing dissolved calcium species, as well as to pore space, both being limited in 1 *g* resulting in a smaller crystallite.

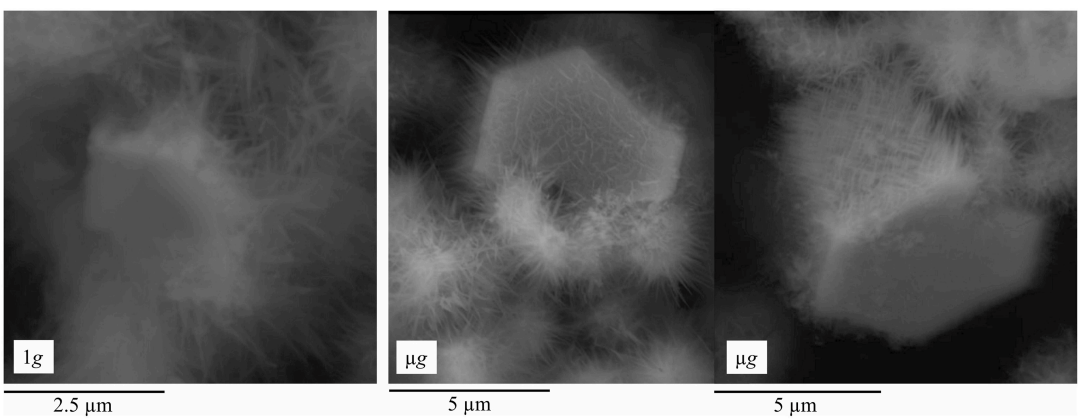

FIGURE 9 | The micrographs show CH crystallite hydrated in 1 *g* (left), resulting in a completely misoriented C-S-H covering its surface, while the CH crystallite formed in μ*g* (right) is covered by an oriented C-S-H. Note the difference in the scale bar, which also highlights that the crystallites are bigger when hydrated under μ*g* condition.

values show that the porosity in the space sample is over 20 percent higher than in the ground sample. The lower porosity in the ground sample could be partially attributed to the bleeding effect, which would lower the effective w/c ratio of the sample and therefore the porosity (Han and Wang, 2016). It is important to keep in mind that high values of porosity were

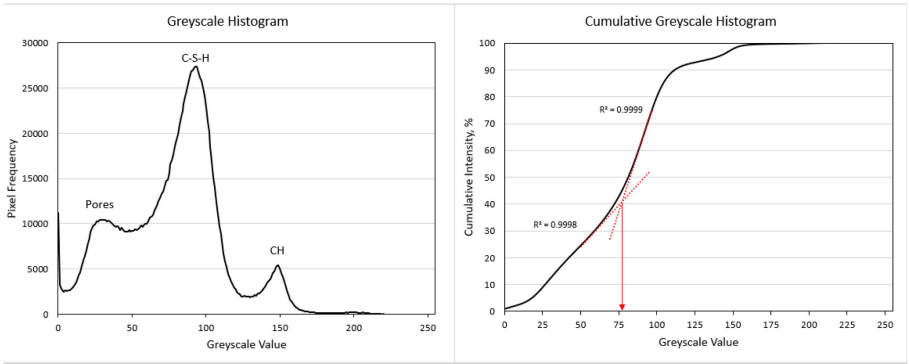

FIGURE 10 | On the left is the typical greyscale histogram seen throughout the images taken of the samples. The peaks correspond to porosity, C-S-H, and CH (from left to right). The slight bump around the greyscale value of 200 would be the minimal anhydrous material. The right side shows the cumulative greyscale histogram used with the overflow method to determine the greyscale value for thresholding.

TABLE 2 | Summary of measured porosity, pore size (D50), and densities of ground and space samples.

	Ground	Space
Porosity per image analysis (%)	48.1	71.7
Porosity per MIP (%)	48.4	69.4
D50 (nm)	390	6,015
Bulk density (g/ml)	0.98	0.55
Skeletal density (g/ml)	1.91	1.79

expected due to the samples having a w/c of 2.0. This analysis further confirms the effect that gravity has on the densities of the samples.

MIP

The results obtained from MIP, summarized in **Table 2**, support the SEM observations and are in good agreement with the image analysis. As expected, the porosity [i.e., the network of interconnected pores (Aligizan, 2006)] is over 20 percent higher in the space sample than in the ground control. It should be noted that the air bubbles (voids) (**Figure 4**) are not included in the measurements of interconnected porosity.

By comparison, the samples hydrated on Earth and space not only differ in terms of the total porosity and density (**Table 2**), but also in terms of pore size distribution. The pore size distribution in cement pastes strongly affects permeability, ion diffusivity (Halamickova et al., 1995; Kim et al., 2012), conductivity (Rajabipour et al., 2007), and mechanical properties (Zhang and Wang, 2016) of cement pastes. As shown in **Figure 11**, the ground sample develops well-distributed pore sizes, ranging between 15 and 10,000 nm. The sample hydrated in space, contrarily, develops over 50 percent of its pores between 6,000 nm and 10,000 nm, which is characterized by the steep slope (**Figure 9**). The calculated D50s (i.e., the pore diameter (nm) at which 50% of the pores are smaller than) are summarized in **Table 2**.

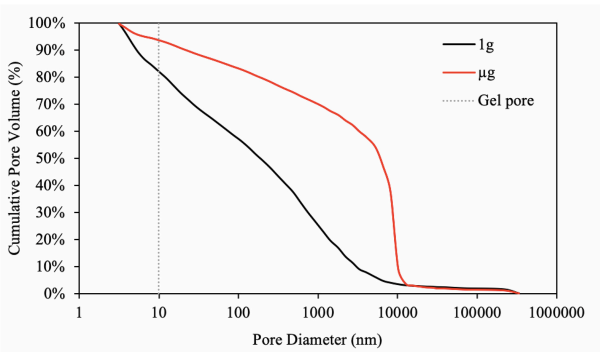

FIGURE 11 | Pore size (diameter) distribution of C_3S paste hydrated in 1 *g* (black) and μg (red). The dashed line indicates the size limit between gel pores (<10 nm) and capillary pores (10 nm < capillary pore < 10,000 nm). The paste hydrated in 1 *g* condition develops well-distributed pore sizes, whereas the paste hydrated in μg condition develops 50 percent of the pores larger than 6,015 nm (D50). This can be seen graphically by the steep slope at the range of 6,000–10,000 nm.

Also shown in **Figure 11**, the curve representing the pore size distribution of the ground control ends abruptly on a steep slope, whereas the curve representing the space sample seems to be slowly plateauing. This suggests that percentage of pores smaller than 3 nm is likely to be greater in the ground sample than the in the space one. The inability of mercury to penetrate into pores smaller than 3 nm (Aligizan, 2006) limits the measurements of pore size distribution but still support the differences found in the skeleton densities (**Table 2**). Additionally, it needs to be mentioned here that MIP measures the entry pore diameter only.

Another important feature pointed out by MIP is the bulk density, which also differs significantly between the space and ground control samples. ASTM D3766-08 (2012) defines bulk density as one including the skeleton of the paste, connected pores, non-connected pores, and air bubbles. The ground control under the influence of a gravity-driven compaction becomes denser, i.e., each gram of hydrated paste should occupy a

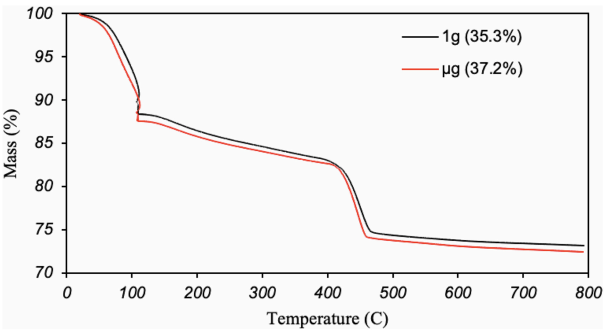

FIGURE 12 | Thermogravimetric curves of C_3S pastes hydrated in 1 *g* (black) and μg (red), showing mass loss upon heating. The steep slope at 110°C is characteristic of loss of free-water, and the steep slope around 400°C is characteristics of dehydration of CH. The numbers within the brackets are the calculated masses of CH, which possibly includes some unreacted lime.

predictable volume, which can be theoretically calculated (Young and Hansen, 1987) or modeled (Lothenbach et al., 2011). Both the empirical equations and model for volume changes would not apply for cements hydrated in µg. In the absence of gravity, cement-based materials should occupy a larger volume, given the lower bulk density (**Table 2**), as verified by visual comparison of the 1*g* and μg samples. The skeleton density also differs between the space sample and ground control. In this case, the volume of the sample excludes the connected porosity from the volume calculations (ASTM D3766-08, 2012), and most likely the air bubbles, suggesting a possible variability of the C-S-H hydrated in μg.

TGA

While it is possible that gravity impacts reaction rates, the results obtained here suggest similar reaction rates between ground and space samples. **Figure 12** shows that the mass of portlandite produced is essentially unaffected by the gravity level, despite the discussed morphological and spatial differences. The analysis of the collected data to quantify the amount of portlandite was performed as suggested by Kim and Olek (Kim and Olek, 2012). The portlandite content in space and ground samples are 35.3 and 37.2 percent by mass, respectively. This difference of <2 percent is attributed to sampling and/or instrumentation errors.

The degree of hydration (α) can also be inferred from the TGA curves through Equation 1 (Zhang and Scherer, 2011):

$$\alpha = \frac{W_n}{n} - LOI \quad (1)$$

where W_n is the normalized weight loss of the sample, n is the mass of non-evaporable water of the fully hydrated paste, and LOI is the loss on ignition or the normalized weight loss of the anhydrous cement. The non-evaporable water for C_3S paste is a fixed value of 0.21 determined by Young and Hansen (Young and Hansen, 1987), whereas the LOI, measured according to ASTM C114 (ASTM C114 – 18., 2018) is 0.9 percent. That gives an 88 percent degree of hydration for both ground and space samples.

XRD

Qualitative XRD data, shown in **Figure 13**, points out the presence of two crystalline phases, identified as portlandite and calcite. Firstly, the diffraction pattern confirms that μg tends to change the growth kinetics of portlandite, resulting in different crystal morphology. More specifically, the length-to-width or aspect ratio of portlandite is reduced in space samples in comparison to the ground control. The diffraction pattern presents several discrepancies among the intensities most pronounced in the indexed portlandite peaks. The main difference observed is at the peak corresponding to the (001) basal plane ($2\theta = 18.066^\circ$) of calcium hydroxide. According to the Powder Diffraction File no. 01-076-0571 (Kabekkodu S. (ed)., 2018), the most intense peak (100% intensity) should be that of (011) ($2\theta = 34.101^\circ$). The presented spectrum (**Figure 13**) is subject to preferred orientation effects, or the tendency of dish-like crystals to lie on the basal plane, parallel to the surface, rather than being randomly oriented in the prepared sample (Grattan-Bellew, 1975). For portlandite, this effect erroneously enhances the relative intensity of the diffracted (001) hexagonal bases, while decreasing the intensity of peaks corresponding to other planes, such as the lateral facets. Despite the error, the diffraction pattern coupled with SEM observations highlight the influence of gravity level on crystal morphology.

Secondly, the peaks resulting from the presence of calcite indicates that the samples experienced carbonation. It is believed that carbonation occurred during sample preparation, since the pouches were sealed and contained limited air. Furthermore, during the extensive SEM analysis on fractured samples, crystals resembling the possible forms of calcite crystals (Mason and Berry, 1968) were not found.

Another important observation inferred from the diffraction pattern is that the peak positions (2θ) corresponding to portlandite in the space samples have not changed relative to the ground control. As such, it implies that the atom positions of the unit cell are the same as those measured by Busing and Levi (Busing and Levy, 1957). The results (**Figure 13**) are also in line with the NaCl crystal grown aboard the ISS (Fontana et al., 2011), which presented morphological differences from those typically grown on Earth, while maintaining the lattice parameters.

CONCLUSIONS

This research presents an experimental comparison between high water-to-cement ratio C_3S pastes hydrated under terrestrial gravity and microgravity conditions. The results revealed that microgravity alters several features of the microstructure of high water-to-cement ratio C_3S paste, including, but not limited to the following:

- Bleeding and sedimentation effects are minimized in microgravity resulting in a paste with a uniform distribution of hydrated phases and, consequently, a uniform density and porosity.
- The lack of self-weight consolidation and segregation in µg leads to 20 percent increase in porosity confirmed by both

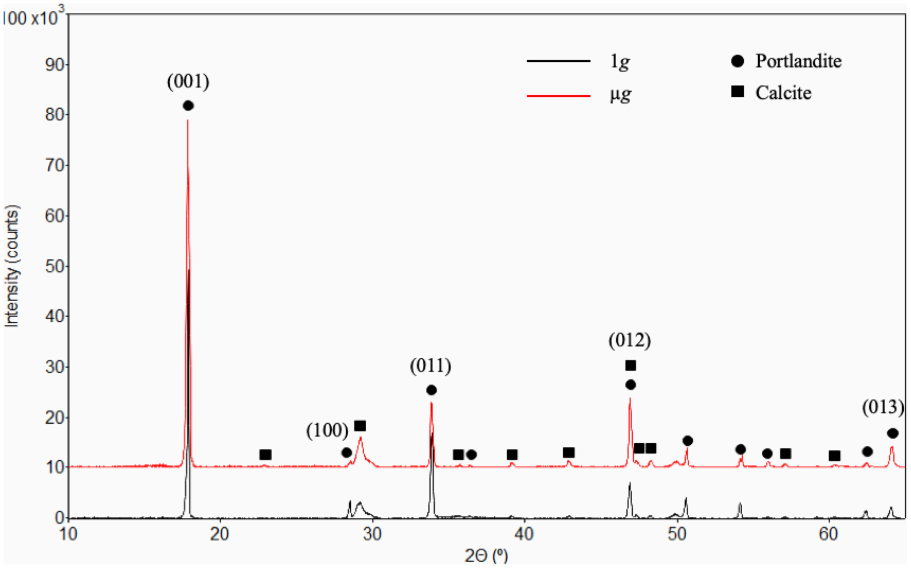

FIGURE 13 | X-ray diffraction pattern collected from C_3S pastes hydrated in 1 *g* (black) and μ*g* (red), both indicating portlandite and calcite phases. Despite the preferred orientation, the indexed peaks correspond to those of portlandite showing the most pronounced differences in intensity, which reflect the morphological dissimilarities between the crystals formed in 1 *g* and μ*g*. It should be mentioned that the background was removed resulting in a flat, horizontal diffraction pattern.

image analysis and MIP. Moreover, the pore diameters for μg are one order of magnitude larger than the ground control.

- Air bubbles remain intermixed within the cementitious paste due to lack of buoyancy forces in microgravity.
- TGA analysis revealed that both ground and space samples reached a degree of hydration of 88% at 151 days.
- The link between microgravity and different crystal morphology is the uniform spatial distribution of the phases in the μ*g* hydrating paste. This, in addition to more room (i.e., higher porosity) allows portlandite to have a larger and more marked dish-like shape. In 1g, bleeding creates a gradient w/c and smaller porosity, which limits the crystal growth.

The results presented here provide a first comparison of cement samples processed on the ground and in a microgravity environment. Lack of physical factors, including buoyancy, sedimentation, and fluid convection resulted in samples with uniform phase distribution and distinct morphologies. Despite using a very high w/c, the observations made here call attention to aspects worthy of being explored in future studies.

AUTHOR CONTRIBUTIONS

JM collected and interpreted most of the data, as well as wrote the manuscript. PC was responsible for image analysis and helped substantially with writing the manuscript. RW contributed by collecting several XRD diffraction patterns and helped analyzing and interpreting the data. RG was present during SEM investigation, provided valuable mentoring and insights about his experience with microgravity research. AR is the principal investigator, advisor, and was awarded with the NASA grant.

FUNDING

All the funding was provided by NASA.

ACKNOWLEDGMENTS

The authors gratefully acknowledge the financial support from the National Aeronautics and Space Administration (NASA)-Grant No. NNX17AC48G, as well as use of MSFC's EM31 Materials Diagnostics laboratory and precious insights from David Donovan, Karen Stephens, and Pam Denkins. Appreciation is expressed to Reviewers of the manuscript, Dr. Farshad Rajabipour, Dr. Barry Scheetz for their feedback during manuscript writing, and the Science Concept Review committee: Jan Olek, Maria Juenger, Kim Kurtis, Jason Ideker, and Sulapha Peethamparan for their valuable suggestions in research planning stages. The authors also express gratitude for collaboration with NIST, in particular Dale Bentz and Jeff Bullard. Thanks to the Leidos team, particularly Micah Johnson, Cole Nelson, and Kile Mouch, for the pre-launch preparation of the samples. Lastly, the authors express immense gratitude for the astronauts of Expedition 56: Drew Fuestel, Serena M. Auñón-Chancellor, Ricky Arnold, Alexander Gerst, Sergey Prokopyev, and Oleg Artemyev, who executed the experiments aboard the ISS.

REFERENCES

Aligizan, K. K. (2006). *Pore Structure of Cement-Based Materials - Testing, Interpretation and Requirements*. New York: Taylor & Francis.

ASTM C114 – 18. (2018). Standard test methods for chemical analysis of hydraulic cement. *Annu. B. ASTM Stand.* 1–33. doi: 10.1520/C0114-18.1.3

ASTM D3766-08 (2012). Standard Terminology Relating to Catalysts and Catalysis. *Annu. B. ASTM Stand.* 08, 26–27. doi: 10.1520/D3766-08.2

Barge, L. M., Cardoso, S. S. S., Cartwright, J. H. E., Cooper, G. J. T., Cronin, L., A., et al. (2015). From chemical gardens to chemobrionics. *Chem. Rev*. 115, 8652–8703. doi: 10.1021/acs.chemrev.5b00014

Bazzoni, A. (2014). *Study of Early Hydration Mechanisms of Cement by Means of Electron Microscopy*. Lausanne: Ecole Polytechnique Federale de Lausane. doi: 10.5075/epfl-thesis-6296

Bentz, D. P., and Garboczi, E. J. (1991). Percolation of phases in a three-dimensional cement paste microstructural model. *Cem. Concr. Res*. 21, 325–344.

Bogue, R. H. (1947). *The Chemistry of Portland Cement*. New York, NY: Reinhold Publishing Corporation.

Boistelle, R., and Astier, J. P. (1988). Crystallization mechanisms in solution. *J. Cryst. Growth*. 90, 14–30. doi: 10.1016/0022-0248(88)90294-1

Bullard, J. W., Enjolras, E., George, W. L., Satterfield, S. G., and Terrill, J. E. (2010). A parallel reaction-transport model applied to cement hydration and microstructure Development. *Model. Simulat. Mater. Scie. Eng.* 18, 1–16. doi: 10.1088/0965-0393/18/2/025007

Bullard, J. W., Jennings, H. M., Livingston, R. A., Nonat, A., Scherer, G. W., Scheitzer, J. S., et al. (2011). Mechanisms of cement hydration. *Cem. Concr. Res*. 41, 1208–1223. doi: 10.1016/B978-0-08-100693-1.00008-4

Busing, W. R., and Levy, H. A. (1957). Neutron diffraction study of calcium hydroxide. *J.* Chem. *Phys*. 26, 563–568.

Cavcar, M. (2000). *The International Standard Atmosphere*. Eskisehir.

Fontana, P., Schefer, J., and Pettit, D. (2011). Characterization of sodium chloride crystals grown in microgravity. *J. Cryst. Growth*. 324, 207–211. doi: 10.1016/j.jcrysgro.2011.04.001

Futron Corporation. (2002). *Space Transportation Costs: Trends in Price Per Pound to Orbit 1990–2000*. Bethesda, MD: Futron Corporation.

Gallucci, E., and Scrivener, K. (2007). Crystallisation of calcium hydroxide in early age model and ordinary cementitious systems. *Cem. Concr. Res*. 37, 492–501. doi: 10.1016/j.cemconres.2007.01.001

Glasser, F. P. (2001). "The role of $Ca(OH)_2$ in Portland cement concretes," in *Materials of Science and Concrete, Calcium Hydroxide in Concrete*, Vol. 58 (New York, NY: Wiley) 11–36.

Grattan-Bellew, P. E. (1975). Effects of Preferred Orientation on X-Ray Diffraction Patterns of Gypsum. *Am. Mineral*. 60, 1127–1129.

Halamickova, P., Detwiler, R. J., Bentz, D. P., and Garboczi, E. J. (1995). Water permeability and chloride ion diffusion in portland cement mortars: relationship to sand content and critical pore diameter. *Cem. Concr. Res*. 25, 790–802. doi: 10.1016/0008-8846(95)00069-O

Han, J., and Wang, K. (2016). Influence of bleeding on properties and microstructure of fresh and hydrated Portland cement paste. *Constr. Build. Mater*. 115, 240–246. doi: 10.1016/j.conbuildmat.2016.04.059

Harutyunyan, V. S., Kirchheim, A. P., Monteiro, P. J. M., Aivazyan, A. P., and Fischer, P. (2009). Investigation of early growth of calcium hydroxide crystals in cement solution by soft X-ray transmission microscopy. *J. Mater. Sci*. 44, 962–969. doi: 10.1007/s10853-008-3198-5

Hu, Q., Aboustait, M., Kim, T., Ley, M. T., Bullard, J. W., Scherer, G., et al. (2016a). Direct measurements of 3d structure, chemistry and mass density during the induction period of C3S hydration. *Cem. Concr. Res*. 89, 14–26. doi: 10.1016/j.cemconres.2016.07.008

Hu, Q., Aboustait, M., Kim, T., Ley, M. T., Hanan, J. C., Bullard, J., et al. (2016b). Direct three-dimensional observation of the microstructure and chemistry of C3S hydration. *Cem. Concr. Res*. 88, 157–169. doi: 10.1016/j.cemconres.2016.07.006

Joseph, S., Bishnoi, S., Van Balen, K., and Cizer, Ö. (2017). Modeling the effect of fineness and filler in early-age hydration of tricalcium silicate. *J. Am. Ceram. Soc*. 100, 1178–1194. doi: 10.1111/jace.14676

Kabekkodu S. (ed). (2018). *PDF-04-10-3117 2011 (Database)*. New Square, PA: The International Centre for Diffraction Data.

Khoshnevis, B. (2004). Automated construction by contour crafting — related robotics and information technologies. *Autom. Constr*. 13, 5–19. doi: 10.1016/j.autcon.2003.08.012

Kim, K. Y., Yun, T. S., Park, K. P., Mo, L., Panesar, D. K., Hu, J., et al. (2012). Pore structure characterization of cement pastes blended with high-volume fly-ash. *Cem. Concr. Res*. 42, 769–777. doi: 10.1016/j.cemconres.2013.03.020

Kim, T., and Olek, J. (2012). Effects of sample preparation and interpretation of thermogravimetric curves on calcium hydroxide in hydrated pastes and mortars effects of sample preparation and interpretation of thermogravimetric curves on calcium hydroxide in hydrated pastes and morta. *Transp. Res. Board*. 2290, 10–18. doi: 10.3141/2290-02

Lei, L., Meier, M. R., Rinkenburger, A., Zheng, B., Fu, L., and Plank, J. (2016). Early hydration of portland cement admixed with polycarboxylates studied under terrestric and microgravity conditions. *J. Adv. Concr. Technol*. 14, 102–107. doi: 10.3151/jact.14.102

Lothenbach, B., Scrivener, K., and Hooton, R. D. (2011). Supplementary cementitious materials. *Cem. Concr. Res*. 41, 1244–1256. doi: 10.1016/j.cemconres.2010.12.001

lsson-Francis, K. O., Billi, D., Teske, A., and de Vera, J.-P. P. (2018). Editorial: habitability beyond earth. *Front. Microbiol*. 9:2645. doi: 10.3389/fmicb.2018.02645

Mason, B., and Berry, L. G. (1968). *Elements of Mineralogy*. San Francisco, CA: W.H. Freeman and Company.

Meier, M. R., and Plank, J. (2016). Crystal growth of [Ca3Al(OH)6.12H2O]2.(SO4)3.2H2O (ettringite) under microgravity: on the impact of anionicity of polycarboxylate comb polymers. *J. Cryst. Growth*. 446, 92–102. doi: 10.1016/j.jcrysgro.2016.04.049

Meier, M. R., Sarigaphuti, M., Sainamthip, P., and Plank, J. (2015). Early hydration of Portland cement studied under microgravity conditions, Constr. *Build. Mater*. 93, 877–883. doi: 10.1016/j.conbuildmat.2015.05.074

Mindess, S., Young, J. F., and Darwin, D. (2003). *Concrete, Second Edition*. Upper Saddle River, NJ: Pearson Education, Inc.

National Research Council (2012). *NASA Space Technology Roadmaps And Priorities: Restoring NASA's Technological Edge and Paving the Way for a New Era in Space*. Washington, DC: National Academy Press. doi: 10.17226/13354

Powers, T. C. (1958). Structure and physical properties of hardened Portland cement paste. *J. Am.* Ceram. *Soc*. 41, 1–6.

Powers, T. C., and Brownyard, T. L. (1946). Studies of the physical properties of hardened portland cement paste. *J. Proc*. 43, 101–132.

Powers, T. C., Copeland, L. E., Hayes, J. C., and Mann, H. M. (1954). The properties of fresh concrete. *J. Proc*. 51, 285–298.

Provis, J. L. (2015). Grand Challenges in Structural Materials, Front. *Mater*. 2, 8–11. doi: 10.3389/fmats.2015.00031.

Qi, X. B., Chen, Y., Kang, X. H., Li, D. Z., and Gong, T. Z. (2017). Modeling of coupled motion and growth interaction of equiaxed dendritic crystals in a binary alloy during solidification. *Sci. Rep*. 7, 1–16. doi: 10.1038/srep45770

Rajabipour, F., Giannini, E., Dunant, C., Ideker, J. H., and Thomas, M. D. A. (2015). Alkali – silica reaction: current understanding of the reaction mechanisms and the knowledge gaps. *Cem. Concr. Res*. 76, 130–146. doi: 10.1016/j.cemconres.2015.05.024

Rajabipour, F., Sant, G., and Weiss, J. (2007). "Development of electrical conductivity-based sensors for health monitoring of concrete materials," in *TRB Annual Conference, CD-Rom Paper# 07-1765* (Washington, DC: Transportation Research Board), 1–16.

Scrivener, K. L. (1989). The Microstructure of Concrete. *Mater. Sci. Concr. III*. 1, 127–161. doi: 10.1016/0008-8846(95)00036-C

Scrivener, K. L. (2004). Backscattered electron imaging of cementitious microstructures: understanding and quantification, Cem. *Concr. Compos*. 26, 935–945. doi: 10.1016/j.cemconcomp.2004.02.029

Scrivener, K. L., Juilland, P., and Monteiro, P. J. M. (2015). Advances in understanding hydration of Portland cement. *Cem. Concr. Res*. 78, 38–56. doi: 10.1016/j.cemconres.2015.05.025

Taylor, H. F. W. (1990). *Cement Chemistry*. New York, NY: Academic Press.

Thomas, J., and Jennings, H. (2019). *The Science of Concrete*. Evanston: Northwester University. Available online at: http://iti.northwestern.edu/cement/index.html

Thomas, J. J., Jennings, H. M., and Chen, J. J. (2009). Influence of nucleation seeding on the hydration mechanisms of tricalcium silicate and cement. *J. Phys. Chem. C*. 113, 4327–4334. doi: 10.1021/jp809811w

Turner, J. S. (1979). *Buoyancy Effects in Fluids*. New York, NY: Cambridge University Press.

Wong, H. S., Head, M. K., and Buenfeld, N. R. (2006). Pore segmentation of cement-based materials from backscattered electron images. *Cem. Concr. Res.* 36, 1083–1090. doi: 10.1016/j.cemconres.2005.10.006

Young, J. F., and Hansen, W. (1987). Volume relationships for C-S-H formation based on hydration stoichiometries. *Mater. Res. Soc.* 85, 313–322.

Zhang, J., and Scherer, G. W. (2011). Cement and concrete research comparison of methods for arresting hydration of cement. *Cem. Concr. Res.* 41, 1024–1036. doi: 10.1016/j.cemconres.2011.06.003

Zhang, Z., and Wang, H. (2016). The Pore characteristics of geopolymer Foam concrete and Their impact on the compressive strength and Modulus. *Front. Mater. Struct. Mater.* 3, 1–10. doi: 10.3389/fmats.2016.00038

Conflict of Interest Statement: The authors declare that the research was conducted in the absence of any commercial or financial relationships that could be construed as a potential conflict of interest.

frontiers in Materials

ORIGINAL RESEARCH
published: 30 April 2019
doi: 10.3389/fmats.2019.00090

Effect of Nano Alumina on Compressive Strength and Microstructure of High Volume Slag and Slag-Fly Ash Blended Pastes

Faiz Uddin Ahmed Shaikh and Anwar Hosan*

School of Civil and Mechanical Engineering, Curtin University, Perth, WA, Australia

This paper presents the effect of nano alumina (NA) on compressive strength and microstructure of cement paste containing high volume blast furnace slag (HVBFS) contents of 70, 80, and 90% as partial replacement of cement and combined blast furnace slag (BFS) and class F fly ash (FA) contents of 70 and 80% as partial replacement of cement. FA is used at 30% as partial replacement of BFS. NA contents are varied from 1 to 4% as partial replacement of BFS and BFS-FA. Results show that the addition of NA improves the compressive strength of high volume BFS and BFS-FA pastes by 2 to 16%. The compressive strength of paste containing 69% BFS, 30% cement, and 1% NA exceeded the compressive strength of control cement paste while the compressive strength of paste containing 77% BFS, 20% cement, and 3% NA is 1% lower than control cement paste. NA significantly reduced the large capillary pores of >0.1 microns of high volume BFS and BFS-FA pastes. No evidence of reduction of $Ca(OH)_2$ in high volume BFS pastes is observed due to addition of NA, however, in high volume BFS-FA paste the $Ca(OH)_2$ is reduced due to addition of NA. Increase in intensity peaks of CAH, Ettringite and CSH in X-ray diffraction analysis is observed in high volume BFS and BFS-FA pastes due to addition of NA, which coincides with the observed more dense microstructure of high volume BFS and BFS-FA pastes containing NA than those without NA.

Keywords: nano alumina, blast furnace slag, fly ash, compressive strength, microstructure

OPEN ACCESS

Edited by:
Maria Juenger,
University of Texas at Austin,
United States

Reviewed by:
Denvid Lau,
City University of Hong Kong,
Hong Kong
Ali Behnood,
Purdue University, United States

****Correspondence:***
Faiz Uddin Ahmed Shaikh
s.ahmed@curtin.edu.au

Specialty section:
This article was submitted to Structural Materials, a section of the journal Frontiers in Materials

Received: *20 December 2018*
Accepted: *10 April 2019*
Published: *30 April 2019*

Citation:
Shaikh FUA and Hosan A (2019) Effect of Nano Alumina on Compressive Strength and Microstructure of High Volume Slag and Slag-Fly Ash Blended Pastes. Front. Mater. 6:90. doi: 10.3389/fmats.2019.00090

INTRODUCTION

Concrete is the most widely used construction materials in the world. Its demand continues due to rapid urbanization and population growth in the world. As a result the demand of cement, the key ingredient of concrete, also increases. However, the manufacturing of cement is energy intensive and contributes about 5–7% of total CO_2 release in to the atmosphere globally (Benhelal et al., 2013). Therefore, there is worldwide initiative to reduce the use of cement in concrete by partial replacement of cement using various industrial by-products such as fly ash, blast furnace slag (BFS), silica fume, rice husk ash, sugarcane bagasse ash, etc. Significant amount of research have been devoted worldwide to investigate various properties of concrete containing above by-products. Very good level of understanding of their use in concrete at low volume as well as at high volume already exists, which result their use in concrete as partial replacement of cement in many countries. However, their use in high volume in concrete often results in reduction in early age mechanical and durability properties due to slow pozzolanic reaction of these materials with

cement hydration product (Oner and Akyuz, 2007; Aghaeipour and Madhkhan, 2017). Various ultrafine and nano materials are used to address the above limitation of slow pozzolanic reaction at early stage of concrete. In a number of studies the effect of various nano materials e.g., nano silica, nano $CaCO_3$, nano TiO_2, nano alumina, carbon nano tube, etc. on the properties of concrete containing fly ash at various volume fractions have been evaluated and promising results in terms of improvement in mechanical and durability properties of concrete containing fly ash are reported (Sato and Diallo, 2010; Hou et al., 2013; Shaikh and Supit, 2014, 2015; Shaikh et al., 2014).

Blast furnace slag is the by-product of iron/steel industry and is widely used in concrete as partial replacement of cement.

TABLE 1 | Physical properties and chemical analysis of OPC, BFS, FA, and NA.

Oxides	Ordinary portland cement (OPC) (wt. %)	Class f fly ash (FA) (wt. %)	Blast furnace slag (BFS) (wt. %)	Nano alumina (NA) (wt. %)
Chemical analysis				
SiO_2	21.1	51.11	32.5	–
Al_2O_3	5.24	25.56	13.56	99.5
Fe_2O_3	3.1	12.48	0.85	–
CaO	64.39	4.3	41.2	–
MgO	1.1	1.45	5.10	–
MnO	–	0.15	0.25	–
K_2O	0.57	0.7	0.35	–
Na_2O	0.23	0.77	0.27	–
P_2O_5	–	0.885	0.03	–
TiO_2	–	1.32	0.49	–
SO_3	2.52	0.24	3.2	–
LOI	1.22	0.57	1.11	–
Physical properties				
Particle size	25–40% ≤7 μm	50% of 10 μm	40% of 10 μm	24–43 nm
Specific gravity	2.7*to*3.2	2.6	–	3.5–3.9

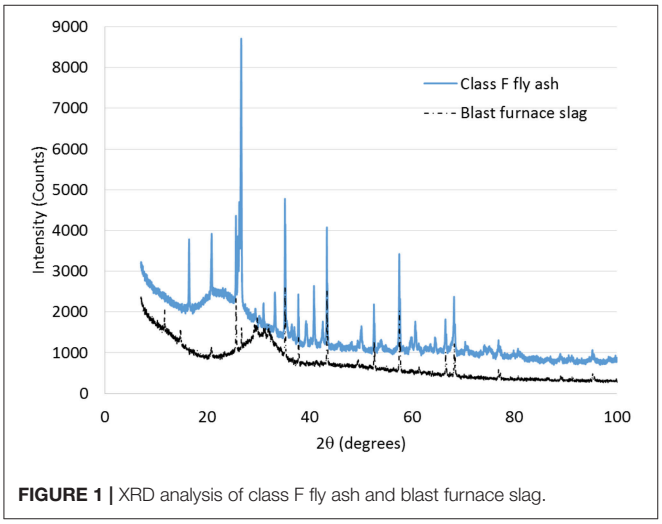

FIGURE 1 | XRD analysis of class F fly ash and blast furnace slag.

Its use up to 60–70% as partial replacement of cement in concrete is researched (Elchalakani et al., 2014). It has been reported that above this limit the mechanical and durability properties are significantly affected (Oner and Akyuz, 2007). Despite the use of various nano materials in concrete containing high volume fly ash, not enough research is reported on the use of nano materials in concrete containing high volume slag above 60%, especially nano alumina which exhibited significant improvement in modulus of elasticity of concrete. Nano alumina, similar to other nano materials, provides synergistic effects in cement hydration process through seeding and filler effects and pozzolanic reaction. In a number of studies the effect of nano alumina on mechanical properties of concrete and cement composite is evaluated. Li et al. (2006) investigated the effect of various nano alumina contents of 3–7% on compressive strength and elastic modulus of cement mortar and reported about 143% improvement in 28 days elastic modulus of cement mortar due to addition of 5% nano alumina due to densification of cement matrix around interfacial transition zone of aggregates in mortar. However, at the same nano alumina content the improvement in compressive strength was not that great. In a separate study, Nazari and Riahi (2011) however, reported significant improvement (about 44%) in compressive strength of cement paste due to addition of 4% nano alumina. Reduction in harmful pores in cement paste due to addition of nano alumina is also observed in their study. On the other hand, Barbhuiya et al. (2014) reported no improvement in 7 days compressive strength of cement paste due to addition of nano alumina despite formation of dense microstructure of cement paste containing nano alumina. Improvement in compressive strength of cement pastes due to addition of nano alumina is also reported by others (Heikal et al., 2015; Gowda et al., 2017). The variation of results on properties of concrete due to addition of NA could be due to their different particle sizes e.g., the size of NA was ∼150nm in the study by Li et al. (2006) whereas Nazari and Riahi (2011) use much smaller size NA particles of about 15 nm. On the other hand, the size of NA was 27–43 nm in Barbhuiya et al. (2014) study.

Mohseni and Tsavdaridis (2016) reported improvement in compressive strength and durability of fly ash mortar containing 25% fly ash due to addition of nano alumina. Reduction in gel and medium capillary pores of fly ash mortar is reported in this study due to addition of nano alumina. So far only one study reported by Nazari and Riahi (2011) evaluated the effect of nano alumina on mechanical and microstructure of self-compacting concrete containing various BFS contents of up to 60% as partial replacement of cement. While nano alumina exhibited improvement in mechanical and durability properties of cement paste and mortars and those containing fly ash and BFS, no study so far reported its effect on the concrete containing high volume slag content above 70% as partial replacement of cement. This paper presents the effect of various nano alumina contents on compressive strength and microstructure of cement pastes containing high volume blast furnace slag (HVBFS) and high volume blast furnace slag and fly ash (HVBFS-FA) as partial replacement of cement.

EXPERIMENTAL PROGRAM

This study is consisted of five parts. In the first three parts, three high volume slag pastes containing 70, 80, and 90% BFS by weight as partial replacement of ordinary Portland cement (OPC) are considered. In the fourth and fifth parts, the effect of two hybrid combinations of BFS and class F fly ash (FA) at total contents of 70 and 80% by weight are considered, where FA is used at 30% by weight of BFS. In all parts the effect of nano alumina (NA) content of 1–4% by weight on the high volume BFS pastes and high volume BFS-FA pastes are evaluated. Therefore, total 26 mixes are considered in this study.

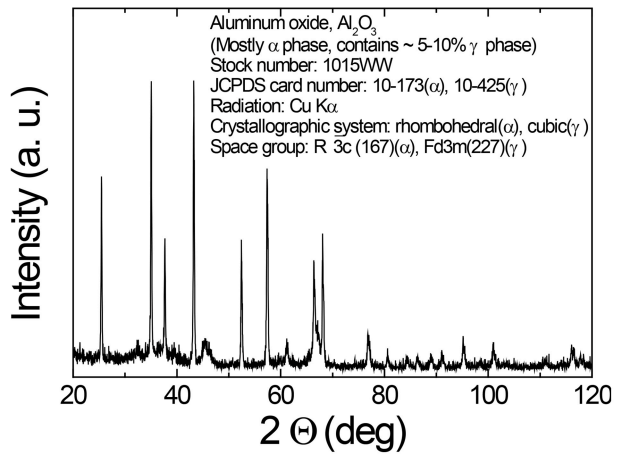

FIGURE 2 | XRD analysis of nano alumina.

MATERIALS, MIX PROPORTIONS, AND CASTING

The cement used in this study was OPC. The fly ash (FA) was class F fly ash supplied by Eraring power station of New South Wales in Australia. The ground granulated BFS was supplied by BGC cement of Australia. The nano alumina (NA) powder was purchased from Nanostructured and Amorphous Materials, Inc. of USA. **Table 1** shows the physical and chemical properties of OPC, FA, BFS, and NA, while **Figures 1**, **2** show the X-ray diffraction (XRD) analysis of FA, BFS and NA. It can be seen by comparing the results that NA was less amorphous compared to FA and BFS. Among FA and BFS, BFS is more amorphous with amorphous content of 95.7% compared to 67.8% amorphous content of FA based on quantitative XRD analysis. Detail mix

TABLE 2 | Mix proportions of high volume slag and high volume slag-fly ash blend cement pastes containing nano alumina (NA).

	Nnao alumina (wt.%)	Mixes	OPC	BFS	Fly ash (FA)	Nano alumina (NA)	Water/binder	Superplasticizer (wt.%)
100% OPC	–	Control	1.0	–	–	–	0.4	–
70% BFS	0	70BFS	0.3	0.7	–	–	0.4	–
	1	69BFS1NA	0.3	0.69	–	0.01	0.4	–
	2	68BFS2NA	0.3	0.68	–	0.02	0.4	–
	3	67BFS3NA	0.3	0.67	–	0.03	0.4	0.5
	4	66BFS4NA	0.3	0.66	–	0.04	0.4	0.5
80% BFS	0	80BFS	0.2	0.8	–	–	0.4	–
	1	79BFS1NA	0.2	0.79	–	0.01	0.4	–
	2	78BFS2NA	0.2	0.78	–	0.02	0.4	0.5
	3	77BFS3NA	0.2	0.77	–	0.03	0.4	0.5
	4	76BFS4NA	0.2	0.76	–	0.04	0.4	0.5
90% BFS	0	90BFS	0.1	0.9	–	–	0.4	–
	1	89BFS1NA	0.1	0.89	–	0.01	0.4	0.5
	2	88BFS2NA	0.1	0.88	–	0.02	0.4	0.5
	3	87BFS3NA	0.1	0.87	–	0.03	0.4	1.0
	4	86BFS4NA	0.1	0.86	–	0.04	0.4	1.0
Combined FA + BFS Total = 70%	0	49BFS21FA	0.3	0.49	0.21	–	0.4	–
	1	49BFS20FA1NA	0.3	0.485	0.205	0.01	0.4	0.5
	2	49BFS19FA2NA	0.3	0.48	0.20	0.02	0.4	0.5
	3	49BFS18FA3NA	0.3	0.475	0.195	0.03	0.4	1.0
	4	49BFS17FA4NA	0.3	0.47	0.19	0.04	0.4	1.0
Combined FA + BFS Total = 80%	0	56BFS24FA	0.2	0.56	0.24	-	0.4	-
	1	56BFS23FA1NA	0.2	0.555	0.235	0.01	0.4	0.5
	2	56BFS22FA2NA	0.2	0.55	0.23	0.02	0.4	0.5
	3	56BFS21FA3NA	0.2	0.545	0.225	0.03	0.4	1.0
	4	56BFS20FA4NA	0.2	0.54	0.22	0.04	0.4	1.0

Superplasticizer was used as wt.% of binder (OPC + BFS + FA + NA).

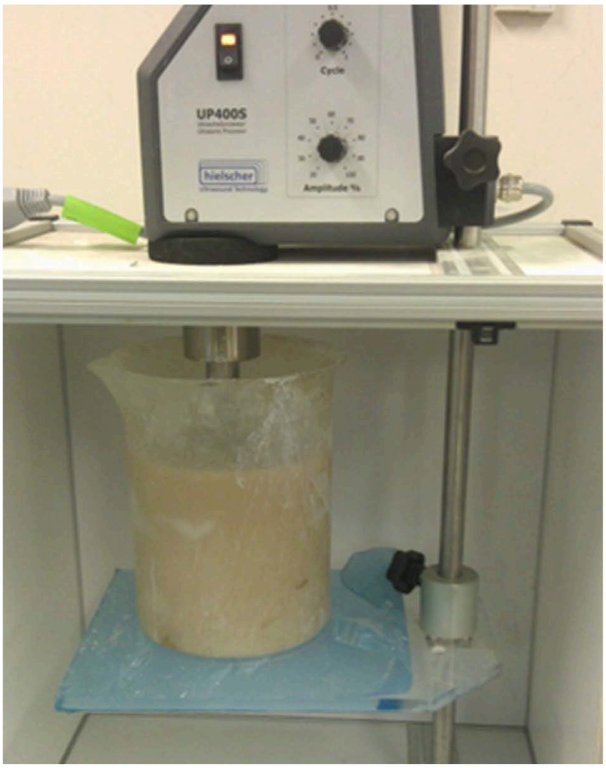

FIGURE 3 | Dispersion of nano alumina in water contining superplasticizer solution in ultrasonication method.

proportions of high volume BFS pastes, high volume BFS-FA pastes and those containing NA are shown in **Table 2**. It can be seen that water/binder ratio of all mixes were kept constant at 0.4. In the case of mixes containing NA, a naphthalene sulfonate based superplasticizer was used to maintain the workability of pastes. All pastes were mixed in Hobart mixer, where cement, FA and BFS were mixed first for ∼3 min. Water was added and mixed for further 3 min. In the case of high volume BFS and high volume BFS-FA pastes containing NA, the NA powder was first ultrasonically dispersed in water containing superplasticizer using ultrasonic mixer for 30 min shown in **Figure 3** and then added with remaining water during mixing. The paste samples of 50 mm cubes were cast and demoulded after 24 h. The specimens were cured in water at room temperature for 28 days.

TESTING METHODS

Compressive strength of the specimens were tested according to ASTM C109 (2012) using a loading rate of 0.7 MPa/s. In order to observe the changes in reaction phases in cement pastes containing high volume BFS and BFS-FA blends due to inclusion of NS thermogravimetric analysis (TGA), X-ray diffraction (XRD) analysis, Mercury intrusion porosimetry (MIP), scanning electron microscopy (SEM), and energy dispersive X-ray spectroscopy (EDS) were done on selected samples.

For the XRD analysis, the samples were measured with a D8 Advance Diffractometer (Bruker-AXS) using copper radiation and a Lynx Eye position sensitive detector. The diffractometer scanned the samples from 7° to 70° (2θ) in steps of 0.015° at a scanning rate of 0.5°/ min. XRD patterns were obtained using Cu Ka lines ($k = 1.5406$ Å). A knife edge collimator was fitted to reduce air scatter. SEM analyses were performed using a Zeiss EVO 40XVP microscope equipped with an energy dispersive X-ray analyser. The thermal stability of the samples was studied by thermogravimetric analysis (TGA). A Mettler Toledo TGA one star system analyser was used for all these measurements. Samples weighing 25 mg were placed in an alumina crucible and the tests were carried out in an Argon atmosphere at a heating rate of 10°C/min from 25 to 1,000°C.

Mercury intrusion porosimetry (MIP) was used to measure the pore volume and pore size distribution of pastes samples. The pore diameter and intruded mercury volume were recorded at each pressure point over a pressure range of 0.0083–207 MPa. The pressures values were converted into equivalent pore diameters using the Washburn expression 1921, as expressed in Equation (1):

$$d = -\frac{4\gamma cos\theta}{p} \quad (1)$$

where, d is the pore diameter (μm), γ is the surface tension (mN/m), θ is the contact angle between mercury and the pore wall (°), and P is the net pressure across the mercury meniscus at the time of the cumulative intrusion measurement (MPa).

RESULTS AND DISCUSSION

Compressive Strength

The effects of various NA contents of 1–4% on compressive strength of high volume BFS pastes are shown in **Figure 4**. **Figure 4A** shows that due to addition of NA the compressive strength of high volume BFS paste containing 70% BFS is higher than that without NA. The compressive strength is increased by 2–16% due to addition of NA. In the case of high volume BFS pastes containing 80 and 90% BFS the improvement in compressive strength due to addition of NA is not better than 70% BFS content. It can be seen in **Figures 4B,C** about 2–8 and 1% improvement in compressive strength due to addition of various amount of NA in pastes containing 80 and 90% BFS, respectively. While the compressive strength of high volume BFS pastes containing 70% and NA is higher than that of control OPC paste, however, the compressive strength of paste containing 80 and 90% BFS is lower than OPC paste despite the addition of NA. This can be due to significantly lower level of Portlandite ($Ca(OH)_2$) generation in these mixes due to very high volume of OPC replacement by BFS. It can also be seen no trend in compressive strength improvement with increase in NA contents in all high volume BFS pastes, however, beyond 3% no improvement in compressive strength is observed presumably due to agglomeration of NA as it has been reported by several researchers. Due to higher van der Waal's forces, the nano alumina particles in water causes agglomeration and hence,

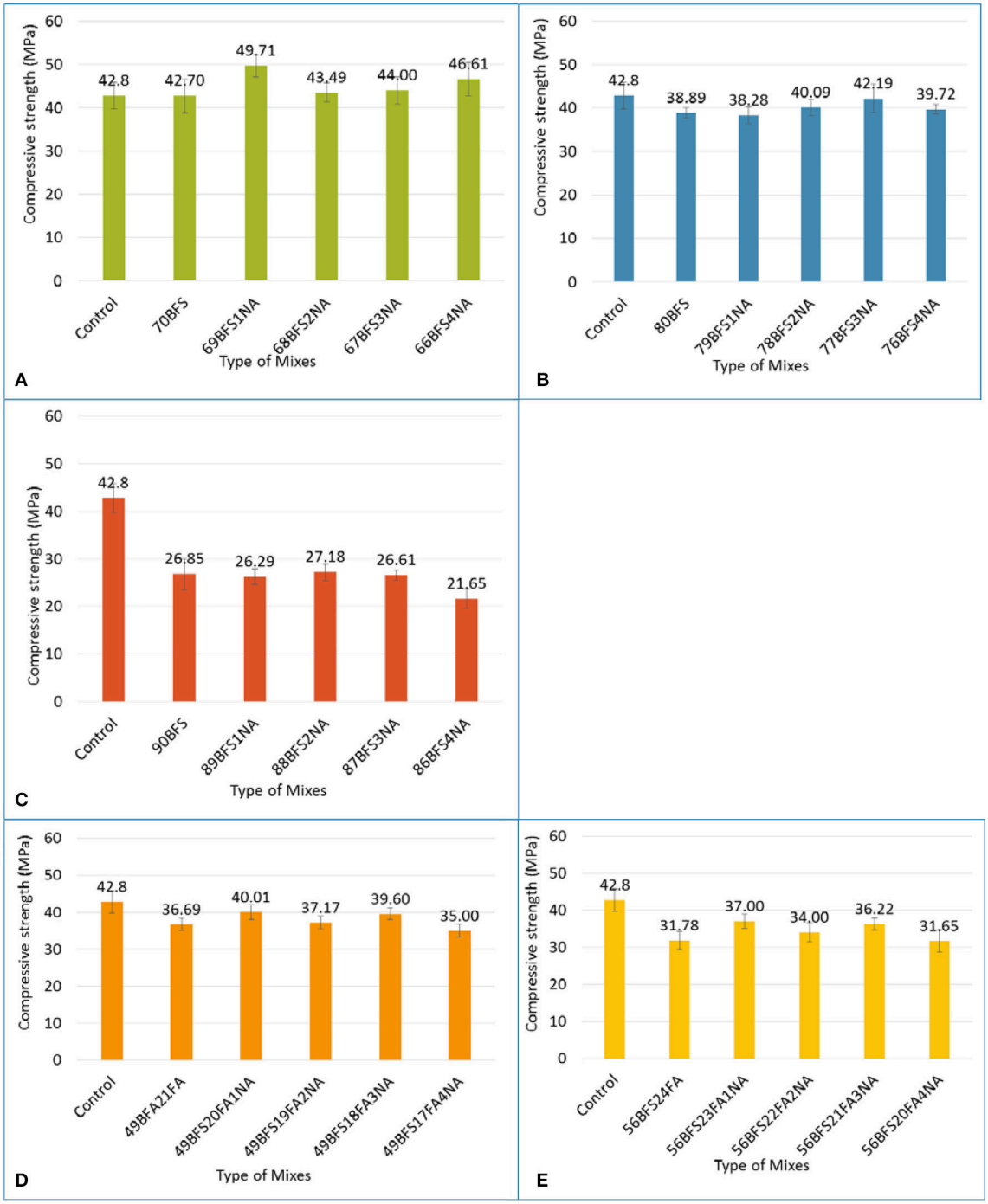

FIGURE 4 | Compressive strength of cement pastes containing **(A)** 70% slag, **(B)** 80% slag, **(C)** 90% slag, **(D)** 70% slag-fly ash blend and **(E)** 80% slag-fly ash blend and those containing various nano alumina contents.

adversely affects their uniform dispersion in the matrix (Senff et al., 2009; Quercia et al., 2012).

The effect of NA on compressive strength of pastes containing combined BFS and FA contents of 70 and 80% is shown in **Figures 4D,E**. It can be seen that the addition of NA improves the compressive strength by up to 9% of paste containing total BFS and FA content of 70%, which is slightly lower than paste containing 70% BFS. In the case of combined BFS and FA

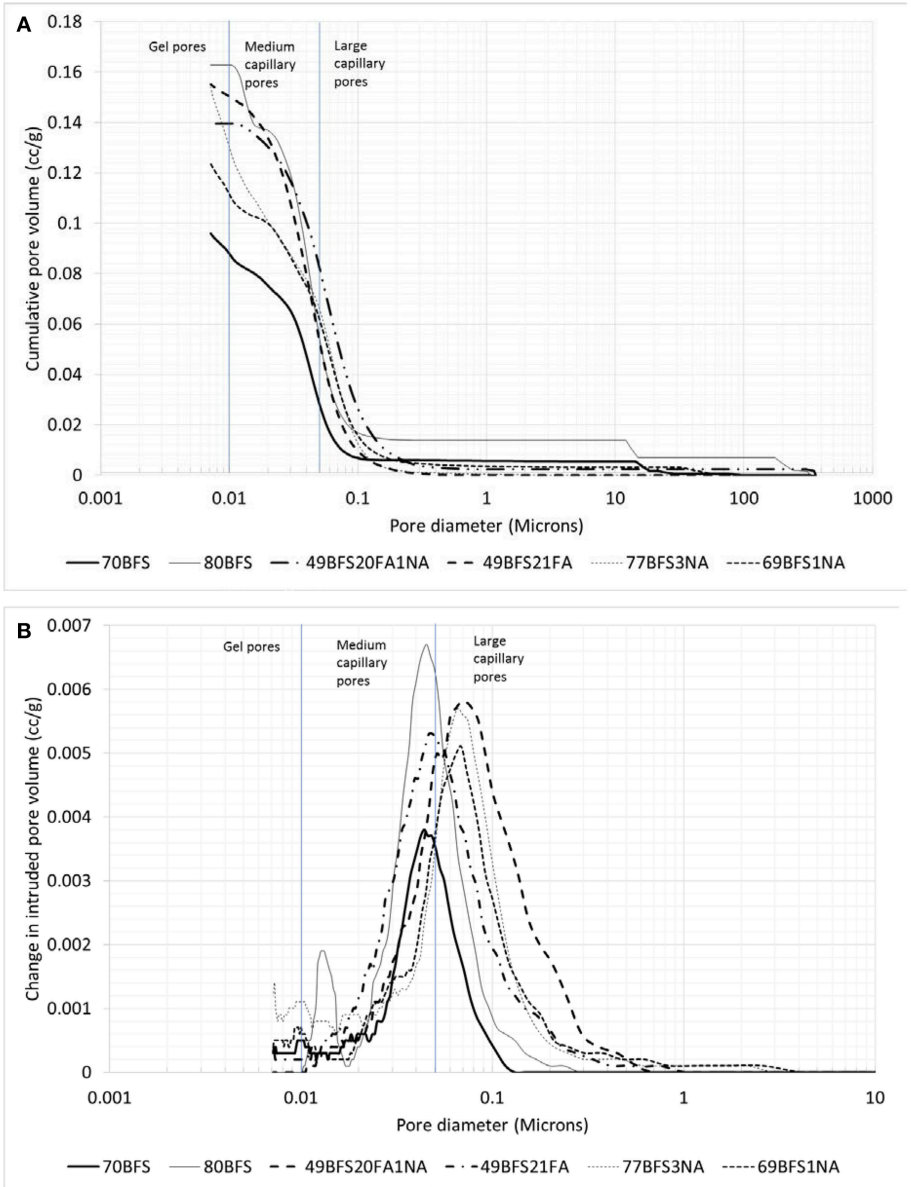

FIGURE 5 | Cumulative pore volume **(A)** and pore size distribution **(B)** of HVS and HVS-FA pastes with and without nano alumina.

content of 80% containing NA up to about 16% improvement in compressive strength is observed which is higher than those containing 80% BFS. However, the compressive strength of these two HVBFS-FA pastes for all NA contents is still lower than that of control OPC paste. The improved compressive strength due to addition of NA in pastes containing combined BFS and FA than the pastes containing BFS can be interpreted as the better dispersion of NA in those mixes due to spherical shape of the FA particles.

Microstructure

It can be seen in above compressive strength results that the high volume BFS paste containing 70% BFS and NA exhibited higher compressive strength than that of control OPC paste. High volume BFS paste containing 80% BFS and combined BFS and FA content of 70% showed about 1 and 7%, respectively, lower compressive strength then that of OPC paste. These mixes contain significantly less OPC hence much lower carbon footprint of concrete made using these blends. Therefore, in the microstructural analysis the changes of microstructures in terms of their pore sizes and volumes, conversion of Portlandite to secondary calcium silicate hydrate (CSH)/calcium aluminate hydrate (CAH) through pozzolanic reaction and formation of new mineral phases are studied due to addition of NA.

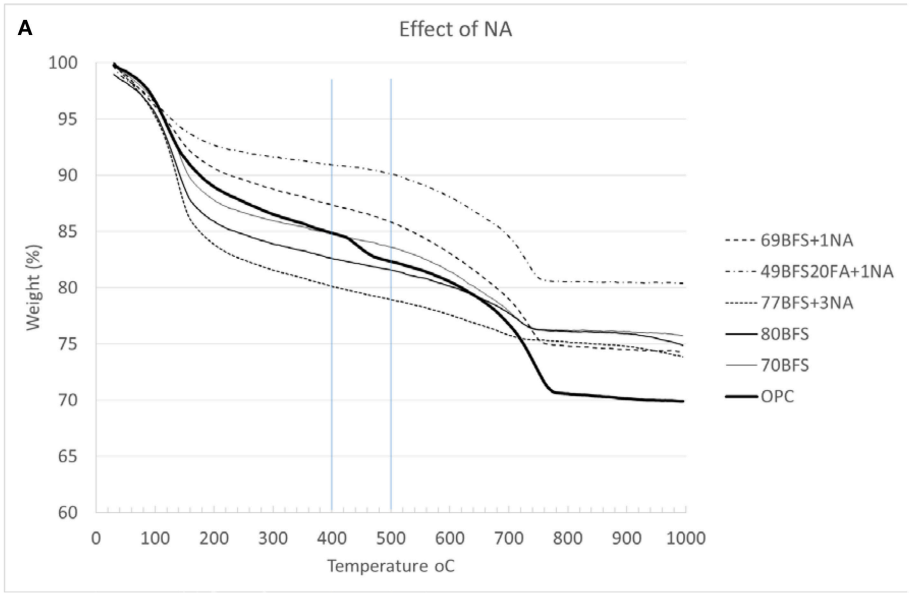

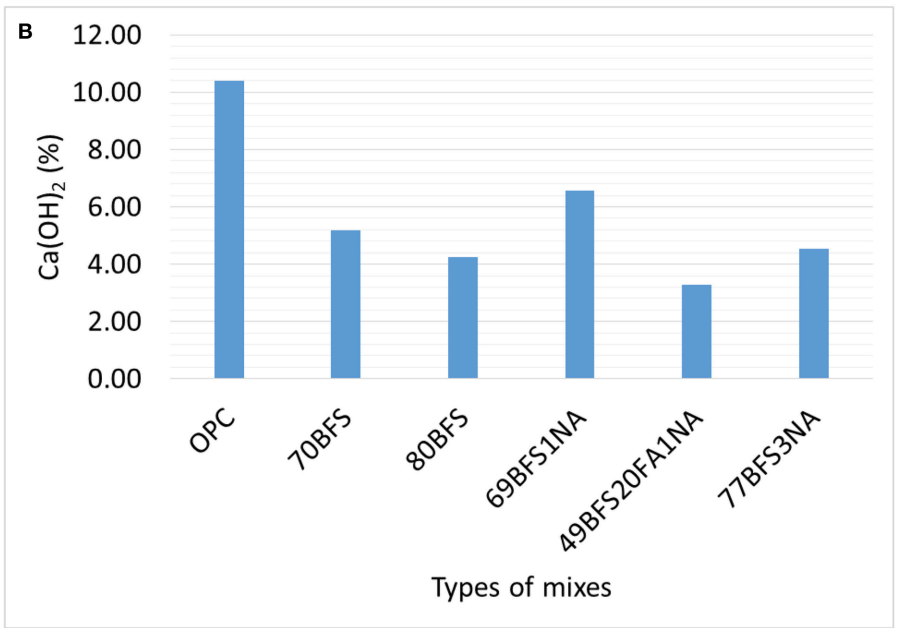

FIGURE 6 | TGA analysis **(A)** and $Ca(OH)_2$ contents **(B)** of HVS and HVS-FA pastes with and without nano alumina.

Mercury Intrusion Porosimetry (MIP)

Figure 5 shows the cumulative pore volume and distribution of various pore sizes of high volume BFS and combined BFS and FA pastes with and without NA. It can be seen in **Figure 5A** that the volume of pores corresponding to pore diameter >0.1 microns increases in cement paste due to addition of high volume BFS contents of 70 and 80% as partial replacement of OPC. However, the volume of medium capillary pores and gel pores corresponding to pore diameters 0.05–0.01 micron and <0.01 microns, respectively, are decreased due to addition of 70% BFS compared to control OPC paste. In the case of paste containing 80% BFS the volume of medium capillary pores and gel pores are higher than OPC paste. By comparing the pastes containing two BFS contents, it can be seen that at 70% BFS content the total pore volume of all pores is less than at 80% BFS content, which might be the reason for observed higher compressive strength in the former paste than the latter as large pores might have caused stress concentration. On the other hand, in the paste containing combined BFS and FA with a total content of 70% the pore volume of larger capillary pores is reduced significantly compared to both high volume BFS pastes and control OPC paste. The distribution of pores having different diameters in

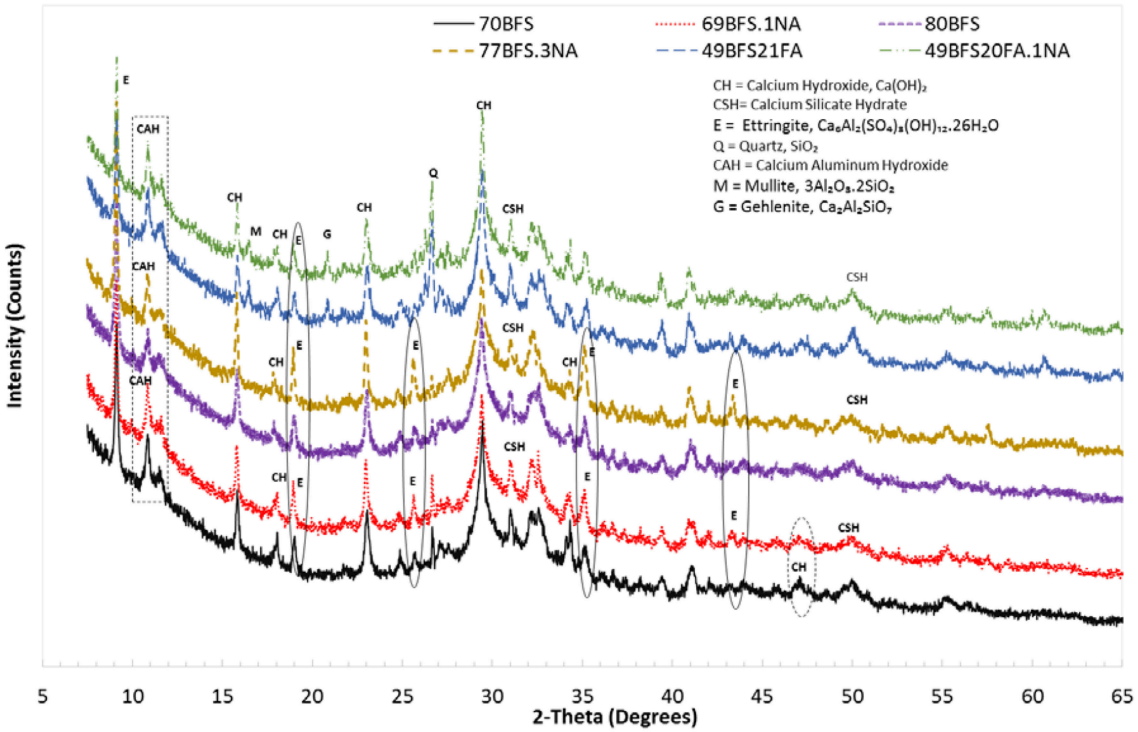

FIGURE 7 | XRD analysis of HVS and HVS-FA pastes with and without nano alumina.

all pastes is shown in **Figure 5B**. The region under the curves represent the concentration of pores and the peak point of the curve represents the critical pore diameter. By comparing different curves its can be seen that the maximum concentration of pores in OPC paste is in 0.03–0.2 microns range which is in lower side of large capillary pores. However, in the case of pastes containing 70 and 80% BFS and combined BFS and FA content of 70% the peak of their curves is shifted toward smaller pore diameter and they fall within medium capillary pores. This indicates that due to addition of BFS and combined BFS and FA the concentration of pores is shifted from large capillary pores to medium capillary pores.

The cumulative pore volume and pore size distribution of high volume BFS and combined BFS and FA pastes containing NA are also shown in **Figure 5**. It can be seen in **Figure 5A** that due to addition of NA the volume of pores corresponding to pore size >0.1 microns is significantly decreased in all high volume BFS and combined BFS and FA pastes. Surprisingly it can also be seen that volume of gel pores and medium capillary pores is increased due to addition of NA in high volume paste containing 70% BFS. The cumulative pore volume of paste containing 80% BFS is reduced from 0.164 to 0.155 cc/g due to addition of 3% NA. In the case of paste containing combined BFS and FA content of 70% the cumulative pore volume is reduced significantly from 0.155 to 0.14 cc/g due to addition of 1% NA. The formation of additional CSH and CAH gels due to enhanced pozzolanic reaction of NA with Portlandite in those high volume BFS and combined BFS and FA pastes could be the reasons for such reduction in volume of large capillary pores in those pastes. However, by looking into the pore size distribution shown in **Figure 5B** it can be seen that the concentration of pores is not significantly changed in high volume BFS and combined BFS and FA pastes due to addition of NA, but the volume of pores in the concentration of pore sizes in each paste containing NA is reduced.

Thermogravimetric Analysis (TGA)

TGA cures of high volume BFS and BFS-FA pastes and those containing NA are shown in **Figure 6A**. TGA curve shows the mass of a substance under control environment as a function of temperature. It has been reported that mass loss between 420 and 540°C corresponds to the dehydration of calcium hydroxide (Keattch and Dollimore, 1975). The amount of calcium hydroxide (CH) can be quantified according to Taylor (1990) formula shown as follows in Equation (2):

$$CH\ (\%) = WL_{CH}(\%)\frac{MW_{CH}}{MW_{H2O}} \quad (2)$$

Where, WLCH is the weight loss during the dehydration of CH between 420 and 540°C as percentage of the ignited weight (%); MWCH is the molecular weight of CH; MWH2O is the molecular weight of H2O.

The calculated CH contents are shown in **Figure 6B** and it can be seen that CH contents of all high volume BFS and BFS-FA pastes and those containing NA are lower than that of OPC paste. This clearly indicate that due to pozzolanic reaction of SiO2 in BFS and FA with CH in those pastes CSH is formed.

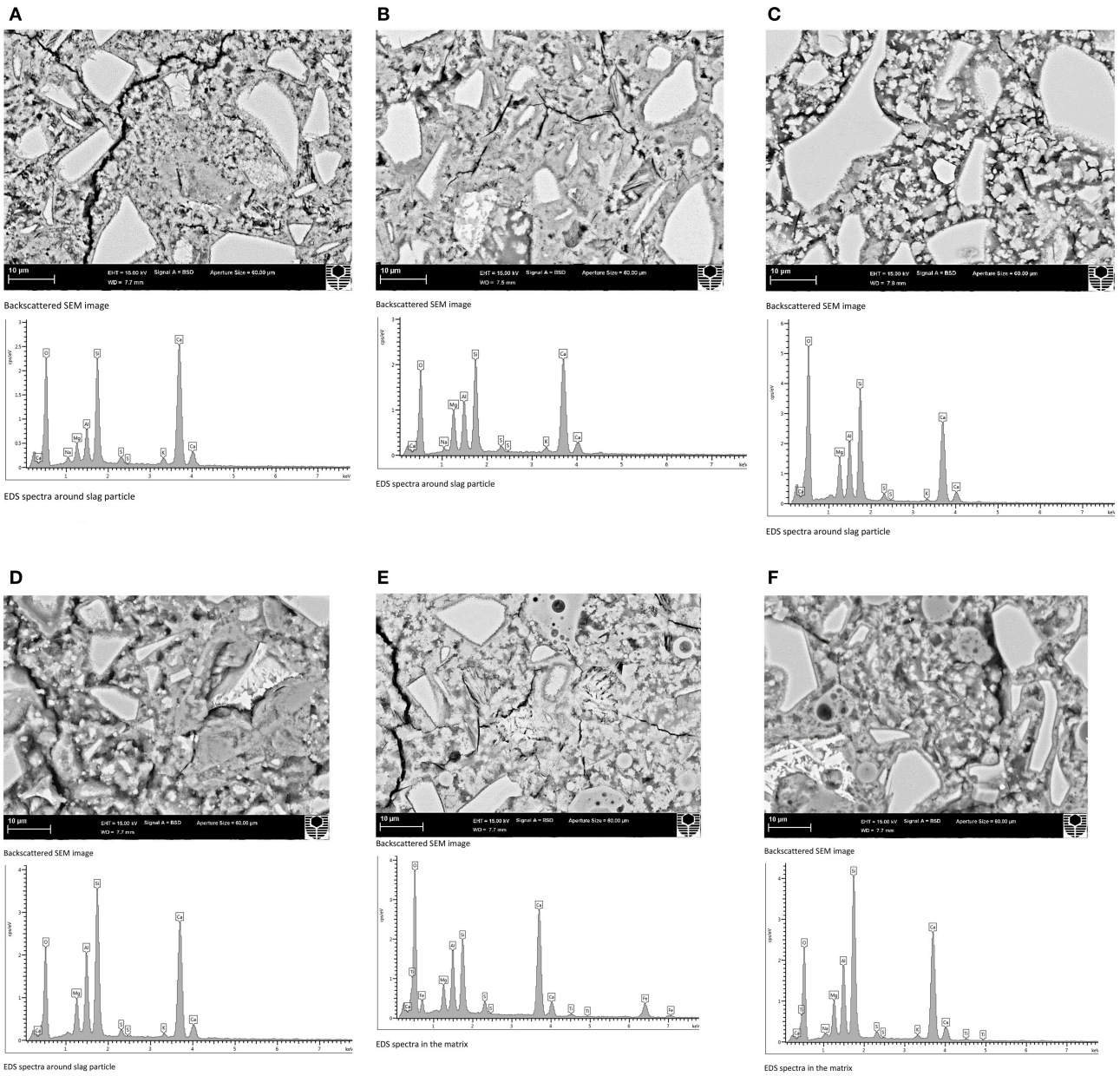

FIGURE 8 | Backscattered scanning electron microscopic (SEM) images and EDS spectra of HVS and HVSFA pastes with and without nano alumina. **(A)** 70BFS paste. **(B)** 69BFS+1NA paste. **(C)** 80BFS paste. **(D)** 77BFS+3NA paste. **(E)** 49BFS21FA paste. **(F)** 48BFS21FA+1NA paste.

In **Figure 6B** it can also be seen slightly higher amount of CH content in high volume BFS pastes containing 77%BFS + 3%NA and 69%BFS + 1%NA pastes than that containing 80% BFS and 70%BFS pastes, respectively. This indicates that Al2O3 in NA did not produce any CSH in the matrix rather formed CAH which is confirmed in XRD and EDS analysis discussed in latter sections. Surprisingly, the CH content is much lower in paste containing 49%BFS + 20%FA + 1%NA then those of pastes containing 70% and 80% BFS. This can be interpreted due to reaction of SiO_2 of FA with CH in that paste.

X-Ray Diffraction (XRD) Analysis

XRD patterns of high volume BFS and combined BFS and FA pastes with and without NA are shown in **Figure 7**. The horizontal scale is the diffraction angels measured in degrees and the vertical scale is the peaks height of the intensity of the diffractions measured in pulses/s. The diffraction spectra analysis of high volume BFS and combined BFA and FA pastes with and without NA indicate the predominance of calcium hydroxide (CH), calcium silicate hydrate (CSH), calcium aluminate hydrate (CAH), Ettringite (E), and Quartz (Q). By comparing the CH peaks of pastes with and without NA it can

be seen that in most occasions intensity of CH peaks is not changed due to addition of NA except at 2θ angles 34.5° and 47° , where intensity of CH is reduced in pastes containing NA. Comparison also shows the formation of Ettringite in high volume BFS pastes containing NA at 2θ angles 43.5° and increase in intensity of Ettringite peaks at 2θ angles 19°, 25.6°, and 35°. The intensity of CAH peak at 2θ angle of 10.8° is also increased in high volume BFS and combined BFA and FA pastes due to addition of NA. In the case of high volume BFS-FA paste new mineral peaks of Mullite (M) and Gehlenite (G) can be seen at 2θ angles 16.5° and 20.8°, respectively, with increase of Gehlenite peak due to addition of NA.

Scanning Electron Microscopy (SEM) and Energy Dispersive X-Ray Spectroscopy (EDS) Analysis

SEM images and EDS spectra of high volume BFS and high volume BFS-FA pastes with and without NA are shown in **Figure 8**. It can be seen by comparing **Figure 8B** with **Figure 8A** that the microstructure of high volume BFS paste containing 69% BFS+1% NA is much denser than paste containing 70% BFS. By comparing both figures it can also be revealed less black spots indicative of pores/voids in high volume BFS paste containing NA than high volume BFS paste indicating formation of additional hydration products such as CSH/CAH as shown in the figure. Similar, improvement can also be seen in the high volume BFS paste containing 80% BFS and that containing NA in **Figures 8C,D** where paste containing 77% BFS and 3% NA in **Figure 8D** exhibited much denser microstructure than high volume BFS paste containing 80% BFS in **Figure 8C**. The EDS spectra in the same figure shows the formation of more CSH/CAH in the high volume BFS pastes containing NA than that of high volume BFS pastes without NA. The similar densification of microstructure of high volume BFS-FA paste due to addition of NA can also be seen by comparing **Figure 8F** with **Figure 8E**, where the peak of silica in EDS is much higher in paste containing NA than without NA indicating formation of more CSH/CAH in the former than the latter. The higher peak of silica in EDS is also evident in high volume BFS pastes containing NA than those without NA.

CONCLUSIONS

The effects of various nano alumina contents on compressive strength and microstructure of cement pastes containing HVBFS and high volume blast furnace slag-fly ash combination are reported. Based on limited study the following conclusion can be drawn:

- The addition of nano alumina (NA) improved the compressive strength of cement pastes containing 70, 80, and 90% BFS by about 16, 8, and 2%, respectively. In the case of combined BFS and FA content of 70 and 80% the improvements are 9 and 16%, respectively, due to addition of NA.
- The compressive strength of high volume BFS paste containing 70% BFS and NA exceeded the compressive strength of control OPC paste. However, not exceeded at 80 and 90% BFS contents and combined BFS and FA content of 70 and 80%.
- The addition of nano alumina significantly reduced the pore volume of large capillary pores of high volume BFS pastes, and increased the gel and medium capillary pores of paste containing 70% BFS. However, in the case of paste containing 80% BFS the volume of gel and medium capillary pores is reduced. The addition of nano alumina however, shifted the critical pore diameter of high volume BFS pastes from medium capillary pores to large capillary pores. However, in the case of high volume BFS-FA paste an opposite trend is observed.
- High volume BFS and combined BFS-FA pastes with and without NA exhibited significant reduction in $Ca(OH)_2$ compared to control OPC paste. However, NA does not reduced the $Ca(OH)_2$ in High volume BFS paste. Reduction in $Ca(OH)_2$ is observed in high volume BFS-FA paste due to addition of NA than the control.
- Intensity of CAH, Ettringite and CSH peaks is increased in high volume BFS pastes due to addition of NA. New crystalline peaks for Mullite and Gehlenite are detected in high volume BFS-FA pastes containing NA.
- SEM images show denser microstructure of High volume BFS and combined BFS-FA pastes containing NA than those without NA. EDS analysis also shows increase in "Si" and "Al" peaks in EDS spectra around slag particles of High volume BFS and combined BFS-FA pastes due to addition of NA indicating formation of CSH/CAH in the matrix.
- The optimum mix could be that containing 69% slag and 1% NA whose compressive strength exceeded the control OPC paste's strength.

AUTHOR CONTRIBUTIONS

FS planned the experimental program, analyzed results, and wrote the manuscript. AH cast and tested all specimens in mechanical and microstructural studies and compiled and analyzed the results.

REFERENCES

Aghaeipour, A., and Madhkhan, M. (2017). Effect of ground granulated blast furnace slag (GGBFS) on RCCP durability. *Constr. Build. Mater.* 141, 533–541. doi: 10.1016/j.conbuildmat.2017.03.019

ASTM C109 (2012). *Standard Test Method for Compressive Strength of Hydraulic Cement Mortars Using 50mm cube Specimens*. West Conshohocken, PA: ASTM.

Barbhuiya, S., Mukherjee, S., and Nikraz, H. (2014). Effects of nano-Al2O3 on early age microstructural properties of cement paste. *Constr. Build. Mater.* 52, 189–193. doi: 10.1016/j.conbuildmat.2013.11.010

Benhelal, E., Zahedi, G., Shamsaei, E., and Bahadori, A. (2013). Global strategies and potentials to curb CO2 emissions in cement industry. *J. Cleaner Prod.* 51, 142–161. doi: 10.1016/j.jclepro.2012.10.049

Elchalakani, M., Aly, T., and Abu-Aisheh, E. (2014). Sustainable concrete with high volume GGBFS to build Masdar City in the UAE. *Case Stud. Constr. Mater.* 1, 10–24. doi: 10.1016/j.cscm.2013.11.001

Gowda, R., Narendra, H., Rangappa, D., and Prabhakar, R. (2017). Effect of nano-alumina on workability, compressive strength and residual strength at elevated temperature of cement mortar. *Mater. Today Proc.* 4, 12152–12156. doi: 10.1016/j.matpr.2017.09.144

Heikal, M., Ismail, M. N., and Ibrahim, N. S. (2015). Physico-mechanical, microstructure characteristics and fire resistance of cement pastes containing Al2O3 nano-particles. *Constr. Build. Mater.* 91, 232–242. doi: 10.1016/j.conbuildmat.2015.05.036

Hou, P.-K., Kawashima, S., Wang, K. J., Corr, D. J., Qian, J. S., and Saha, S. P. (2013). Effects of colloidal nanosilica on rheological and mechanical properties of fly ash–cement mortar. *Cem. Concr. Composites* 35, 12–22. doi: 10.1016/j.cemconcomp.2012.08.027

Keattch, C. J., and Dollimore, D. (1975). *Introduction to Thermogravimetry*, Vol. 45. London: Heydon.

Li, Z., Wang, H., He, S., Lu, Y., and Wang, M. (2006). Investigations on the preparation and mechanical properties of the nano-alumina reinforced cement composite. *Mater. Lett.* 60, 356–359. doi: 10.1016/j.matlet.2005.08.061

Mohseni, E., and Tsavdaridis, K. D. (2016). Effect of nano-alumina on pore structure and durability of class F fly ash self-compacting mortar. *Am. J. Eng. Appl. Sci.* 9, 323–333. doi: 10.3844/ajeassp.2016.323.333

Nazari, A., and Riahi, S. (2011). Effects of Al2O3 nanoparticles on properties of self-compacting concrete with ground granulated blast furnace slag as binder. *Sci. China Technol. Sci.* 54, 2327–2338. doi: 10.1007/s11431-011-4440-y

Oner, A., and Akyuz, S. (2007). An experimental study on optimum usage of GGBS for the compressive strength of concrete. *Cem. Concr. Composites* 29, 505–514. doi: 10.1016/j.cemconcomp.2007.01.001

Quercia, G., Husken, G., and Brouwers, H. J. H. (2012). Water demand of amorphous nano silica and its impact on the workability of cement paste. *Cem Concr Res.*42, 344–357. doi: 10.1016/j.cemconres.2011.10.008

Sato, T., and Diallo, F. (2010). Seeding effect of nano-CaCO3 on the hydration of tri-calcium silicate. *J. Transp. Res. Board* 2141, 61–67. doi: 10.3141/2141-11

Senff, L., Hotza, D., Repette, W. L., Ferreira, V. M., and Labrincha, J. A. (2009). Influence of added nanosilica and/or silica fume on fresh and hardened properties of moratrs and cement pastes. *Adv. Appl. Ceram.*108, 418–428. doi: 10.1179/174367609X422108

Shaikh, F. U. A., and Supit, S. W. M (2014). Mechanical and durability properties of high volume fly ash (HVFA) concrete containing calcium carbonate (CaCO3) nanoparticles. *Constr. Build. Mater.* 70, 309–321. doi: 10.1016/j.conbuildmat.2014.07.099

Shaikh, F. U. A., and Supit, S. W. M. (2015). Chloride induced corrosion durability of high volume fly ash concretes containing nano particles. *Constr. Build. Mater.* 99, 208–225. doi: 10.1016/j.conbuildmat.2015.09.030

Shaikh, F. U. A., Supit, S. W. M., and Sarker, P. K. (2014). A study on the effect of nano silica on compressive strength of high volume fly ash mortars and concretes. *Mater. Design.* 60, 433–442. doi: 10.1016/j.matdes.2014.04.025

Taylor, H. F. W. (1990). *Cement Chemistry.* London: Academic Press Limited.

Washburn, E. W. (1921). Note on a method of determining the distribution of pore sizes in a porous material. *Proc. Nat. Acad. Sci. U.S.A.* 7, 115–116.

Conflict of Interest Statement: The authors declare that the research was conducted in the absence of any commercial or financial relationships that could be construed as a potential conflict of interest.

frontiers in Materials

ORIGINAL RESEARCH
published: 01 May 2019
doi: 10.3389/fmats.2019.00097

Characteristics of Ferrite-Rich Portland Cement: Comparison With Ordinary Portland Cement

Yogarajah Elakneswaran[1], Natsumi Noguchi[1], Kazuki Matumoto[1], Yuka Morinaga[1], Takashi Chabayashi[2], Hiroyoshi Kato[2] and Toyoharu Nawa[3]*

[1] Division of Sustainable Resources Engineering, Faculty of Engineering, Hokkaido University, Sapporo, Japan, [2] Cement Business Division, Development Department, Tokuyama Corporation, Yamaguchi, Japan, [3] Hokkaido University, Sapporo, Japan

The cement industry is an energy-intensive industry, and improving the energy efficiency of cement has become necessary to reduce its carbon footprint and to compete in the global market. Clinker production consumes more than 90% of the total energy used in the cement industry. Therefore, a reduction in the burning temperature of the cement clinker can reduce the energy consumption; however, it alters the mineralogy of the clinker composition. Ferrite-rich Portland cement can be produced by lowering the burning temperature by ∼100°C (i.e., at 1,350°C), which can reduce the energy consumption by ∼5% in comparison with ordinary Portland cement (OPC) clinker. In this study, the hydration reaction and properties of the ferrite-rich Portland cement were examined by experimental techniques and thermodynamic modeling approach, and the results were compared with that of OPC. The produced ferrite-rich cement has almost twice the amount of ferrite phase and half the amount of belite phase contents present in the OPC. The hydration reaction and the composition of hydrates were studied by the X-ray diffraction (XRD)/Rietveld analysis and thermogravimetry (TG) and differential thermal analysis (DTA). The different proportions of the ferrite and belite phases in ferrite-rich cement change their hydration reaction from that of the OPC, but not the total hydration of cement. The XRD results reveal similar phases in both the cements, and the analysis could not identify the new phases formed in the ferrite-rich cement. An equal degree of hydration and quantified hydrates at the early age results in almost identical initial and final setting times in both the cements. The ferrite-rich cement demonstrates a high early strength and relatively slower strength development; however, it can develop adequate strength at 28 days. The thermodynamic model predicts the hydration of ferrite-rich cement and shows comparatively high amount of Fe-containing phases, mainly Fe-ettringite and Fe-siliceous hydrogarnet. Model predictions of the hydrates compositions agreed with the experimental results, and a relationship between the predicted total porosity and the measured compressive strength was derived.

Keywords: Fe-containing phases, hydration, thermodynamic modeling, X-ray diffraction, compressive strength, setting time

OPEN ACCESS

Edited by:
Miroslav Komljenovic, University of Belgrade, Serbia

Reviewed by:
Frantisek Soukal, Brno University of Technology, Czechia
Tongbo Sui, Sinoma International Engineering Co., Ltd., China

****Correspondence:***
Yogarajah Elakneswaran
elakneswaran@eng.hokudai.ac.jp

Specialty section:
This article was submitted to Structural Materials, a section of the journal Frontiers in Materials

Received: *11 January 2019*
Accepted: *15 April 2019*
Published: *01 May 2019*

Citation:
Elakneswaran Y, Noguchi N, Matumoto K, Morinaga Y, Chabayashi T, Kato H and Nawa T (2019) Characteristics of Ferrite-Rich Portland Cement: Comparison With Ordinary Portland Cement. Front. Mater. 6:97. doi: 10.3389/fmats.2019.00097

INTRODUCTION

The cement industry is a high-energy consuming sector, and the production of ordinary Portland cement (OPC) is responsible for ∼5% of the total anthropogenic greenhouse gas emission by limestone calcination (Imbabi et al., 2012; Amato, 2013). Reduction of CO_2 emission associated with the cement manufacturing process without affecting the cement demand is a very challenging task for the cement and concrete industry. Investigations on novel cement systems and low-carbon concretes are thus important to reduce the environmental impact of cement. A number of novel cement systems and low-carbon concretes are currently being developed as alternatives for the OPC (Gartner, 2004; Gartner and Macphee, 2011). Replacement of clinker or OPC by supplementary cementitious materials can help to mitigate the carbon footprint of the OPC (Lothenbach et al., 2011), and various alternative clinkers have been proposed to reduce the limestone amount in the raw mix of cement production (Morin et al., 2017).

Over the years, cement industry has been reducing the CO_2 emission associated with the heating process by improving the energy efficiency, increasing the use of alternative fuels, and deploying renewable energy sources (Morin et al., 2011; Folliet et al., 2017). However, it needs further energy conservation technologies to reduce its carbon footprint. The conventional OPC clinker is burnt at a very high temperature of about 1,450°C, and the heating process is the most energy-consuming part in cement manufacture. Therefore, decreasing the clinker burning temperature reduces both the energy consumption and CO_2 emission. Various technologies have been developed to reduce the energy consumption during the burning process, such as changing the mineral composition of the clinker or using alternative clinkers for OPC and using mineralizers to reduce the burning temperature (Yamashita and Tanaka, 2011). However, studies on the systematic adjustment of the mineral composition of clinker to reduce the burning temperature are limited.

Authors' previous study has reported that compared to the other components of the clinker, the ferrite phase contributes the most to the sintering of the clinker, and the contributions of the various components to clinker burnability is in the order, $C_4AF > C_3A > C_2S > C_3S$ (Chabayashi et al., 2012, 2015). A low-burning-temperature clinker, which sinters at 1,350°C,

TABLE 1 | Physical properties and chemical composition of cements used (Oxide in wt.%).

Cement	OPC	FC
Blaine specific surface area (cm^2/g)	3220	3220
Density(g/cm3)	3.19	3.20
LoI	0.80	0.76
f-CaO	0.82	0.81
SiO_2	21.40	18.53
Al_2O_3	5.36	6.83
Fe_2O_3	3.06	5.67
CaO	65.44	63.83
MgO	0.91	0.96
SO_3	1.99	2.04
Na_2O	0.11	0.17
K_2O	0.15	0.31
TiO_2	0.24	0.31
P_2O_5	0.26	0.31
MnO	0.04	0.03
SrO	0.04	0.05
Cl	0	0
MINERAL COMPOSITION		
C_3S	57.6	59.1
C_2S	18.0	8.6
C_3A	9.0	8.5
C_4AF	9.3	17.2
RAW MATERIALS		
Limestone	80.1	78.4
Silica stone	7.7	0.7
Coal ash	10.4	16.1
Iron source	1.8	4.8

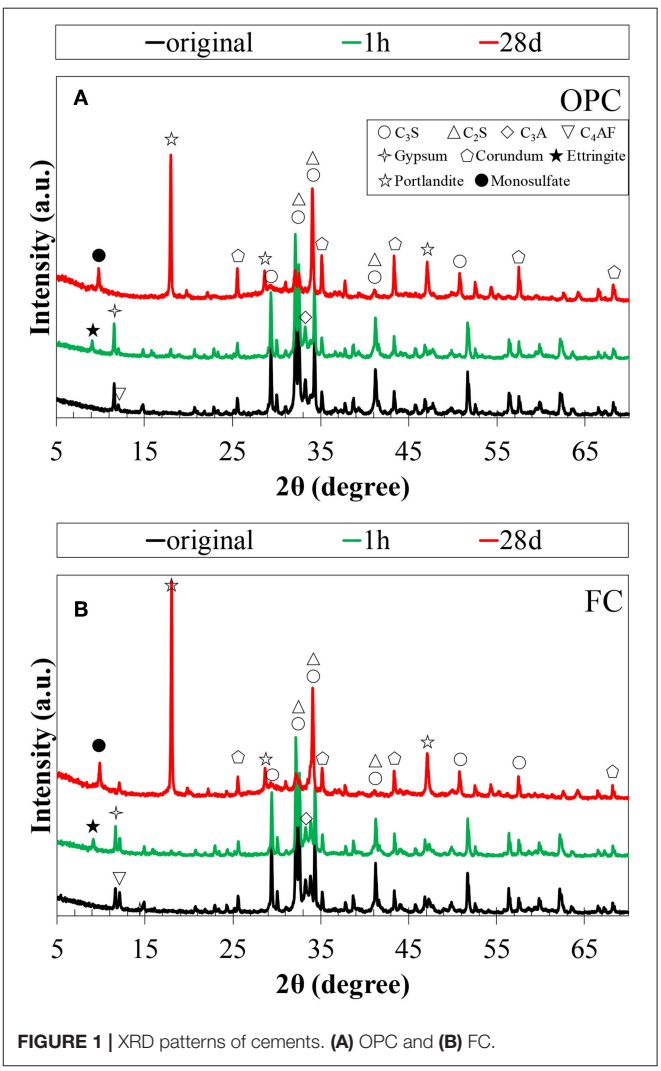

FIGURE 1 | XRD patterns of cements. **(A)** OPC and **(B)** FC.

which is ∼100°C lesser than temperature required for the OPC clinker, was produced by increasing the C_4AF and decreasing the C_2S proportions while targeting a strength equal to that of the conventional OPC. It was successfully burnt in an actual kiln as well (Chabayashi et al., 2015). The cement manufactured using this low-burning-temperature clinker is called ferrite-rich Portland cement (FC), and it can reduce ∼5% of total CO_2 emission compared to the OPC during the clinkering process (Chabayashi et al., 2015). Furthermore, the amount of limestone required for cement production, calculated from mineral composition of clinker, proved that compared to the OPC, the FC would reduce ∼1.29% of CO_2 emission during the heating of limestone. Therefore, the overall CO_2 emission in cement manufacturing process can be decreased by 2.77% by replacing OPC with FC (Shinmi et al., 2017). The characteristics of FC are investigated in this study.

To the best of authors' knowledge, only a few studies have been reported on the production, hydration, property development, and performance of FC. It has been reported that use of FC delays the strength development compared to those with less ferrite and more aluminates (Gartner and Myers, 1993). Furthermore, chemical admixtures are necessary to enhance the hydration reaction of the ferrite phase (Gartner and Myers,

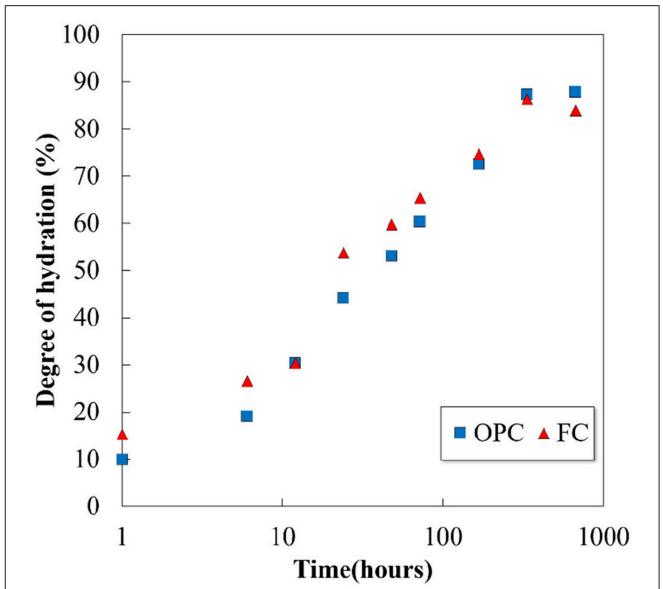

FIGURE 3 | Hydration degree of cements as a function of hydration time determined by XRD.

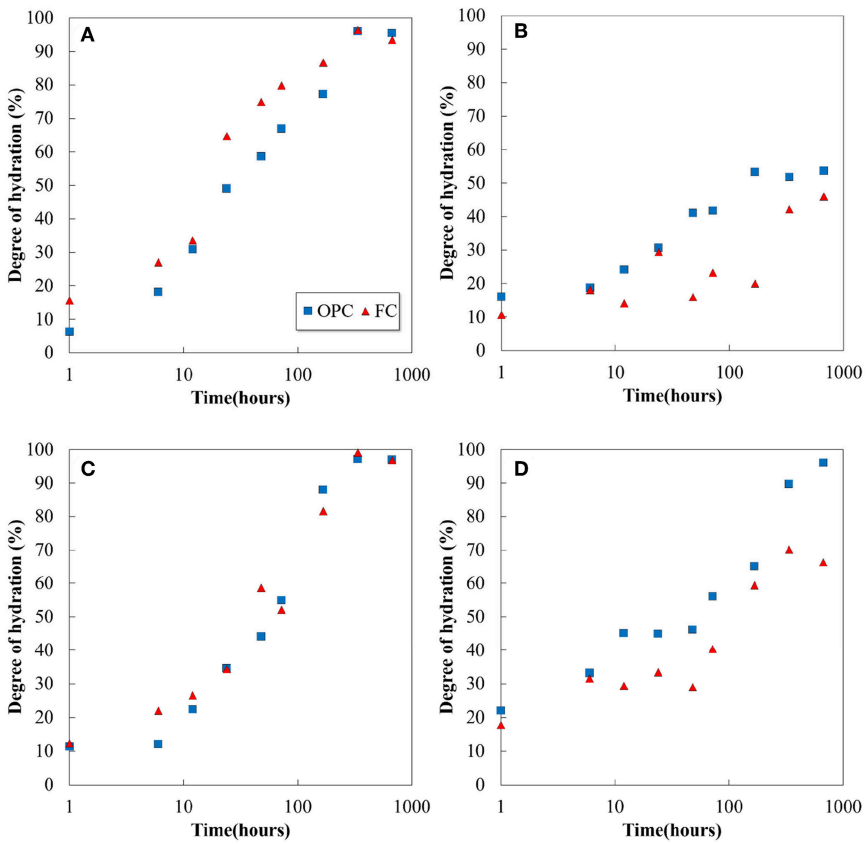

FIGURE 2 | Hydration of **(A)** C_3S, **(B)** C_2S, **(C)** C_3A, and **(D)** C_4AF in the cements as a function of time from the XRD/Rietveld analysis.

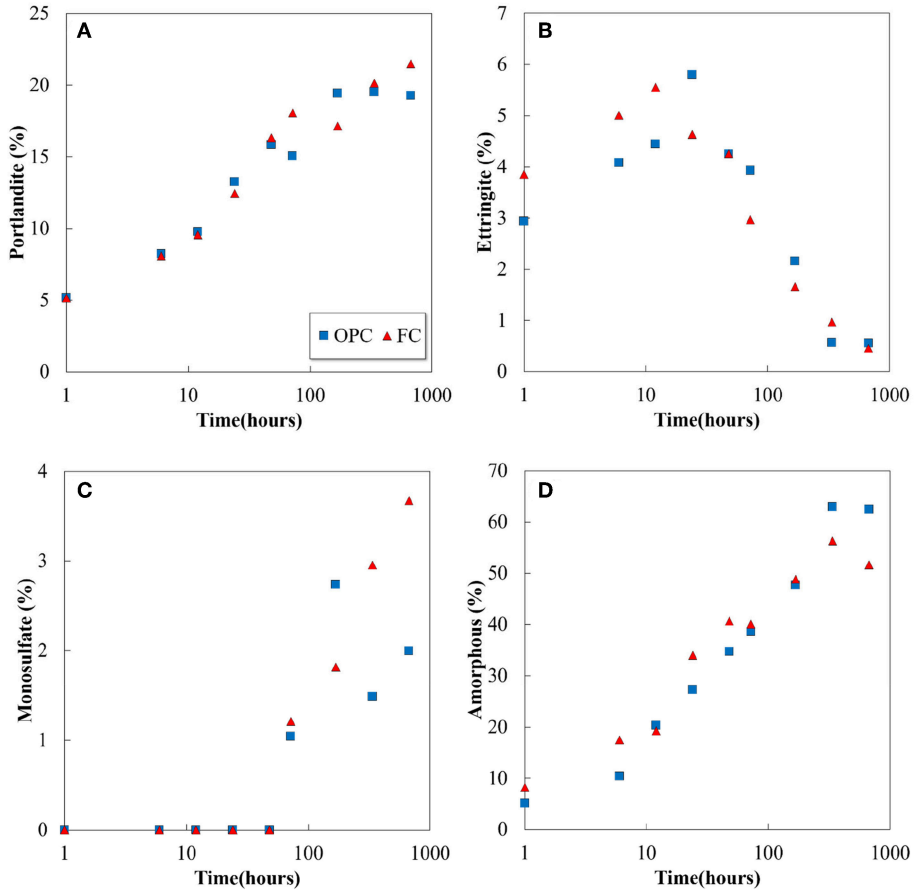

FIGURE 4 | Experimentally determined **(A)** portlandite, **(B)** ettringite, **(C)** monosulfate, and **(D)** amorphous contents variations as a function of hydration time for OPC and FC.

1993; Schwarz, 1995); this in turn contributes to later-age strength development. Poor crystalline Fe-containing phases could form during the hydration of the ferrite phase (Dilnesa et al., 2011, 2014), influencing the properties of the cement matrix. Difficulties in understanding the hydration reaction of the ferrite phase and the identification of Fe-containing phases in the hydration products limit the development and application of FC. Therefore, the objectives of this study are to understand and evaluate the hydration reaction and mechanical performance of FC and to compare the results with that of the conventional OPC. The X-ray diffraction (XRD)/Rietveld analysis and thermogravimetry (TG) and differential thermal analysis (DTA) were used to identify and quantify the clinker minerals and their hydration products as well as to estimate the amount of amorphous in the hydration products. The thermodynamic hydration model developed in authors' previous study (Elakneswaran et al., 2016) was applied to the FC to predict the hydration reaction and to estimate the hydration products. The modeling results were verified with the experimental results. Finally, a relationship between the measured compressive strength of the cement paste and predicted total porosity was derived.

MATERIALS AND METHODS

Clinker and Cement Production

The limestone, silica stone, coal ash, and iron source were used for the clinker production of both cements. The mixture of raw materials for OPC was first heated to 1,000°C using electric furnace in 30 min and burnt at that temperature for another 30 min. Further, the temperature was increased to 1,470°C in 47 min and kept constant for 90 min to limit the amount of free lime to <1%. The calcination of FC up to 1,000°C follows the same procedure as that used for OPC; thereafter, the temperature is raised to 1,370°C in 37 min and sustained for 90 min.1 The clinkers were rapidly cooled to room temperature in the air. Finally, gypsum (gypsum: bassanite = 1:1) was added to the produced clinkers in an amount equal to 2% of SO_3, and the mixture was then ground using a ball mill to the target Blaine value of 3,200 ± 50 cm^2g^{-1} to produce the cements. The Blaine specific surface area and the density based on JIS R 5201, the oxide composition by X-ray fluorescence (XRF), and the mineral composition by Bogue analysis were determined for the produced cements; the results are listed in **Table 1**.

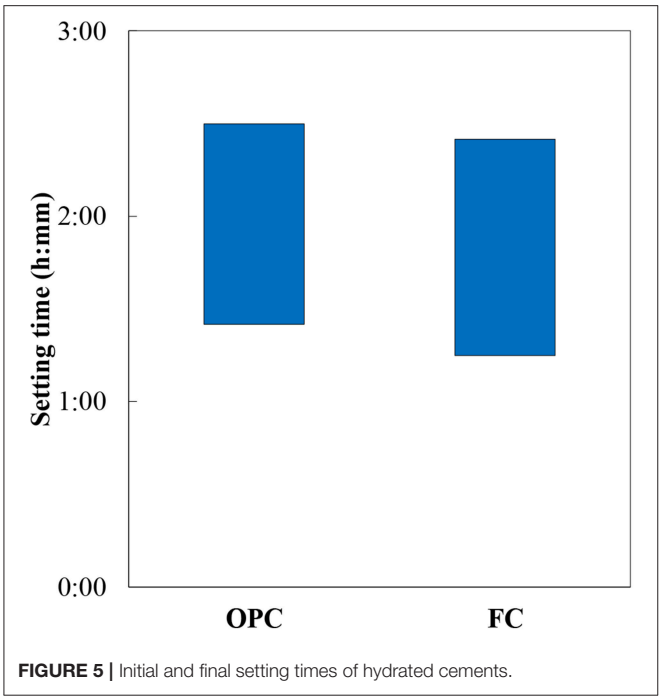

FIGURE 5 | Initial and final setting times of hydrated cements.

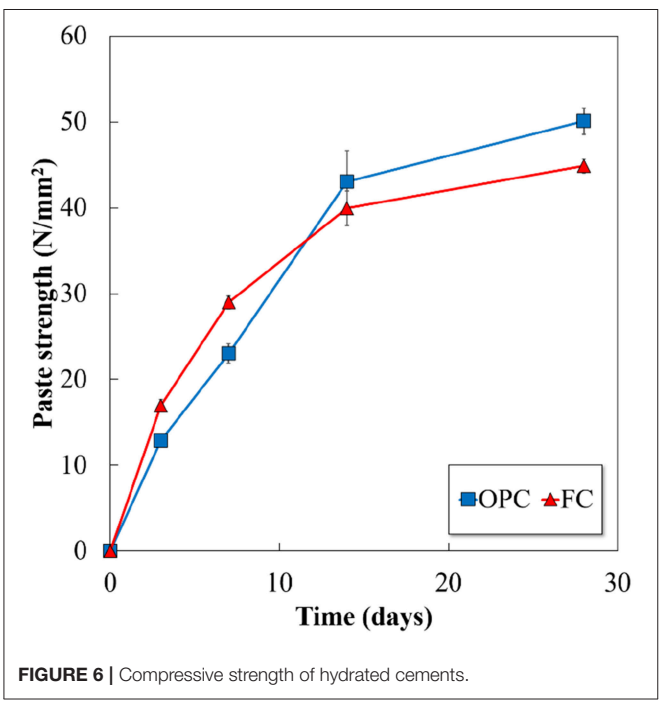

FIGURE 6 | Compressive strength of hydrated cements.

Sample Preparation

The cement was mixed with distilled water at a water to cement ratio of 0.5. The mixture was stirred manually until bleeding stopped. Further, it was cast into cylindrical molds and sealed-cured at 20°C. The samples that reached the predetermined curing time (1, 6, and 12 h and 1, 2, 3, 7, 14, and 28 days) were ground and immersed in acetone for 1 h to stop the hydration. Thereafter, the samples were removed from the acetone solution by suction filtration using an aspirator. Finally, the samples were kept in an oven at 40°C until they reached a constant mass. The prepared samples were ground and powdered for XRD and TG measurements. The 2 × 2 × 8 cm paste specimens were prepared for compressive strength measurement using a mixer given in JIS R 5201.

Experimental Methods

The fine powders of the samples were blended with 10 wt.% of corundum (α-Al_2O_3) and analyzed by XRD. The XRD was performed using a Rigaku MultiFlex X-ray generator with CuKα radiation. The measurement was performed under the following conditions: tube voltage of 40 kV, tube current of 40 mA, scan speed of 1°2θ min^{-1}, scan range of 2θ = 5–70°, and step width of 0.02°. Siroquant Version 4.0, manufactured by Sietronics, was used for quantitative Rietveld analysis. In the Rietveld analysis, monotrinic and triclinic C_3S, α- and β-C_2S, cubic C_3A, C_4AF, Gypsum, Bassanite, Portlandite, Ettringite, Monosulfoaluminate (simply called monosulfate), and Corundum (α-Al_2O_3) were assigned as targets. The quantitative value of C_3S was taken as the sum of the measured values of polymorphic minerals with different crystal structures. The amount of amorphous phase content was calculated according to Equation (1) from the quantitative value obtained by adding 10% mass of corundum (α-Al_2O_3).

$$P = \frac{100}{(100 - A)} \times \left(1 - \frac{A}{R}\right) \times 100 \quad (1)$$

where P is the amount of amorphous phase content (% mass); A is the mixing rate of corundum (% mass); and R is the quantitative value of corundum (% mass). The amount of amorphous phase content in the sample was calculated from the quantitative value obtained by the Rietveld analysis using corundum as an internal standard substance, according to Equation (1). This result was used to correct the determined values of cement minerals. The loss on ignition was obtained as a mass loss between 105 and 950°C, using the mass measured after the ignition loss. To determine the hydration degree against the unhydrates, the value obtained by the Rietveld analysis was corrected with the ignition loss value using Equation (2).

$$Q = Q_0 \times \frac{100}{100 - LOI} \quad (2)$$

where: Q is the corrected quantitative value (%); Q_0 is the quantitative value before the correction (%); and LOI is the loss on ignition (%).

TG/DTA measurements were performed in nitrogen using a HITACHI TG/DTA 7220 analyser at a heating rate of 5°C/min up to 1,000°C. Cement setting time experiment was conducted according to JIS R 5201 and the compressive strength of the paste specimens was measured on 3, 7, 14, and 28 days of curing.

Modeling Approach

The coupled thermodynamic model developed in our previous work (Elakneswaran et al., 2016) was used to model the hydrate assemblage of OPC and FC as a function of hydration time. The thermodynamic model combines the IPhreeqc module (Charlton and Parkhurst, 2011) and Excel for computations. The thermodynamic properties of various phases including Fe-containing hydrates and minerals in the cement system were collected from Cemdata18 (Lothenbach et al., 2008a, 2019) and others (Myers et al., 2014), and the data were converted into a format suitable for PHREEQC. The converted data by Elakneswaran et al. (2016) along with the PHREEQC default thermodynamic database (Parkhust and Appelo, 1999) were used for the calculations.

RESULTS AND DISCUSSION

The XRD patterns of un-hydrated cements and their pastes hydrated for 1 h and 28 days are shown in **Figure 1**. In addition to the cement clinker minerals, peaks of portlandite, ettringite, and monosulfate were identified in both the cements, and calcium silicate hydrates (C-S-H) exists in amorphous phase. The quantitative amounts of the phases were determined by Rietveld analysis and TG/DTA, and the results are discussed later. No qualitative difference is observed in the product formation in the decreasing of the C_2S proportion and increasing of the C_4AF proportion in FC. Ettringite production is noted from 1 h in the hydration products, and it transformed to monosulfate after 3 days of hydration in both the cements. Further, the results suggest that the Fe-hydrates may exist in their amorphous states as they cannot be identified by XRD. **Figure 2** illustrates the hydration degree of each clinker mineral in OPC and FC, while the total degree of hydration as a function of time is plotted in **Figure 3**. As given in **Table 1**, both the cements have almost the same proportions of C_3S and C_3A; therefore, variation in their hydration degree with time is the same. However, the change in the proportions of C_2S and C_4AF affects their hydration; ∼20% difference was observed between the C_4AF hydrations of OPC and FC at 28 days. Nevertheless, the differences did not influence on the total degree of cement hydration (**Figure 3**).

The XRD/Rietveld analysis reveals that the portlandite, ettringite, monosulfate, and amorphous phase contents are the

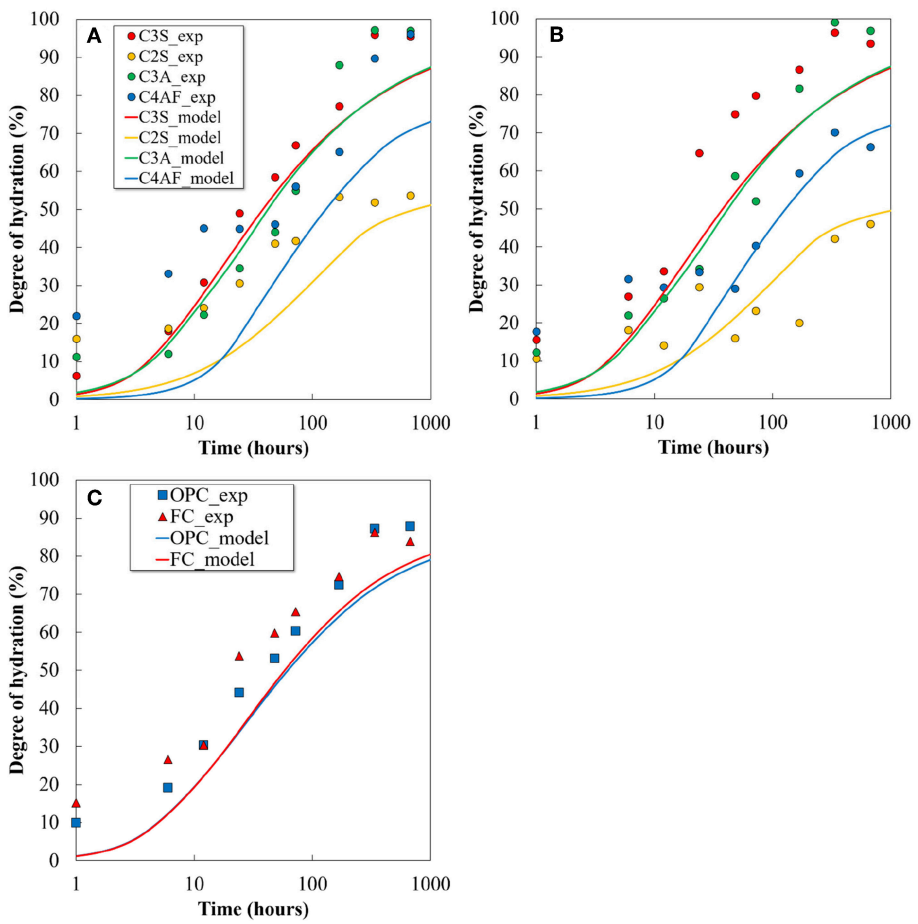

FIGURE 7 | Comparison of calculated hydration degree of each clinker mineral and cements with the quantitative value determined by XRD: **(A)** OPC, **(B)** FC, and **(C)** comparison of total hydration degree.

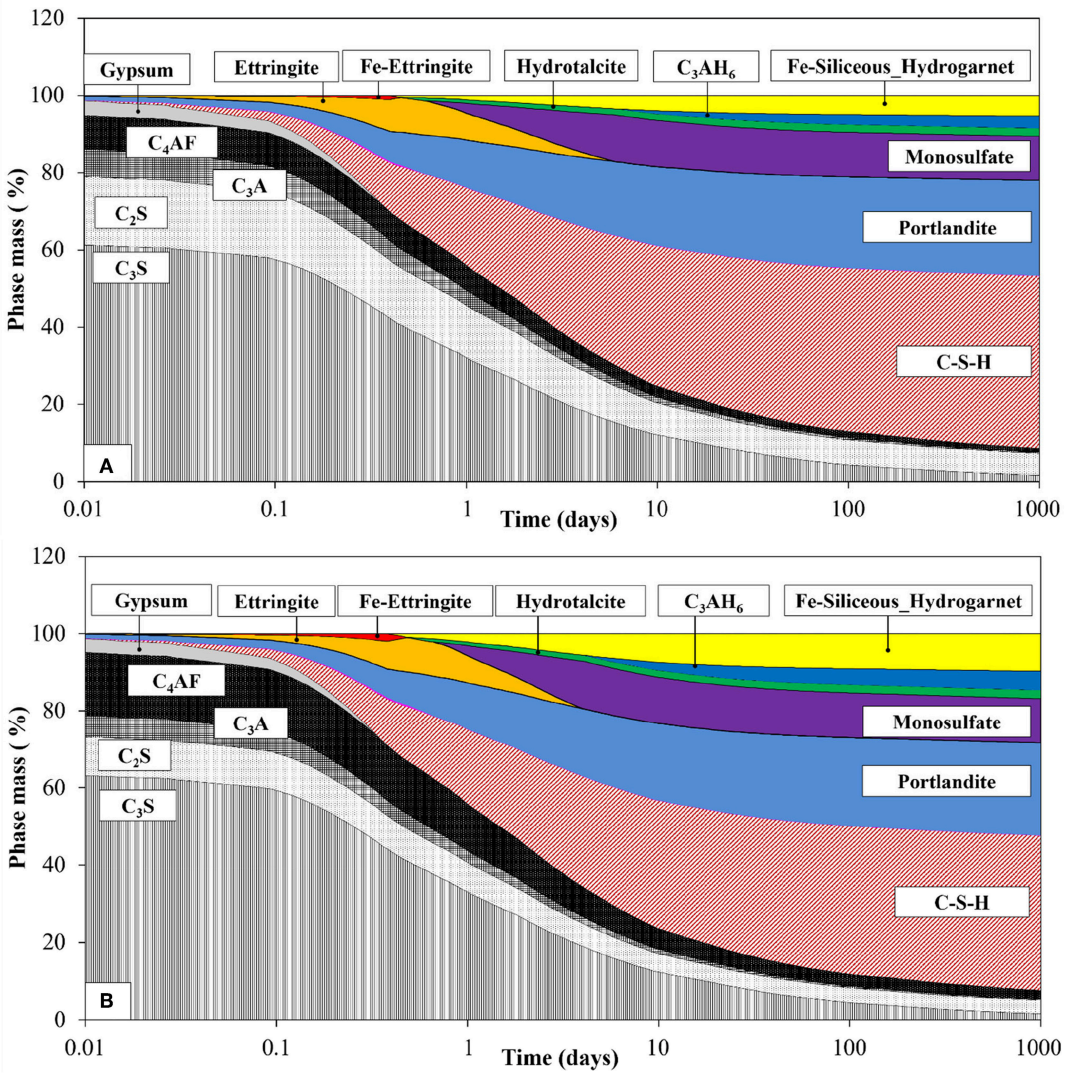

FIGURE 8 | Calculated mass of hydrates as a function of hydration time for **(A)** OPC and **(B)** FC.

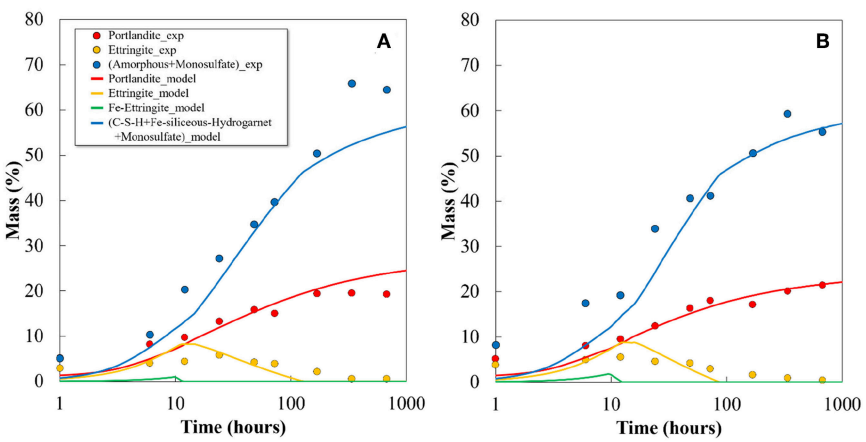

FIGURE 9 | Comparison of calculated hydrates with quantitative value determined by XRD Rietveld analysis and TG/DTA for **(A)** OPC and **(B)** FC.

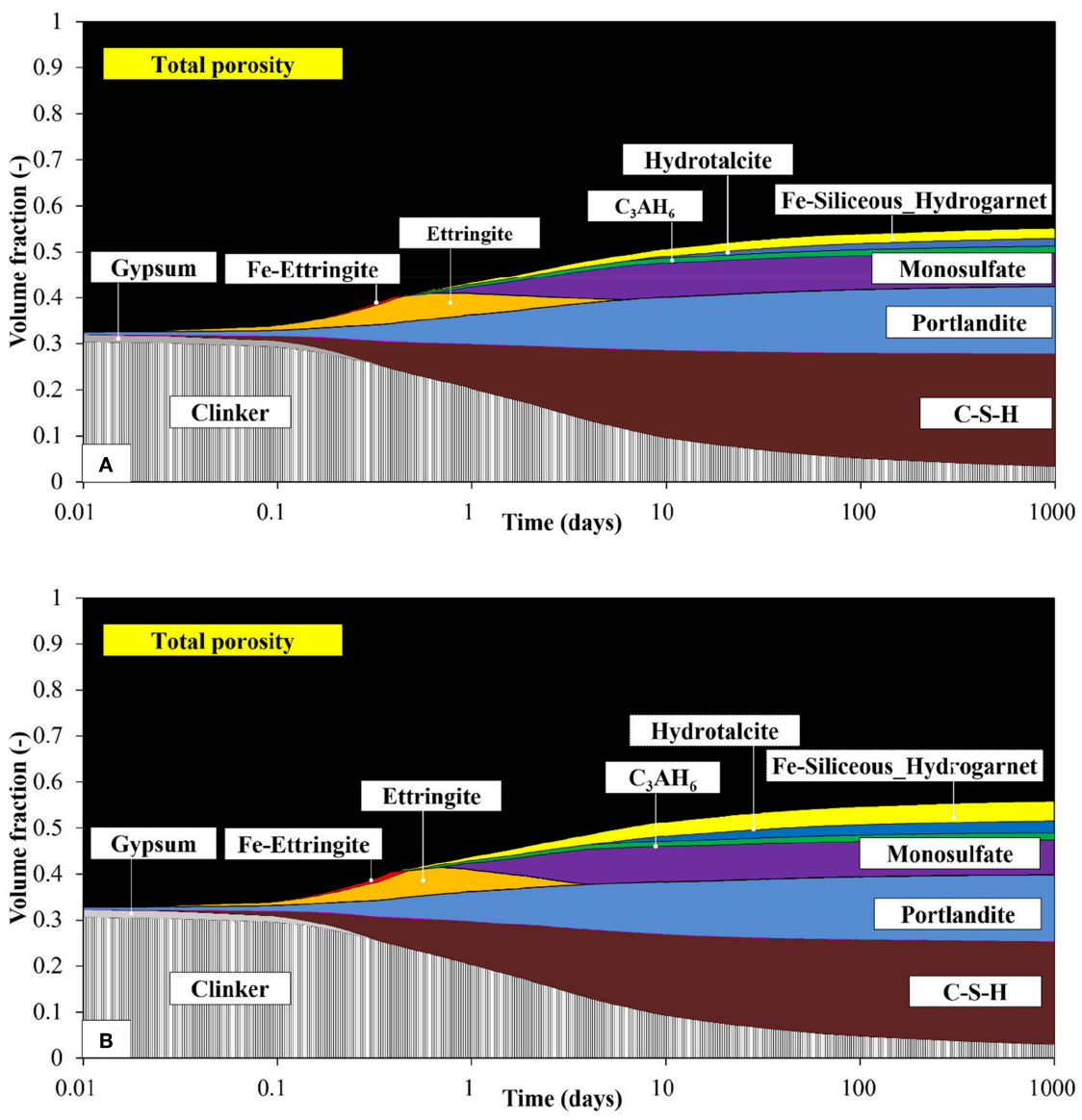

FIGURE 10 | Calculated volume of hydrates as a function of hydration time for **(A)** OPC and **(B)** FC.

main hydration products of both OPC and FC, and the variation in their quantities with respect to the hydration time are plotted in **Figure 4**. The phenomenon of hydration in FC is similar to that observed in the conventional Portland cement system: portlandite and amorphous phase contents are formed from the beginning of the hydration process and increase with hydration time, and the decrease in the amount of ettringite correlates with the formation of monosulfate. It can be observed that the increase in ferrite and the decrease in belite in FC do not significantly influence the quantitative value of hydration products at an early age. However, at a later age, a difference is observed particularly in amorphous phase contents. The hydration degree of belite and ferrite in FC further affects the difference (**Figure 2**). Although it is difficult to distinguish the amorphous phase contents using XRD/Rietveld analysis, it is believed that the hydration products which containing Fe are quantified as amorphous.

Figure 5 illustrates the setting time results of OPC and FC. With an identical value of Blaine specific surface area, both the cements demonstrate similar initial and final setting times. As shown in **Figures 3**, **4**, the hydration reaction and the amounts of solid products formed in FC are equivalent to that of OPC, which attribute to the similar setting time in both the cements. The measured compressive strength of the hydrated cements, mean of 4 samples, is shown in **Figure 6** (standard deviation is shown by bars). It demonstrates that the strength continues to develop

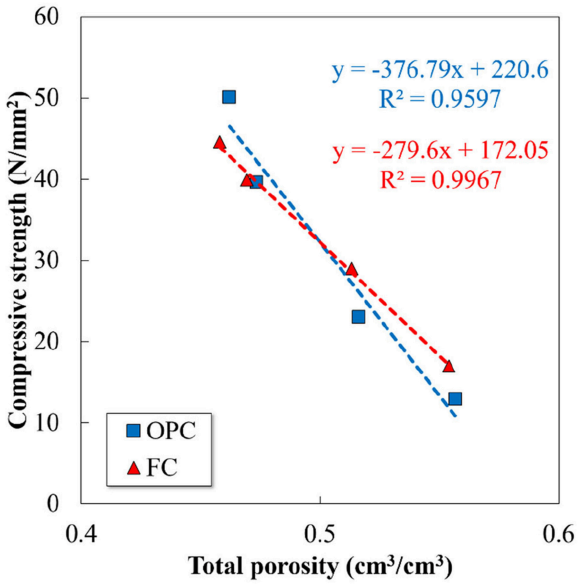

FIGURE 11 | Relationship between calculated total porosity and measured compressive strength.

with the hydration time in both the cements, and the ferrite-rich cement displays a higher compressive strength at early age and becomes equal to OPC at 14 days. Early age compressive strength of OPC paste is slightly lower than the values reported in the hydrated paste, however it shows the similar strength at 28 days (Hoshino et al., 2006). Although the 28 days compressive strength of FC is lower than that of OPC, but it is sufficiently developed.

A coupled thermodynamic model, proposed in a previous study for OPC and slag-blended cementitious materials (Elakneswaran et al., 2016), is employed without any modifications in this study to understand the hydration reaction of the ferrite-rich cement system. The coupled model solves the kinetic equation of the clinker minerals in Excel, and the dissolved quantities are input to PHREEQC for the thermodynamic equilibrium and solid solution calculations. An ideal solid-solution model consisting of six end-members was considered for C-S-H. Prior to predicting the hydration products, the kinetic model is used to predict the hydration degree of the clinker minerals and the total degree of hydration in both the cements. The comparison of results estimated from the model and that obtained from XRD/Rietveld analysis are shown in **Figure 7**. Despite certain discrepancies between the calculation results and the experimental data on individual clinker hydration, the kinetic equations and constants (Elakneswaran et al., 2016) can predict the hydration reaction of ferrite-rich cement and its clinker minerals.

The hydration degree or amount of dissolved clinker phases was used in the thermodynamic calculations with the thermodynamic database for cement minerals and phases. It has been reported that the Fe-siliceous hydrogarnet is expected to form in the hydrated cement system, and it is more stable than Al-siliceous hydrogarnet (Lothenbach et al., 2019). Fe-ettringite, Fe-monosulfate, and Fe-siliceous hydrogarnet were considered in addition to other hydrates commonly found in the hydrated cement system for the calculations of both the cements. For the input of the clinker composition of cement determined by XRD/Rietveld analysis and the mixing conditions, the predicted phase-assemblage composition of the hydrated OPC and FC in mass percentage, relative to the total amount of solid products, is shown in **Figure 8**. Both the cement systems form the same kind of phases with the hydration time, but the initial clinker proportion influences their quantitative values. The presence of Fe-containing phases from the model prediction is consistent with the experimental observation (Dilnesa et al., 2011). Fe-ettringite formed at early age, destabilized and transformed to form Al-ettringite; Fe-monosulfate was not produced. The stable Fe-siliceous hydrogarnet starts to form from early age and continues with the hydration time. The dissolved Fe from the ferrite phase transforms into Fe-ettringite and Fe-siliceous hydrogarnet. The high quantity of ferrite phase in the FC enhances the formation of the Fe-containing phases.

The predicted mass percentage of portlandite, ettringite, and amorphous phase content are compared with the experimental data in **Figure 9**. As reported, the poor crystalline phases of AFm and Fe-containing phases are difficult to quantify by XRD/Rietveld analysis, since they might exist in the amorphous phase as well (Matschei et al., 2007; Lothenbach et al., 2008b). Therefore, the summation of the total amorphous phase content and monosulfate was compared with the addition of the predicted C-S-H, monosulfate, and Fe-siliceous hydrogarnet. Apart from certain variations, the calculated phase assemblage generally agrees well with the experimentally determined values, both qualitatively and quantitatively. A high proportion of the Fe-containing phases formed from the hydration of ferrite phase in the FC contributes significantly to the increase in the calculated amorphous phase content. The composition of the phase assemblage in terms of volume fraction is shown in **Figure 10**. The volume of each hydrate was calculated from its molar volume, and the total porosity is estimated based on the volumes of hydrates and un-hydrated cement at any time and the initial volume of the paste, assuming that chemical shrinkage does not occur. The calculated total porosity is found to be closely associated with the measured compressive strength, as shown in **Figure 11**, and the relationship is found to be more prominent in FC. As shown in **Figure 10**, the porosity does not change significantly with the increase in ferrite and decrease in belite phase proportions in FC, though certain differences are observed between the quantitative values of the hydration products of the two cements.

CONCLUSIONS

Burning of clinker at ∼1,350°C, which is 100°C lower than the burning temperature of OPC, produces a high-ferrite and low-belite content cement. The manufacturing process of this cement

may release 5% lesser CO_2 than that of OPC, thus demonstrating a potential to substitute the OPC. The hydration behavior of the FC is similar to that of OPC, but the different proportions of the clinkers influence their hydration degree; low hydration degree of C_2S and C_4AF are found in FC, in contrast to the OPC. The hydration products were identified and quantified by the XRD/Rietveld analysis and TG/DTA, except the C-S-H and Fe-containing phases that were accounted as amorphous phase contents. The degree of hydration and hydration products of ferrite-rich cement are comparatively similar to that of the OPC; therefore, both the cements exhibit the same initial and final setting times. The ferrite-rich cement develops higher initial compressive strength than the OPC, and displays slow strength development at later age, but achieves the required final strength. Thermodynamic modeling results reveal the hydration reaction of FC. Fe-siliceous hydrogarnet is the main Fe-containing phase formed during the hydration of both FC and OPC, and Fe-ettringite is produced at a very early age and then converted to Al-ettringite. The predicted quantities of the Fe-containing phases strongly depend on the proportion of ferrite in the cement. The estimated compositions of portlandite, ettringite, and amorphous phase contents agree satisfactorily with the XRD/Rietveld analysis and TG/DTA results. Furthermore, the predicted total porosity correlates well with the measured compressive strength.

The present study focuses on the hydration reaction of FC and compares it with that of the OPC. The next step would be identifying and quantifying the Fe-containing phases formed in the cement and verifying it with a thermodynamic model, which requires additional thermodynamic data for the other Fe-containing phases. In addition, Mancini (Mancini et al., 2018) has recently pointed out that Fe can incorporate into C-S-H as well, which should be included in the C-S-H model by either surface complexation or phase equilibrium.

AUTHOR CONTRIBUTIONS

YE, TC, HK, NN, YM, and TN designed the experimental plan. NN, KM, YM, TC conducted the experiments and data analysis. YE and NN carried out the modeling work. YE, NN, YM, and TC drafted the manuscript. TC, HK, and TN contributed to the discussions.

REFERENCES

Amato, I. (2013). Green cement: concrete solutions. *Nature* 494, 300–301. doi: 10.1038/494300a

Chabayashi, T., Nagata, H., Nakamura, A., and Kato, H. (2012). Reduction of burning temperature of cement clinker by adjusting of mineral composition. *Cement Sci. Concrete Technol.* 66, 217–222. doi: 10.14250/cement.66.217

Chabayashi, T., Nagata, H., Shinmi, T., and Kato, H. (2015). Burning test result of the low burning-temperature type clinker by actual kiln and properties of the cement. *Cement Sci. Concrete Technol.* 69, 124–130. doi: 10.14250/cement.69.124

Charlton, S. R., and Parkhurst, D. L. (2011). Modules based on the geochemical model PHREEQC for use in scripting and programming languages. *Comput. Geosci.* 37, 1653–1663. doi: 10.1016/j.cageo.2011.02.005

Dilnesa, B. Z., Lothenbach, B., Le Saout, G., Renaudin, G., Mesbah, A., Filinchuk, Y., et al. (2011). Iron in carbonate containing AFm phases. *Cement Concrete Res.* 41, 311–323. doi: 10.1016/j.cemconres.2010.11.017

Dilnesa, B. Z., Wieland, E., Lothenbach, B., Dähn, R., and Scrivenerc, K. L. (2014). Fe-containing phases in hydrated cements. *Cement Concrete Res.* 58, 45–55. doi: 10.1016/j.cemconres.2013.12.012

Elakneswaran, Y., Owaki, E., Miyahara, S., Ogino, M., Maruya, T., and Nawaa, T. (2016). Hydration study of slag-blended cement based on thermodynamic considerations. *Construct. Build. Mater.* 124, 615–625. doi: 10.1016/j.conbuildmat.2016.07.138

Folliet, M., Saiz, M. R., and Shah, J. (2017). *Improving Thermal and Electric Energy Efficiency at Cement Plants: International Best Practice*. International Finance Corporation Report.

Gartner, E. (2004). Industrially interesting approaches to "low-CO2" cements. *Cement Concrete Res.* 34, 1489–1498. doi: 10.1016/j.cemconres.2004.01.021

Gartner, E., and Macphee, D. E. (2011). A physico-chemical basis for novel cementitious binders. *Cement Concrete Res.* 41, 736–749. doi: 10.1016/j.cemconres.2011.03.006

Gartner, E., and Myers, D. (1993). Influence of tertiary alkanolamines on portland cement hydration. *J. Am. Ceram. Soc.* 76, 1521–1530. doi: 10.1111/j.1151-2916.1993.tb03934.x

Hoshino, S., Yamada, K., and Hiro, H. (2006). XRD/Rietveld analysis of the hydration and strength development of slag and limestone blended cement. *J. Adv. Concrete Technol.* 4, 357–367. doi: 10.3151/jact.4.357

Imbabi, M. S., Carrigan, C., and McKenna, S. (2012). Trends and development in green cement and concrete technology. *Int. J. Sustain. Built Environ.* 1, 194–216. doi: 10.1016/j.ijsbe.2013.05.001

Lothenbach, B., Kulik, D. A., Matschei, T., Balonis, M., Baquerizo, L., Dilnesa, B., et al. (2019). Cemdata18: a chemical thermodynamic database for hydrated Portland cements and alkali-activated materials. *Cement Concrete Res.* 115, 472–506. doi: 10.1016/j.cemconres.2018.04.018

Lothenbach, B., Le Saout, G., Gallucci, E., and Scrivener, K. (2008b). Influence of limestone on the hydration of Portland cements. *Cement Concrete Res.* 38, 848–860. doi: 10.1016/j.cemconres.2008.01.002

Lothenbach, B., Matschei, T., Möschner, G., and Glasserb, F. P. (2008a). Thermodynamic modelling of the effect of temperature on the hydration and porosity of portland cement. *Cement Concrete Res.* 38, 1–18. doi: 10.1016/j.cemconres.2007.08.017

Lothenbach, B., Scrivener, K., and Hooton, R. D. (2011). Supplementary cementitious materials. *Cement Concrete Res.* 41, 1244–1256. doi: 10.1016/j.cemconres.2010.12.001

Mancini, A., Wieland, E., and Lothenbach, B. (2018). *Interaction of Fe(II, III) With Cement Phases in Anoxic Conditions*. Avignon: NUWCEM.

Matschei, T., Lothenbach, B., and Glasser, F. P. (2007). The AFm phase in Portland cement. *Cement Concrete Res.* 37, 118–130. doi: 10.1016/j.cemconres.2006.10.010

Morin, V., Termkhajornkit, P., Huet, B., and Pham, G. (2017). Impact of quantity of anhydrite, water to binder ratio, fineness on kinetics and phase assemblage of belite-ye'elimite-ferrite cement. *Cement Concrete Res.* 99, 8–17. doi: 10.1016/j.cemconres.2017.04.014

Morin, V., Walenta G., Gartner E., Termkhajomkit P., Baco I., and Casabonne J. M. (2011). "Hydration of belite calcium sulfo-aluminate cement aether^{TM}," in *International Congress on the Chemistry of Cement,* Madrid.

Myers, R. J., Bernal, S. A., and Provis, J. L. (2014). A Thermodynamic model for C-(N-)A-S-H Gel: CNASH_ss. Derivation and validation. *Cement Concrete Res.* 66, 27–47. doi: 10.1016/j.cemconres.2014.07.005

Parkhust, D. L., and Appelo, C. A. J. (1999). *A Computer Program for Speciation, Batch-Reaction, One-Dimensional Transport and Inverse Geochemical Calculations*. USGS report.

Schwarz, W. (1995). Novel cement matrices by accelerated hydration of the ferrite phase in Portland cement via chemical activation: kinetics and cementitious properties. *Advn Cem Bas Mat.* 2, 189–200. doi: 10.1016/1065-7355(95)90003-9

Shinmi, T., Chabayashi, T., Kato, H., and Kawai, K. (2017). Long-term strength development, durability and environmental impact assessment of concrete using the low burning-temperature type general-purpose cement. *Concrete Eng.* 39, 1999–2004.

Yamashita, M., and Tanaka, H. (2011). Low-temperature burnt Portland cement clinker using mineralizer. *Cement Sci. Concrete Technol.* 65, 82–87. doi: 10.14250/cement.65.82

Conflict of Interest Statement: The authors declare that the research was conducted in the absence of any commercial or financial relationships that could be construed as a potential conflict of interest.

frontiers in Materials

ORIGINAL RESEARCH
published: 03 May 2019
doi: 10.3389/fmats.2019.00099

Effect of Pre-dispersing Metakaolin in Water on the Properties, Hydration, and Metakaolin Distribution in Mortar

Haining Geng[1], Wei Chen[2], Qiu Li[2], Zhonghe Shui[2] and Bo Yuan[3]*

[1] Department of Civil Engineering, Hubei Urban Construction Vocational and Technological College, Wuhan, China, [2] State Key Laboratory of Silicate Materials for Architectures, Wuhan University of Technology, Wuhan, China, [3] School of Materials Science and Engineering, Wuhan University of Technology, Wuhan, China

The effects of pre-dispersing metakaolin (MK) in water on the properties and hydration of mortar and distribution of MK particles in mortar were characterized by analytical techniques. Zeta-potential of MK-water dispersion significantly decreased with the increase of pH of solution, resulting in a stable dispersion at pH of 8 with zeta-potential of −40 mV. The bulk density of MK-water slurry rapidly increased with water/MK ratio due to the surface tension force of water and filling of spaces by water, resulting in a maximum bulk density of 665.2 kg/m^3 at water/MK ratio of 1.0. Comparing to that of powder MK, pre-dispersing MK in water did not alter hydration products, slightly improved compressive strength, and pore structure, but further reduced shrinkage and significantly improved the uniformed distribution of MK particles in mortar.

Keywords: zeta-potential, viscosity, hydration products, compressive strength, shrinkage, coefficient of variation

OPEN ACCESS

Edited by:
Maria Juenger,
University of Texas at Austin,
United States

Reviewed by:
Maria Stefanidou,
Aristotle University of Thessaloniki,
Greece
Zehra Canan Girgin,
Yildiz Technical University, Turkey

****Correspondence:***
Qiu Li
qiu-li@whut.edu.cn

Specialty section:
This article was submitted to Structural Materials, a section of the journal Frontiers in Materials

Received: *09 February 2019*
Accepted: *17 April 2019*
Published: *03 May 2019*

Citation:
Geng H, Chen W, Li Q, Shui Z and Yuan B (2019) Effect of Pre-dispersing Metakaolin in Water on the Properties, Hydration, and Metakaolin Distribution in Mortar. Front. Mater. 6:99. doi: 10.3389/fmats.2019.00099

INTRODUCTION

Concrete is one of the most used man-made materials for construction, due to its availability, suitable workability, properties, and durability. However, concrete has been criticized in recent decades for its contribution to CO_2 footprint, which is mainly from one of its components, Portland cement (Scrivener and Kirkpatrick, 2008). To reduce the CO_2 footprint of construction industry, mineral additives have been introduced to concrete in the aim to reduce the amount of Portland cement required. Mineral additives include fly ash, silica fume, slag, and metakaolin (MK). Mineral additives are usually amorphous in nature with high silicate/aluminate content, which can react with calcium hydroxide formed during hydration of Portland cement through pozzolanic reaction (Taylor, 1997).

MK attracted much attention among mineral additives recently due to its high contribution to strength and durability when introduced to concrete (Frias and Cabrera, 2000; Aquino et al., 2001; Gueneyisi et al., 2008; Goncalves et al., 2009; Shui et al., 2010; Fernandez et al., 2011; Rashad, 2013), resulting from its effect of acceleration of hydration of Portland cement and refinement of pore structure of concrete or mortar (Buchwald et al., 2007; Lagier and Kurtis, 2007; Cassagnabere et al., 2010; Li et al., 2010; Kadri et al., 2011). MK is manufactured by calcining kaolin at 650–800°C to remove interlayer water and OH^- resulting in the deterioration of long-range order of silicon-aluminum layer structure (Murat and Comel, 1983; He et al., 1995; Badogiannis et al., 2005; Rashad, 2013). Amorphous MK with pozzolanic activity was obtained with formula of $Al_2O_3{\cdot}2SiO_2$ (Coleman and McWhinnie, 2000; Sabir et al., 2001; Love et al., 2007; Bich et al., 2009; Fernandez et al., 2011). When MK was added into concrete, the compressive strength could be improved, permeability, and porosity could be decreased and pore structure could be refined due to the filler

effect, acceleration of hydration, and pozzolanic reaction with CH to form C-S-H (Wild et al., 1996; Aquino et al., 2001; Lagier and Kurtis, 2007; Gueneyisi et al., 2008; Shui et al., 2010; Fernandez et al., 2011; Kadri et al., 2011). The compressive strength increased with the content of MK, and the maximum effect was reached at 28 days as observed by many researchers previously (Justice and Kurtis, 2007; Khatib, 2008, 2009; Arikan et al., 2009; Johari et al., 2011; Kadri et al., 2011; Antoni et al., 2012; Li et al., 2015). The early age (before 24 h) autogenous shrinkage of concrete decreased with the increase of content of MK due to the dilution effect of MK, although the long-term autogenous shrinkage of concrete containing MK could be higher than that of control specimen, due to the acceleration of Portland cement hydration, and pozzolanic reaction by MK with calcium hydroxide (Kinuthia et al., 2000; Brooks and Johari, 2001). With the increase of MK addition, the drying shrinkage of concrete could be significantly reduced by 50%, comparing to the control specimen, due to the reduced amount of evaporable water as a result of hydration, and pozzolanic reaction (Brooks and Johari, 2001).

Due to the high specific surface area and small particle size, there is a high tendency for MK particles to agglomerate, resulting in the non-uniform properties of concrete when MK was introduced as SCMs. The low stacking density of MK, which is ~1,500 kg/m^3, reduced the capacity and efficiency of transportation. Approximately over 40% of MK particles is under the size of 2.5 μm, which could pollute the environment and be harmful to the respiratory system of human. The authors' preliminary study suggested non-uniform hydration products,

TABLE 1 | Chemical composition and physical properties of cement and metakaolin used in this study.

Oxides (wt%)	Cement	MK
SiO_2	19.05	57.37
Al_2O_3	4.15	38.63
Fe_2O_3	3.29	0.77
CaO	64.43	0.03
MgO	1.60	0.07
K_2O	0.77	0.49
Na_2O	0.09	0.39
SO_3	3.32	0.15
TiO_2	–	0.40
P_2O_5	–	0.61
Loss on ignition	2.43	1.04
Specific surface area (m^2/kg)	437	2,800
Density (g/cm^3)	3.05	–
Initial setting (min)	128	–
Final setting (min)	220	–

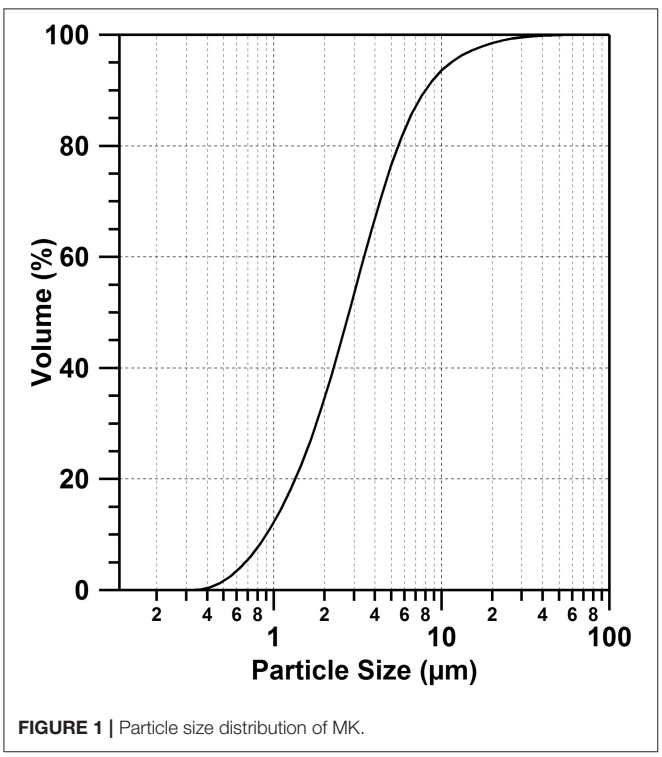

FIGURE 1 | Particle size distribution of MK.

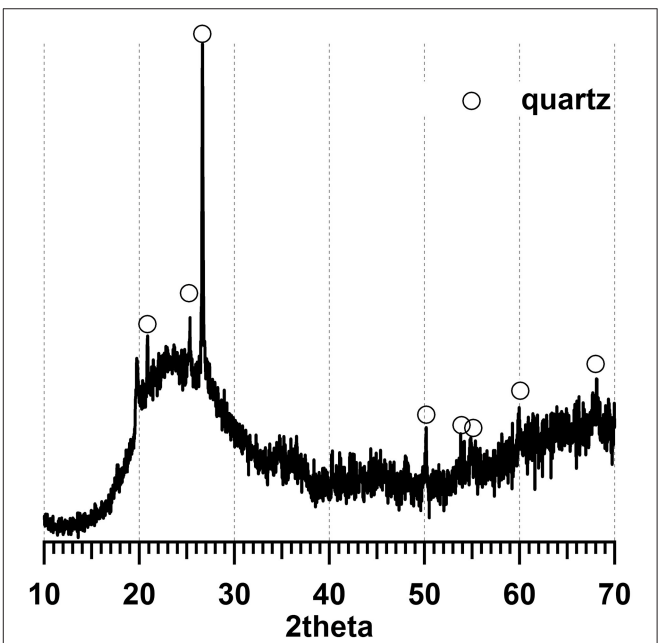

FIGURE 2 | XRD results of MK. The majority of metakaolin is amorphous.

TABLE 2 | Sand grading.

Size (mm)	Weight of screen residue (wt%)
4.75	6.7
2.36	16.4
1.18	37.8
0.60	62.7
0.30	88.6
0.15	99.2

mechanical properties, and durability of concrete specimens with MK addition, resulted from the uneven distribution of MK particles after introducing into concrete due to the agglomeration of MK particles. Some previous research also reported that the agglomeration of MK reduced the pozzolanic activity of MK, together with a lower compressive strength, different microstructure and macrostructure of paste, and geopolymer (Medri et al., 2010; Ilic et al., 2018).

In this study, aiming to improve the capacity and efficiency of transportation, prevent the air pollution caused by MK powder, reduce the agglomeration and improve the uniform distribution of MK particles in mortar matrix and the properties of mortar, MK was pre-dispersed in water as slurry before being added in mortar to increase the density and homogeneity. A range of analytical techniques was employed to characterize the effect of pH of solution and water/MK ratio on the physical properties and stability of dispersion of MK-water slurry, and the effect of pre-dispersed MK slurry on the properties and hydration of cement mortar was evaluated, together with the improvement of distribution of MK particles in mortar after pre-dispersing.

MATERIALS AND EXPERIMENTAL

Materials

In this study, ordinary Portland cement (OPC) (Huaxin Cement Co. Ltd., China) was used MK was provided by Maoming Kaolin Science and Technology Co. Ltd., China, with a specific surface area of 2,800 m^2/kg. **Table 1** shows the chemical composition and properties of OPC and MK. The particle size distribution of MK is shown in **Figure 1**, which was analyzed with Malvern Mastersizer 2000 particle size analyser (Malvern, UK) by dispersing in sodium hexametaphosphate solution. According to X-ray diffraction (XRD) pattern in **Figure 2**, MK is mainly amorphous. Fine aggregate is natural sand with an apparent density of 2,640 kg/m^3, stacking density of 1,458 kg/m^3 and fineness modulus of 2.91. The grading of fine aggregate is shown in **Table 2**.

Experimental Details

Zeta Potential Test

MK-water colloidal dispersion was prepared with water/MK ratio of 1,500 for zeta potential test under various pH value of solution. The pH value of the MK-water dispersion was varied by addition of HNO_3 and NaOH. The pH value of MK-water dispersion was measured by Inesa PHSJ-3F pH Meter (China). Zeta potentials of MK particles in solution with various pH value were conducted by Zeta-Meter System 3.0+ (USA). All measurement was conducted under room temperature.

Bulk Density and Viscosity of MK-Water Slurry Test

The bulk density of MK-water slurry was measured by adding water into MK powder with various water/MK ratio, mechanically mixing the slurry with a ball miller for 30 min,

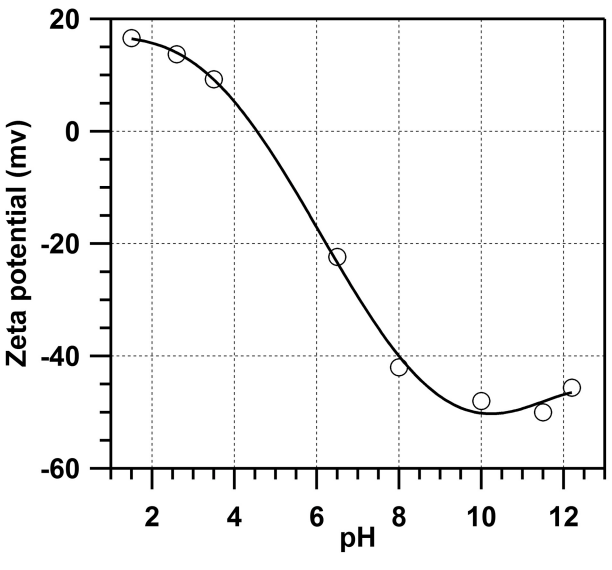

FIGURE 3 | Zeta potential of MK-water dispersion in solution with different pH value.

TABLE 3 | Mix design parameters (kg/m^3).

	Mix	Cement	Powder MK	Pre-dispersed MK		Sand	Water	Water/(cement+MK) ratio
				MK	Water			
Mortar	M0	450.0	–	–	–	1,350	225	0.5
	MMK5	427.5	22.5	–	–	1,350	225	0.5
	MMK10	405.0	45.0	–	–	1,350	225	0.5
	MDMK5	427.5	–	22.5	41.8	1,350	183.2	0.5
	MDMK10	405.0	–	45	83.6	1,350	141.4	0.5
Paste	P0	500.0	–	–	–	–	250	0.5
	PMK5	475.0	25.0	–	–	–	250	0.5
	PMK10	450.0	50.0	–	–	–	250	0.5
	PDMK5	475.0	–	25.0	46.4	–	203.6	0.5
	PDMK10	450.0	–	50.0	92.9	–	157.1	0.5

TABLE 4 | Zeta-potential of MK dispersion under various pH in solution with MK/water ratio of 1,500.

pH	1.5	2.6	3.5	6.5	8	10	11.5	12.2
Zeta-potential (mv)	16.6	13.7	9.26	−22.3	−42.0	−48.0	−50.0	−45.6

then measuring the weight, and volume of slurry. The viscosity of MK-water slurry with various water/MK ratio was evaluated by Brookfield R/S-SST (USA) with shear rate of 60 r/min. The VANE rotor for the test was V40-20, the container used was Griffin beaker of 600 ml and the temperature was constant at room temperature of 25 ± 5°C.

Stability of MK-Water Slurry With Time

The stability of MK-water slurry with water/MK ratio of 1.86 was evaluated by the differences of viscosity at 0 h and 24 h after mixing and the segregation of water from the slurry at 24 and 48 h after mixing. The segregation of water was measured as follows.

One hundred milliliter of slurry was put in the measuring cylinder after mixing. The volume of water segregated from slurry was recorded from the top of slurry after 24 and 48 h. The measurement was performed under room temperature and no vibration was applied.

Mix Design and Curing Conditions

The pre-dispersed MK slurry used in this study was with water/MK ratio of 1.86. The mix design of mortar and paste is shown in **Table 3**. OPC was substituted by 5 or 10 wt% powder MK or pre-dispersed MK slurry in mortar and paste. The water/binder ratio was 0.5 for all mortar and paste mixes. Specimens were demoulded at 1 day and cured in a fog room under standard moist curing condition with temperature of 20°C and relative humidity above 90%.

Compressive Strength and Porosity Test

For compressive strength test, the mortar and paste specimens were cast into the size of 40 × 40 × 160 mm. Nine specimens from each mix were used for compressive strength test. The compressive strength test was performed at 3, 7, and 28 days for all mixes according to Chinese standard GB/T 50081-2002[1]. The results from all specimens were included for the calculation of compressive strength and standard deviation. Porosity test was conducted on paste specimens according to ASTM C642-13[2].

Phase Assemblage

XRD analysis was conducted on the paste specimens at 3 and 28 days. Crystalline minerals in freshly ground paste specimens was characterized by Bruker D8 Advance with Cu Kα = 1.5406 Å, step size of 0.019°, measuring time of 141.804 s/step, start position 5° and end position 70°. The obtained XRD pattern was analyzed by PANalytical X'pert Highscore Plus software with PDF2004 database.

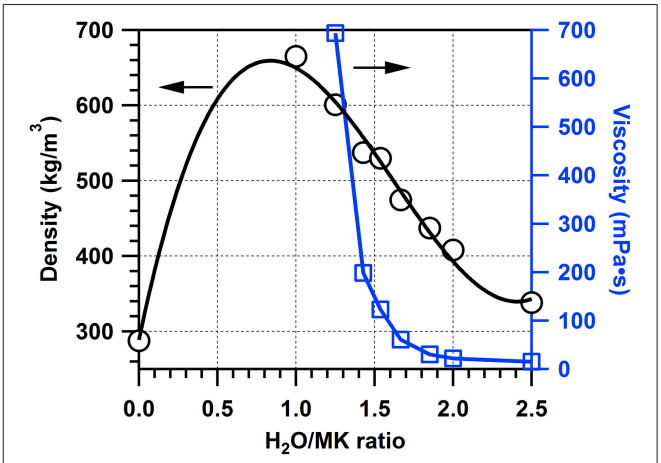

FIGURE 4 | Density and viscosity of MK-water slurry under various H_2O/MK ratio.

Shrinkage

The shrinkage of mortar specimens was evaluated according to Chinese standard JGJ/T70-2009[3]. Mortar specimens were cast into the size of 40 × 40 × 160 mm and cured under standard moist conditions for 7 days before demoulding, where cement mortar without MK addition, cement mortar with 10 wt% MK addition as dry powder and cement mortar with 10 wt% MK addition as dispersed slurry were named as M0, MMK10, and MDMK10, respectively. Then the initial length of specimens were recorded and the specimens were cured under temperature of 20 ± 2°C and relative humidity of 60 ± 5%. The lengths of specimens were measured at 7, 14, 21, 28, 35, and 42 days after demoulding. Three measurement were performed on each age. The shrinkage was calculated by the following equation.

$$\varepsilon_t = \frac{L_0 - L_t}{L - L_d} \quad (1)$$

Where ε_t is the shrinkage of mortar at t days, L_0 is the length of specimen at demoulding (mm), L is the standard length of 160 mm, L_d is the length of test head in the mortar (mm), and L_t is the length of specimen at t days (mm).

Coefficient of Variation of Compressive Strength

The coefficient of variation (C_v) is a standardized measure of dispersion of a probability distribution. It is defined as the ratio

[1] *Standard for Test Method of Mechanical Properties on Ordinary Concrete*. Ministry of Construction of the People's Republic of China (2002).

[2] *ASTM C642-13: Standard Test Method for Density, Absorption, and Voids in Hardened Concrete*. West Conshohocken, PA: ASTM International (2013).

[3] *JGJ/T70-2009: Standard for Test Method of Performance on Building Mortar*. Beijing: Ministry of Housing and Urban-Rural Development of People's Republic of China (2009).

of the standard deviation (SD) to the mean (μ), as follows.

$$C_v = \frac{SD}{\mu} \quad (2)$$

In this study, the coefficient of variation was used to express the distribution of compressive strength test results of mortar specimens of M0, MMK10, and MDMK10 at 28 days. Eighteen specimens were tested for each mix. The mean value, standard deviation and coefficient of variation were calculated to assess the distribution of MK particles in mortar matrix. The results from all specimens were included for the calculation of mean value, standard deviation, and coefficient of variation, to evaluate the homogeneity.

RESULTS AND DISCUSSION

Stability of MK-Water Dispersion Under Various pH

Zeta potential is a key indicator of the stability of colloidal dispersion. The magnitude of zeta potential indicates the electrostatic repulsion between adjacent, similarly charged particles in the dispersion, with a higher zeta potential indicating better stability, and less aggregation. According to the relationship between zeta potential and pH value of MK-water dispersion with water/MK ratio of 1,500 observed in this study (**Figure 3** and **Table 4**), zeta potential of MK-water dispersion significantly decreased with the increase of pH of solution, from 16.4 to −48.2 mV when pH increased from 1.5 to 10. The concentration of OH^- increases with pH value, providing more OH^- available to attach to the surface of metakaolin particles, resulting in the continuous decrease of zeta potential to ∼-40 mV at pH of 8, indicating that the MK-water dispersion was stably dispersed. In solution of pH over 10, pozzolanic reaction of MK will take place, which is not beneficial for the purpose of storage and dispersion of metakaolin for construction. Severe aggregation was observed when pH was more than 10 in this study, indicating the activation of MK due to the pozzolanic reaction (He et al., 1995). Considering the stability of dispersion of MK slurry, dispersing MK with water, which has a pH value of 7, should result in a stable dispersion without pozzolanic reaction. In this study, de-ionized water was used for dispersing at pH of 7.

Bulk Density and Viscosity Under Various Water/MK Ratio

To improve the bulk density of MK slurry and distribution of MK in mortar, MK-water slurry with water/MK ratio of 0–2.5 were prepared and the bulk density and viscosity were evaluated. According to the results shown in **Figure 4**, the bulk density of MK slurry rapidly increased with the addition of water due to the decrease of distance between particles by surface tension force of water and filling of water between particles, reaching the maximum of 665.2 kg/m^3 at water/MK weight ratio of 1.0, where the packing of MK particles reached the closest packing. Then the bulk density of MK slurry gradually decreased with the increase of water/MK ratio, due to the increase of distance between MK particles by continuous addition of water.

The viscosity was measured at water/MK ratio over 1.3, where the bulk density of MK slurry started to decrease (**Figure 4** and **Table 5**). The viscosity decreased rapidly with the increase of water/MK ratio, from 693.5 mPa·s at water/MK ratio of 1.25 to 30.0 mPa·s at water/MK ratio of 1.85. To obtain a low viscosity and relative high MK content, water/MK ratio of 1.86 was chosen to evaluate the effect of pre-dispersed MK slurry on the properties and hydration of cement mortar in this study.

The stability of MK-water slurry with water/MK ratio of 1.86 was evaluated. The viscosity of MK slurry increased from 28.6 mPa·s at 0 h after mixing to 49.3 mPa·s at 24 h after mixing. The

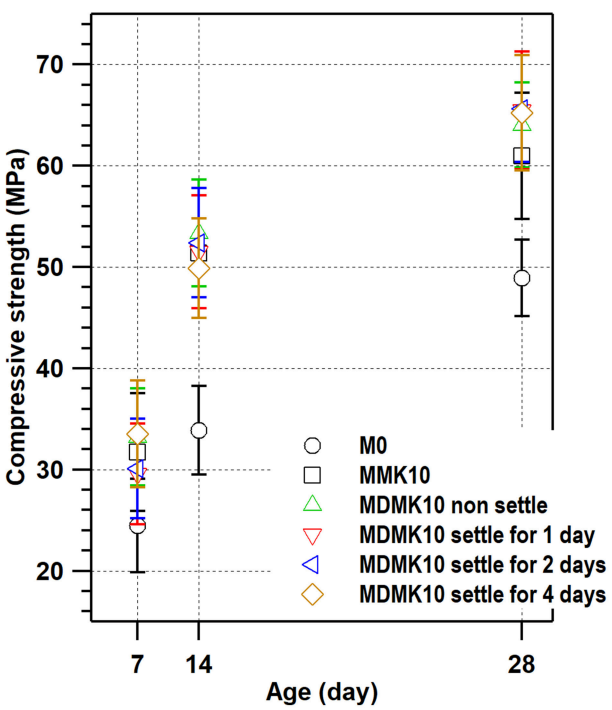

FIGURE 5 | Compressive strength of mortars with powder MK, pre-dispersed MK, and per-dispersed MK settled for 1, 2, and 4 days before addition.

TABLE 5 | Density and viscosity of MK slurry under various water/MK ratio.

Water/MK	0.00	1.00	1.25	1.43	1.54	1.67	1.85	2.00	2.50
Density (kg/m^3)	287.5	665.2	600.8	537.3	529.7	474.5	437.2	408.2	338.3
Viscosity (mPa·s)	–	–	693.48	198.48	123.04	60.65	30.00	21.96	15.22

water segregation of MK slurry was 4.7 ml water per 100 ml slurry at 24 h after mixing and 8.2 ml water per 100 ml slurry at 48 h after mixing.

Compressive Strength

The compressive strength of specimen M0, MMK10, MDMK10 at 3, 7 and 28 days were shown in **Figure 5** and **Table 6**. For MDMK10 specimens, the pre-dispersed MK slurry was added in mortar after preparing or settling for 1, 2, and 4 days, respectively. Comparing to the compressive strength of M0 specimen, by addition of 10 wt% powder MK, the compressive strength increased by 29.4, 51.6, and 24.7% at 3, 7, and 28 days, respectively. Comparing the compressive strength of mortar with pre-dispersed MK with those with powder MK, pre-dispersing of MK did not hinder the effect of MK on the compressive strength of mortar. At 28 days, the compressive strength of mortar with pre-dispersed MK was slightly higher than that with powder MK. With a pH value of 7, water could not activate MK, which was activated later by calcium hydroxide formed during the hydration of cement in mortar. The improvement of compressive strength of mortar by MK was due to the accelerated hydration of cement, filler effect, and pore structure refinement by MK, as reported in previous studies (Li et al., 2015).

Comparing with the compressive strength of mortar with non-settled pre-dispersed MK specimen, the settlement of pre-dispersed MK up to 4 days did not alter the effect of MK on the compressive strength of mortar with pre-dispersed MK, indicating that there was no reaction between water and MK during settlement up to 4 days and MK particles were stably dispersed in water as being suggested by results from zeta-potential test under various pH values.

Porosity

The porosity of paste specimens is shown in **Figure 6** and **Table 7**, together with the relationship between porosity and compressive strength. For the pastes with powder or pre-dispersed MK addition, the compressive strength and porosity did not alter much at 3 days, comparing to that of the control specimen P0. However, at 7 and 28 days, while the porosity was slightly lower than that of the control specimen at the same age, the compressive strength greatly increased with ages, comparing to those of the control specimen P0. There is a linear relationship between the compressive strength and porosity of mortar for each group, where the compressive strength increased with the decrease of porosity, which is similar to previous studies (Frias and Cabrera, 2000). Although the relationship between porosity and compressive strength kept linear for the control, powder MK and pre-dispersed MK specimens, these results indicate that the pore structure was refined through addition of powder or pre-dispersed MK while the porosity did not change much. The relationships between porosity and compressive strength of powder and pre-dispersed MK specimens were similar, indicating that the pore structure refinement effect of MK was not affected by pre-dispersing MK in water. It is notable that the relationship is valid in the porosity range of 28–46% in this study. When the porosity is close to 0, the relationship could be invalid.

Hydration Products

The crystalline phases of paste specimens were characterized by XRD (**Figure 7**). According to these results, the hydration products of ettringite, Portlandite, calcite, hemicarboaluminate (Hc), and monocarboaluminate (Mc) were identified for P0, PMK10, and PDMK10 specimens at 3 and 28 days, except for P0 at 3 days, where monocarboaluminate was not identified. The hydration products identified were similar to those from previous studies (Frias et al., 2012; Gameiro et al., 2012; Tironi et al., 2013). The intensity of peaks attributed to monocarboaluminate

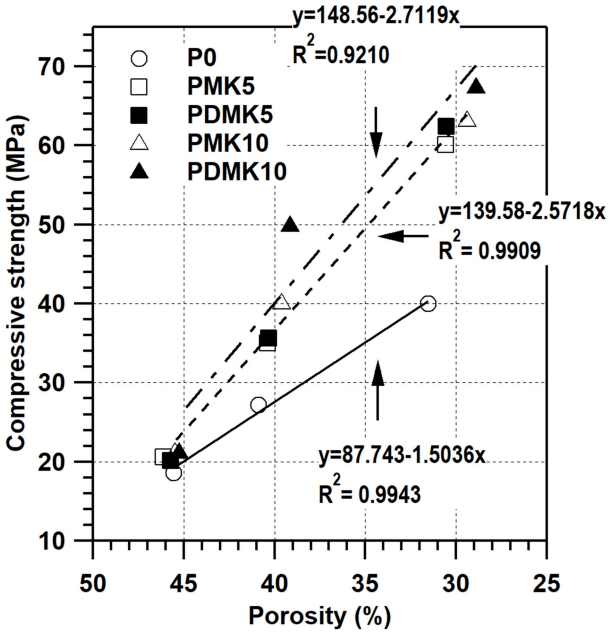

FIGURE 6 | Relationship between the compressive strength and porosity of cement paste, pastes with powder MK, and pre-dispersed MK. Specimens with a porosity of ~45% were cured for 3 days, those with a porosity of 35–42% were cured for 7 days and those with a porosity of 25–35% were cured for 28 days.

TABLE 6 | Compressive strength of mortar specimens (MPa).

Age (day)	M0	MMK10	MDMK10 non-settle	MDMK10 settle for 1 day	MDMK10 settle for 2 days	MDMK10 settle for 4 days
3	24.5 ± 4.6	31.7 ± 5.8	33.2 ± 4.8	29.6 ± 5.0	30.1 ± 4.9	33.6 ± 5.3
7	33.9 ± 4.4	51.4 ± 6.4	53.4 ± 5.3	51.5 ± 5.6	52.4 ± 5.4	49.9 ± 4.9
28	48.9 ± 3.8	61.0 ± 6.2	64.0 ± 4.2	65.5 ± 5.8	65.6 ± 5.3	65.3 ± 5.7

TABLE 7 | Compressive strength with standard deviation and porosity of paste specimens.

Age (day)	P0	PMK5	PMK10	PDMK5	PDMK10
COMPRESSIVE STRENGTH (MPa)					
3	18.6 ± 2.5	20.6 ± 3.0	21.2 ± 3.1	20.1 ± 2.8	21.2 ± 2.7
7	27.2 ± 2.8	35.0 ± 3.6	40.0 ± 3.8	35.6 ± 3.4	49.9 ± 3.2
28	40.0 ± 3.1	60.1 ± 4.3	63.1 ± 4.5	62.4 ± 4.2	67.4 ± 3.8
POROSITY (%)					
3	45.58	46.13	45.49	45.73	45.25
7	40.88	40.38	39.61	40.33	39.16
28	31.55	30.57	29.41	30.53	28.92

increased with age for P0, PMK10, and PDMK10 specimens, indicating the increase of content of monocarboaluminate with age. The intensity of peaks of these hydration products was similar in PMK10 and PDMK10 specimens at the same age, indicating that the effects of powder MK and pre-dispersed MK on the hydration of cement were similar and the effects of MK on cement hydration were not hindered by dispersing in water, as being indicated by the compressive strength and porosity tests. The reason is that MK was not activated by water, with a pH value of 7. There was no reaction between water and MK observed.

Shrinkage

The shrinkage of mortar was evaluated and the results are shown in **Figure 8** and **Table 8**. The shrinkage of mortar was reduced at all ages through addition of powder MK, due to the refined pore structure of mortar by addition of MK, as indicated by previous studies (Li and Yao, 2001), which suggested that the reduced shrinkage by MK addition can be attributed to the lower amount of evaporable water available due to the hydration and pozzolanic reaction of cement and MK. At 28 days, the shrinkage was reduced by 21%, which was similar to previous studies (Brooks and Johari, 2001; Khatib, 2008; Guneyisi et al., 2010, 2012; Cheng et al., 2016). Pre-dispersing of MK reduced the shrinkage of mortar by 41% at 28 days, due to the internal curing effect by water stored in the interlayer of MK during the pre-dispersing process.

Distribution of MK in Mortar Matrix

Preliminary study showed that the agglomeration of MK in mortar or concrete matrix resulted in the non-uniform properties or hydration degree of mortar or concrete. In this study, the distribution of MK particles of powder or pre-dispersed MK were evaluated by coefficient of variation of compressive strength results of 18 specimens from each mortar mix at 28 days. The variation of coefficient is unit-less and represents the distribution of results. The variation of coefficient of results with different mean value can be compared, unlike the standard deviation. The compressive strengths with the range of results, standard deviation, and coefficient of variation were shown in **Figure 9** and **Table 9** for M0, MMK10, and MDMK10 at 28 days. According to these results, the compressive strength of mortar improved by MK addition, and pre-dispersing of MK further improved the compressive strength, as discussed above. Comparing to that of the control specimen, the range of compressive strength of specimens from the same mix significantly increased by addition of powder MK and slightly increased by addition of pre-dispersed MK. Similar to the range of compressive strength, standard deviation (SD) of compressive strength was greatly increased by powder MK and slightly increased by pre-dispersed MK, comparing to that of control specimen. The coefficient of variation (C_v), which indicates the evenness of distribution of MK particles, shown as the size of circle in **Figure 9**, significantly increased by powder MK addition and approximately doubled by pre-dispersing MK addition, comparing to that of M0 specimens.

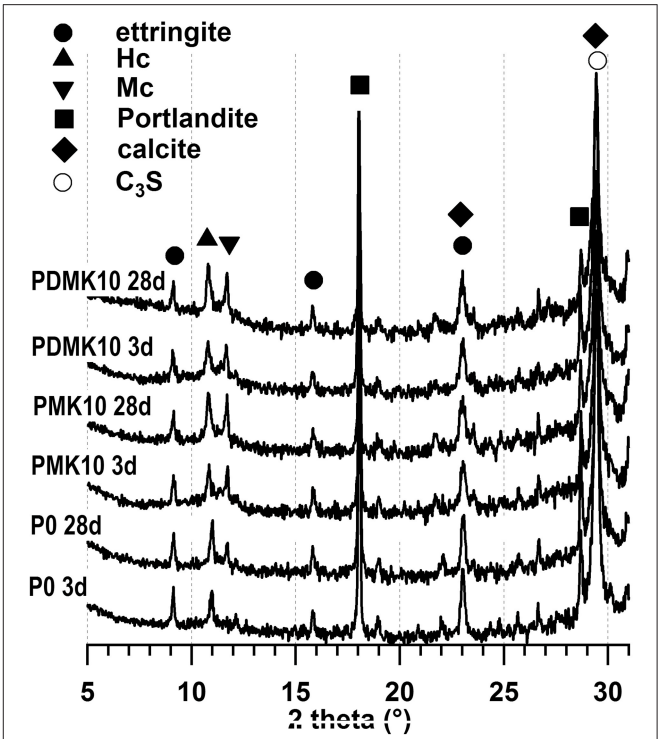

FIGURE 7 | XRD patterns of cement paste, pastes with powder or pre-dispersed MK at 3 and 28 days. Tricalcium silicate, calcite, Portlandite, monocarboaluminate (Mc), hemicarboaluminate (Hc), and ettringite were identified from these specimens.

These results suggest that the particle of powder MK distributed unevenly in the mortar and pre-dispersing of MK by water improved the uniformness of distribution of MK particles in mortar. As indicated by the zeta-potential of dispersed MK slurry, pre-dispersing improved the distribution of MK particles in slurry, and formed a stable dispersing system. Viscosity was also significantly improved through dispersing in water, so as to improve the uniformness of distribution of MK particles in mortar during mixing, although the hydration of cement and MK was not affected by pre-dispersing, as indicated by XRD results.

CONCLUSIONS

The effects of dispersing MK in water on the properties of MK, the properties and hydration of mortar and the distribution of MK particles in mortar were characterized by a range of analytical techniques. According the results, the following conclusions can be drawn.

Zeta-potential of MK-water dispersion significantly decreased with the increase of pH of solution, with zeta-potential of ∼-40 mV at pH of 8, indicating a stable dispersion, due to more OH^- attachment on the surface of MK particles without activation of MK.

During the addition of water, the bulk density of MK-water slurry firstly rapidly increased with water/MK ratio, due to the decrease of distance between MK particles by surface tension force of water and filling of spaces between particles by water. The maximum bulk density was 665.2 kg/m^3 at water/MK ratio of 1.0, indicating the closest packing of MK particles. Then the bulk density gradually decreased with the increase of water/MK ratio, due to the increase of distance between MK particles by continuous addition of water. Viscosity of MK-water slurry decreased rapidly with the increase of water/MK ratio.

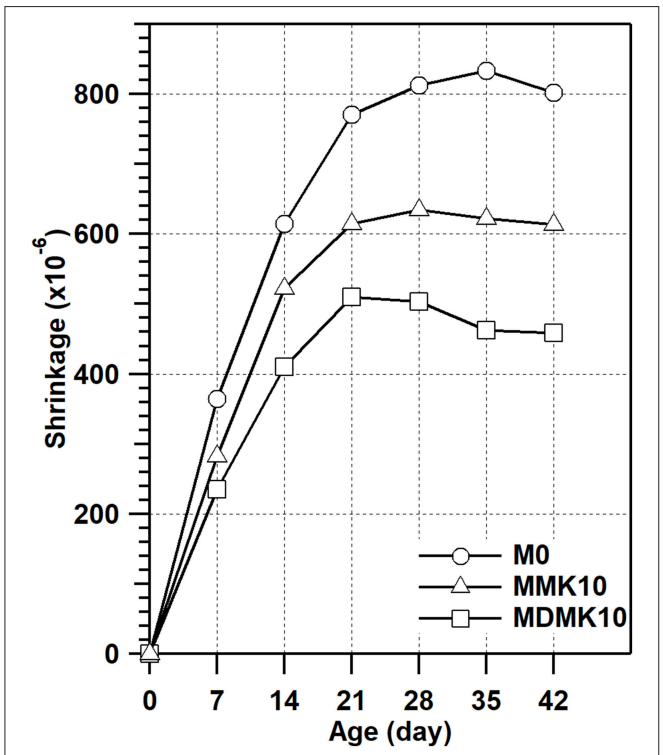

FIGURE 8 | Shrinkage of cement mortar, and mortar with powder or pre-dispersed MK up to 42 days.

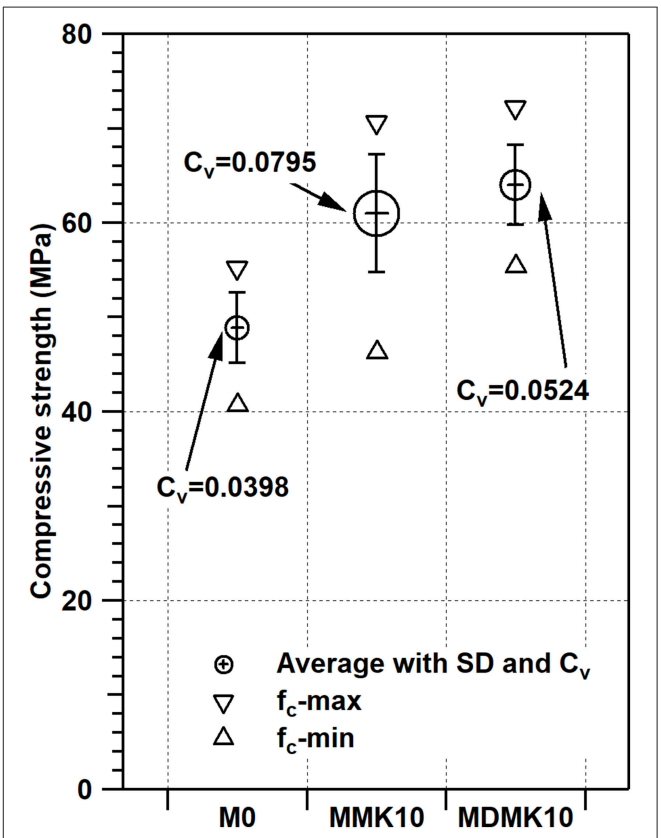

FIGURE 9 | Compressive strength of cement mortar, and mortar with powder or pre-dispersed MK. The results are shown as mean value of 18 specimens of each mix, range of results (f_c-max and f_c-min), standard deviation and coefficient of variation (size of circle).

TABLE 8 | Shrinkage of mortar specimens (×10^{-6}).

Age (day)	0	7	14	21	28	35	42
M0	0	364	615	771	812	833	802
MMK10	0	235	410	510	503	462	458
MDMK10	0	283	522	615	635	622	614

TABLE 9 | Average value, standard deviation, range, and coefficient of deviation of compressive strength at 28 days by calculating 18 specimens.

Specimen	Compressive strength (MPa)	SD (MPa)	f_c-max (MPa)	f_c-min (MPa)	C_v
M0	48.9	3.8	55.2	40.7	0.0398
MMK10	61.0	6.2	70.6	46.3	0.0795
MDMK10	64.0	4.2	72.2	55.4	0.0524

Both powder MK and pre-dispersed MK increased the compressive strength of mortar. There was linear relationship between the compressive strength and porosity of mortar. Neither pre-dispersing MK in water nor settlement of pre-dispersed MK slurry hindered the effect of MK on the compressive strength. Pre-dispersing MK in water slightly decreased the porosity of mortar, comparing to that with powder MK. The hydration products were not affected by pre-dispersing MK in water. Addition of powder MK reduced the shrinkage of mortar, which was reduced further by pre-dispersing MK in water.

Comparing to powder MK, pre-dispersed MK improved the uniformed distribution of MK particles in mortar according to the range, standard deviation, and coefficient of variation of compressive strength results, due to the stable dispersing of MK particle in pre-dispersed MK slurry.

AUTHOR CONTRIBUTIONS

HG, WC, QL, and ZS contributed conception and design of the study. BY performed the properties tests. HG, WC, and QL performed the microstructure and statistical analysis. HG wrote the first draft of the manuscript. WC, QL, ZS, and BY wrote sections of the manuscript. All authors contributed to manuscript revision, read, and approved the submitted version.

ACKNOWLEDGMENTS

Thanks to Dr. Jian Huang (Wuhan University of Technology) for beneficial discussion on the viscosity test. This research was financially supported by the Natural Science Foundation of China (project 51611530545, 51672199), the YangFan Innovative and Entrepreneurial Research Team Project (No. 201312C12) and the Research Fund of State Key Laboratory of Silicate Materials for Architectures (Wuhan University of Technology).

REFERENCES

Antoni, M., Rossen, J., Martirena, F., and Scrivener, K. (2012). Cement substitution by a combination of metakaolin and limestone. *Cement Concrete Res.* 42, 1579–1589. doi: 10.1016/j.cemconres.2012.09.006

Aquino, W., Lange, D. A., and Olek, J. (2001). The influence of metakaolin and silica fume on the chemistry of alkali-silica reaction products. *Cement Concrete Compos.* 23, 485–493. doi: 10.1016/S0958-9465(00)00096-2

Arikan, M., Sobolev, K., Ertuen, T., Yeginobali, A., and Turker, P. (2009). Properties of blended cements with thermally activated kaolin. *Constr. Build. Mater.* 23, 62–70. doi: 10.1016/j.conbuildmat.2008.02.008

Badogiannis, E., Kakali, G., and Tsivilis, S. (2005). Metakaolin as supplementary cementitious material - Optimization of kaolin to metakaolin conversion. *J. Thermal Anal. Calorimetry.* 81, 457–462. doi: 10.1007/s10973-005-0806-3

Bich, C., Ambroise, J., and Pera, J. (2009). Influence of degree of dehydroxylation on the pozzolanic activity of metakaolin. *Appl. Clay Sci.* 44, 194–200. doi: 10.1016/j.clay.2009.01.014

Brooks, J. J., and Johari, M. A. M. (2001). Effect of metakaolin on creep and shrinkage of concrete. *Cement Concrete Compos.* 23, 495–502. doi: 10.1016/S0958-9465(00)00095-0

Buchwald, A., Hilbig, H., and Kaps, C. (2007). Alkali-activated metakaolin-slag blends - performance and structure in dependence of their composition. *J. Mater. Sci.* 42, 3024–3032. doi: 10.1007/s10853-006-0525-6

Cassagnabere, F., Mouret, M., Escadeillas, G., Broilliard, P., and Bertrand, A. (2010). Metakaolin, a solution for the precast industry to limit the clinker content in concrete: mechanical aspects. *Constr. Build. Mater.* 24, 1109–1118. doi: 10.1016/j.conbuildmat.2009.12.032

Cheng, S. K., Shui, Z. H., Li, Q., Sun, T., and Yang, R. H. (2016). Properties, microstructure and hydration products of lightweight aggregate concrete with metakaolin and slag addition. *Constr. Build. Mater.* 127, 59–67. doi: 10.1016/j.conbuildmat.2016.09.135

Coleman, N. J., and McWhinnie, W. R. (2000). The solid state chemistry of metakaolin-blended ordinary Portland cement. *J. Mater. Sci.* 35, 2701–2710. doi: 10.1023/A:1004753926277

Fernandez, R., Martirena, F., and Scrivener, K. L. (2011). The origin of the pozzolanic activity of calcined clay minerals: a comparison between kaolinite, illite and montmorillonite. *Cement Concrete Res.* 41, 113–122. doi: 10.1016/j.cemconres.2010.09.013

Frias, M., and Cabrera, J. (2000). Pore size distribution and degree of hydration of metakaolin-cement pastes. *Cement Concrete Res.* 30, 561–569. doi: 10.1016/S0008-8846(00)00203-9

Frias, M. R., Vigil de la Villa, M. I., Sanchez de Rojas Medina, C., and Juan Valdes, A. (2012). Scientific aspects of kaolinite based coal mining wastes in pozzolan/Ca(OH)2 system. *J. Am. Ceram. Soc.* 95, 386–391. doi: 10.1111/j.1551-2916.2011.04985.x

Gameiro, A., Santos Silva, A., Veiga, R., and Velosa, A. (2012). Hydration products of lime-metakaolin pastes at ambient temperature with ageing. *Thermochim. Acta.* 535, 36–41. doi: 10.1016/j.tca.2012.02.013

Goncalves, J. P., Tavares, L. M., Toledo Filho, R. D., and Fairbairn, E. M. R. (2009). Performance evaluation of cement mortars modified with metakaolin or ground brick. *Constr. Build. Mater.* 23, 1971–1979. doi: 10.1016/j.conbuildmat.2008.08.027

Gueneyisi, E., Gesoglu, M., and Mermerdas, K. (2008). Improving strength, drying shrinkage, and pore structure of concrete using metakaolin. *Mater. Struct.* 41, 937–949. doi: 10.1617/s11527-007-9296-z

Guneyisi, E., Gesoglu, M., Karaoglu, S., and Mermerdas, K. (2012). Strength, permeability and shrinkage cracking of silica fume and metakaolin concretes. *Constr. Build. Mater.* 34, 120–130. doi: 10.1016/j.conbuildmat.2012.02.017

Guneyisi, E., Gesoglu, M., and Ozbay, E. (2010). Strength and drying shrinkage properties of self-compacting concretes incorporating multi-system blended mineral admixtures. *Constr. Build. Mater.* 24, 1878–1887. doi: 10.1016/j.conbuildmat.2010.04.015

He, C., Osbaeck, B., and Makovicky, E. (1995). Pozzolanic reactions of six principal clay minerals: activation, reactivity assessments and technological effects. *Cement Concrete Res.* 25, 1691–1702. doi: 10.1016/0008-8846(95)00165-4

Ilic, B., Mitrovic, A., Radonjanin, V., Malesev, M., and Zdujic, M. (2018). "Compressive strength improvements of cement-based composites achieved with additional milling of metakaolin," in *Calcined Clays for Sustainable Concrete,* eds F. Martirena, A. Favier, and K. Scrivener (Dordrecht: Springer), 212–218. doi: 10.1007/978-94-024-1207-9_34

Johari, A. M., Brooks, J. J., and Kabir, S., Rivard, P. (2011). Influence of supplementary cementitious materials on engineering properties of high strength concrete. *Constr. Build. Mater.* 25, 2639–2648. doi: 10.1016/j.conbuildmat.2010.12.013

Justice, J. M., and Kurtis, K. E. (2007). Influence of metakaolin surface area on properties of cement-based materials. *J. Mater. Civil Eng.* 19, 762–771. doi: 10.1061/(ASCE)0899-1561(2007)19:9(762)

Kadri, E.-H., Kenai, S., Ezziane, K., Siddique, R., and De Schutter, G. (2011). Influence of metakaolin and silica fume on the heat of hydration and compressive strength development of mortar. *Appli. Clay Sci.* 53, 704–708. doi: 10.1016/j.clay.2011.06.008

Khatib, J. M. (2008). Metakaolin concrete at a low water to binder ratio. *Constr. Build. Mater.* 22, 1691–1700. doi: 10.1016/j.conbuildmat.2007.06.003

Khatib, J. M. (2009). Low temperature curing of metakaolin concrete. *J. Mater. Civil Eng.* 21, 362–367. doi: 10.1061/(ASCE)0899-1561(2009)21:8(362)

Kinuthia, J. M., Wild, S., Sabir, B. B., and Bai, J. (2000). Self-compensating autogenous shrinkage in Portland cement-metakaolin-fly ash pastes. *Adv. Cement Res.* 12, 35–43. doi: 10.1680/adcr.2000.12.1.35

Lagier, F., and Kurtis, K. E. (2007). Influence of Portland cement composition on early age reactions with metakaolin. *Cement Concrete Res.* 37, 1411–1417. doi: 10.1016/j.cemconres.2007.07.002

Li, C., Sun, H., and Li, L. (2010). A review: the comparison between alkali-activated slag (Si plus Ca) and metakaolin (Si plus Al) cements. *Cement Concrete Res.* 40, 1341–1349. doi: 10.1016/j.cemconres.2010.03.020

Li, J. Y., and Yao, Y. (2001). A study on creep and drying shrinkage of high performance concrete. *Cement Concrete Res.* 31, 1203–1206. doi: 10.1016/S0008-8846(01)00539-7

Li, Q., Geng, H., Shui, Z., and Huang, Y. (2015). Effect of metakaolin addition and seawater mixing on the properties and hydration of concrete. *Appl. Clay Sci.* 115, 51–60. doi: 10.1016/j.clay.2015.06.043

Love, C. A., Richardson, I. G., and Brough, A. R. (2007). Composition and structure of C-S-H in white Portland cement-20% metakaolin pastes hydrated at 25 degrees C. *Cement Concrete Res.* 37, 109–117. doi: 10.1016/j.cemconres.2006.11.012

Medri, V., Fabbri, S., Dedecek, J., Sobalik, Z., Tvaruzkova, Z., and Vaccari, A. (2010). Role of the morphology and the dehydroxylation of metakaolins on geopolymerization. *Appli. Clay Sci.* 50, 538–545. doi: 10.1016/j.clay.2010.10.010

Murat, M., and Comel, C. (1983). Hydration reaction and hardening of calcined clays and related minerals III. Influence of calcination process of kaolinite on mechanical strengths of hardened metakaolinite. *Cement Concrete Res.* 13, 631–637. doi: 10.1016/0008-8846(83)90052-2

Rashad, A. M. (2013). Metakaolin as cementitious material: history, scours, production and composition - a comprehensive overview. *Constr. Build. Mater.* 41, 303–318. doi: 10.1016/j.conbuildmat.2012.12.001

Sabir, B. B., Wild, S., and Bai, J. (2001). Metakaolin and calcined clays as pozzolans for concrete: a review. *Cement Concrete Compos.* 23, 441–454. doi: 10.1016/S0958-9465(00)00092-5

Scrivener, K. L., and Kirkpatrick, R. J. (2008). Innovation in use and research on cementitious material. *Cement Concrete Res.* 38, 128–136. doi: 10.1016/j.cemconres.2007.09.025

Shui, Z., Sun, T., Fu, Z., and Wang, G. (2010). Dominant factors on the early hydration of metakaolin-cement paste. *J. Wuhan Univ. Technol. Mater. Sci. Edn.* 25, 849–852. doi: 10.1007/s11595-010-0106-z

Taylor, H. F. W. (1997). *Cement Chemistry, 2 Edn. London: Thomas Telford Services Ltd.* doi: 10.1680/cc.25929

Tironi, A., Trezza, M. A., Scian, A. N., and Irassar, E. F. (2013). Assessment of pozzolanic activity of different calcined clays. *Cement Concrete Compos.* 37, 319–327. doi: 10.1016/j.cemconcomp.2013.01.002

Wild, S., Khatib, J. M., and Jones, A. (1996). Relative strength, pozzolanic activity and cement hydration in superplasticised metakaolin concrete. *Cement Concrete Res.* 26, 1537–1544. doi: 10.1016/0008-8846(96)00148-2

Conflict of Interest Statement: The authors declare that the research was conducted in the absence of any commercial or financial relationships that could be construed as a potential conflict of interest.

frontiers in Materials

REVIEW
published: 07 May 2019
doi: 10.3389/fmats.2019.00106

Silico-Aluminophosphate and Alkali-Aluminosilicate Geopolymers: A Comparative Review

*Yan-Shuai Wang, Yazan Alrefaei and Jian-Guo Dai**

Department of Civil and Environmental Engineering, The Hong Kong Polytechnic University, Hong Kong, Hong Kong

Chemically activated materials (often termed as geopolymer) have received attracting attentions in civil, material and environmental research fields as a toolkit alternative to traditional Portland cement in specific applications. This paper presents a comparative review on silico-aluminophosphate (SAP) geopolymers in terms of definition, chemistries involved during geopolymerization, mechanical performance, durability, environmental impacts, and their potentials in applications relative to conventional alkali-aluminosilicate (AAS) geopolymers. Recommendations for future applications are also highlighted. It is found that S-A-P gels with six-coordinated aluminum environment dominate in SAP geopolymers, while the aluminum in N-A-S-H gels formed in the AAS geopolymers is characterized by four-coordinated features. Besides, the slow performance development of SAP geopolymer matrix under ambient temperature curing can be compensated through incorporating additional countermeasures (e.g., metal sources) which allow the tailored design of such geopolymers for certain *in-situ* applications. Generally, the calcium-bearing C-(A)-S-H gels co-existing with N-A-S-H gels are dominant in AAS geopolymers, while the S-A-P gels enhanced by phosphate-containing crystalline/amorphous phases are the main products in SAP geopolymers. The SAP geopolymers show their environmental friendliness relative to the AAS geopolymers due to the utilization of phosphate activators that require lower production energy relative to silicate-containing activators. However, the higher cost of phosphate activators may confine the applications of SAP geopolymers in some exquisite or special fields.

Keywords: silico-aluminophosphate, alkali-aluminosilicate, geopolymerization mechanism, environmental impacts, sustainable development

OPEN ACCESS

Edited by:
Miroslav Komljenovic, University of Belgrade, Serbia

Reviewed by:
Kenneth John MacKenzie, MacDiarmid Institute for Advanced Materials and Nanotechnology, New Zealand
Yingwu Zhou, Shenzhen University, China
Hubert Rahier, Vrije University Brussel, Belgium

***Correspondence:**
Jian-Guo Dai
cejgdai@polyu.edu.hk

Specialty section:
This article was submitted to Structural Materials, a section of the journal Frontiers in Materials

Received: *14 January 2019*
Accepted: *23 April 2019*
Published: *07 May 2019*

Citation:
Wang Y-S, Alrefaei Y and Dai J-G (2019) Silico-Aluminophosphate and Alkali-Aluminosilicate Geopolymers: A Comparative Review. Front. Mater. 6:106. doi: 10.3389/fmats.2019.00106

GENERAL ABOUT CEMENT AND GEOPOLYMER BINDERS

Cement, routinely denoted as ordinary Portland cement (OPC), is described as a cohesive material that can set and bind sands and gravels together; such binder is excessively used to prop up the modern urban agglomerations (Taylor, 1997; Neville, 2011; Shi et al., 2011). However, the annual huge consumption of contemporary cement has caused several environmental issues worldwide due to the high carbon footprint (e.g., the inescapable decarbonation of limestone) during cement production. Geopolymer binders, characterized by higher durability and greenness relative to the conventional OPC, have gained many attentions recently as a promising partial substitute to OPC (Provis and Bernal, 2014; Provis et al., 2015).

Initially, the geopolymer was strictly defined as the alkali-activation of raw aluminosilicates (e.g., metakaolin as a precursor) without (or with little) other components (i.e., Ca, Mg, etc.) (Davidovits, 2011). The geopolymer formation can be described as a polymer-like condensation process (as shown in Equation 1) where the loss of water between two hydroxyl groups occurs in inorganic materials (Wilson and Nicholson, 2005; Davidovits, 2011). Such chemistry is also extended to the reaction between two different hydroxyl-containing groups, e.g., the isolated aluminate (IV) and silicate (IV) units to reconstruct connected gels with chain or ring network structure through condensation chemistry in alkali-activated aluminosilicate binders, as shown in Equation (2) (De Jong et al., 1983). Thus, such high-connectivity molecular structures of the formed products can perform excellently in terms of strength and durability (Walkley et al., 2017). Later on, the phosphate-activated aluminosilicate was developed and incorporated into the geopolymer category due to the similar condensation process (Liu et al., 2010; Davidovits, 2011; Guo et al., 2016; Wang et al., 2017, 2018b).

$$\equiv Q - OH + HO - Q \equiv \overset{Catalysis}{\Longrightarrow} \equiv Q - O - Q \equiv + H_2O \quad (1)$$

where, Q denotes the hydroxyl-containing group (e.g., orthosilicic group).

$$\equiv Si - OH + HO - Al \equiv \overset{Alkaline}{\Longrightarrow} \equiv Si - O - Al \equiv + H_2O \quad (2)$$

The catalytic activation process of un-doped aluminosilicate precursors is usually enhanced by external energies (e.g., heat, ultraviolet, and microwave), otherwise it requires a long hardening duration, depending on the reactivity of the aluminosilicate sources (Agarwal, 2006; Zhang et al., 2016). Such special curing methods are acceptable in precast geopolymer industry, yet very challenging to be implemented in *in-situ* constructional operations (Provis and Bernal, 2014). Therefore, it is imperative to develop other chemical processes for room-temperature hardening mechanism in geopolymers.

In alkali-activated systems, the calcium-containing solid aluminosilicate sources, such as ground granulated blast-furnace slag (GGBS) or high-calcium fly ash (FA), are habituated under high alkaline environment to form C-(A)-S-H gels rapidly (Wang et al., 1994; Shi and Qian, 2000; Li et al., 2010). It should be noted that the high volume of calcium species in FA (e.g., Class C) greatly influences the operating time of their corresponding binders due to their flash setting, which needs to be overcome by the use of retarding additives, e.g., sodium tetraborate (Nicholson et al., 2005; Tailby and MacKenzie, 2010). The C-(A)-S-H gel shows some similar features to that of C-S-H gel that is dominant in the conventional OPC cement. In the meantime, soluble silicates (sometimes mixed with aluminates) are generally introduced into the alkaline activating solution with the same aim of obtaining a rapid sol/gel transition (Benavent et al., 2016). Such actions provide the alkali-activated binders matrices with high efficiency in terms of mechanical performance and durability (Ding et al., 2016, 2018; Shang et al., 2018; Xue et al., 2018).

As a comparison, in phosphate-activated systems, some solid agents (e.g., alkali metals) can be incorporated into the aluminosilicate sources to induce an acid-base chemistry which generally facilitates the formation of crystalline (e.g., products in magnesium/calcium phosphate cement) or amorphous phosphate phases during the chemical activation of aluminosilicates (Wagh, 2016; Wang, 2018). Such acid-base chemistry can be described in Equations (3–5). Initially, the release of cations from the metal oxides occurs through hydrolysis reaction (shown in Equation 3), following, the metal cations react with water to form the aquo ions (hydration reaction in Equation 4). The polyacids generated by the acidic salt or acid (e.g., phosphate radicals) react with the aquo ions (e.g., $Mg[H_2O]_6^{2+}$) as described in Equation (5) (Ding et al., 2012). The whole conversion process from sols (i.e., colloidal solutions) to gels can be described as exothermic and rapid. Such fast acid-base chemistry can be used for possible improvements in the early performance of the phosphate activation of aluminosilicate.

$$MO_{\frac{p}{2}} + \frac{p}{2}H_2O \Rightarrow M^{p+} + pOH^- \quad (3)$$

$$M^{p+} + qH_2O \Rightarrow [M(H_2O)_q]^{p+} \quad (4)$$

$$H_nPO_4^{-(3-n)} + [M(H_2O)_q]^{p+} \Rightarrow [M(H_nPO_4)]^{n+p-3} + qH_2O \quad (5)$$

Due to the environmental concerns, the currently used aluminosilicate sources in the geopolymer production are usually industrial byproducts (e.g., FA and GGBS) rather than the materials available naturally (e.g., metakaolin [MK]) (Toniolo and Boccaccini, 2017). The MK [$2SiO_2{\cdot}Al_2O_3$] is the product of the dehydroxylated clay mineral kaolinite [$Si_2O_5Al_2(OH)_4$] upon calcination under high temperature (Sperinck et al., 2011) to yield disordered aluminosilicates with Si-O-Al(1O) (i.e., Al in five-fold coordination) and Si-O-Al(2O) (i.e., Al in four-fold coordination), which is an ideal precursor for geopolymer preparation. Due to the limited availability of clay mineral and high temperature calcination that may cause undesirable high cost and energy consumption, the MK is still confined to laboratory use with the aim of investigating the mechanism of geopolymer formation (Khale and Chaudhary, 2007); however, the use of MK is recommended for some practical low-volume high-value applications (e.g., bioactive ceramics, electronic ceramics, drug delivery agents, etc.) (MacKenzie, 2015). On the other hand, the industrial raw materials (typically the byproducts of power stations like FA and iron & steel industries like GGBS) are chemically complex due to their diverse production technologies (Pacheco-Torgal et al., 2008; Yao et al., 2015; Xu and Shi, 2018). Thus, some "impurities" (the impurities mean different available components in the precursor other than aluminosilicates) in the byproducts will induce non-geopolymeric chemistries, thus the acidic or alkaline activators will generate different chemical compositions, crystallinities and phases. Accordingly, the formation process of the impurity-contained geopolymer (i.e., silico-aluminophosphate [SAP] geopolymer and alkali-aluminosilicate [AAS] geopolymer) can be illustrated based on the acidic and alkaline activation conditions as shown in **Figure 1**. In addition to the different pH conditions, the resulting

molecular structures of the SAP and AAM geopolymers vary to wide extent, especially the chemical environment of Al in the formed gels, which behaves as Al(VI) and Al(IV) in SAP geopolymer and AAS geopolymer, respectively. Such formation model and mechanism will be discussed in section Formation Model and Mechanism of Geopolymer.

Recently, the AAS geopolymers have been investigated from multiple angles, such as the synthesis mechanism and chemistry (Provis, 2013; Provis and Bernal, 2014; Provis et al., 2015), properties and durability (Bernal et al., 2014; Arbi et al., 2016; Ding et al., 2016), life cycle analysis (Habert et al., 2011; Ouellet-Plamondon and Habert, 2015), and multi-field applications (MacKenzie, 2015; Rao and Liu, 2015; Luukkonen et al., 2019). Yet, the available review related to the SAP geopolymer is limited even though such type of geopolymer was termed as aluminosilicate phosphate cement (Khabbouchi et al., 2017; Katsiki, 2019), phosphoric acid-based geopolymer (Liu et al., 2012; Guo et al., 2016), phosphate-based geopolymer (Wang et al., 2017), acid-based geopolymers (Mathivet et al., 2019), and phosphate-bonded materials (MacKenzie, 2015). This paper mainly reviews the development of the SAP geopolymers in reference with the conventional AAS geopolymers.

TERMINOLOGY AND CLASSIFICATION

The research era of alkali-activated materials (AAMs) started in 1908 (Kühl, 1908; Provis and Van Deventer, 2013), and since then AAMs were explained as cement-like materials formed by the reaction between an aluminosilicate precursor and an alkaline activator. Then, the tranquility was broken by the term "geopolymer" coined by Davidovits who inadvertently produced an inorganic polymer-like material with good fire-resistance (Davidovits, 2011). The traditional geopolymer was predominantly confined to the binder prepared by the aluminosilicate sources with marginal impurities. Such geopolymer binder mainly highlights the chemical behaviors of aluminate and silicate species, including bonds breaking (i.e., decomposition reaction) and remaking (i.e., polymerization reaction). Afterwards, the activation approach of aluminosilicate precursors was extended to phosphate species and termed as phosphate-based geopolymer (Wagh, 2004; Davidovits, 2011). The empirical formulas of the AAS and SAP geopolymers are shown in Equations (6, 7), respectively (Cui et al., 2008; Davidovits, 2011; Wagh, 2016).

$$M_n[-(SiO_2)_z - AlO_2]_n \cdot mH_2O \quad (6)$$

$$[-(Si-O)_z - Al-O-P]_n \cdot mH_2O \quad (7)$$

where n is the degree of geopolymerization, z is 1, 2, or 3, and M is an alkali cation (e.g., K or Na).

Recently, the term "chemically-activated materials" (CAMs) was also proposed to describe the aluminosilicate sources that can be activated to create cementitious matrices using some chemical solutions (e.g., alkali-silicate, phosphate and other chemicals) (CAM2017 International Conference, Gold Coast, Australia). However, the term "geopolymer" seems to be more attractive to (even widely-used by) engineers because such term is more concise and easy-spreading. In this paper, all the binders primarily prepared by aluminosilicate materials and some chemical activators were named as modern geopolymer for the convenient circulation in academic, engineering and business communities. The modern geopolymers are further classified into two categories according to the activation approach: alkali-aluminosilicate (AAS) geopolymer and silico-aluminophosphate (SAP) geopolymer. The terminology and development of the geopolymers are summarized in **Figure 2**. In modern geopolymer, the AAS geopolymer denotes the alkali activation of aluminosilicate precursors such as the calcium-containing sources (e.g., alkali-activated GGBS binder), the low-impurity aluminosilicates (e.g., alkali-activated FA/MK binder), or their blends (e.g., alkali-activated GGBS/FA blends), while the SAP geopolymer implies that the aluminosilicate sources are pre-mixed with some metals and activated by the acid phosphate or other phosphates. It is good to mention that the activation methods assisted by external energies [e.g., microwave (Chindaprasirt et al., 2013a), autoclaved (Rashad et al., 2012), and mechanical activation (Kumar and Kumar, 2011)] are not involved in this review.

FORMATION MODEL AND MECHANISM OF GEOPOLYMER

AAS Geopolymer

As commonly explained, the three-dimensional network of alkali-aluminosilicate geopolymer is configured with the negative $[AlO_4]^{5-}$ and $[SiO_4]^{4-}$ tetrahedrons in addition to positive alkali metal ions (e.g., Na^+ or K^+) (Duxson et al., 2006; Buchwald et al., 2011). Recent research has indicated that the hydroxyl free radicals (·OH) released in the alkaline solutions catalyze the disintegration of the aluminosilicate precursor by breaking the bonds of Si-O-Si, Al-O-Si, and Al-O-Al, besides catalyzing the promotion of isolated aluminate and silicate anions reconstruction via remaking the bonds of Si-O-Si, Al-O-Si, and Al-O-Al (Feng et al., 2016). Thus, the tetrahedrons of silicon and aluminum are combined by oxygen bridges to form the high-connectivity chain or ring network structures. The negative charge given by tetra-coordinated aluminum is compensated by the alkali metal ions (Xu et al., 2001). However, the lower-silica gels in such geopolymer matrix (e.g., high molar ratio of Na_2O/SiO_2 in the activating solution or low molar ratio of Si/Al in the aluminosilicate source) tend to be transformed into some loose particulate units [i.e., pseudo-zeolitic structure (mainly Q^4)] rather than continuous well-connected N-A-S-H gels (He et al., 2013; Provis et al., 2015). It was found that a reasonable content of silicate species in the activating solution could yield compact alkali-aluminosilicate geopolymer matrix with more continuous gels, especially when using the solid aluminosilicate precursor with lower Si/Al ratio (Duxson and Provis, 2008).

The results of solid-state nuclear magnetic resonance (NMR) confirmed the chemical environment of silicon and aluminum in the calcium-free geopolymer made by low-impurity aluminosilicate precursor (Buchwald et al., 2007). The

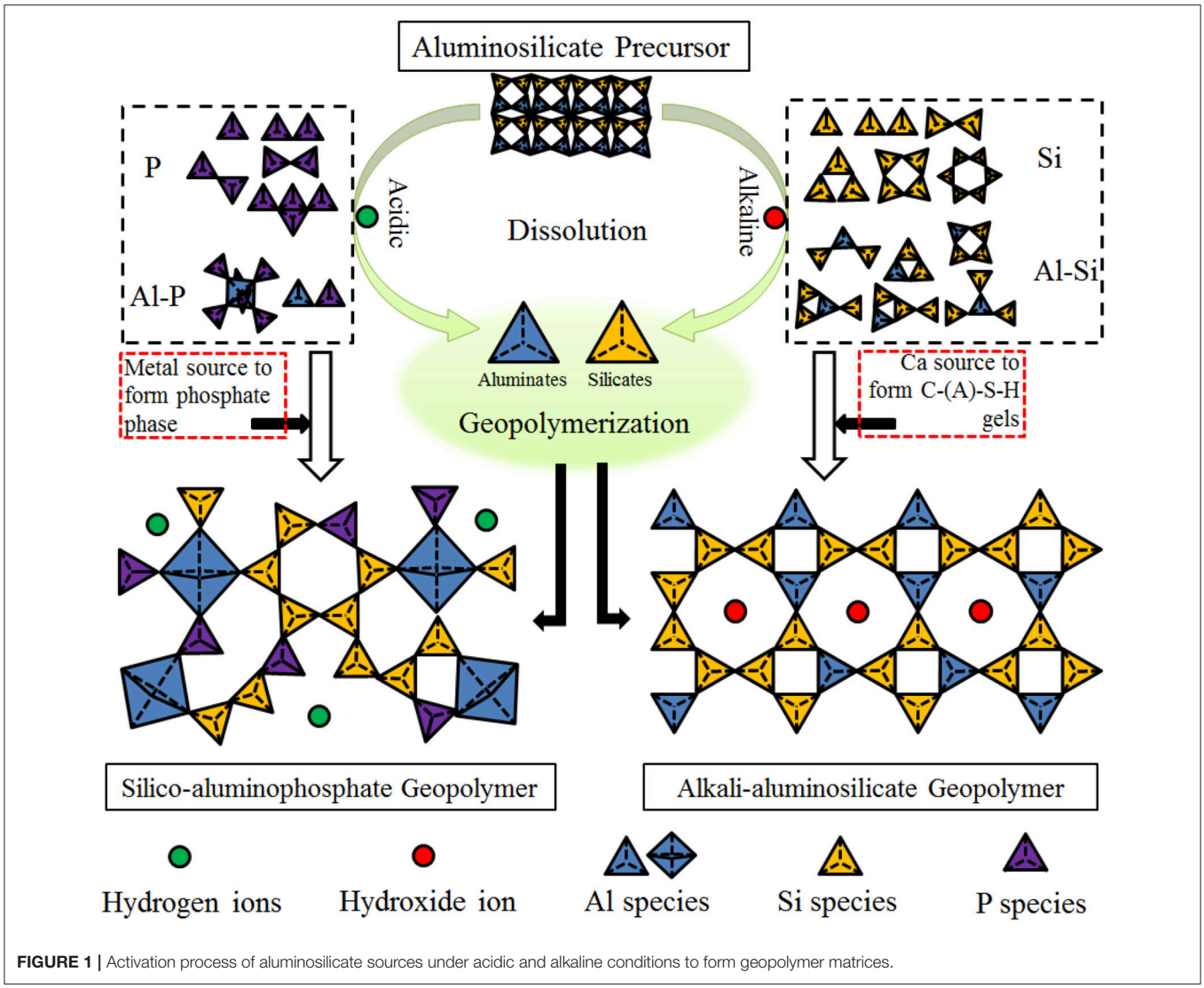

FIGURE 1 | Activation process of aluminosilicate sources under acidic and alkaline conditions to form geopolymer matrices.

higher intensity of the $Q^4(4Al)$ and AlO_4 signals shown by NMR curves indicated that the tetra-coordinated silicate and aluminate species dominate the N-A-S-H gels formed in alkali-aluminosilicate geopolymer (Xu et al., 2018).

The microstructure and strength developments of the low-calcium FA-based geopolymer activated by an alkaline solution were descriptively explained beforehand (Fernández-Jiménez et al., 2005, 2006). When reacted with alkaline solution, the FA grains are chemically opened which dissolves the active silicate and aluminate phases to form microscopic imperfections (e.g., points or holes). The dissolved species are condensed into gels through geopolymerization and nucleation which result in compact geopolymer matrix with relatively adequate strength (Pacheco-Torgal et al., 2008). A three-stage corresponding relationship between microstructure evolution and geopolymerization is established to interpret the mechanical strength development in the AAS geopolymer (Fernández-Jiménez et al., 2006). The first stage is the "dissolution stage" of the glassy aluminosilicate phases. Since the matrix is not yet formed during this period, no mechanical strength can be achieved. The second stage is the "induction period," where massive metastable gels (denoted Gel 1 in Fernández-Jiménez et al. (2006)) are formed and precipitated. As the dissolution of silicate is comparatively slower than that of aluminate, the Gel 1 includes relatively high amount of reactive aluminum which is associated with the initial setting of the geopolymer paste. It is good to mention that the mechanical strength development is usually initialized at the second stage. The final stage is the "silicon incorporation stage" that describes the transformation of Gel 1 into Gel 2 (as indicated in Fernández-Jiménez et al., 2006) wherein the reactive aluminum is embedded into the Si-rich gels to form Gel 2. According to the aluminosilicate precursor and activator used, the mechanical strength of the formed matrix will usually be lower when the content of Gel 1 is higher than that of Gel 2 in hardened geopolymer matrix. Conversely, the mechanical strength can be higher in case the content of Gel 2 outnumbers that of Gel 1, as reported by Criado et al. (2008).

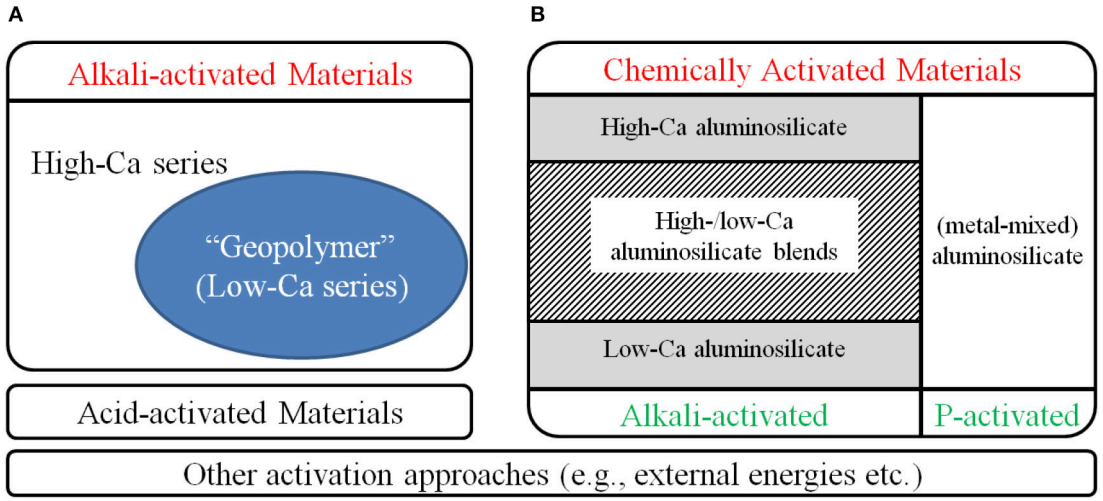

FIGURE 2 | Summary of the terminology and development of the geopolymer. **(A)** Traditional geopolymer. **(B)** Modern geopolymer.

Effect of "Impurities" in AAS Geopolymer

Regarding the role of calcium in alkali-aluminosilicate geopolymer, it is usually claimed that calcium aluminate silicate hydrate (C-A-S-H) gels with tobermorite-like structure (mostly Q^2 and some Q^1) are generated during the geopolymerization (Richardson et al., 1994). The calcium source can induce the aluminosilicate precursor to produce different chemical products in AAS geopolymer. The chemical environments of silicon in calcium-incorporated AAS geopolymer behave as Q^1 and $Q^2(1Al)$ forms, while the $Q^4(2Al)$, $Q^4(3Al)$, and $Q^4(4Al)$ chemical forms of silicon appear in calcium-free AAS geopolymer (Buchwald et al., 2007). The AlO_4-dominated C-(A)-S-H gels and the hydrotalcite (AlO_6) exist in the calcium-incorporated AAS geopolymer as the main chemical configurations of aluminum, which shows significant differences compared to calcium-free AAS geopolymer (AlO_4-dominated N-S-A-H gels).

The combined utilization of GGBS and low-calcium FA can produce N-A-S-H and C-A-S-H gels which are entangled together to form strength-giving gels. The molecular structure of C-A-S-H gels in high-calcium AAS geopolymer can be generalized as the Al-substituted C-S-H gels (Richardson et al., 1993; Brough et al., 2001; Lodeiro et al., 2010). Such gels have Ca/Si ratio lower than that formed in Portland cement (Wang and Scrivener, 1995). This interpretation is similar to the chemistry of supplementary cementitious materials (SCMs) in OPC. The Si-rich phase improves the lower Ca/Si ratio of hydrates by consuming portlandite (i.e., pozzolanic reaction), while Al-rich phase promotes the Al-uptake of hydration products (Lothenbach et al., 2011).

Although the glassy aluminosilicate source with high calcium content can easily generate C-A-S-H gels in alkali environment, the reactivity of available calcium in raw materials may be varied substantially depending on its existence forms. Besides, the GGBS and high-calcium FA have similar calcium and glassy aluminosilicate contents, yet they behave differently in the alkali activation process. The high reactivity of GGBS is mainly attributed to the fast cooling technology (e.g., water quenching granulation) which generates amorphous phases with the network-forming anions $[SiO_4]^{4-}$, $[AlO_4]^{5-}$, and $[MgO_4]^{6-}$ in addition to the network-modifying cations Ca^{2+}, Al^{3+}, and Mg^{2+} (Garcia-Lodeiro et al., 2015). The existence of calcium species can lower the polymerization degree of silicon network which can equip the GGBS with high pozzolanic activity. On contrary, the high-calcium FA particles usually form crystalline phases (e.g., mullite and quartz) due to the slow cooling collection method which presents minimal or no cementitious properties. Therefore, the use of high-calcium FA as main raw material for the preparation of alkali-aluminosilicate geopolymer is significantly challenging at room temperature.

In many existing studies on the durability and mechanical properties of AAS geopolymers regardless of "two-part" (i.e., liquid activators) or "one-part" (i.e., solid activators) mixing approaches, the use of GGBS and FA combination with a certain ratio as an aluminosilicate precursor achieves a geopolymer binder that can roughly meet the engineering requirements (Ismail et al., 2014; Bernal et al., 2015, 2016; Alrefaei and Dai, 2018; Alrefaei et al., 2019). The incorporation of high-calcium materials (i.e., to seed calcium species) with low-calcium raw materials (i.e., main source of alumina and silica) greatly affects the formation of the main binding gels (Bernal et al., 2016). The N-A-S-H type gels generated in low-calcium systems exhibit a relatively slower reaction rate compared to the C-A-S-H type gels in high-calcium systems; however, N-A-S-H gels promote highly cross-linked and compact products through extending the curing time (Bernal et al., 2016). In other words, the synergistic effect of the high- and low-calcium aluminosilicate precursors is witnessed in the coexistence of these molecular structures, where the C-A-S-H gels ensure early performances (e.g., setting time and early strength), while the N-A-S-H

gels contribute to long-term characteristics (e.g., durability and strength development).

SAP Geopolymer

The Egyptian pyramids proved their reliability and durability for thousands of years although the construction materials used in the Pyramids are not fully clear (MacKenzie et al., 2011). However, limited research declared that the surface of pyramids' blocks spontaneously grew a white/red coating that was complicated geopolymeric phosphate compounds made of crystalline hydroxyapatite and brushite embedded in a poly(sialate)/SiO_2 matrix (Barsoum et al., 2006; Davidovits, 2011). Later on, the aluminosilicate precursors consolidated by phosphates or orthophosphoric acids were explored for preparing refractory castables (Kingery, 1950, 1952) which can be defined as phosphate activation of the aluminosilicates to yield an SAP geopolymer with excellent durability and high temperature resistance (Wagh, 2016). The use of phosphate or phosphoric acid as an activator allows the chemical interaction with the aluminosilicates to produce geopolymeric binder with condensed poly(silico-alumino-phosphate) phases (Cao et al., 2005; Liu et al., 2010).

Regarding the molecular structure in SAP geopolymer, the $[AlO_4]^{5-}$, $[SiO_4]^{4-}$, and $[PO_4]^{3-}$ units act as basic blocks (He et al., 2013). Compared with AAS geopolymer, the $[PO_4]^{3-}$ unit replaces the alkali metal ion, as reported by Cui et al. (2011). Cui's model revealed that partial replacement of $[SiO_4]^{4-}$ unit by $[PO_4]^{3-}$ in the broken Si-O-Al bonds may occur in low polymeric network. Thus, the charge balance within the molecular structure can be achieved without the involvement of monovalent cations. Previous research showed that the updated Si-O-Al linkage (i.e., Al-O-P) can balance the charge due to the aluminum chemical shift ranging from octahedral or/and pentahedral coordination to tetradentate form (Cao et al., 2005). However, many studies indicated that the hexa-coordinated aluminum dominates in SAP geopolymers (Davidovits, 2011; Louati et al., 2014, 2016). It should be noted that an amorphous Si-Al-P structure was reported in AAS geopolymer wherein the tetrahedral P was identified to occupy a proportion of site of silicate (Mackenzie et al., 2005).

Since the model of microstructure evolution of SAP geopolymer was barely reported in previous literature, some result-derived interpretations and hypotheses are introduced in this paper based on existing studies (Duxson et al., 2006; Cui et al., 2008, 2011; Wagh, 2016). Cui et al. (2011) synthesized SAP geopolymer using pure Al_2O_3-$2SiO_2$ powders (synthesized in the lab) and phosphoric acid with P/Si molar ratio of 1.2. The XRD patterns showed no clear trace of newly-formed crystalline peaks in the phosphate activated geopolymers. Instead, a broad diffused peak in the range of 15–40° (2θ) appeared in all the samples. The diffraction peak was shifted from 22° (2θ) in calcined Al_2O_3-$2SiO_2$ powder to about 26° (2-theta) in geopolymers, with a marginal change in the diffraction intensity. It was claimed that the molecular structure and interlayer spacing were chemically shifted after geopolymerization in acid phosphorus environment relative to the raw Al_2O_3-$2SiO_2$ powders.

Besides, the natural aluminosilicate materials like Tunisian clay and metakaolin were also investigated when activated by phosphate acid with various Si/P molar ratios (Douiri et al., 2014; Louati et al., 2014). A shift in the wide broad band from 18–30° (2θ) to 22–35° (2θ) was observed in both calcined clay and synthesized geopolymers, as well as the diffraction intensity changed in some crystalline peaks e.g., aluminum phosphate ($AlPO_4$), augelite ($Al_2(PO_4)(OH)_3$), and monetite ($CaHPO_4$). Such differences in the XRD patterns of the raw aluminosilicates and phosphate activated aluminosilicates (i.e., SAP geopolymer) could be attributed to the geopolymerization of the aluminosilicate precursors.

Perera et al. (2008) also performed a comparative study on the metakaolin-based geopolymer when activated by alkali and phosphate solutions. Similar to Cui et al. (2011) observations, the XRD results confirmed the amorphousness of SAP geopolymer. Further investigations by the transmission electron microscope (TEM) equipped with energy dispersive X-ray spectroscopy (EDXS) and selected area electron diffraction (SAED) indicated that such amorphous phases contained Si, Al, P, and O. The SAED image exhibited some blurred rings and spots instead of crystal lattices which further ensured the availability of amorphous phases in SAP geopolymer (Perera et al., 2008).

Furthermore, magic angle spinning-nuclear magnetic resonance (MAS-NMR) analysis was conducted on the SAP geopolymer by Perera et al. (2008). A single $[PO_4]^{3-}$ resonance was observed at around−16 ppm which could be deconvolved into two resonances (−4 and −16 ppm) due to its asymmetric line shape. A cross polarization (CP) NMR of P was identified to enhance the dominance at −16 ppm. The ^{27}Al results indicated that the main chemical environment of aluminum in SAP geopolymer was six-coordination (VI) as evidenced by the single resonance at an apparent shift of around −12 ppm. Thus, the phosphate activation promoted the metakaolin to produce mixed octahedral Al(VI) environment with both P and Si, which influenced the oxo-bridged second coordination sphere. This was mainly unlike the AAS geopolymer where Al(VI) was converted to tetrahedral sites, i.e., Al(IV). The three resonances (e.g., −91.8, −101.6, and −110.8 ppm) in ^{29}Si NMR curve described the Q^3, Q^4 (Al or P), and Q^4 silicon chemical environments, respectively (Provis et al., 2015). The intensity of Q^3 was the lowest which meant that most of metakaolin was dissolved. The mixed environment of Si-Al-P phase in SAP geopolymer was assigned as the Q^4 (Al or P), while the Q^4 was described as siliceous or Al-free portions that might not fully connect to P phase (Cao et al., 2005).

Effect of "Impurities" in SAP Geopolymer

In order to improve the modest early performance of SAP geopolymer, the incorporation of some alkali metals as setting agents (e.g., solid Mg/Ca source) with aluminosilicate precursors can produce a setting-controlled SAP geopolymer matrix (Luz et al., 2015). Such agents essentially initiate acid-base chemistries (i.e., between phosphate and setting agents) in addition to geopolymerization of the aluminosilicates, which enables the fast formation of amorphous or crystalline phosphates to modify the workability and early strength of such geopolymer (Wang

et al., 2018b). Relative to the aluminosilicate precursors, the added setting agents can be regarded as "impurities" here. The chemistry of such setting agents is elaborated below.

"Phosphate cement" is a general term that describes the phosphate as a main ingredient of the cement (Walling and Provis, 2016). Since phosphate cement is usually a binder that hardens through acid-base and/or hydrolysis chemical reactions (usually generate crystalline phosphates as main products) at room temperature, it is also named as chemically bonded phosphate ceramic (CBPC) (Roy, 1987). CBPCs were discovered and developed as dental cements in the nineteenth century which were extended to construction field later on as patching materials for rapid rehabilitation of runway and bridge. The formation of CBPC experiences the dissolution of alkali metals and phosphates to form crystalline structures (i.e., phosphate compounds) with excellent adhesive and mechanical properties. It is expected that such chemical mechanism (i.e., the chemistry between alkali metals and phosphates) can be introduced into SAP geopolymer as a room temperature hardening mechanism to address its weak early properties (Wang, 2018). The reaction products of CBPCs are directly linked to the raw materials used; more specifically, the material recipe (e.g., ratio, reactivity etc.) is related to the reaction environments (e.g., pH condition, ions concentration etc.). Here, the calcium- and magnesium-based sources are comprehensively introduced because other alkali-metal sources (e.g., Fe and Zn) fails to form well-crystallized phases due to the violent reaction process (Wagh and Jeong, 2003a,b).

Calcium-based CBPC is often termed as "calcium phosphate cement" (CPC) which is used as a bioceramic material in orthopedic industry due to its excellent bioactivity and biocompatibility (Ben-Nissan, 2014). The chemical reactions involved during the CPC setting consist of three stages: dissolution, supersaturation, and precipitation (Zhang J. et al., 2014). In acidic phosphate solution, the calcium donors slowly release the calcium ions and react with (hydro)-phosphate groups to form a supersaturated solution (i.e., paste). When reaching the critical values (e.g., ions concentration or pH condition), the nucleated and precipitated new phase grows along with the continuous dissolution of calcium. According to the composition of final products, the CPC is classified into apatite cement [β-tricalcium phosphate, $Ca_5(PO_4)_3(OH/Cl/F)$ or $Ca_3(PO_4)_2$] and brushite cement ($CaHPO_4{\cdot}2H_2O$) (Tamimi et al., 2012; Ben-Nissan, 2014). In general, according to the recipe (e.g., solubility and Ca/P ratio) and reaction conditions (e.g., pH value and hydrothermal environment), the possible chemical processes involved in the formation of CPC matrix can be described in Equations (8–10).

$$3Ca^{2+} + 2[H_nPO_4]^{n-3} \rightarrow Ca_3(PO_4)_2 + 2nH^+ \quad (8)$$

$$5Ca^{2+} + 3[H_nPO_4]^{n-3} + H_2O \rightarrow Ca_5(PO_4)_3(OH) + (3n+1)H^+ \quad (9)$$

$$Ca^{2+} + [H_nPO_4]^{n-3} + 2H_2O \rightarrow CaHPO_4.2H_2O + (n-1)H^+ \quad (10)$$

Fresh CPC is a castable paste which is preferable for bone defects reconstruction with minimum invasive surgery since it can be resorbed under physiological conditions after embedding into the body (Xue et al., 2012; Inzana et al., 2014; Xu et al., 2017). Thus, the moldable properties of calcium-blended SAP geopolymer extend its applications to 3D printing for building arts in civil engineering or other aesthetic fields.

Magnesium phosphate cement (MPC) is another typical CBPC that is widely used in civil engineering because of its excellent performance (Wang and Dai, 2017). In the early research stage, the MPC was fabricated with magnesia and phosphoric acid (Wagh, 2016). The lower pH environment induces a rapid and highly exothermic reaction where the reaction product is water-soluble magnesium dihydrogen phosphate [$Mg(H_2PO_4)_2{\cdot}nH_2O$]. Subsequently, attempts were made to use less acidic diphosphate. The employment of diphosphate and calcined magnesia further mitigates the reaction rate and heat release during MPC formation. The soluble diphosphates can create an acidic environment in water which facilitates the dissolution of magnesia. When the concentration and pH are approaching ideal value, crystal generation and growth occur in the supersaturated slurry (Chauhan et al., 2008). The general reaction of MPC is described in Equation (11). The resulting phase is crystalline struvite or its analogs (e.g., struvite-K or struvite-Na) with 6–8 crystal waters (Chauhan et al., 2011; Chauhan and Joshi, 2014). Such hydrates have excellent cementitious and mechanical properties (Ding et al., 2012). Finch and Sharp (1989) also studied the reaction of mono-aluminum phosphate and magnesia in terms of molar ratio and final products, showing that the crystalline Newberyite ($MgHPO_4{\cdot}3H_2O$) appeared instead of struvite analog in case of the Mg/P molar ratio of 4. The phosphate species might involve in the formation of amorphous phase as well.

$$MgO + XH_2PO_4 + nH_2O \rightarrow MgXPO_4 \cdot (n+1)H_2O \quad (11)$$

The characteristics of crystalline calcium/magnesium phosphate phases including mineral name, chemical formula and main application fields are listed in **Table 1**. Ca-based apatites are mostly used as biomaterials for dental applications and mimic bones due to their good biocompatibility (Xu and Simon, 2005; Giocondi et al., 2010). The variants of Ca-based apatites can also be employed to immobilize the heavy metal pollutants (e.g., Pb, Cd, Zn, or Cr) by embedding them into the respective apatite minerals (e.g., Ca/Zn replacement) (Saxena and D'Souza, 2006). On the other hand, the final products containing struvite or its analogs (i.e., Mg series) are usually used as rapid repair materials in civil engineering due to their high mechanical performance and adhesive property (Ma et al., 2014).

Model Comparison of AAS and SAP Geopolymers

Alkali activation process of Ca sources (i.e., C-A-S-H gel formation) and acid-base reaction process of Ca/Mg and phosphate (i.e., amorphous or crystalline phosphates) can promote both rapid setting at room temperature and strength upscaling by forming new phases. Their simplified synthesis models of the two "Hybrid" geopolymers are conceptualized in **Figure 3**.

Figure 4 shows a comparative flow chart between the formation processes of AAS and SAP geopolymers wherein

TABLE 1 | Specific crystalline products in calcium/magnesium phosphate cement.

Mineral name		Chemical formula	Application
Ca series	Brushite/Monetite	$CaHPO_4{\cdot}2H_2O/CaHPO_4$	
	Hydroxyapatite (HAp)	$Ca_5(PO_4)_3{\cdot}OH$	Biomaterial, Phosphor material,
	Chloroapatite (ClAp)	$Ca_5(PO_4)_3{\cdot}Cl$	
	Fluoroapatite (FAp)	$Ca_5(PO_4)_3{\cdot}F$	Waste treatment
Mg series	Struvite	$Mg(NH_4)PO_4{\cdot}6H_2O$	
	Struvite-K (Ceramicrete)	$MgKPO_4{\cdot}6H_2O$	Building material,
	Struvite-Na	$MgNaPO_4{\cdot}7H_2O$	Waste encapsulation
	Newberyite	$MgHPO_4{\cdot}3H_2O$	

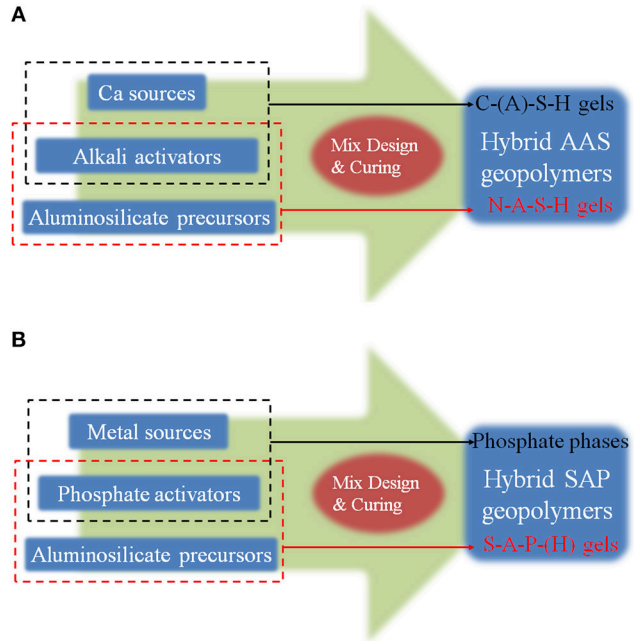

FIGURE 3 | Simplified conceptual models of two "Hybrid" geopolymers. **(A)** Hybrid AAS Geopolymers. **(B)** Hybrid SAP Geopolymers.

the key stages from the raw materials to the final geopolymer binders are outlined. The Ca-containing AAS geopolymer was investigated for many years (as shown in **Figure 4A**), including dissolution, speciation, gelation, reorganization and final polymerization (Duxson et al., 2006). The chemically-dissolved aluminosilicate precursors accessibly form the C-(A)-S-H gels when encountering the free Ca species. This chemical process is relatively faster than that of N-A-S-H gels at ambient temperature. In most cases, the two gels co-exist in the final geopolymer matrix as resulting products.

As a comparison, the synthesis process of SAP geopolymer is simplified in **Figure 4B**. However, the research related to SAP geopolymer is rare, so it should be noted that the synthesis process of such geopolymer is deduced according to the classical interpretations on the CBPC and the AAS geopolymer. The transformation of phosphate species from sol state to gel state, including the dissolution and speciation of (hydro)-phosphate ions, is the first step during SAP geopolymer formation (Perera et al., 2008). Usually, the acid-base reaction between Ca or Mg sources and (hydro)-phosphate ions is initiated before the dissolution of aluminosilicate precursors. The gelation and reorganization among aluminate, silicate and phosphate form S-A-P gels via the condensation processes. Final polymerization of these species gradually synthesizes the SAP geopolymer matrix. Unlike AAS geopolymer, phosphate-bearing crystalline or amorphous phases may occur in some cases when reasonable molar ratios (metal ion to phosphorus) and pH environment are available (Guo et al., 2016).

ENVIRONMENTAL IMPACT

Portland Cement and Geopolymer Binders

Due to the vast of mineral resource consumptions, intensive energy usage and high carbon emissions companioned with ordinary Portland cement (OPC) production, it is believed that the geopolymer binders should be strongly proposed as green building materials to partially replace cement in future construction applications (Walkley et al., 2017). Usually, the life cycle assessment (LCA) methodology, also known as the "cradle to grave" approach, is internationally normalized to provide quantitative information for the environmental burden of each product manufacture system (ISO, 2006; Passuello et al., 2017). However, the recent findings related to the LCA-based comparison between geopolymer and OPC products showed a wide variation, even some conflicting results, depending on the goal, scope, the needs, and the targeted audience used in LCA analysis (Ouellet-Plamondon and Habert, 2015).

The aroused controversies regarding the LCA of geopolymer binders are derived from several complexities such as the local resources availability, the process of raw materials, thermal treatment and the mix design parameters (e.g., alkali content, Si/Al molar ratio, water-to-binder ratio etc.), as shown in **Figure 5** (Duxson et al., 2007; Habert et al., 2011; Ouellet-Plamondon and Habert, 2015; Habert and Ouellet-Plamondon, 2016). Another challenge of the LCA application in geopolymer binders is that such binders mainly include two different industrial products (i.e., aluminosilicate precursors and activators) unlike the OPC that deals with a single material industry. When the solid precursor is treated as a waste material in the LCA analysis (e.g., in Europe, *Directive 2008/98/EC of the European Parliament and of the Council on waste and repealing certain Directives*. L312: 3–30), the energy consumed during the production process (i.e., FA and GGBS from power stations and steel production, respectively, as shown in **Figure 5**) does not negatively impact the CO_2 balance of the geopolymer binders. As a comparison, the cement clinker calcination consumes a large quantity of fossil fuel energy and releases additional CO_2 through the decarbonation reaction. Thus, the geopolymer binders are considered as a groundbreaking solution for the environmental issues caused by Portland cement industry (Duxson et al., 2007). On the other hand, such binders adversely impact the environment when the precursor is considered as a raw material since the thermal input of the solid precursor should be involved in the LCA calculation. Besides, Habert et al. (2011) claimed that the production of a typical AAS

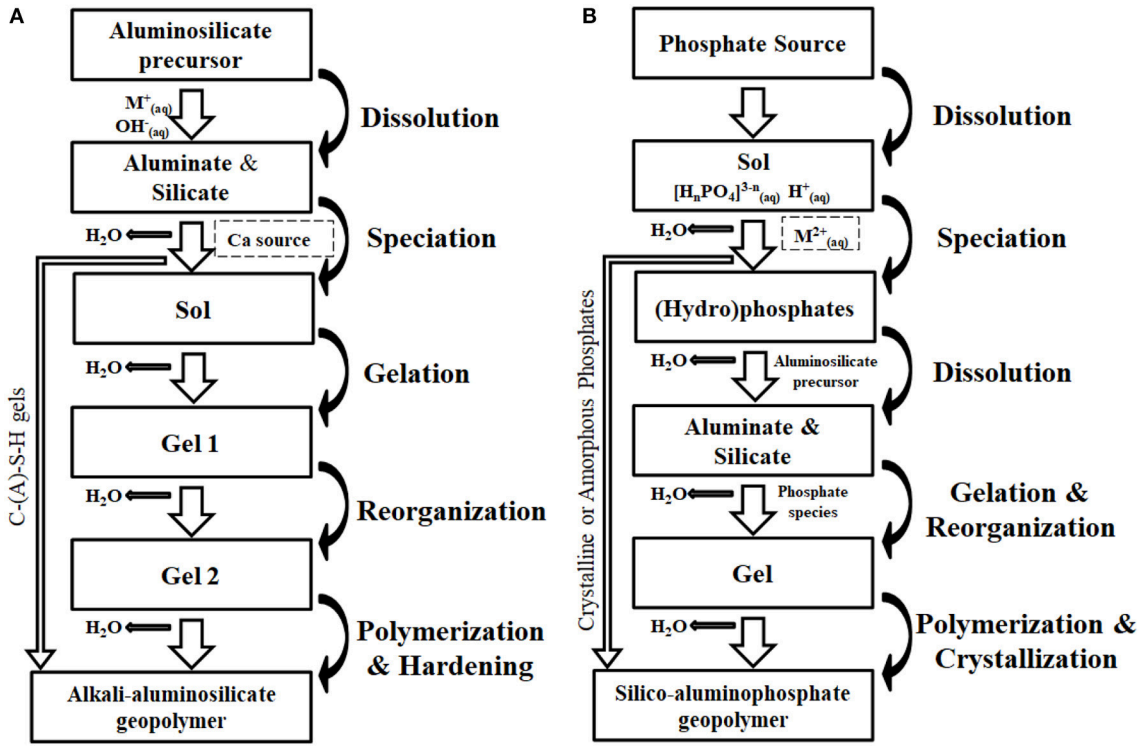

FIGURE 4 | Flow chart of conceptual formation process of AAS and SAP geopolymers containing impurities. **(A)** AAS geopolymer. **(B)** SAP geopolymer.

geopolymer concrete presents a slightly lower impact on the global warming compared to standard OPC concrete, mainly due to the energy expenditure of activators (e.g., mining, treatment, manufacture, and transport). Regarding the SAP geopolymer, it was reported that the energy usage during the production of phosphate binders (mainly the phosphate products) accounts for around one-fourth of that consumed in Portland cement industry (Wagh, 2016).

AAS and SAP Geopolymers

When comparing the two types of geopolymer (i.e., AAS and SAP), the key point lies in the environmental impact of activating solutions. During the preparation of AAS geopolymer, it is necessary to use soluble sodium silicates to address the performance requirements (e.g., mechanical properties; Ding et al., 2016) of geopolymer concrete, especially when aluminosilicate precursors with lower Si/Al ratio is employed (Krizan and Zivanovic, 2002). However, the silicate solutions are always contentious due to their high cost and aggressiveness to the environment during production (e.g., intensive energy consumption and global warming potential) (Fawer et al., 1999). On the other hand, for SAP geopolymer, the phosphate solutions are majorly manufactured through the reaction between phosphate rock and sulfuric acid at $<100°C$. Thus, the environmental impacts of the phosphate solutions are largely determined by the sulfuric acid production industry (Kongshaug, 1998). Generally, modest emissions (e.g., carbon dioxide) are linked to the modern sulfuric acid production industry. Besides, the exothermic reactions involved in such production may generate net energy (i.e., heat released) that can be totally employed in other industries (Wood and Cowie, 2004). Further, emission standard of pollutants for sulfuric acid industry is severely implemented all over the world (*China Emission Standard of Pollutants for Sulfuric Acid Industry*, 2011; *EU Best Available Techniques for Pollution Prevention and Control in the European Sulphuric Acid and Fertilizer Industries*, 2000; *US Guidelines for Limitation of Contact Sulfuric Acid Plant Emissions*, 1971). Accordingly, the phosphate solutions seem to be more sustainable and environmentally friendly relative to the alkali-silicate solutions in terms of the gas emission and energy expenditure.

In addition to their moderate carbon emissions and energy consumption, the application of the SAP geopolymer products may form a virtuous eco-system as the phosphorus available in such binders can be absorbed or extracted to form the P-containing fertilizers for crops after abandoning (Bartos et al., 1991; Raven and Loeppert, 1996). These biological and chemical actions may further form mineral deposits (e.g., phosphate rocks). Such eco-friendly loop makes the phosphate-based products greener and more sustainable which meets the concept of industrial ecology in the long run (Jelinski et al., 1992). Adversely, the alkali-silicate activators (varying modulus of sodium silicate) used for preparing the AAS geopolymer products are usually non-recyclable. Some researchers are exploring some waste-derived activators (e.g., silica fume and rice husk ash) and non-silicate activators (e.g., carbonate and sulfate)

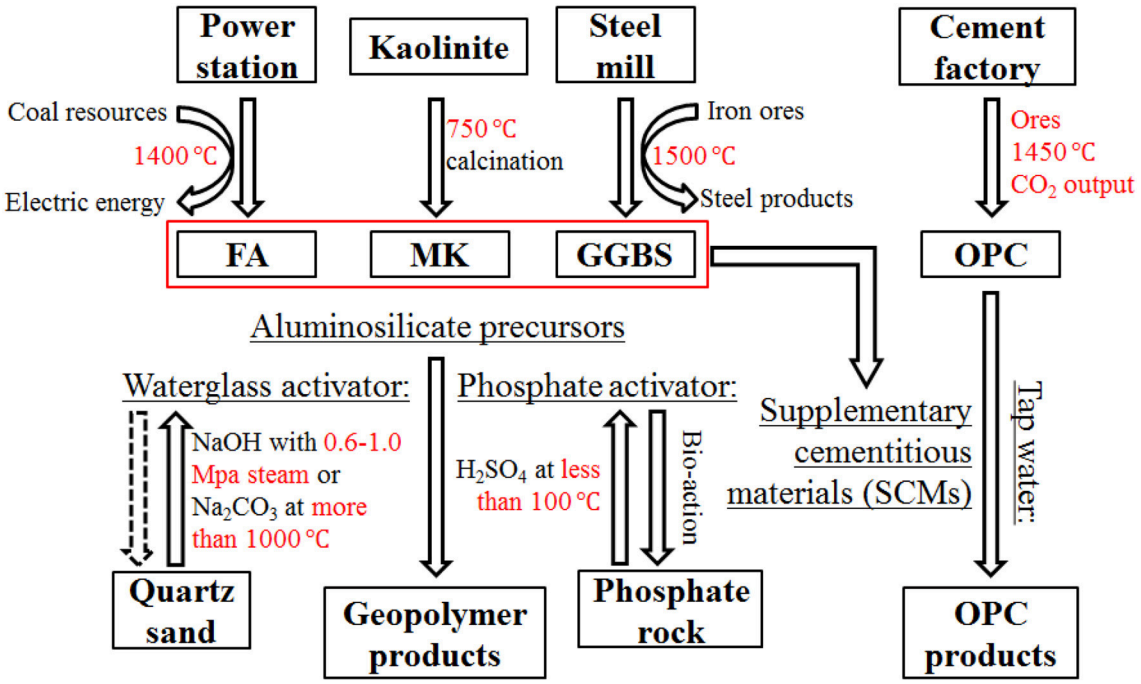

FIGURE 5 | Energy expenditure diagram of geopolymer and OPC products.

to replace commercial silicate solutions for AAS geopolymer preparation (Nazari et al., 2011; Bernal et al., 2012; He et al., 2013), which may reduce environmental burden caused by waterglass industry.

PERFORMANCE, DURABILITY, COST, AND ACCESSIBILITY

Compressive Strength

The mechanical strengths reported in the published literature varied widely owing to the differences in raw materials (e.g., attribute and recipe), curing condition (e.g., temperature and moisture) and sample preparation technology (e.g., size and age). The 28 days compressive strengths of the geopolymer obtained from literature survey, including low- and high-calcium AAS geopolymers in addition to SAP geopolymers, are shown in **Figure 6** (Davidovits, 2011; Chindaprasirt et al., 2012, 2013b; Nath and Kumar, 2013; Nematollahi and Sanjayan, 2014; Atiş et al., 2015; Guo et al., 2016; He et al., 2016; Reddy et al., 2016; Wang et al., 2016; Wang, 2018). Clearly, the statistics showed that the compressive strengths of the AAS geopolymer (i.e., 15–65 MPa for low-calcium series and 70–110 MPa for high-calcium series) significantly outperformed that of the SAP geopolymer (i.e., 10–50 MPa).

Ding et al. (2016) summarized the mechanical properties of AAS geopolymer concrete, revealing that the compressive strength and elastic modulus can moderately meet the requirements of Portland cement concrete design codes. Reddy et al. (2016) made an attempt to investigate the influences

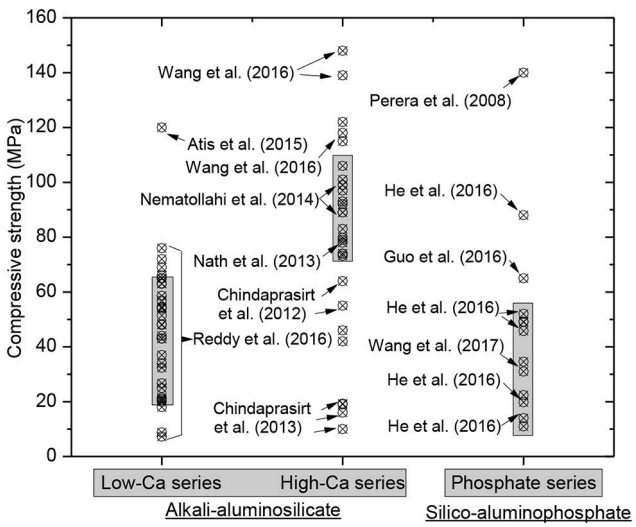

FIGURE 6 | Literature survey on 28 days compressive strength of the geopolymer binders. It should be noted that the statistics ignore the attribute and recipe of raw materials and curing conditions used.

of oxide composition of precursors on the compressive strength of the AAS geopolymer products. Perera et al. (2008) synthesized (60°C curing for 24 h) SAP geopolymer with compressive strength approaching 140 MPa which is two-fold that of AAS geopolymer. On the other hand, Wang et al. (2017) reported that the final setting time was more than

48 h and the compressive strength reached 31 MPa at 28 days for the metakaolin (MK)-based geopolymer activated by mono-aluminum phosphate at room temperature curing. Guo et al. (2016) obtained the phosphate-based geopolymer using MK and disused phosphate liquid which resulted in a compressive strength of 62–67 MPa when the matrix experienced 7 days curing at 60°C. The activating effect of disused phosphate liquid exceeded that of phosphoric acid because of the presence of aluminum ions and thermal curing.

Thermal Stability, Dielectricity, and Efflorescence

As previously reported, the MK-based geopolymers activated by phosphoric acid exhibited good thermal and volume stability (Liu et al., 2012). Phase transition (from aluminum hydrogen phosphate to berlinite) was observed when the geopolymer sample was subjected to elevated temperatures (900–1,550°C). In the AAS geopolymer, the presence of calcium source could reduce the curing cost and increase early strength as previously explained. The early compressive strength of such hybrid geopolymer matrix is augmented along with the increased use of GGBS (Guerrieri and Sanjayan, 2010). However, such practice lowers the ability of geopolymer to resist fire and high temperatures (Buchwald et al., 2007) due to the existence of the non-fire-resistant C-(A)-S-H gels.

Cui et al. (2011) compared the dielectric loss of two types of geopolymers. It was found that the SAP geopolymer held a very low dielectric loss (around 0.01 for frequencies more than 300 MHz) at 300°C dried for 2 h. On the other hand, the AAS geopolymer was temperature-dependent due to the availability of free metal and hydroxyl ions; thus, it was difficult to decrease the dielectric losses resulting from ion transfer.

Besides, the efflorescence is also a serious issue with relatively little attention in research (Najafi Kani et al., 2012; Allahverdi et al., 2015; Pacheco-Torgal, 2015). Efflorescence in AAS geopolymer is the result of the incomplete consumption of alkaline and/or soluble silicates that leads to form sodium carbonate in the pores or on the surface of geopolymer matrix (Xue et al., 2018). This can be because the presence of water weakens the bond of sodium in geopolymer; besides, the efflorescence rate is strongly activation-dependent. In case of the same alkali content and curing temperature, NaOH-activated geopolymers show less and slower efflorescence relative to geopolymers activated by sodium silicate. Geopolymers with high Na_2O/Al_2O_3 ratio may suffer from unsightly efflorescence as well (Najafi Kani et al., 2012). The use of calcium blended precursors (i.e., FA/GGBS-based geopolymers) in addition to the hydrothermal curing process usually generates geopolymer binders with relatively weaker efflorescence, yet the GGBS addition appears to delay rather than mitigate the effect of efflorescence (Zhang Z. et al., 2014). Najafi Kani et al. (2012) stated that the alumina-rich admixtures can reduce the efflorescence. Therefore, the well-designed mix proposition and chemical composition of the geopolymer binders can mitigate or even eliminate the efflorescence, e.g., providing hydrothermal curing, sufficient Al-rich mineral admixtures for gel formation and alkali consumption (Allahverdi et al., 2015). On the other hand, SAP geopolymers have high resistance to efflorescence relative to the AAS geopolymers; thanks to the acidic synthesis environment.

Cost and Availability

In addition to the performance comparison, the cost and the availability of both types of geopolymers (i.e., AAS and SAP) are also crucial to practical engineering. Although quotations form regional suppliers (e.g., Alibaba) indicate that the price of phosphoric acid is more than three-fold that of sodium silicate, the SAP geopolymer can act as a complement to AAS geopolymer in the field of geopolymer category. In other words, the SAP geopolymer shall be further explored as small-scale or specifically-required functional materials (e.g., as fire-proof material, dielectric ceramics, coating materials, fast-rapid materials, and 3D printing materials), while the goal of AAS geopolymer is to reduce the traditional cement consumption.

The complexity of aluminosilicate sources, especially aluminosilicate-containing industrial byproducts, is a major concern for geopolymer production. Fly ash as a typical aluminosilicate source for geopolymer preparation is an anthropogenic material with polymorphic, polycrystal, and multi-component system (Blissett and Rowson, 2012). According to different regions, more than 316 individual minerals and 188 mineral groups in coal fly ash have been identified and characterized, which may cause even more differences in non-crystalline phases and particle characteristics (Vassilev and Vassileva, 2005). The diversity of raw materials results in wide differences in the geopolymer mechanical properties, even when using the same formula and mix design. Therefore, if the aluminosilicates are properly characterized, classified and pretreated, the properties of geopolymer products can be tailored for certain applications and performances. The geopolymer turns out to possess multi-phase, multi-component, and multi-morphology; however, its performance is strongly reliable on the types of raw materials. In order to achieve a high performance geopolymer matrix, the following three assessment indices of aluminosilicate are required for preparing different geopolymers (Luxán et al., 1989; De Rojas and Frías, 1996; Agarwal, 2006).

(1) Material characterization: The characterization indices of aluminosilicates include their compositions (oxide and phase) and physical features (particle size, specific gravity, surface, and loss of ignition), which can greatly influence the performances of geopolymer products.

(2) Reactivity test: The reactivity of the aluminosilicate precursors is closely associated with their phases. The combined use of Rietveld analysis (Hill and Howard, 1987) and PONKCS (partial or no known crystal structure; Scarlett and Madsen, 2012) are relatively useful for initial gauging of the crystalline and amorphous phase contents. Glassy phase composition of some aluminosilicates can be captured by SEM-EDXS with multispectral image analysis, to differentiate the inert crystalline and the reactive amorphous phases in case of similar elemental composition (Chancey et al., 2010; Durdzinski

et al., 2015). The participation degree of aluminosilicates during geopolymerization heavily determines the properties of geopolymer products.

(3) Performance enhancements: For improper aluminosilicate sources, particle size reduction and minerals addition seem to be valid. However, the thermal and chemical pretreatments can be more effective because such pretreatments increase the amorphous proportion and decreases the loss of ignition (Handoo et al., 2002; Škvára et al., 2009; Bentz et al., 2012).

POTENTIAL APPLICATIONS

Application in Construction

One of the large-scale applications of geopolymers (mainly AAS geopolymer) is in construction due to their good mechanical behavior and durability. Some modified AAS geopolymer binder has been commercially branded for infrastructure projects, such as PYRAMENT cement (Davidovits, 2011). Currently, the SAP geopolymer is being researched in labs, especially with the focus on the unclear chemistries between phosphate and aluminosilicate. In cases of high-volume content of FA-blended phosphate binder, FA particles are conventionally considered as a diluent or inert filler that modifies the aesthetics of the formed products (e.g., change color and reduce porosity) to be comparable with Portland cement as a rapid healant. Recently, some reports have conversely indicated that the high mechanical strength of the FA-blended phosphate binders is also attributed to the formation of secondary amorphous phase (e.g., phospho-siloxonate geopolymeric phases; Gardner et al., 2015).

Application in Waste Management

The waste production is directly related to population increase. In order to stop the contaminants from flowing into the food chain of human, some effective and low-cost amendments are applied to stabilize/solidify the hazardous or radioactive waste streams (Morrissey and Browne, 2004; Temuujin et al., 2014). According to the definition of stabilization/solidification, stabilization process is defined as the chemical converting of contaminants into their insoluble, immobile or nontoxic forms without spillage, leakage, and disintegration in a long term, while solidification is defined as changing the physical consolidating sludges, liquids, or powders into solid forms so that they will not be dispersed during transportation, long-term storage or disposal. Recently, AAS geopolymer binders are used for the remediation of heavy metals-contaminated soils through stabilization/solidification (S/S) (Luna Galiano et al., 2011). It is claimed that the heavy metals can be fixed in the molecular network during geopolymerization, either chemically through embedment into the molecular structure for charge balance or physically by being trapped in the surrounding 3D network (Van Jaarsveld et al., 1997). In SAP geopolymer, the phosphate ions are also chemically combined with detrimental metal species to form highly insoluble phosphates (e.g., pyromorphite during Pb S/S; Wang et al., 2018a).

Application in Biomaterials

Considering the biocompatibility, resorbability, and customization of living body, the SAP geopolymer with Ca-containing setting agent is considered as an excellent suitable candidate. The tailor-made shape can be pre-prepared using 3D printing technique due to the good injectability of such materials (Chia and Wu, 2015). Except for precast skeletal structure, SAP geopolymer can be injected as a paste into selected regions in the biological body. Not only that paste cements the adjacent tissues, but also has less intrusion properties compared to the implants made of hardened biomaterials. Since bones and teeth mainly contain calcium phosphate compounds, Ca-containing SAP geopolymer can provide the necessary compositions for better biocompatibility. The zinc and magnesium species enable the performance enhancement (e.g., strength) in calcium enriched mixture (CEM) matrix as blended phosphate biomaterials (Utneja et al., 2015). Besides, the viable biocompatible AAS geopolymers have been demonstrated (MacKenzie et al., 2010).

Application in 3D Printing

3D printing is a promising technique that can rapidly manufacture products with spatial complicity and precise distribution (Bassoli et al., 2007; Rengier et al., 2010; Lim et al., 2012). Such attractive rapid prototyping (RP) is based on the additive manufacturing (AM), defined by ASTM International as "the process of joining materials to create objects from 3D model data, usually layer upon layer" (*ASTM F2791-10*). The customized imaging database (e.g., computed tomography scans) can be visualized via 3D printing system. Nevertheless, how to select the appropriate material with appropriate rheology, setting time, temperature, strength, durability, and other special requirements, is the major problem. Recently, the 3D printing of biomaterials has been applied for surgical planning and prosthetics using phosphate materials due to its biocompatibility in human body (Guvendiren et al., 2016). The "two-part" geopolymer (aluminosilicate and activator) is also potentially applicable for 3D printing in construction (Xia and Sanjayan, 2016; Zhong et al., 2017).

CONCLUDING REMARKS

This paper provides a comprehensive review and comparison between alkali and phosphate activations of aluminosilicate materials. According to the activation mode, the chemically activated aluminosilicates can be termed as alkali-aluminosilicate (AAS) geopolymer or silico-aluminophosphate (SAP) geopolymer, where both of geopolymers need extra promotions (e.g., thermal curing or setting agent) to obtain reasonable engineering properties. The thermal curing is usually inappropriate for *in-situ* applications, while the incorporation of fast-setting chemistries (induced by setting agents) during geopolymerization can easily facilitate an ambient-temperature setting mechanism in geopolymer preparation. Just like the formation of C-(A)-S-H gels in AAS geopolymer, the SAP geopolymer can produce crystalline or amorphous phosphate phases during geopolymerization when metal ions are

incorporated with the aluminosilicates. The different activation modes generate various potential values of these "hybrid" geopolymers in a wide range of research fields. According to the performance, cost and accessibility, the two types of geopolymers are mutually supplemented in terms of function and application fields.

AUTHOR CONTRIBUTIONS

Y-SW collected the data and wrote the paper. YA wrote some parts of the paper besides linguistic and grammar editing. J-GD supervised and finalized the paper.

ACKNOWLEDGMENTS

The authors would like to acknowledge the financial support received from the Hong Kong-Guangzhou Technology and Innovation Partnership Program (Project No. 201807010055), National Science Foundation of China (NSFC) (Projects No. 51638008 and 51478406), HKSAR Innovation Technology Fund (Project code: ITS/009/17) and the Hong Kong Ph.D. Fellowship Scheme (HKPFS) awarded to the second author. The authors would also like to thank Prof. John L. Provis for his advice toward the paper during the study visit of the first author at the University of Sheffield.

REFERENCES

Agarwal, S. (2006). Pozzolanic activity of various siliceous materials. *Cement Concrete Res.* 36, 1735–1739. doi: 10.1016/j.cemconres.2004.06.025

Allahverdi, A., Kani, E. N., Hossain, K., and Lachemi, M. (2015). "Methods to control efflorescence in alkali-activated cement-based materials," in *Handbook of Alkali-Activated Cements, Mortars and Concretes*, eds F. Pacheco-Torgal, J. Labrincha, C. Leonelli, A. Palomo, and P. Chindaprasit (Cambridge, UK: Elsevier), 463–483. doi: 10.1533/9781782422884.3.463

Alrefaei, Y., and Dai, J. G. (2018). Tensile behavior and microstructure of hybrid fiber ambient cured one-part engineered geopolymer composites. *Constr. Build. Mater.* 184, 419–431. doi: 10.1016/j.conbuildmat.2018.07.012

Alrefaei, Y., Wang, Y. S., and Dai, J. G. (2019). The effectiveness of different superplasticizers in ambient cured one-part alkali activated pastes. *Cement Concrete Compos.* 97, 166–174. doi: 10.1016/j.cemconcomp.2018.12.027

Arbi, K., Nedeljkovic, M., Zuo, Y. B., and Ye, G. (2016). A review on the durability of alkali-activated fly ash/slag systems: advances, issues, and perspectives. *Ind. Eng. Chem. Res.* 55, 5439–5453. doi: 10.1021/acs.iecr.6b00559

Atiş, C., Görür, E., Karahan, O., Bilim, C., Ilkentapar, S., and Luga, E. (2015). Very high strength (120 MPa) class F fly ash geopolymer mortar activated at different NaOH amount, heat curing temperature and heat curing duration. *Constr. Build. Mater.* 96, 673–678. doi: 10.1016/j.conbuildmat.2015.08.089

Barsoum, M., Ganguly, A., and Hug, G. (2006). Microstructural evidence of reconstituted limestone blocks in the great Pyramids of Egypt. *J. Am. Ceram. Soc.* 89, 3788–3796. doi: 10.1111/j.1551-2916.2006.01308.x

Bartos, J., Mullins, G., Sikora, F., and Copeland, J. (1991). Availability of phosphorus in the water-insoluble fraction of monoammonium phosphate fertilizers. *Soil Sci. Soc. Am. J.* 55, 539–543. doi: 10.2136/sssaj1991.03615995005500020042x

Bassoli, E., Gatto, A., Iuliano, L., and Grazia Violante, M. (2007). 3D printing technique applied to rapid casting. *Rapid Prototyp. J.* 13, 148–155. doi: 10.1108/13552540710750898

Benavent, V., Steins, P., Sobrados, I., Sanz, J., Lambertin, D., Frizon, F., et al. (2016). Impact of aluminum on the structure of geopolymers from the early stages to consolidated material. *Cement Concrete Res.* 90, 27–35. doi: 10.1016/j.cemconres.2016.09.009

Ben-Nissan, B. (2014). *Advances in Calcium Phosphate Biomaterials*. Berlin: Springer. doi: 10.1007/978-3-642-53980-0

Bentz, D. P., Sato, T., De la Varga, I., and Weiss, W. J. (2012). Fine limestone additions to regulate setting in high volume fly ash mixtures. *Cement Concrete Compos.* 34, 11–17. doi: 10.1016/j.cemconcomp.2011.09.004

Bernal, S., Rodríguez, E., Mejía de Gutiérrez, R., and Provis, J. L. (2015). Performance at high temperature of alkali-activated slag pastes produced with silica fume and rice husk ash based activators. *Mater. Constr.* 65, 1–10. doi: 10.3989/mc.2015.03114

Bernal, S. A., Nicolas, R. S., van Deventer, J. S. J., and Provis, J. L. (2016). Alkali-activated slag cements produced with a blended sodium carbonate/sodium silicate activator. *Adv. Cement Res.* 28, 262–273. doi: 10.1680/jadcr.15.00013

Bernal, S. A., Provis, J. L., and Green, D. J. (2014). Durability of alkali-activated materials: progress and perspectives. *J. Am. Ceram. Soc.* 97, 997–1008. doi: 10.1111/jace.12831

Bernal, S. A., Rodríguez, E. D., de Gutiérrez, R. M., Provis, J. L., and Delvasto, S. (2012). Activation of metakaolin/slag blends using alkaline solutions based on chemically modified silica fume and rice husk ash. *Waste Biomass Valoriz.* 3, 99–108. doi: 10.1007/s12649-011-9093-3

Blissett, R. S., and Rowson, N. A. (2012). A review of the multi-component utilisation of coal fly ash. *Fuel.* 97 1–23. doi: 10.1016/j.fuel.2012.03.024

Brough, A., Katz, A., Sun, G.-K., Struble, L., Kirkpatrick, R., and Young, J. (2001). Adiabatically cured, alkali-activated cement-based wasteforms containing high levels of fly ash: formation of zeolites and Al-substituted CSH. *Cement Concrete Res.* 31, 1437–1447. doi: 10.1016/S0008-8846(01)00589-0

Buchwald, A., Hilbig, H., and Kaps, C. (2007). Alkali-activated metakaolin-slag blends—performance and structure in dependence of their composition. *J. Mater. Sci.* 42, 3024–3032. doi: 10.1007/s10853-006-0525-6

Buchwald, A., Zellmann, H.-D., and Kaps, C. (2011). Condensation of aluminosilicate gels—model system for geopolymer binders. *J. Non-Cryst. Solids*. 357 1376–1382. doi: 10.1016/j.jnoncrysol.2010.12.036

Cao, D., Su, D., Lu, B., and Yang, Y. (2005). Synthesis and structure characterisation of geoplolymeric material based on metakaolin and phosphoric acid. *Guisuanyan Xuebao (J. Chin. Ceram. Soc.)* 33, 1385–1389.

Chancey, R. T., Stutzman, P., Juenger, M. C., and Fowler, D. W. (2010). Comprehensive phase characterization of crystalline and amorphous phases of a class F fly ash. *Cement Concrete Res.* 40, 146–156. doi: 10.1016/j.cemconres.2009.08.029

Chauhan, C., Vyas, P., and Joshi, M. (2011). Growth and characterization of Struvite-K crystals. *Cryst. Res. Technol.* 46, 187–194. doi: 10.1002/crat.201000587

Chauhan, C. K., Joseph, K., Parekh, B., and Joshi, M. (2008). Growth and characterization of struvite crystals. *Ind. J. Pure Appl. Phys.* 46, 507–512. Available online at: http://nopr.niscair.res.in/handle/123456789/1897 (accessed April 29, 2019).

Chauhan, C. K., and Joshi, M. J. (2014). Growth and characterization of struvite-Na crystals. *J. Cryst. Growth*. 401 221–226. doi: 10.1016/j.jcrysgro.2014.01.052

Chia, H. N., and Wu, B. M. (2015). Recent advances in 3D printing of biomaterials. *J. Biol. Eng.* 9:4. doi: 10.1186/s13036-015-0001-4

Chindaprasirt, P., De Silva, P., Sagoe-Crentsil, K., and Hanjitsuwan, S. (2012). Effect of SiO_2 and Al_2O_3 on the setting and hardening of high calcium fly ash-based geopolymer systems. *J. Mater. Sci.* 47, 4876–4883. doi: 10.1007/s10853-012-6353-y

Chindaprasirt, P., Rattanasak, U., and Taebuanhuad, S. (2013a). Role of microwave radiation in curing the fly ash geopolymer. *Adv. Powder Technol.* 24, 703–707. doi: 10.1016/j.apt.2012.12.005

Chindaprasirt, P., Thaiwitcharoen, S., Kaewpirom, S., and Rattanasak, U. (2013b). Controlling ettringite formation in FBC fly ash geopolymer concrete. *Cement Concrete Compos.* 41, 24–28. doi: 10.1016/j.cemconcomp.2013.04.009

Criado, M., Fernández-Jiménez, A., Palomo, A., Sobrados, I., and Sanz, J. (2008). Effect of the SiO_2/Na_2O ratio on the alkali activation of fly ash. Part II: 29Si MAS-NMR Survey. *Microporous Mesoporous Mater.* 109, 525–534. doi: 10.1016/j.micromeso.2007.05.062

Cui, X. M., Liu, L. P., He, Y., Chen, J. Y., and Zhou, J. (2011). A novel aluminosilicate geopolymer material with low dielectric loss. *Mater. Chem. Phys.* 130, 1–4. doi: 10.1016/j.matchemphys.2011.06.039

Cui, X. M., Zheng, G. J., Han, Y. C., Su, F., and Zhou, J. (2008). A study on electrical conductivity of chemosynthetic Al_2O_3-$2SiO_2$ geoploymer materials. *J. Power Sourc.* 184, 652–656. doi: 10.1016/j.jpowsour.2008.03.021

Davidovits, J. (2011). *Geopolymer Chemistry and Applications, 3rd Edn*. Saint-Quentin: Geopolymer Institute.

De Jong, B., Schramm, C. M., and Parziale, V. E. (1983). Polymerization of silicate and aluminate tetrahedra in glasses, melts, and aqueous solutions—IV. Aluminum coordination in glasses and aqueous solutions and comments on the aluminum avoidance principle. *Geochim. Cosmochim. Acta* 47, 1223–1236. doi: 10.1016/0016-7037(83)90064-9

De Rojas, M. S., and Frías, M. (1996). The pozzolanic activity of different materials, its influence on the hydration heat in mortars. *Cement Concrete Res.* 26, 203–213. doi: 10.1016/0008-8846(95)00200-6

Ding, Y., Dai, J. G., and Shi, C. J. (2016). Mechanical properties of alkali-activated concrete: A state-of-the-art review. *Constr. Build. Mater.* 127, 68–79. doi: 10.1016/j.conbuildmat.2016.09.121

Ding, Y., Dai, J. G., and Shi, C. J. (2018). Fracture properties of alkali-activated slag and ordinary Portland cement concrete and mortar. *Constr. Build. Mater.* 165, 310–320. doi: 10.1016/j.conbuildmat.2017.12.202

Ding, Z., Dong, B., Xing, F., Han, N., and Li, Z. (2012). Cementing mechanism of potassium phosphate based magnesium phosphate cement. *Ceram. Int.* 38, 6281–6288. doi: 10.1016/j.ceramint.2012.04.083

Douiri, H., Louati, S., Baklouti, S., Arous, M., and Fakhfakh, Z. (2014). Structural, thermal, and dielectric properties of phosphoric acid-based geopolymers with different amounts of H_3PO_4. *Mater. Lett.* 116, 9–12. doi: 10.1016/j.matlet.2013.10.075

Durdzinski, P. T., Dunant, C. F., Haha, M. B., and Scrivener, K. L. (2015). A new quantification method based on SEM-EDS to assess fly ash composition and study the reaction of its individual components in hydrating cement paste. *Cement Concrete Res.* 73, 111–122. doi: 10.1016/j.cemconres.2015.02.008

Duxson, P., Fernández-Jiménez, A., Provis, J. L., Lukey, G. C., Palomo, A., and van Deventer, J. S. J. (2006). Geopolymer technology: the current state of the art. *J. Mater. Sci.* 42, 2917–2933. doi: 10.1007/s10853-006-0637-z

Duxson, P., and Provis, J. L. (2008). Designing precursors for geopolymer cements. *J. Am. Ceram. Soc.* 91, 3864–3869. doi: 10.1111/j.1551-2916.2008.02787.x

Duxson, P., Provis, J. L., Lukey, G. C., and Van Deventer, J. S. (2007). The role of inorganic polymer technology in the development of 'green concrete'. *Cement Concrete Res.* 37, 1590–1597. doi: 10.1016/j.cemconres.2007.08.018

Fawer, M., Concannon, M., and Rieber, W. (1999). Life cycle inventories for the production of sodium silicates. *Int. J. Life Cycle Assess.* 4:207. doi: 10.1007/BF02979498

Feng, G., Cheng, P., Yan, W., Boronat, M., Li, X., Su, J. H., et al. (2016). Accelerated crystallization of zeolites via hydroxyl free radicals. *Science* 351, 1188–1191. doi: 10.1126/science.aaf1559

Fernández-Jiménez, A., Palomo, A., and Criado, M. (2005). Microstructure development of alkali-activated fly ash cement: a descriptive model. *Cement Concrete Res.* 35, 1204–1209. doi: 10.1016/j.cemconres.2004.08.021

Fernández-Jiménez, A., Palomo, A., Sobrados, I., and Sanz, J. (2006). The role played by the reactive alumina content in the alkaline activation of fly ashes. *Microporous Mesoporous Mater.* 91, 111–119. doi: 10.1016/j.micromeso.2005.11.015

Finch, T., and Sharp, J. H. (1989). Chemical reactions between magnesia and aluminium orthophosphate to form magnesia-phosphate cements. *J. Mater. Sci.* 24, 4379–4386. doi: 10.1007/BF00544516

Garcia-Lodeiro, I., Palomo, A., and Fernández-Jiménez, A. (2015). "An overview of the chemistry of alkali-activated cement-based binders," in *Handbook of Alkali-Activated Cements, Mortars and Concretes*, eds F. Pacheco-Torgal, J. Labrincha, C. Leonelli, A. Palomo, and P. Chindaprasit (Cambridge, UK: Elsevier), 19–47. doi: 10.1533/9781782422884.1.19

Gardner, L. J., Bernal, S. A., Walling, S. A., Corkhill, C. L., Provis, J. L., and Hyatt, N. C. (2015). Characterisation of magnesium potassium phosphate cements blended with fly ash and ground granulated blast furnace slag. *Cement Concrete Res.* 74, 78–87. doi: 10.1016/j.cemconres.2015.01.015

Giocondi, J. L., El-Dasher, B. S., Nancollas, G. H., and Orme, C. A. (2010). Molecular mechanisms of crystallization impacting calcium phosphate cements. *Philos. Trans. A Math. Phys. Eng. Sci.* 368, 1937–1961. doi: 10.1098/rsta.2010.0006

Guerrieri, M., and Sanjayan, J. G. (2010). Behavior of combined fly ash/slag-based geopolymers when exposed to high temperatures. *Fire Mater. Int. J.* 34, 163–175. doi: 10.1002/fam.1014

Guo, C. M., Wang, K. T., Liu, M. Y., Li, X. H., and Cui, X. M. (2016). Preparation and characterization of acid-based geopolymer using metakaolin and disused polishing liquid. *Ceram. Int.* 42, 9287–9291. doi: 10.1016/j.ceramint.2016.02.073

Guvendiren, M., Molde, J., Soares, R. M., and Kohn, J. (2016). Designing biomaterials for 3D printing. *ACS Biomater. Sci. Eng.* 2, 1679–1693. doi: 10.1021/acsbiomaterials.6b00121

Habert, G., d'Espinose de Lacaillerie, J. B., and Roussel, N. (2011). An environmental evaluation of geopolymer based concrete production: reviewing current research trends. *J. Cleaner Prod.* 19, 1229–1238. doi: 10.1016/j.jclepro.2011.03.012

Habert, G., and Ouellet-Plamondon, C. (2016). Recent update on the environmental impact of geopolymers. *RILEM Technol. Lett.* 1, 17–23. doi: 10.21809/rilemtechlett.2016.6

Handoo, S., Agarwal, S., and Agarwal, S. (2002). Physicochemical, mineralogical, and morphological characteristics of concrete exposed to elevated temperatures. *Cement Concrete Res.* 32, 1009–1018. doi: 10.1016/S0008-8846(01)00736-0

He, Y., Cui, X. M., Liu, X. D., Wang, Y. P., Zhang, J., and Liu, K. (2013). Preparation of self-supporting NaA zeolite membranes using geopolymers. *J. Membr. Sci.* 447, 66–72. doi: 10.1016/j.memsci.2013.07.027

He, Y., Liu, L., He, L., and Cui, X. (2016). Characterization of chemosynthetic H_3PO_4-Al_2O_3-$2SiO_2$ geopolymers. *Ceram. Int.* 42, 10908–10912. doi: 10.1016/j.ceramint.2016.03.224

Hill, R., and Howard, C. (1987). Quantitative phase analysis from neutron powder diffraction data using the Rietveld method. *J. Appl. Crystal.* 20, 467–474. doi: 10.1107/S0021889887086199

Inzana, J. A., Olvera, D., Fuller, S. M., Kelly, J. P., Graeve, O. A., Schwarz, E. M., et al. (2014). 3D printing of composite calcium phosphate and collagen scaffolds for bone regeneration. *Biomaterials* 35, 4026–4034. doi: 10.1016/j.biomaterials.2014.01.064

Ismail, I., Bernal, S. A., Provis, J. L., San Nicolas, R., Hamdan, S., and van Deventer, J. S. J. (2014). Modification of phase evolution in alkali-activated blast furnace slag by the incorporation of fly ash. *Cement Concrete Compos.* 45, 125–135. doi: 10.1016/j.cemconcomp.2013.09.006

ISO (2006). *Environmental Management: Life Cycle Assessment; Principles and Framework*. Geneva: International Organization for Standardization.

Jelinski, L. W., Graedel, T. E., Laudise, R. A., McCall, D. W., and Patel, C. K. (1992). Industrial ecology: concepts and approaches. *Proc. Natl. Acad. Sci. U.S.A.* 89, 793–797. doi: 10.1073/pnas.89.3.793

Katsiki, A. (2019). Aluminosilicate phosphate cements–a critical review. *Adv. Appl. Ceram.* doi: 10.1080/17436753.2019.1572339. [Epub ahead of print].

Khabbouchi, M., Hosni, K., Mezni, M., Zanelli, C., Doggy, M., Dondi, M., et al. (2017). Interaction of metakaolin-phosphoric acid and their structural evolution at high temperature. *Appl. Clay Sci.* 146, 510–516. doi: 10.1016/j.clay.2017.07.006

Khale, D., and Chaudhary, R. (2007). Mechanism of geopolymerization and factors influencing its development: a review. *J. Mater. Sci.* 42, 729–746. doi: 10.1007/s10853-006-0401-4

Kingery, W. D. (1950). Fundamental study of phosphate bonding in refractories: I, literature review. *J. Am. Ceram. Soc.* 33, 239–241. doi: 10.1111/j.1151-2916.1950.tb14171.x

Kingery, W. D. (1952). Fundamental study of phosphate bonding in refractories: IV, mortars bonded with monoaluminum and monomagnesium phosphate. *J. Am. Ceram. Soc.* 35, 61–63. doi: 10.1111/j.1151-2916.1952.tb13069.x

Kongshaug, G. (1998). "Energy consumption and greenhouse gas emissions in fertilizer production," in *IFA Technical Conference* (Marrakech: I International Fertilizer Industry Association).

Krizan, D., and Zivanovic, B. (2002). Effects of dosage and modulus of water glass on early hydration of alkali–slag cements. *Cement Concrete Res.* 32, 1181–1188. doi: 10.1016/S0008-8846(01)00717-7

Kühl, H. (1908). *Slag Cement and Process of Making the Same*. US Patent. No. 900939.

Kumar, S., and Kumar, R. (2011). Mechanical activation of fly ash: Effect on reaction, structure and properties of resulting geopolymer. *Ceram. Int.* 37, 533–541. doi: 10.1016/j.ceramint.2010.09.038

Li, C., Sun, H., and Li, L. (2010). A review: the comparison between alkali-activated slag (Si+ Ca) and metakaolin (Si+ Al) cements. *Cement Concrete Res.* 40, 1341–1349. doi: 10.1016/j.cemconres.2010.03.020

Lim, S., Buswell, R. A., Le, T. T., Austin, S. A., Gibb, A. G. F., and Thorpe, T. (2012). Developments in construction-scale additive manufacturing processes. *Autom. Constr.* 21, 262–268. doi: 10.1016/j.autcon.2011.06.010

Liu, L. P., Cui, X. M., He, Y., Liu, S. D., and Gong, S. Y. (2012). The phase evolution of phosphoric acid-based geopolymers at elevated temperatures. *Mater. Lett.* 66, 10–12. doi: 10.1016/j.matlet.2011.08.043

Liu, L. P., Cui, X. M., Qiu, S. H., Yu, J. L., and Zhang, L. (2010). Preparation of phosphoric acid-based porous geopolymers. *Appl. Clay Sci.* 50, 600–603. doi: 10.1016/j.clay.2010.10.004

Lodeiro, I. G., Fernández-Jiménez, A., Palomo, A., and Macphee, D. E. (2010). Effect on fresh CSH gels of the simultaneous addition of alkali and aluminium. *Cement Concrete Res.* 40, 27–32. doi: 10.1016/j.cemconres.2009.08.004

Lothenbach, B., Scrivener, K., and Hooton, R. (2011). Supplementary cementitious materials. *Cement Concrete Res.* 41, 1244–1256. doi: 10.1016/j.cemconres.2010.12.001

Louati, S., Baklouti, S., and Samet, B., (2016). Acid based geopolymerization kinetics: effect of clay particle size. *Appl. Clay Sci.* 132–133, 571–578. doi: 10.1016/j.clay.2016.08.007

Louati, S., Hajjaji, W., Baklouti, S., and Samet, B., (2014). Structure and properties of new eco-material obtained by phosphoric acid attack of natural tunisian clay. *Appl. Clay Sci.* 101, 60–67. doi: 10.1016/j.clay.2014.07.015

Luna Galiano, Y., Fernández Pereira, C., and Vale, J. (2011). Stabilization/solidification of a municipal solid waste incineration residue using fly ash-based geopolymers. *J. Hazard. Mater.* 185, 373–381. doi: 10.1016/j.jhazmat.2010.08.127

Luukkonen, T., Heponiemi, A., Runtti, H., Pesonen, J., Yliniemi, J., and Lassi, U., (2019). Application of alkali-activated materials for water and wastewater treatment: a review. *Rev. Environ. Sci. BioTechnol.* doi: 10.1007/s11157-019-09494-0. [Epub ahead of print].

Luxán, M. P., Madruga, F., and Saavedra, J. (1989). Rapid evaluation of pozzolanic activity of natural products by conductivity measurement. *Cement Concrete Res.* 19, 63–68. doi: 10.1016/0008-8846(89)90066-5

Luz, A. P., Gomes, D. T., and Pandolfelli, V. C. (2015). High-alumina phosphate-bonded refractory castables: Al(OH)3 sources and their effects. *Ceram. Int.* 41, 9041–9050. doi: 10.1016/j.ceramint.2015.03.276

Ma, H., Xu, B., and Li, Z. (2014). Magnesium potassium phosphate cement paste: degree of reaction, porosity and pore structure. *Cement Concrete Res.* 65, 96–104. doi: 10.1016/j.cemconres.2014.07.012

MacKenzie, K. (2015). "Innovative applications of inorganic polymers (geopolymers)," in *Handbook of Alkali-Activated Cements, Mortars and Concretes*, eds F. Pacheco-Torgal, J. Labrincha, C. Leonelli, A. Palomo, and P. Chindaprasit (Cambridge, UK: Elsevier), 777–805. doi: 10.1533/9781782422884.5.777

Mackenzie, K. J., Brew, D., Fletcher, R., Nicholson, C. L., Vagana, R., and Schmucker, M. (2005). "Towards an understanding of the synthesis mechanisms of geopolymer materials," in *Proceedings of the World Geopolymer , Geopolymer Green Chemestry Sustainable Development Solutions* (Saint-Quentin), 41–44.

MacKenzie, K. J., Rahner, N., Smith, M. E., and Wong, A. (2010). Calcium-containing inorganic polymers as potential bioactive materials. *J. Mat. Sci.* 45:999. doi: 10.1007/s10853-009-4031-5

MacKenzie, K. J., Smith, M. E., Wong, A., Hanna, J. V., Barry, B., and Barsoum, M. W. (2011). Were the casing stones of Senefru's Bent Pyramid in Dahshour cast or carved?: multinuclear NMR evidence. *Mater. Lett.* 65, 350–352. doi: 10.1016/j.matlet.2010.10.035

Mathivet, V., Jouin, J., Gharzouni, A., Sobrados, I., Celerier, H., Rossignol, S., et al. (2019). Acid-based geopolymers: understanding of the structural evolutions during consolidation and after thermal treatments. *J. Non Cryst. Solids* 512, 90–97. doi: 10.1016/j.jnoncrysol.2019.02.025

Morrissey, A. J., and Browne, J. (2004). Waste management models and their application to sustainable waste management. *Waste Manage.* 24, 297–308. doi: 10.1016/j.wasman.2003.09.005

Najafi Kani, E., Allahverdi, A., and Provis, J. L. (2012). Efflorescence control in geopolymer binders based on natural pozzolan. *Cement Concrete Compos.* 34, 25–33. doi: 10.1016/j.cemconcomp.2011.07.007

Nath, S., and Kumar, S. (2013). Influence of iron making slags on strength and microstructure of fly ash geopolymer. *Constr. Build. Mater.* 38, 924–930. doi: 10.1016/j.conbuildmat.2012.09.070

Nazari, A., Bagheri, A., and Riahi, S. (2011). Properties of geopolymer with seeded fly ash and rice husk bark ash. *Mater. Sci. Eng. A* 528, 7395–7401. doi: 10.1016/j.msea.2011.06.027

Nematollahi, B., and Sanjayan, J. (2014). Effect of different superplasticizers and activator combinations on workability and strength of fly ash based geopolymer. *Mater. Des.* 57, 667–672. doi: 10.1016/j.matdes.2014.01.064

Neville, A. M. (2011). *Properties of Concrete, 4th Edn*. London: Pearson Education Limited.

Nicholson, C. L., Murray, B. J., Fletcher, R. A., Brew, D., Mackenzie, K. J., and Schmücker, M. (2005). "Novel geopolymer materials containing borate structural units," in *World Congress Geopolymer* (Saint-Quentin), 31–33.

Ouellet-Plamondon, C., and Habert, G. (2015). "Life cycle assessment (LCA) of alkali-activated cements and concretes," in *Handbook of Alkali-Activated Cements, Mortars and Concretes*, eds F. Pacheco-Torgal, J. Labrincha, C. Leonelli, A. Palomo, and P. Chindaprasit (Cambridge, UK: Elsevier), 663–686. doi: 10.1533/9781782422884.5.663

Pacheco-Torgal, F. (2015). "Introduction to handbook of alkali-activated cements, mortars and concretes," in *Handbook of Alkali-Activated Cements, Mortars and Concretes*, eds F. Pacheco-Torgal, J. Labrincha, C. Leonelli, A. Palomo, and P. Chindaprasit (Cambridge, UK: Elsevier), 1–16. doi: 10.1533/9781782422884.1

Pacheco-Torgal, F., Castro-Gomes, J., and Jalali, S. (2008). Alkali-activated binders: a review - Part 1. Historical background, terminology, reaction mechanisms and hydration products. *Construct. Build. Mater.* 22, 1305–1314. doi: 10.1016/j.conbuildmat.2007.10.015

Passuello, A., Rodriguez, E. D., Hirt, E., Longhi, M., Bernal, S. A., Provis, J. L., et al. (2017). Evaluation of the potential improvement in the environmental footprint of geopolymers using waste-derived activators. *J. Clean. Prod.* 166, 680–689. doi: 10.1016/j.jclepro.2017.08.007

Perera, D. S., Hanna, J. V., Davis, J., Blackford, M. G., Latella, B. A., Sasaki, Y., et al. (2008). Relative strengths of phosphoric acid-reacted and alkali-reacted metakaolin materials. *J.Mater. Sci.* 43, 6562–6566. doi: 10.1007/s10853-008-2913-6

Provis, J. L. (2013). Geopolymers and other alkali activated materials: why, how, and what? *Mater. Struct.* 47, 11–25. doi: 10.1617/s11527-013-0211-5

Provis, J. L., and Bernal, S. A. (2014). Geopolymers and related alkali-activated materials. *Annu. Rev. Mater. Res.* 44, 299–327. doi: 10.1146/annurev-matsci-070813-113515

Provis, J. L., Palomo, A., and Shi, C. (2015). Advances in understanding alkali-activated materials. *Cement Concrete Res.* 78, 110–125. doi: 10.1016/j.cemconres.2015.04.013

Provis, J. L., and Van Deventer, J. S. (2013). *Alkali Activated Materials: State-of-the-Art Report, RILEM TC 224-AAM*. Dordrecht: Springer Science Business Media. doi: 10.1007/978-94-007-7672-2

Rao, F., and Liu, Q. (2015). Geopolymerization and its potential application in mine tailings consolidation: a review. *Miner. Process. Extract. Metall. Rev.* 36, 399–409. doi: 10.1080/08827508.2015.1055625

Rashad, A. M., Zeedan, S. R., and Hassan, H. A. (2012). A preliminary study of autoclaved alkali-activated slag blended with quartz powder. *Construct. Build. Mater.* 33, 70–77. doi: 10.1016/j.conbuildmat.2011.12.104

Raven, K., and Loeppert, R. (1996). Microwave digestion of fertilizers and soil amendments. *Commun. Soil Sci. Plant Anal.* 27, 2947–2971. doi: 10.1080/00103629609369754

Reddy, M. S., Dinakar, P., and Rao, B. H. (2016). A review of the influence of source material's oxide composition on the compressive

strength of geopolymer concrete. *Microporous Mesoporous Mater.* 234, 12–23. doi: 10.1016/j.micromeso.2016.07.005

Rengier, F., Mehndiratta, A., Von Tengg-Kobligk, H., Zechmann, C. M., Unterhinninghofen, R., Kauczor, H. U., et al. (2010). 3D printing based on imaging data: review of medical applications. *Int. J. Comput. Assist. Radiol. Surg.* 5, 335–341. doi: 10.1007/s11548-010-0476-x

Richardson, I., Brough, A., Groves, G., and Dobson, C. (1994). The characterization of hardened alkali-activated blast-furnace slag pastes and the nature of the calcium silicate hydrate (CSH) phase. *Cement Concrete Res.* 24, 813–829. doi: 10.1016/0008-8846(94)90002-7

Richardson, I. G., Brough, A. R., Brydson, R., Groves, G. W., and Dobson, C. M. (1993). Location of aluminum in substituted calcium silicate hydrate (C-S-H) gels as determined by 29Si and 27Al NMR and EELS. *J. Am. Ceram. Soc.* 76, 2285–2288. doi: 10.1111/j.1151-2916.1993.tb07765.x

Roy, D. M. (1987). New strong cement materials: chemically bonded ceramics. *Science* 235, 651–658. doi: 10.1126/science.235.4789.651

Saxena, S., and D'Souza, S. (2006). Heavy metal pollution abatement using rock phosphate mineral. *Environ. Int.* 32, 199–202. doi: 10.1016/j.envint.2005.08.011$$$

Scarlett, N. V. Y., and Madsen, I. C. (2012). Quantification of phases with partial or no known crystal structures. *Powder Diffract.* 21, 278–284. doi: 10.1154/1.2362855

Shang, J., Dai, J. G., Zhao, T. J., Guo, S. Y., Zhang, P., and Mu, B. (2018). Alternation of traditional cement mortars using fly ash-based geopolymer mortars modified by slag. *J. Clean. Prod.* 203, 746–756. doi: 10.1016/j.jclepro.2018.08.255

Shi, C., Jiménez, A. F., and Palomo, A. (2011). New cements for the 21st century: the pursuit of an alternative to Portland cement. *Cement Concrete Res.* 41, 750–763. doi: 10.1016/j.cemconres.2011.03.016

Shi, C., and Qian, J. (2000). High performance cementing materials from industrial slags-a review. *Resour. Conserv. Recycl.* 29, 195–207. doi: 10.1016/S0921-3449(99)00060-9

Škvára, F., Kopecký, L., Myšková, L., Šmilauer, V., Alberovska, L., and Vinšová, L. (2009). Aluminosilicate polymers-influence of elevated temperatures, efflorescence. *Ceram.-Silikáty* 53, 276–282. Available online at: http://www.ceramics-silikaty.cz/2009/pdf/2009_04_276.pdf (accessed April 29, 2019).

Sperinck, S., Raiteri, P., Marks, N., and Wright, K. (2011). Dehydroxylation of kaolinite to metakaolin-a molecular dynamics study. *J. Mater. Chem.* 21, 2118–2125. doi: 10.1039/C0JM01748E

Tailby, J., and MacKenzie, K. J. (2010). Structure and mechanical properties of aluminosilicate geopolymer composites with Portland cement and its constituent minerals. *Cement Concrete Res.* 40, 787–794. doi: 10.1016/j.cemconres.2009.12.003

Tamimi, F., Sheikh, Z., and Barralet, J. (2012). Dicalcium phosphate cements: brushite and monetite. *Acta Biomater.* 8, 474–487. doi: 10.1016/j.actbio.2011.08.005

Taylor, H. F. (1997). *Cement Chemistry*. New York, NY: Thomas Telford. doi: 10.1680/cc.25929

Temuujin, J., Minjigmaa, A., Davaabal, B., Bayarzul, U., Ankhtuya, A., Jadambaa, T., et al. (2014). Utilization of radioactive high-calcium Mongolian flyash for the preparation of alkali-activated geopolymers for safe use as construction materials. *Ceram. Int.* 40, 16475–16483. doi: 10.1016/j.ceramint.2014.07.157

Toniolo, N., and Boccaccini, A. R. (2017). Fly ash-based geopolymers containing added silicate waste. A review. *Ceram. Int.* 43, 14545–14551. doi: 10.1016/j.ceramint.2017.07.221

Utneja, S., Nawal, R. R., Talwar, S., and Verma, M. (2015). Current perspectives of bio-ceramic technology in endodontics: calcium enriched mixture cement-review of its composition, properties and applications. *Restor. Dent. Endod.* 40, 1–13. doi: 10.5395/rde.2015.40.1.1

Van Jaarsveld, J., Van Deventer, J., and Lorenzen, L. (1997). The potential use of geopolymeric materials to immobilise toxic metals. *Miner. Eng.* 10, 659–669. doi: 10.1016/S0892-6875(97)00046-0

Vassilev, S. V., and Vassileva, C. G. (2005). Methods for characterization of composition of fly ashes from coal-fired power stations: a critical overview. *Energy Fuels* 19, 1084–1098. doi: 10.1021/ef049694d

Wagh, A. S. (2004). "Chemically bonded phosphate ceramics-a novel class of geopolymers," in *Advances in Ceramic Matrix Composites X: Proceedings of the 106th Annual Meeting of the American Ceramic Society* (Indianapolis, IN), 107. doi: 10.1002/9781118408353.ch10

Wagh, A. S. (2016). *Chemically Bonded Phosphate Ceramics: Twenty-First Century Materials With Diverse Applications*. Oxford, UK: Elsevier. doi: 10.1016/B978-0-08-100380-0.00002-6

Wagh, A. S., and Jeong, S. Y. (2003a). Chemically bonded phosphate ceramics: I, a dissolution model of formation. *J. Am. Ceram. Soc.* 86, 1838–1844. doi: 10.1111/j.1151-2916.2003.tb03569.x

Wagh, A. S., and Jeong, S. Y. (2003b). Chemically bonded phosphate ceramics: III, reduction mechanism and its application to iron phosphate ceramics. *J. Am. Ceram. Soc.* 86, 1850–1855. doi: 10.1111/j.1151-2916.2003.tb03571.x

Walkley, B., Nicolas, R. S., Sani, M. A., Bernal, S. A., van Deventer, J. S. J., and Provis, J. L. (2017). Structural evolution of synthetic alkali-activated CaO-MgO-Na2O-Al2O3-SiO2 materials is influenced by Mg content. *Cement Concrete Res.* 99, 155–171. doi: 10.1016/j.cemconres.2017.05.006

Walling, S. A., and Provis, J. L. (2016). Magnesia-based cements: a journey of 150 years, and cements for the future? *Chem. Rev.* 116, 4170–4204. doi: 10.1021/acs.chemrev.5b00463

Wang, S. D., and Scrivener, K. L. (1995). Hydration products of alkali activated slag cement. *Cement Concrete Res.* 25, 561–571. doi: 10.1016/0008-8846(95)00045-E

Wang, S. D., Scrivener, K. L., and Pratt, P. (1994). Factors affecting the strength of alkali-activated slag. *Cement Concrete Res.* 24, 1033–1043. doi: 10.1016/0008-8846(94)90026-4

Wang, W. C., Wang, H.-Y., and Tsai, H.-C. (2016). Study on engineering properties of alkali-activated ladle furnace slag geopolymer. *Constr. Build. Mater.* 123, 800–805. doi: 10.1016/j.conbuildmat.2016.07.068

Wang, Y. S. (2018). *Influence of Metal Ions on Formation of Silico-Aluminophosphate Geopolymer*. Kowloon: The Hong Kong Polytechnic University.

Wang, Y. S., and Dai, J. G. (2017). Use of magnesia sand for optimal design of high performance magnesium potassium phosphate cement mortar. *Constr. Build. Mater.* 153, 385–392. doi: 10.1016/j.conbuildmat.2017.07.099

Wang, Y. S., Dai, J. G., Ding, Z., and Xu, W.-T. (2017). Phosphate-based geopolymer: formation mechanism and thermal stability. *Mater. Lett.* 190, 209–212. doi: 10.1016/j.matlet.2017.01.022

Wang, Y. S., Dai, J. G., Wang, L., Tsang, D. C. W., and Poon, C. S. (2018a). Influence of lead on stabilization/solidification by ordinary Portland cement and magnesium phosphate cement. *Chemosphere* 190, 90–96. doi: 10.1016/j.chemosphere.2017.09.114

Wang, Y. S., Provis, J. L., and Dai, J. G. (2018b). Role of soluble aluminum species in the activating solution for synthesis of silico-aluminophosphate geopolymers. *Cement Concrete Compos.* 93, 186–195. doi: 10.1016/j.cemconcomp.2018.07.011

Wilson, A. D., and Nicholson, J. W. (2005). *Acid-base Cements: Their Biomedical and Industrial Applications*. Cambridge, UK: Cambridge University Press.

Wood, S., and Cowie, A. (2004). *A Review of Greenhouse Gas Emission Factors for Fertiliser Production*. IEA Bioenergy Task.

Xia, M., and Sanjayan, J. (2016). Method of formulating geopolymer for 3D printing for construction applications. *Mater. Des.* 110, 382–390. doi: 10.1016/j.matdes.2016.07.136

Xu, G., and Shi, X. (2018). Characteristics and applications of fly ash as a sustainable construction material: a state-of-the-art review. *Resour. Conserv. Recycl.* 136, 95–109. doi: 10.1016/j.resconrec.2018.04.010

Xu, G., Zhong, J., and Shi, X. (2018). Influence of graphene oxide in a chemically activated fly ash. *Fuel* 226, 644–657. doi: 10.1016/j.fuel.2018.04.033

Xu, H., Van Deventer, J., and Lukey, G. (2001). Effect of alkali metals on the preferential geopolymerization of stilbite/kaolinite mixtures. *Ind. Eng. Chem. Res.* 40, 3749–3756. doi: 10.1021/ie010042b

Xu, H. H., and Simon, C. G. Jr. (2005). Fast setting calcium phosphate-chitosan scaffold: mechanical properties and biocompatibility. *Biomaterials* 26, 1337–1348. doi: 10.1016/j.biomaterials.2004.04.043

Xu, W., Dai, J.-G., Ding, Z., and Wang, Y. (2017). Polyphosphate-modified calcium aluminate cement under normal and elevated temperatures: Phase evolution, microstructure, and mechanical properties. *Ceram. Int.* 43, 15525–15536. doi: 10.1016/j.ceramint.2017.08.102

Xue, X., Liu, Y. L., Dai, J. G., Poon, C. S., Zhang, W. D., and Zhang, P. (2018). Inhibiting efflorescence formation on fly ash-based geopolymer via silane surface modification. *Cement Concrete Compos.* 94, 43–52. doi: 10.1016/j.cemconcomp.2018.08.013

Xue, Z., Zhang, H., Jin, A., Ye, J., Ren, L., Ao, J., et al. (2012). Correlation between degradation and compressive strength of an injectable macroporous calcium phosphate cement. *J. Alloys Compd.* 520, 220–225. doi: 10.1016/j.jallcom.2012.01.022

Yao, Z. T., Ji, X. S., Sarker, P. K., Tang, J. H., Ge, L. Q., Xia, M. S., et al. (2015). A comprehensive review on the applications of coal fly ash. *Earth-Sci. Rev.* 141, 105–121. doi: 10.1016/j.earscirev.2014.11.016

Zhang, J., Liu, W., Schnitzler, V., Tancret, F., and Bouler, J. M. (2014). Calcium phosphate cements for bone substitution: chemistry, handling and mechanical properties. *Acta Biomater.* 10, 1035–1049. doi: 10.1016/j.actbio.2013.11.001

Zhang, Z., Provis, J. L., Reid, A., and Wang, H. (2014). Fly ash-based geopolymers: the relationship between composition, pore structure and efflorescence. *Cement Concrete Res.* 64, 30–41. doi: 10.1016/j.cemconres.2014.06.004

Zhang, Z., Provis, J. L., Zou, J., Reid, A., and Wang, H. (2016). Toward an indexing approach to evaluate fly ashes for geopolymer manufacture. *Cement Concrete Res.* 85, 163–173. doi: 10.1016/j.cemconres.2016.04.007

Zhong, J., Zhou, G. X., He, P. G., Yang, Z. H., and Jia, D. C. (2017). 3D printing strong and conductive geo-polymer nanocomposite structures modified by graphene oxide. *Carbon* 117, 421–426. doi: 10.1016/j.carbon.2017.02.102

Conflict of Interest Statement: The authors declare that the research was conducted in the absence of any commercial or financial relationships that could be construed as a potential conflict of interest.

frontiers in Materials

ORIGINAL RESEARCH
published: 22 May 2019
doi: 10.3389/fmats.2019.00092

Waste Stream Porous Alkali Activated Materials for High Temperature Application

Diana Bajare, Laura Vitola, Laura Dembovska and Girts Bumanis*

Department of Building Materials and Products, Riga Technical University, Riga, Latvia

The growing interest of using industrial waste as recycled raw materials for the production of new, innovative materials is associated with effective use of natural resources and circular (zero-waste) economy. The research object is waste stream materials coming from chemical and processing industries, such as aluminum scrap recycling waste, chamotte-like precursor, firebricks sawing residues, and their use in production of high-temperature resistant, porous insulation materials by using alkali activation technique with 6 M NaOH solution. Adding aluminum scrap recycling waste to the composition of the tested alkali activated materials (AAM) contributed to the porous structure of the material with the pore size ranging from 1,000 to 5,000 μm (detected by Micro-XCT, SEM). Lightweight (350–850 kg/m^3) and heat-resistant (up to 1,000°C) AAM with compressive strength from 1.0 to 3.0 MPa was obtained. The mineralogical composition of the obtained AAM was detected (XRD) and the heat resistant minerals in the structure of AAM were identified. It was concluded that the increased amount of Al_2O_3 in the raw material composition resulted in improved thermal stability of the AAM. In case where SiO_2/Al_2O_3 ratio is <2, the formation of high-temperature resistant minerals, such as carnegeite and nepheline, was observed. The obtained AAM could resist up to 8 thermal shock cycles and it could be easily adapted to the industrial production and application such as thermal insulation layer in laboratory furnaces.

Keywords: alkali activated material, porous materials, heat resistance, application in high temperature, aluminum scrap recycling waste

OPEN ACCESS

Edited by:
Maria Juenger,
University of Texas at Austin,
United States

Reviewed by:
Sriramya Duddukuri Nair,
Cornell University, United States
Ru Mu,
Hebei University of Technology, China

****Correspondence:***
Laura Vitola
laura.vitola_1@rtu.lv

Specialty section:
This article was submitted to Structural Materials, a section of the journal Frontiers in Materials

Received: *18 January 2019*
Accepted: *12 April 2019*
Published: *22 May 2019*

Citation:
Bajare D, Vitola L, Dembovska L and Bumanis G (2019) Waste Stream Porous Alkali Activated Materials for High Temperature Application. Front. Mater. 6:92. doi: 10.3389/fmats.2019.00092

HIGHLIGHTS

- For the first time alkali activated materials were created on the chamotte-like and firebricks sawing residue precursors.
- Highly porous (up to 80 vol.%) structure of alkali activated materials were obtained by aluminum scrap recycling waste.
- For the first time the porous alkali activated materials was evaluated for high temperature application.
- The porous alkali activated materials manufacture is simple, sustainable, and based on mostly waste stream materials.
- Firebrick waste increased the temperature cycling performance of the material and proved to be highly suitable for industrial application.

INTRODUCTION

Low calcium alkali activated materials (AAM) or "Geopolymers" in some cases are the terms used to describe aluminosilicate-based inorganic polymers produced by mixing pozzolanic compounds or aluminosilicate source precursors and highly alkaline solutions (Davidovits, 1991). Production of AAM provide an opportunity to convert a variety of waste stream materials and by-products into useful, high value materials (Singh et al., 2015). Many factors can contribute to the alkali activation reaction mechanism and the properties of the final products, including (but not limited to) the aluminosilicate source precursors (Bumanis et al., 2017), the type of activator solution (Criado et al., 2007), the calcium content in the raw material mixture composition (Canfield et al., 2014), and the mixing and curing conditions (Moukannaa et al., 2018) as well as pore forming process (Bajare et al., 2014; Strozi et al., 2014; Seabra et al., 2016). AAM have attracted an increasing interest as fireproof materials associated with circular economy, namely, their production have low energy requirements and the final product is characterized by good mechanical performance, thermal behavior, and durability (Rashad et al., 2016). The existing publications on fire resistance and performance of AAM under high temperature conditions are promising.

The stability at high temperatures of binders made by the alkaline activation of aluminosilicate precursors is clearly distinct from the behavior observed in Portland cement at high temperatures (Martin et al., 2015). The shrinkage of AAM up to 600°C temperature occurs due to evaporation of the adsorbed and weakly bound water. Several reports indicate that the strength of AAM increases by the treatment at temperature between 600 and 800°C as densification occurs on the contrary with Portland cement-based materials (Fernández-Jiménez et al., 2010). In many cases melting process of AMM starts up to the temperature of 1,100°C (Kim and Kim, 2017). The resistance to high temperatures of AAM strongly depends from the composition of raw materials, i.e., Dupuy et al. has reported that all argillite-based AAM samples show low resistance to thermal shock (800°C, 10 min) and strength decreased up to 10 times (Dupuy et al., 2018), while other report by K. Hemra and P. Aungkavattana states that thermal shock resistance of metakaolin-based AAM at temperature of 800°C could reach up to 15 cycles (Hemra and Aungkavattana, 2016). In comparison with traditional refractory brick performance these results seems promising as their thermal shock resistance varies from 10 to 30 cycles (Philip, 2014).

One of the basic approaches to improve thermal properties of the AAM is to use fillers based on refractory materials. Bernal et al. reported that thermal behavior of metakaolinbased AAM with ground refractory brick filler (10–15 vol.%) could reduce the volumetric contraction and increase the residual compressive strength up to three times after exposure to high temperature in comparison with the AAM without fillers (Bernal et al., 2012).

Type and concentration of alkali activation solution play a dual role which calls for a certain compromise in the AAM design. On one hand, high alkali content in activation solution (8 to 12 M NaOH solutions) is necessary to accelerate the activation reactions of precursors and to obtain AAM with high initial strength, but at the same time increased concentration of alkalis could act as fluxes at high temperatures. Therefore, the content of alkalis in the alkali activation solution must be limited to generate thermally stable materials (Martin et al., 2015). It has been reported that the alkali concentration in the activation solution could be reduced event to 2 M (Huiskes et al., 2016). The results of previous research show that increasing the SiO_2/Na_2O molar ratio of the activation solution the setting time of AAM mixture could also increase (Tchakoute et al., 2013). It has been reported that in cases, when ratio of SiO_2/Na_2O of activation solution is beyond optimum (>3.0), physical properties of the AAM can draw down quickly—water absorption increases while the bulk density does not change (Lemougna et al., 2011).

The aim of the present study is to assess the thermal stability of chamotte-like precursor based AAM with refractory brick by-product additive in order to achieve high mechanical properties after heat treatment and thermal shock resistance of the obtained material. The study includes development and demonstration of AAM production and application methods.

MATERIALS AND METHODS

Raw Materials

Commercially produced chamotte-like precursor (CH), where 36.9% of particles were with size lower than 45 μm was used in the research (Keramserviss Ltd). According to the XRD analysis CH contains the following minerals: cristobalite (SiO_2), quartz (SiO_2), and mullite ($Al_6Si_2O_{13}$). Also minor amorphous phase as background hump was identified (**Figure 1**).

Firebrick sawing residues (K26) (Morgan Thermal Ceramics Ltd.) is classified as a by-product from the sawing process of insulation material typically used for furnace production. The K26 is aluminosilicate material and its chemical composition is given in **Table 1**. K26 was ground for 30 min by using planetary ball mill Retsch PM 400. 96.3% of the particles were with the size lower than 45 μm. According to the technical data sheet, working temperatures of the K26 range from 1,260 to 1,790°C. The K26 is made from high-purity refractory clay with high amount of Al_2O_3 (up to 60%). According to the XRD analysis, mullite ($Al_6Si_2O_{13}$) and corundum (Al_2O_3) as well as small background hump indicating amorphous phase were identified (**Figure 1**). K26 was considered as additional aluminum silicate source and as filling material which could improve thermal stability of the AAM.

Aluminum scrap recycling waste (ASRW) was received from the aluminum scrap recycling facility (Dilers Ltd). ASRW is the final waste, which is obtained from black dross in aluminum recovery process. ASRW was ground for 30 min by using planetary ball mill Retsch PM 400. Chemical composition of ASRW is given in **Table 1**; main oxides are Al_2O_3 (63.2 wt.%), SiO_2 (7.9 wt.%), CaO (2.6 wt.%), and $Na_2O+ K_2O$ (7.7 wt.%). According to the XRD analysis, the ASRW contains quartz (SiO_2), spinel ($MgAl_2O_4$), iron (III) oxide (Fe_2O_3), calcium iron aluminum oxide ($CaAlFe_4O_{10}$), magnesium aluminum silicate ($Mg_2Al_2Si_3O_{12}$), aluminum iron oxide ($FeAlO_3$), and gibbsite ($Al(OH)_3$) (**Figure 1**). Ground ASRW with fraction <1 mm was

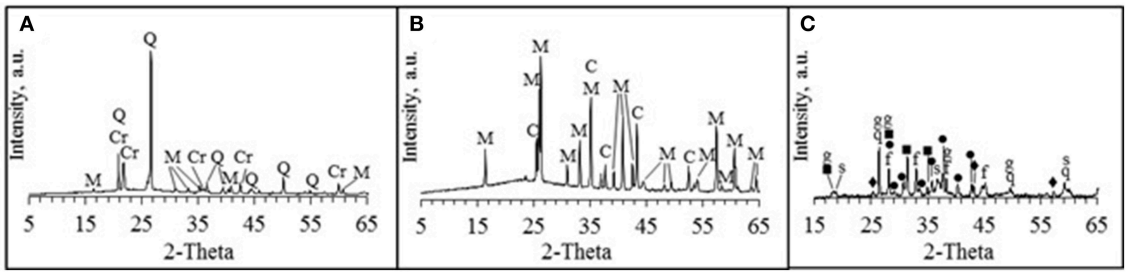

FIGURE 1 | X-ray analysis of solid raw materials, **(A)** CH, **(B)** K26, **(C)** ASRW; Q / q, quartz (85-0798 / 83-2187); Cr, cristobalite (03-0267); M, mullite (01-0613); C, corundum (71-1124); s, spinel (75-1799); f, iron oxide (32-0469); ■, calcium aluminum iron oxide (21-0830); ♦, magnesium aluminum silicate (30-0788); •, aluminum iron oxide (18-0633); g, gibbsite (70-2038).

TABLE 1 | Chemical composition of solid raw materials, (weight %).

Raw materials	Al_2O_3	SiO_2	CaO	SO_3	TiO_2	MgO	Fe_2O_3	Na_2O	K_2O	Other	LOI, 1,000°C
CH	18.8	76.7	0.3	0.0	1.2	0.5	0.7	1.0	0.8	0.3	0.00
K26	58.0	39.1	0.1	0.0	0.1	0.2	0.7	0.8	0.9	0.1	0.00
ASRW	63.2	7.9	2.6	0.4	0.5	4.4	4.5	3.8	3.8	2.6	6.21

TABLE 2 | Compositions of studied samples and amount of main oxides in pastes.

Composition	Mixture design, mass part				Main oxides in pastes, mass %			SiO_2 / Al_2O_3	SiO_2 / Na_2O	Al_2O_3 / Na_2O
	ASRW	CH	K26	6M NaOH	SiO_2	Al_2O_3	Na_2O			
Ref	0.10	1.00	0.00	0.36	53.08	17.21	3.41	3.1	11.1	5.0
0.1FB	0.10	0.90	0.10	0.36	50.50	19.89	3.40	2.5	10.6	5.9
0.3FB	0.10	0.70	0.30	0.36	45.35	25.26	3.37	1.8	9.6	7.5
0.5FB	0.10	0.50	0.50	0.36	40.20	30.63	3.34	1.3	8.6	9.2

used as the pore forming agent due to gas emissions, when it reacts with an activation solution (Bajare et al., 2012).

6 M NaOH solution, which was prepared by using sodium hydroxide flakes with 99% purity (Tianye Chemicals Ltd., China), was used as alkali activating solution.

Mixture Design and Sample Preparation

The basic AAM mixture compositions consisted of CH and ASRW with the mass ratio of 10:1. The mass ratio of the alkali activation solution to total solid raw materials ratio was 0.33. CH was partially substituted with sawing residues K26 up to 50 wt.% (**Table 2**). The theoretically calculated oxide ratios by mass are given in **Table 2**. The SiO_2 / Al_2O_3 ratio for studied AAM is in the range from 1.3 to 3.1, SiO_2 / Na_2O ratio—from 8.6 to 11.1 and Al_2O_3 / Na_2O—5.0 to 9.2. According to the report of Peigang He, the increased ratio of SiO_2/Al_2O_3 can increase mechanical properties of the AAM due to the increased amount of Si-O-Si bonds, which could appear in the polymerization process and presence of residual silica, which can operate as reinforcement (He et al., 2016). The decrease of Na_2O/Al_2O ratio could cause less dissolution of precursors due to lower content of NaOH resulting in weaker active alkali activation reaction (Siyal et al., 2016).

The solid raw materials were mixed together and activation solution was added. After mixing with electrical twin shaft mixer for 2 min, the paste was immediately poured into prismatic molds (40 × 40 × 160 mm) sealed with plastic film and after formation of porous structure molds were covered and samples were cured at 80°C for 24 h. For thermal conductivity test and industrial application AAM plates of 45 × 45 × 5 cm were prepared. To characterize the effect of heat treatment on AAM properties prepared samples were treated at 800 and 1,000°C temperatures with the heating rate of 10°C/min and kept for 3 h at the max temperature. Three series of samples were prepared: Ref, 0.1FB, 0.3FB, and 0.5FB without heat treatment (i), Ref-800, 0.1FB-800, 0.3FB-800, and 0.5FB-800 with heat treatment at temperature 800°C (ii) and Ref-1000, 0.1FB-1000, 0.3FB-1000, and 0.5FB-1000 with heat treatment at temperature 1,000°C (iii). The obtained AAM samples were kept at ambient temperature (20 ± 2°C) for further testing.

Techniques

Chemical composition of the raw materials was determined according to LVS EN 196-2 with sensibility ±0.5 wt.%. The elemental analysis of ASRW was carried out with inductively coupled plasma optical emission spectrometry (ICP-OES) for Al

and Si, atomic absorption spectrometry (AAS) for Na, Mg, K, Ca, Fe, Cu, Zn, Pb. Potentiometer titration analysis (PTA) was used to determine Cl and combustion process—to determine S.

Thermogravimetric-differential thermal analysis (DTA/TG) was carried out by using Netzsch STA 409 PC from 0 to 1,200°C with the heating rate of 10°C/min. High temperature microscopy (HTOM) EM201, HT163 was used to determinate heat resistance and shrinkage of the AAM in temperatures up to 1,400°C. Samples were tested by heating rate 80°C/min up to 500°C temperature and then switched to 15°C/min, while reaching 1,400°C temperature.

The material density of AAM was measured by the geometric method using 40 × 40 × 40 mm specimens. The Archimedes principle (using water as immersion fluid) was employed to evaluate the specimens' water absorption, and combined with geometric measurements to determine the open porosity. The true density was determined for powdered AAM by using Le Chatelier flask and then the total porosity was calculated. X-ray computed tomography (XCT, Xradia μCT-400, XRadia, Concord, USA with Avizo Fire 3D software) was employed to obtain 3D images of the AAM. Pore structure and porosity were assessed by using the XCT data and comparing the results to the traditional methods.

The AAM macro and microstructure was observed by using optical microscope and scanning electron microscope ("TESCAN Mira / LMU Field-Emission-Gun"). The thermal conductivity was measured with heat flow meter instrument LaserComp FOX 660.

Flexural and compressive strength of the prepared AAM samples 9 aged 28 days) were tested according to the LVS EN 196-1.

To determine the mineralogical composition of solid raw materials and AAM before and after heat treatment the X-ray diffraction (XRD) patterns of the powdered samples were recorded on a "RIGAKU ULTIMA+" diffractometer using CuKα radiation, the test was run in a 2-Theta range of 5–70° step-scan and 10 s/step.

The thermal cycling of the prismatic samples 40 × 40 × 160 mm was conducted in accordance with testing of refractory concrete (GOST 20910-90 Refractory concretes, 1991). The samples were kept for 60 min in a furnace heated to 800°C, then the samples were cooled for 20 min by a stream of air from a fan (700 W, 1,000 rpm). After each thermal cycle the speed of an ultrasonic pulse (SUSP) in the samples was determined and its decrease with respect to the SUSP values after heat treatment at 800°C was determined (Antonovich et al., 2011).

RESULTS

Thermal Analysis

DTA/TG

The changes of AAM during heat treatment up to 1,200°C could be described in four distinct phases (**Figure 2**). The first phase consists of evaporation of physically adsorbed water from the material matrix. Exothermic effect is appearing in DTA curve before heating temperature rises to 100–150°C (Djobo et al., 2016). The second phase begins at 150°C and proceeds up to 600°C involving evaporation of the chemically bound water. It comes from dissolution of aluminosilicate raw materials, when aluminate and silicate species are formed. In this phase significant processes contributing to the knowledge base about the extent of alkali activation reaction can be observed (Firdous et al., 2018). Namely, the TGA result showed similar behavior of AAM, when between 150 and 600°C the mass loss was 2.91 and 2.67% respectively. The mass loss ∼5% in the temperature between 500 and 700°C as well as start of another mass loss region at 900°C along with minor features on the differential scanning calorimeter represented various phases of crystallization (Canfield et al., 2014). The densification of AAM occurs at 820–920°C. Onset temperatures decrease slightly and sharply appear due to softening and viscous sintering (Barbosa and MacKenzie, 2003; Villaquirán-Caicedo et al., 2017). Another minor weight loss of 0.4% at the temperature around 800°C is associated with the decomposition of calcite which in minor parts was detected in ASRW. Finally, rapid densification and weight loss was observed above 1,000°C.

High Temperature Microscopy (HTOM)

HTOM results can be divided in three relative intervals which correlate well with DTA/TG results: (a) specific area changes at the temperature up to 800°C; (b) from 800 to 1,000°C; and (c) from 1,000 to 1,200°C (**Figure 3**; **Table 3**). Shrinkage of the AAM with the intensity from 3.2 to 4.9% was observed at the temperature up to 1,000°C.

Physical and Mechanical Properties

The physical properties of the porous AAM are given in **Figure 4**. The density of porous AAM was in the range from 670 to 755 kg/m^3. The total porosity of the obtained materials was between 71 and 75 vol.%. The open porosity was from 27 to 30 vol.%. The pore structure of the obtained materials remain open which corresponds to the water absorption. The water absorption of the AAM was between 45 and 48 wt.%.

The thermal conductivity of prepared porous AAM plates (45 × 45 × 5 cm) was measured. The measured thermal conductivity was from 0.14 to 0.15 W/m·K and it was not affected by the mixture composition of AAM but correlated well with total porosity of the material.

The porosity measured by the micro-XCT indicated the total pore value ranging from 41.2 to 52.7 vol.% with the pore structure of the AAM, pore distribution as well as the measurement technique being the factors contributing to these differences. Three-dimensional internal pore structure of the specimens was made and pore size distribution was reconstructed using 3D-image analysis software (Avizo Fire) (**Table 4**). According to the research results the size of most of the pores in the material (90.2 vol.%) was between 1,000 and 5,000 μm. It can be clearly seen in the pore sieving images obtained by using the Avizo Fire 3D software. The pores within the range from 7E+9 to 9E+9 μm^3 have a blue color, whereas the pores having a size greater than 9E+9 μm^3 have a green color (**Figure 5**).

The compressive and flexural strength results of the AAM are presented in **Figure 6**. The compressive strength was 1.1 MPa for Ref and increased to 2.0 MPa for 0.5FB. After sample

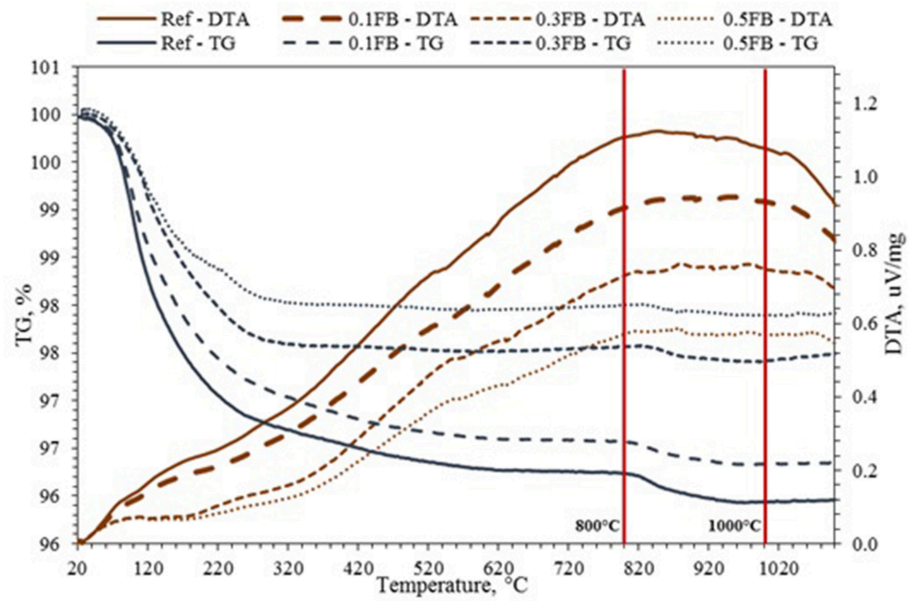

FIGURE 2 | DTA /TG curves for the porous AAM.

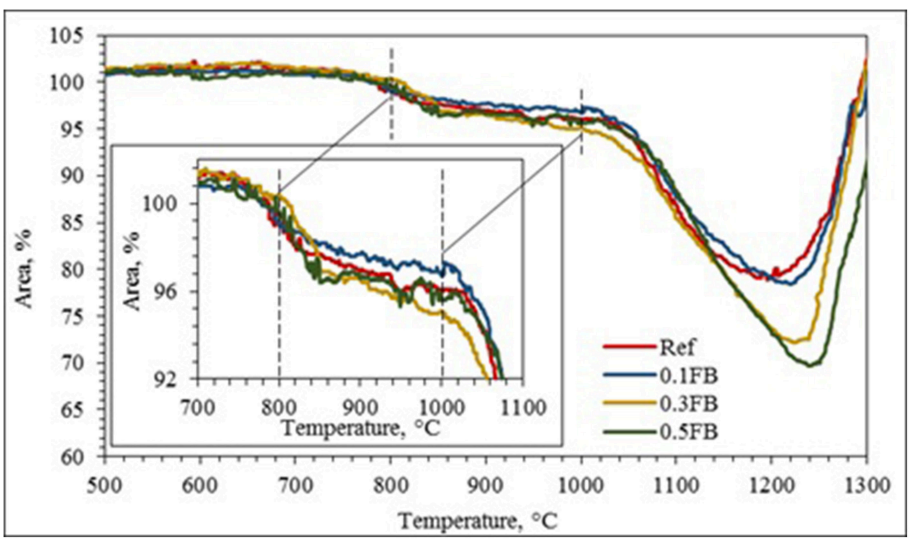

FIGURE 3 | Thermal response of the porous AAM determined by high temperature microscopy.

TABLE 3 | Relative area changes of obtained porous AAM.

Composition	Temperature/shrinkage		Shrinkage/temperature			
	800°C	1,000°C	5%	10%	15%	20%
Ref	0.5%	4.0%	1,042°C	1,080°C	1,109°C	1,165°C
0.1FB	1.0%	3.2%	1,052°C	1,087°C	1,124°C	1,177°C
0.3FB	−0.4%	4.9%	984°C	1,073°C	1,104°C	1,148°C
0.5FB	0.5%	4.3%	1,036°C	1,091°C	1,118°C	1,146°C

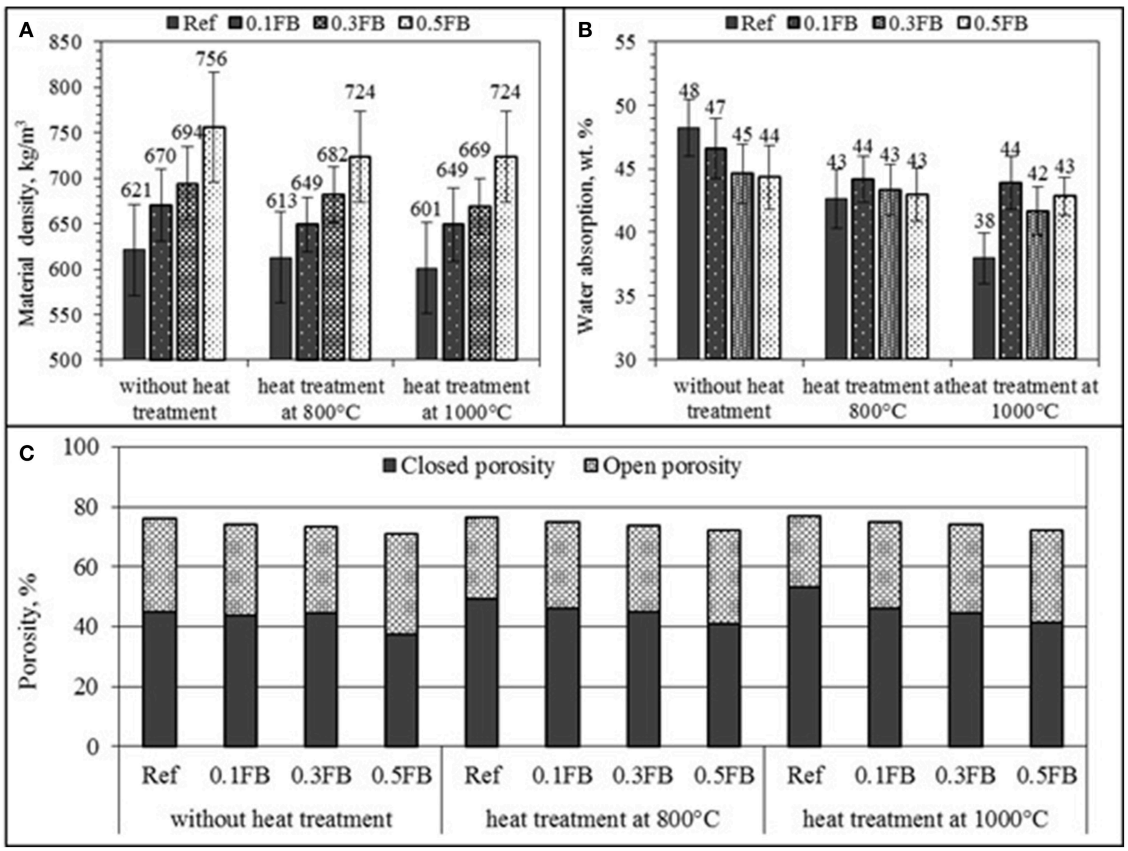

FIGURE 4 | The physical properties of porous AAM, **(A)** material density, **(B)** water absorption, **(C)** porosity.

TABLE 4 | Volumetric pore size distribution (vol. %) of 0.5FB determined by Micro-XCT.

≤100 μm	100–250 μm	250–500 μm	500–1,000 μm	1,000–5,000 μm	≥5,000 μm
0.0	0.5	1.9	4.3	90.2	3.1

treatment at 800°C, compressive strength was 0.7 for Ref and 0.9 MPa for 0.1FB. Slight strength increase was for 0.3FB, while for the 0.5FB strength increased to 2.5 MPa. The heat treatment at 1,000°C slightly increased strength comparing to samples treated at 800°C for the mixture compositions Ref, 0.1FB and 0.3FB. The composition 0.5FB had compressive strength 2.7 MPa.

The flexural strength for all samples except for 0.5FB before heat treatment was in a range from 0.5 to 0.6 MPa, while the strength of 0.5FB samples was 0.8 MPa. The flexural strength decreased to 0.3–0.5MPa for samples with Ref, 0.1FB, 0.3FB but the increase of flexural strength was observed for 0.5FB—reaching 1.0 MPa. Similar tendency was observed for the heat treated samples at 1,000°C. Structural integrity was preserved and insignificant or no strength loss was observed compared with specimens treated at 800°C temperature.

X-Ray Diffraction

The XRD was determined for blends of solid raw material (**Figure 7** with index raw), prepared porous AAM before and after heat treatment at 800 and 1,000°C for mixture compositions Ref and 0.5FB. After alkali activation slight phase change was observed for Ref but almost all minerals detected in mix of raw materials were still present in the AAM. The composition Ref had crystalline phases, which have remained from precursors (CH) like mullite ($Al_{4.56}Si_{1.44}O_{9.72}$), quartz ($SiO_2$), and cristobalite ($SiO_2$). After alkali activation low intensity peaks of analcime appeared, but after heat treatment at 800 and 1,000°C crystalline phase of analcime disappeared and new crystalline phases have not been detected. Meanwhile composition 0.5FB had crystalline phases, which had remained from precursors like mullite ($Al_{4.56}Si_{1.44}O_{9.72}$), quartz ($SiO_2$), corundum ($Al_2O_3$), and cristobalite ($SiO_2$). Hydroxy sodalite ($1.08Na_2O{\cdot}Al_2O_3{\cdot}1.68SiO_2{\cdot}1.8H_2O$; sodalite group zeolites) and N-A-S-H gel which are formed during the activation process were also detected. The hydroxy sodalite was not detected after heat treatment of specimens at 800°C temperature, but new crystalline phase carnegeite ($NaAlSiO_4$) was present. After heat treatment at 1,000°C phases such as quartz, mullite, corundum, and crystabolite remained, but new crystalline phase—nepheline ($Na_{6.65}Al_{6.24}Si_{9.76}O_{32}$) was detected.

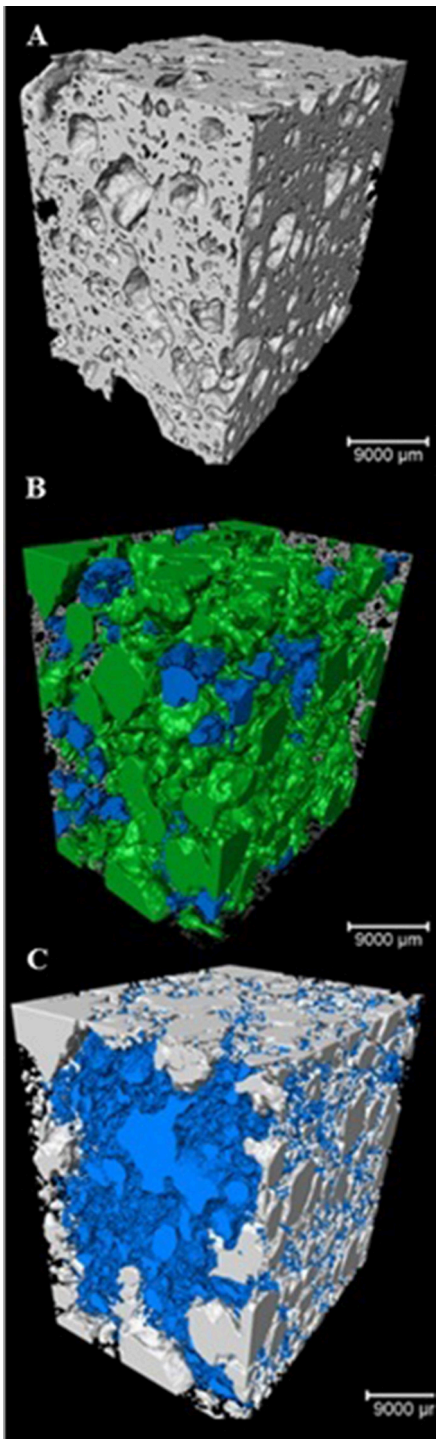

FIGURE 5 | 3D visualization and pore size analysis of 0.5FB with Avizo Fire 3D, **(A)** 3D scan, **(B)** pore sieving image of pores within the range from 7E + 9 to 9E + 9 μm^3 (blue) and >9E +9 μm^3 (green), **(C)** closed pores (blue).

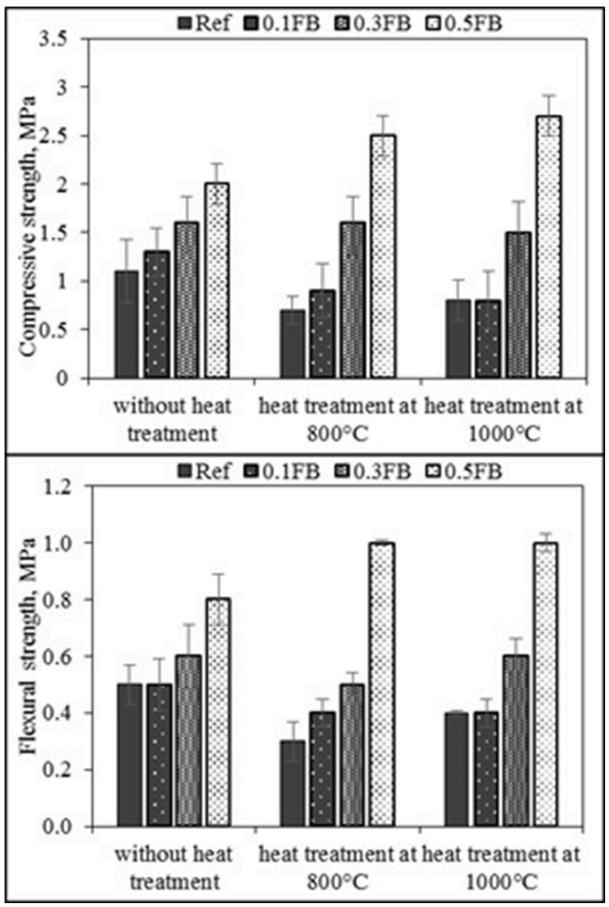

FIGURE 6 | Flexural and compressive strength of AAM.

Cycling Performance

The cyclic performance of the prepared AAM was evaluated (**Figure 8**). Pre-treatment of separate batch of samples was done to reduce first thermal shock induced by the formation of new minerals inside the AAM previously detected by the XRD. The ultrasonic pulse velocity was measured to evaluate the performance. The cycling results are given in **Table 5**. The first thermal cycle at the temperature of 800°C reduced the initial ultrasonic pulse velocity by 30 to 50%, while the critical value of 300 m/s was not reached. The 2nd high temperature cycle was crucial for the samples Ref, Ref_800 and 0.1FB with the ultrasonic pulse velocity decrease below 300 m/s. With the increasing proportion of K26 in the mixture composition of AAM the thermal cycle performance improved and up to 7 cycles were achieved for the specimens 0.5FB_800.

DISCUSSION

The mass loss intensity during TGA analysis can be used to measure the extent of alkali activation (**Figure 2**). Higher overall mass loss relates to higher extent of alkali activation as more water is attracted to hydrated NASH gel (Vogt et al., 2016). Increased weight loss was observed for 0.5FB as higher amount of K26 filler was incorporated in the mixture composition of AAM, showing the positive role of K26 in alkali activation process.

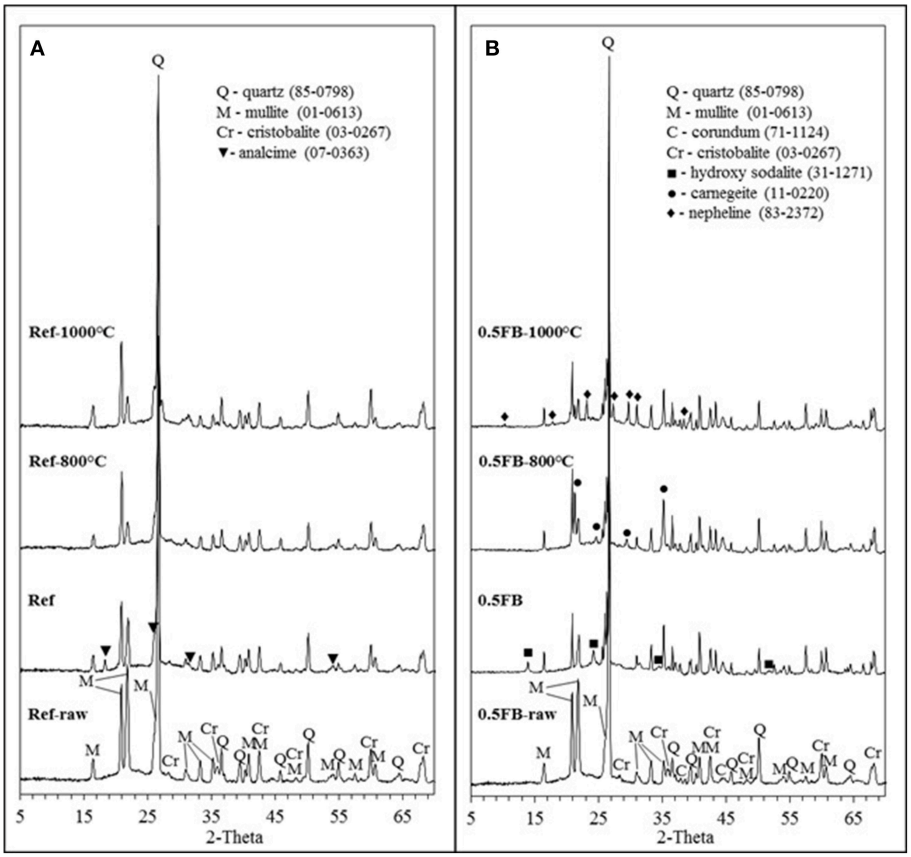

FIGURE 7 | XRD analysis of obtained porous AAM and solid raw material mixtures, **(A)** porous AAM based on chamotte-like clay (Ref), **(B)** porous AAM based on chamotte-like clay and firebricks sawing residues (0.5FB).

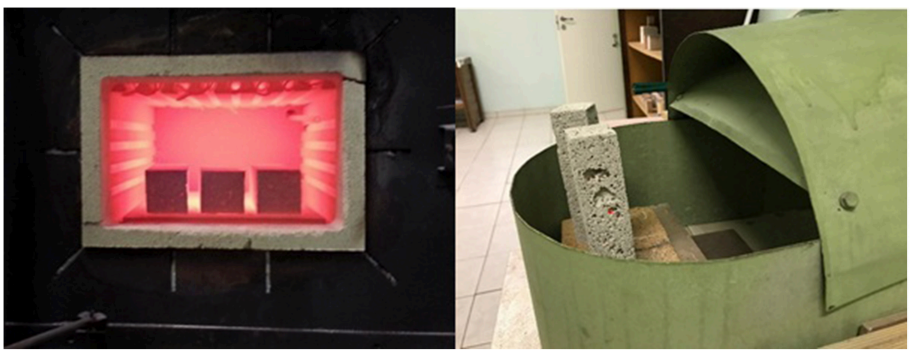

FIGURE 8 | High temperature cyclic performance of AAM. Heating and cooling cycle.

The DTA/TG results showed that at the interval between 800 and 1,000°C the structural changes could take place; therefore, further investigation was done at selected temperatures. Since the DTA/TG results showed similar performance between Ref up to 0.5FB with different K26 concentration in mixture composition, for the ease of result interpretation compositions Ref and 0.5FB were compered except in cases, where noticeable differences were detected.

Thermal expansion can be limited by highly porous structure of the AAM (**Figure 3**). The deformations in specimen can take place inside the pores and true expansion value could be even greater. Some expansion was attributed to the transformation of α-quartz to the β-quartz which follows the volume increase of specimens at the temperature 573°C. Due to transformation of quartz and expansion of specimens the microstructure of AAM could be damaged, which could have negative influence on the

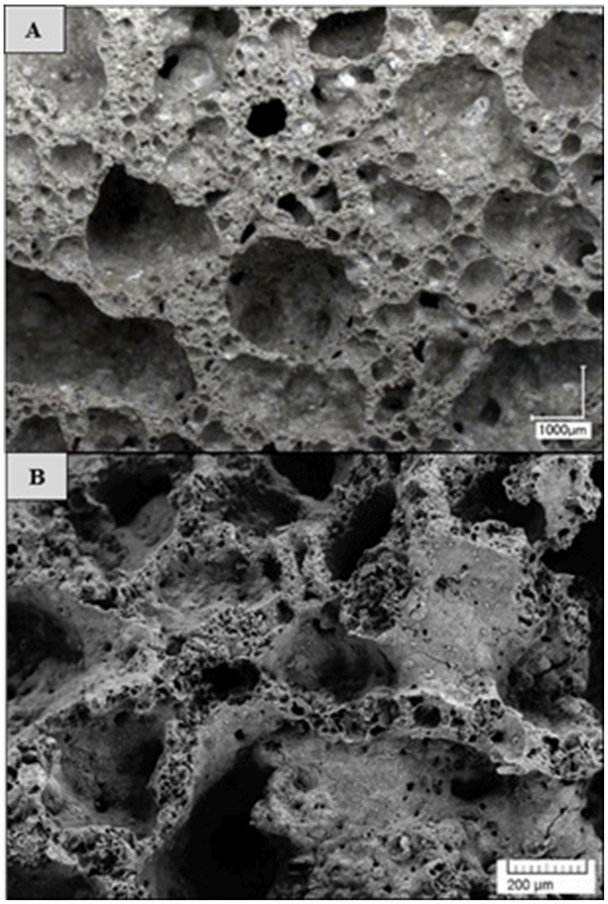

FIGURE 9 | Porous structure of 0.5FB, **(A)** optical microscope image with magnification x40, **(B)** SEM image with magnification x200.

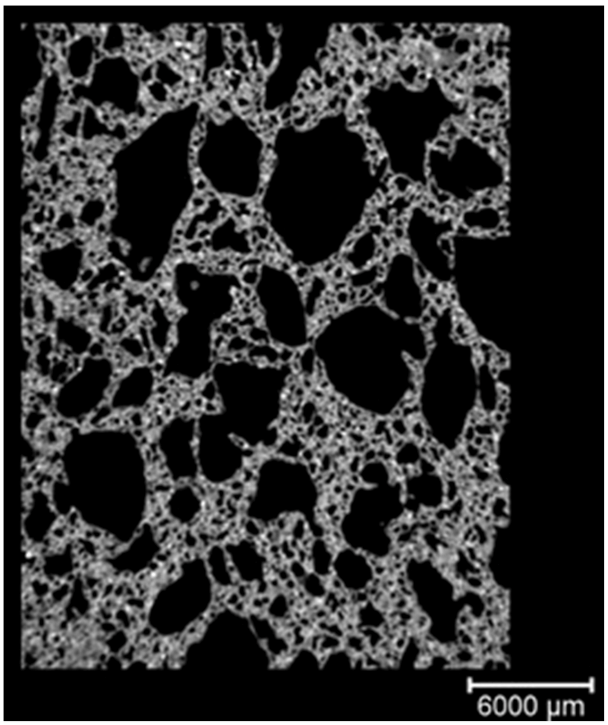

FIGURE 10 | The structure of obtained AAM detected by Micro-XCT.

mechanical properties. According to the literature the second interval from 800 to 1,000°C is associated with melting of alkalis. At temperatures over 800°C solid raw materials are attacked by alkalis, which causes partial sintering in the contact zone between the geopolymer matrix and the aggregate, which in this case is unreacted crystalline phases remained from raw materials. This effect plays a substantial role in the improvement of residual mechanical properties after exposure to 1,000°C and helps AAM to resist higher temperatures without damage (Mandal et al., 2011; Rovnaník and Šafránková, 2016).

The physical and mechanical properties were slightly affected by the selected mixture compositions. Porosity within the material structure, as well as the material density, depends on the gas supply in the fresh paste. The chemical reaction between the ASRW and the alkali solution as well as generated heat flux leads to gas formation in the fresh paste. Low viscosity of the fresh paste and the pressure of evolved gasses in the process of pore formation are the factors, which cause breaking down of the walls and coalescence of pores, thus small bubbles diffuse into the bubbles, which are larger (**Figures 9**, **10**). The above mentioned observations show the differences between the pore formation using ASRW as pore formation agent and other possible solutions such as H_2O_2 (Ducman and Korat, 2016). Structure formation, gas release, and the evaporation of free water during initial setting of AAM are the factors contributing to high open porosity (up to 33%). In the SEM microphotographs it is possible to observe micropores not exceeding few micrometers (**Figure 9B**). As these small micropores were not detected by the Avizo Fire 3D software due to insufficient resolution of X-ray computed tomography, it is possible that some of the pores are not included in the calculations of porosity by the micro-XCT (Dembovska et al., 2017). The results of the pore analysis obtained using Avizo Fire 3D software include only the pores being larger than 48 µm (identified as macropores), whereas the difference between the total porosity detected by using the Le Chatelier flask and the porosity detected by the Avizo Fire 3D software show both micro and capillary pores.

The amount and structure of pores had influence on compressive strength of the AAM giving characteristically low compressive strength associated with highly porous materials. The increase of K26 amount in the composition of AAM increased the initial compressive strength. The heat treatment of samples at the temperature of 800°C reduced compressive strength for Ref and 0.1FB to 0.7 and 0.9 MPa, respectively, indicating strength reduction by 36 and 32% while for the 0.5FB strength increase was 24% reaching 2.5 MPa. The heat treatment at 1,000°C led to slight strength gain comparing to the samples treated at 800°C for the mixture compositions Ref, 0.1FB and 0.3FB, while it was still lower comparing to the samples without heat treatment. The composition 0.5FB had further strength increase up to 2.7 MPa (8% increase

TABLE 5 | Ultrasonic pulse velocity after high temperature cycling.

No of cycle	Ultrasonic pulse velocity, m/s							
	Ref	Ref_800	0.1FB	0.1FB_800	0.3FB	0.3FB_800	0.5FB	0.5FB_800
0	1661	889	1,682	898	1,590	1,084	1,520	1,433
1	681	480	794	574	831	737	1,365	1,101
2	160	213	262	379	515	466	1,100	705
3	139	236	218	158	411	325	787	624
4	–	139	144	161	266	325	763	625
5	–	–	–	–	178	384	569	572
6	–	–	–	–	171	384	482	593
7	–	–	–	–	153	175	306	317

Acceptable results has been highlighted green, i.e. values over 300.

comparing to the strength at 800°C) indicating the improved structure performance with the incorporation of higher proportion of K26.

The XRD results indicate the N-A-S-H gel formation during alkali activation process and it was detected by the shift of halo at 2-Theta = 10−30° to higher degrees (Zhang et al., 2012) in both cases (for Ref and 0.5FB before heat treatment respectively). The phase transformation was identified during heat treatment of AAM. It could be explained by transformation of initially detected hydroxide sodalite into zeolite X, which melts at 760°C temperature and becomes amorphous but later it recrystallizes again at 800°C and crystallizes as carnegeite (Jacobs, 1984). After further temperature increase the nepheline transforms from the carnegeite at the temperature around 900–1,000°C. Considerable change of the N-A-S-H gel after heat treatment at different temperatures was not detected by X-ray diffraction.

Also phase changes was detected by XRD and the first controlled pre-treatment at the temperature of 800°C was applied for porous AAM, it did not improve the overall cyclic performance of AAM and only initiated the early deterioration of AAM structure by showing possible relationship between pre-treatment and first cyclic load for untreated samples. Each additional cycle continued to damage structure of the AAM.

HIGH TEMPERATURE CYCLIC PERFORMANCE AND INDUSTRIAL APPLICATION

Technological Perspective of High Temperature AAM Production: Production Process

The schematic diagram of the AAM production process is given in **Figure 11**. The estimation of AAM mixture composition regarding raw material chemical composition should be calculated to cover the optimum range of main oxide ratios. The production process consists of dosage of raw materials and pre-mixing to obtain homogenous precursor for alkali activation. It should be noted that ASRW and K26 components must be pre-treated by milling to obtain fine, powder-like material. After adding alkali activation solution and mixing, paste should be molded instantly to allow blowing agent to react and form porous structure of the AAM. If prolonged mixing or molding time is necessary, the cooling process of raw materials should be considered (reaching −20°C) to delay the initial exothermic reaction provided by the ASRW, which determines rapid setting of the AAM. The further process control related to the curing regime should be maintained at 80°C for 24 h. The ventilation and filtering of gasses emitted by the ASRW during blowing of AAM should be ensured to provide safe production process and to avoid environmental pollution. After the AAM are demoulded, high temperature pre-treatment at 800°C could be applied to the allow phase change transformations take place to ensure further dimensional stability before cutting the material and creating final shape of the detail.

Technological Perspective of High Temperature AAM Production: Industrial Approbation

Following the previously described technological process, AAM plates for industrial application were prepared. 45 × 45 × 5 cm porous AAM plates were made in the laboratory conditions and provided to the producer of laboratory furnaces. During further processing of the prepared AAM plates they proved to be workable with traditional tools (**Figure 12**). The high temperature oven prototype was created by combining prepared porous AAM insolation plates with traditional refractory insulation materials. The prepared AAM was placed as outer insulation layer of the oven. The possible limitations of the AAM described is the relatively low strength of the material which is associated with high porosity; therefor the application of the material is suggested to be used as the interlayer material in high temperature furnaces which main function would be heat insulation. Other limitation which is related with production process is associated with the availability of the raw materials and its nature, as most of them are industrial wastes and by-products so the production of the material must be carefully controlled.

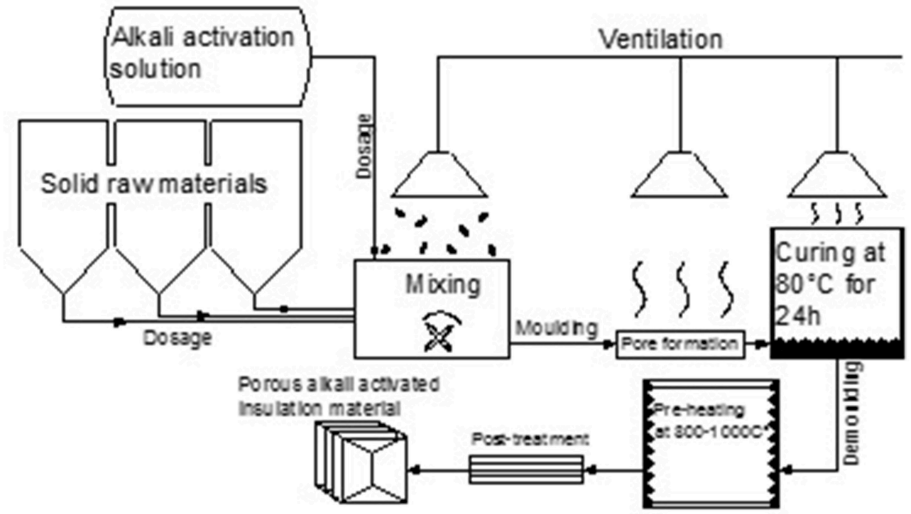

FIGURE 11 | Technological guidelines for the manufacture of high temperature insulation material.

FIGURE 12 | The processing of prepared AAM plates with simple tools (a) and created prototype of high temperature oven.

CONCLUSIONS

The investigated porous alkali activated material (AAM), which is based on chamotte-like precursor, firebrick sawing residues and aluminum scrap recycling waste, proved to be suitable for industrial production and applications.

The tested alkali activated material had high porosity (open porosity 25–30 vol.%, total porosity 71–75 vol.%), reasonable strength (before heat treatment from 1.1 to 2.1 MPa and after treatment at 1,000°C 0.8–2.6 MPa, respectively) and effective working temperature up to 800 (shrinkage from −0.4 to 1.0%) and 1,000°C (shrinkage from 3.2 to 4.9%).

High thermal stability of porous AAM reaching up to 8 thermal shock cycles was obtained. It is suggested that the ultrasonic pulse velocity lower limit of 300 m/s could be acceptable for non-destructive testing method for porous AAM, as samples withstand thermal cycling load and remain solid appearance and still reasonable strength.

The macropore (>48 μm) structure of AAM could be effectively determined by the X-ray computed tomography with Avizo Fire 3D software giving possibility to test structure with non-destructible method i.e., for quality control during the production. Though to characterize the total porosity test methods based on the Archimedes principle should be used.

The obtained material has a simple, reproducible and low-cost manufacture ensuring maximal valorization of waste into a heat-resistant material with high added value. The firebrick sawing residue incorporation in the composition of AAM improved the performance of heat resistance as the increase of Al_2O_3 content was achieved. This innovative waste-based material was treated at temperature 1,000°C and proved to be suitable for application at the temperature up to 1,000°C.

It was proved that the developed material is effective for industrial production and could be a promising for using as outer insulation layer in high temperature furnaces.

AUTHOR CONTRIBUTIONS

All co-authors are working together on porous AAM for different kind of applications since 2013. DB is the main author of this manuscript and supervisor of all other co-authors. LV is a Ph.D. student and her responsibility at this research was to analyze XRD results, as well as other obtained data. LD is the last year Ph.D. student and this research is included in her thesis, so most of the tests have been done by LD. GB is leading researcher, as his Ph.D. thesis was about porous AAM and he has the experience of the work with aluminum scrap recycling waste usage in AAM production he was helping with data interpretation.

REFERENCES

Antonovich, V., Shyukshta, M., Pundene, I., and Stonis, R. (2011). Procedural elements in estimation of the thermal shock resistance of different types of refractory concrete based on chamotte filler. *Refract. Ind. Ceram*. 52, 70–74. doi: 10.1007/s11148-011-9369-y

Bajare, D., Bumanis, G., Korjakins, A., and Sele, L. (2014). Reuse of non-metallic residues from aluminium recycling industry in production of porous building materials. *Constr. Mater. Struct*. 1, 136–144. doi: 10.3233/978-1-61499-466-4-136

Bajare, D., Korjakins, A., Kazjonovs, J., and Rozenstrauha, I. (2012). Pore structure of lightweight clay aggregate incorporate with non-metallic products coming from aluminium scrap recycling industry. *J. Eur. Ceram. Soc*. 32, 141– 148. doi: 10.1016/j.jeurceramsoc.2011.07.039

Barbosa, V. F. F., and MacKenzie, K. J. D. (2003). Thermal behaviour of inorganic geopolymers and composites derived from sodium polysialate. *Mater. Res. Bull*. 38, 319–331. doi: 10.1016/S0025-5408(02)01022-X

Bernal, S. A., Bejarano, J., Garzón, C., Mejía De Gutiérrez, R., Delvasto, S., and Rodríguez, E. D. (2012). Performance of refractory aluminosilicate particle/fiber-reinforced geopolymer composites. *Compos. Part B Eng*. 43, 1919–1928. doi: 10.1016/j.compositesb.2012.02.027

Bumanis, G., Vitola, L., Bajare, D., Dembovska, L., and Pundiene, I. (2017). Impact of reactive SiO2/Al2O3 ratio in precursor on durability of porous alkali activated materials. *Ceram. Int*. 43, 5471–5477. doi: 10.1016/j.ceramint.2017.01.060

Canfield, G. M., Eichler, J., Griffith, K., and Hearn, J. D. (2014). The role of calcium in blended fly ash geopolymers. *J. Mater. Sci*. 49, 5922–5933. doi: 10.1007/s10853-014-8307-z

Criado, M., Fernández-Jiménez, A., and Palomo, A. (2007). Alkali activation of fly ash: effect of the SiO2/Na2O ratio. Part I: FTIR study. *Microporous Mesoporous Mater*. 106, 180–191. doi: 10.1016/j.micromeso.2007.02.055

Davidovits, J. (1991). Geopolymers. *J. Therm. Anal*. 37, 1633–1656. doi: 10.1007/BF01912193

Dembovska, L., Bajare, D., Ducman, V., Korat, L., and Bumanis, G. (2017). The use of different by-products in the production of lightweight alkali activated building materials. *Constr. Build. Mater*. 135, 315–322. doi: 10.1016/j.conbuildmat.2017.01.005

Djobo, J. N. Y., Elimbi, A., Tchakouté, H. K., and Kumar, S. (2016). Reactivity of volcanic ash in alkaline medium, microstructural and strength characteristics of resulting geopolymers under different synthesis conditions. *J. Mater. Sci*. 51, 10301–10317. doi: 10.1007/s10853-016-0257-1

Ducman, V., and Korat, L. (2016). Materials Characterization Characterization of geopolymer fl y-ash based foams obtained with the addition of Al powder or H 2 O 2 as foaming agents. *Mater. Charact*. 113, 207–213. doi: 10.1016/j.matchar.2016.01.019

Dupuy, C., Gharzouni, A., Sobrados, I., Texier-Mandoki, N., Bourbon, X., and Rossignol, S. (2018). Thermal resistance of argillite based alkali-activated materials. Part 2: identification of the formed crystalline phases. *Mater. Chem. Phys*. 218, 262–271. doi: 10.1016/J.MATCHEMPHYS.2018.07.036

Fernández-Jiménez, A., Pastor, J. Y., Martín, A., and Palomo, A. (2010). High-temperature resistance in alkali-activated cement. *J. Am. Ceram. Soc*. 93, 3411–3417. doi: 10.1111/j.1551-2916.2010.03887.x

Firdous, R., Stephan, D., and Yankwa Djobo, J. N. (2018). Natural pozzolan based geopolymers : a review on mechanical, microstructural and durability characteristics. *Constr. Build. Mater*. 190, 1251–1263. doi: 10.1016/j.conbuildmat.2018.09.191

GOST 20910-90 Refractory concretes (1991). *Specifications*. Available online at: http://docs.cntd.ru/document/9052226 (accessed October 17, 2018).

He, P., Wang, M., Fu, S., Jia, D., Yan, S., Yuan, J., et al. (2016). Effects of Si/Al ratio on the structure and properties of metakaolin based geopolymer. *Ceram. Int*. 42, 14416–14422. doi: 10.1016/J.CERAMINT.2016.06.033

Hemra, K., and Aungkavattana, P. (2016). Effect of cordierite addition on compressive strength and thermal stability of metakaolin based geopolymer. *Adv. Powder Technol*. 27, 1021–1026. doi: 10.1016/J.APT.2016.04.019

Huiskes, D.M. A., Keulen, A., Yu, Q. L., and Brouwers, H. J. H. (2016). Design and performance evaluation of ultra-lightweight geopolymer concrete. *Mater. Des*. 89, 516–526. doi: 10.1016/J.MATDES.2015.09.167

Jacobs, P. A. (1984). "Structure and reactivity of modified zeolites," in *Proceedings of an International Conference* (Prague: Elsevier). Available online at: https://books.google.lv/books?id=lekhAQAAQBAJ&pg=PA171&dq=%22carnegeite%22+zeolite&hl=en&sa=X&ved=0ahUKEwiC0prjndPTAhXiDZoKHb8fCmUQ6AEIJzAB#v=onepage&q=%22carnegeite%22zeolite&f=false (accessed September 19, 2018).

Kim, S., and Kim, Y. (2017). *Ceramic Processing Research Property Enhancement of Geopolymers After Heat Treatment*. Available online at: http://jcpr.kbs-lab.co.kr/file/JCPR_vol.18_2017/JCPR18-1/11.2016-182_59-63.pdf (accessed October 17, 2018).

Lemougna, P. N., MacKenzie, K. J. D., and Melo, U. F. C. (2011). Synthesis and thermal properties of inorganic polymers (geopolymers) for structural and refractory applications from volcanic ash. *Ceram. Int*. 37, 3011–3018. doi: 10.1016/j.ceramint.2011.05.002

Mandal, K. K., Thokchom, S., and Roy, M. (2011). Effect of Na2O content on performance of fly ash geopolymers at elevated temperature. *Int. J. Environ. Chem. Ecol. Geol. Geophys. Eng*. 5, 7–13. doi: 10.5281/zenodo.1058857

Martin, A., Pastor, J. Y., Palomo, A., and Fernández Jiménez, A. (2015). Mechanical behaviour at high temperature of alkali-activated aluminosilicates (geopolymers). *Constr. Build. Mater*. 93, 1188–1196. doi: 10.1016/J.CONBUILDMAT.2015.04.044

Moukannaa, S., Loutou, M., Benzaazoua, M., Vitola, L., Alami, J., and Hakkou, R. (2018). Recycling of phosphate mine tailings for the production of geopolymers. *J. Clean. Prod*. 185, 891–903. doi: 10.1016/j.jclepro.2018.03.094

Philip, C. (2014). Performance evaluation of refractory bricks produced from locally sourced clay materials. *J. Appl. Sci. Environ. Manag*. 18, 151–157. doi: 10.4314/jasem.v18

Rashad, A. M., Hassan, A. A., and Zeedan, S. R. (2016). An investigation on alkali-activated Egyptian metakaolin pastes blended with quartz powder subjected to elevated temperatures. *Appl. Clay Sci*. 132–133, 366–376. doi: 10.1016/J.CLAY.2016.07.002

Rovnaník, P., and Šafránková, K. (2016). Thermal behaviour of metakaolin/fly ash geopolymers with chamotte aggregate. *Materials* 9:535. doi: 10.3390/ma9070535

Seabra, M. P., Labrincha, J. A., Novais, R. M., Buruberri, L. H., and Ascens, G. (2016). Porous biomass fl y ash-based geopolymers with tailored thermal conductivity. *J. Clean. Prod*. 119, 99–107. doi: 10.1016/j.jclepro.2016.01.083

Singh, B., Gupta, M., and Bhattacharyya, S. (2015). Geopolymer concrete: a review of some recent developments. *Constr. Build. Mater*. 85, 78–90. doi: 10.1016/j.conbuildmat.2015.03.036

Siyal, A. A., Azizli, K. A., and Ullah, H. (2016). Effects of parameters on the setting time of fly ash based geopolymers using taguchi method. *Procedia Eng*. 148, 302–307. doi: 10.1016/J.PROENG.2016.06.624

Strozi, M., Raymundo, M., and Colombo, P. (2014). Effect of process parameters on the physical properties of porous geopolymers obtained by gelcasting. *Ceram. Int*. 40, 13585–13590. doi: 10.1016/j.ceramint.2014.05.074

Tchakoute, H. K., Elimbi, A., Yanne, E., and Djangang, C. N. (2013). Utilization of volcanic ashes for the production of geopolymers cured at ambient temperature. *Cement Concrete Compos*. 38, 75–81. doi: 10.1016/j.cemconcomp.2013.03.010

Villaquirán-Caicedo, M., Mejía de Gutiérrez, R., and Gallego, N. C. (2017). A novel MK-based geopolymer composite activated with rice husk ash and KOH : performance at high temperature. *Mater. Constr*. 67, 1–13. doi: 10.3989/mc.2017.02316

Vogt, O., Ukrainczyk, N., Steindlberger, E., and Koenders, E. A. B. (2016). *Geopolymerisation Activity of Eifel Tuff*. Available online at: http://tubiblio.ulb.tu-darmstadt.de/81306/ (accessed October 17, 2018).

Zhang, Z., Wang, H., Provis, J. L., Bullen, F., Reid, A., and Zhu, Y. (2012). Quantitative kinetic and structural analysis of geopolymers. Part 1. The activation of metakaolin with sodium hydroxide. *Thermochim. Acta* 539, 23–33. doi: 10.1016/j.tca.2012.03.021

Conflict of Interest Statement: The authors declare that the research was conducted in the absence of any commercial or financial relationships that could be construed as a potential conflict of interest.

frontiers in Materials

ORIGINAL RESEARCH
published: 28 August 2019
doi: 10.3389/fmats.2019.00212

Inorganic Polymers From $CaO\text{-}FeO_x\text{-}SiO_2$ Slag: The Start of Oxidation of Fe and the Formation of a Mixed Valence Binder

Arne Peys[1]*, *Alexios P. Douvalis*[2], *Vincent Hallet*[1], *Hubert Rahier*[3], *Bart Blanpain*[1] and *Yiannis Pontikes*[1]

[1] Department of Materials Engineering, KU Leuven, Leuven, Belgium, [2] Department of Physics, University of Ioannina, Ioannina, Greece, [3] Department of Materials and Chemistry, Vrije Universiteit Brussel, Brussels, Belgium

Belonging to the family of alternative cementitious materials, inorganic polymers are rising in importance because of the drive to decrease CO_2 emissions of concrete production. A synthetic Fe-rich slag resembling industrial copper or lead slags, was mixed with a sodium silicate activating solution. ^{57}Fe Mössbauer spectra analyses indicate that the oxidation reactions are taking place simultaneously with the polymerization reactions. The slag contains Fe^{2+} states and a small amount of Fe^{3+}. During polymerization a new octahedral Fe^{2+} state is formed, while oxidation is manifested through the appearance of an additional Fe^{3+} state. The reactions continue after setting, lowering the relative contributions of the slag in the Mössbauer and FTIR spectra of the samples. The Na^+/Fe^{3+} molar ratio in the mixture that makes up the binder after 28 days is ~1, suggesting the participation of tetrahedral Fe^{3+} in the silicate framework, charge balanced by Na^+.

Keywords: alkali activated materials, geopolymers, ^{57}Fe Mössbauer spectroscopy, non-ferrous slag, *ex-situ* kinetics, FTIR spectroscopy

OPEN ACCESS

Edited by:
Andrew C. Heath, University of Bath, United Kingdom

Reviewed by:
Hongyan Ma, Missouri University of Science and Technology, United States
Zuhua Zhang, University of Southern Queensland, Australia
Rupert Jacob Myers, University of Edinburgh, United Kingdom

***Correspondence:**
Arne Peys
arnepeys@hotmail.com

Specialty section:
This article was submitted to Structural Materials, a section of the journal Frontiers in Materials

Received: *22 February 2019*
Accepted: *14 August 2019*
Published: *28 August 2019*

Citation:
Peys A, Douvalis AP, Hallet V, Rahier H, Blanpain B and Pontikes Y (2019) Inorganic Polymers From $CaO\text{-}FeO_x\text{-}SiO_2$ Slag: The Start of Oxidation of Fe and the Formation of a Mixed Valence Binder. Front. Mater. 6:212. doi: 10.3389/fmats.2019.00212

INTRODUCTION

In search for alternative cementitious materials, geopolymers (Davidovits, 2008), and alkali activated materials (AAM) (Provis and van Deventer, 2014) have received wide attention. More recently, a push for circularization of the economy encouraged metallurgical companies to find alternatives for their residues. In light of this, research in inorganic polymers (IPs) is expanding to ferrosilicate precursors, for instance slags from the non-ferrous metal industries. It was shown that these residues can be increased in reactivity by rapid cooling (Pontikes et al., 2013) or hot stage slag engineering (Van De Sande et al., 2017), while the IPs thereof obtain mechanical properties comparable to geopolymers, i.e., compressive strengths reaching up to 80 MPa (Kriskova et al., 2015). They have shown to be environmentally important, reducing environmental impacts down to 17% of that of ordinary Portland cement (OPC) (Peys et al., 2018a).

Despite these interesting properties and because of the novelty of the understanding that ferrosilicate precursors can be used in alkali-activation, fundamental knowledge on the chemistry of the system and the structural rearrangements during formation is scarce. Using isothermal calorimetry it was shown that, chemically, iron-rich inorganic polymers seem to follow a two stage reaction pattern: dissolution and polymerization (Kriskova et al., 2015; Onisei et al., 2015). As such,

they are comparable to their aluminosilicate counterparts, where calorimetric techniques are often used to distinguish these two reaction stages (Rahier et al., 2007; Zhang et al., 2013) or to compare the reactivity of different formulations (Kumar et al., 2007; Lemougna et al., 2014; Peys et al., 2016). More thorough analysis of calorimetry results also enables the calculation of the reaction enthalpy and subsequent determination of the stoichiometry of the chemical system (Rahier et al., 1997) or the determination of the rate limiting step in the formation (Rahier et al., 2003). In terms of the evolution of the molecular structure, *in-situ* Fourier transform infrared (FTIR) spectroscopy is probably the most used technique, mainly because of its accessibility. Although success is seen for aluminosilicates (Rees et al., 2007; Hajimohammadi et al., 2010), *in-situ* FTIR by itself did not show the evolution of the structure (Onisei et al., 2015) sufficiently clearly and the exact reaction mechanism therefore remains unclear. However, more recent developments (Peys et al., 2017; Onisei et al., 2018) have increased the understanding of the infrared spectrum of ferrosilicate precursors and their alkali-activated products. The main interesting feature in the spectra is the Si-O stretching band. The position of this band in the precursors varies between 950 and 850 cm^{-1}, depending on the amount of network modifiers per silicon atom in the silicate phases of the slag (Peys et al., 2017). This band shifts to ∼950 cm^{-1} after alkali-activation (Kriskova et al., 2015; Peys et al., 2017; Onisei et al., 2018). This was attributed to a higher degree of polymerization observed in recent work (Peys et al., 2018b), because of the (at least partial) incorporation of the Fe^{3+} species in the network.

The aforementioned oxidation was experimentally observed using ^{57}Fe Mössbauer spectroscopy (Lemougna et al., 2013; Onisei et al., 2018). In these works the success in providing information for the oxidation state of iron (Fe^{3+}) in the IP binder, did not expand to the level of the exact description of the coordination of iron (Lemougna et al., 2013; Onisei et al., 2018). Both referred papers suggest an average 4- or 5-fold coordination. Similarly, X-ray absorption spectroscopy (XAS) measurements (Simon et al., 2018) confirm the oxidation state of the binder phase and suggest an average coordination number of 5. An important characteristic referred to the formation of the binder is that the evolution over time of the oxidation reaction is unknown. Mössbauer spectroscopy measurements can be performed on solutions after freezing in liquid nitrogen temperatures (Silver et al., 1979; Douglas et al., 1984). As this practically decelerates the reaction kinetics toward negligible speeds, it enables their *ex-situ* study (Krebs et al., 2005; Kamnev et al., 2014). *In-situ* kinetic studies have also been performed using synchrotron radiation techniques, e.g., X-ray/neutron total scattering on the alkali-activation of metakaolin (Bell et al., 2008; White et al., 2011, 2013a), blast furnace slag (White et al., 2013b; Garg and White, 2017) and on conventional cements (Grangeon et al., 2017; Bae et al., 2018; Cuesta et al., 2019). With these techniques, the short and intermediate range ordering can be investigated in great detail. The results of these studies are often interpreted with the help of theoretical modeling techniques (White et al., 2010; Yang and White, 2016; Geng et al., 2017; Zhou et al., 2017), which increases the understanding of the molecular structure or formation mechanism to a great extent.

In the present work, the reaction mechanism of Fe-silicate IPs is clarified with respect to the behavior of Fe in the first 28 days after mixing. A combination of ^{57}Fe Mössbauer spectroscopy and attenuated total reflectance Fourier transform infrared (ATR-FTIR) spectroscopy is performed *ex-situ* to provide details on the evolution of the local environment of Fe and the connectivity of the silicate network throughout the reaction. These observations are combined to provide new information on our binder system, such as the timing of oxidation reactions. Additionally, they provide detailed information on the local atomic environment of Fe in potential intermediate stages of the material, formed between the initial slag and the final IPs studied in previous works. As such, a step is taken in unraveling the mechanism of formation of Fe-silicate IPs.

EXPERIMENTAL METHODS AND MATERIALS

The precursor slag with chemical composition given in **Table 1** was synthesized by melting iron ore, limestone, and sand in a pilot scale furnace. After a complete melt was obtained, the slag was tapped and granulated by spraying the slag with pressurized water jets into droplets to maximize the amount of glassy phase in the precursor. The precursor hereby replicates a composition often used in non-ferrous metallurgy, but including only the major elements FeO, SiO_2, CaO, and Al_2O_3 (a minor content of MgO was detected due to impurities in the raw materials). This methodology to produce synthetic glasses at pilot scale is described in more detail in Machiels et al. (2017). Milling was performed to reach a specific surface of 4,000 ± 200 cm^2/g measured by the Blaine method. The chemical composition was measured standard-less with wavelength dispersive X-ray fluorescence (XRF) on a Philips PW 2,400. The glassy phase in the precursor was quantified by X-ray diffraction (XRD) after mixing with 10 wt.% of internal zincite standard in a McCrone mill. A Bruker D2-Phaser with Cu K_α radiation was used for these measurements under 30 kV−10 mA, a slit size of 0.6 mm and an anti-scatter slit of 1 mm. With these settings, no crystalline peaks could be observed apart from those of zincite; the amount of glassy phase is estimated to be > 97 wt.%. The diffractogram is added in the supplementary information (**Figure S1**) for interested readers. The IP mixture consisted of the above described precursor and a sodium silicate solution with molar ratios SiO_2/Na_2O of 1.6 and H_2O/Na_2O of 20. The solution/slag mass ratio was 0.45. Pastes using these ratios were mixed by hand and used in all experimental techniques below.

TABLE 1 | Chemical composition of precursor slag in wt.%, obtained from XRF (estimated relative error 10%).

FeO	SiO_2	CaO	Al_2O_3	MgO
47	34	12	5	2

Isothermal calorimetry was performed using a TAM Air at 20°C. A sample with 4 g of slag was mixed for 90 s and transferred into the microcalorimeter. Data are presented after 53.5 min of stabilization in the machine to avoid the influence of the temperature difference between the calorimeter and sample (+26.5 min preparation). The first dissolution and wetting heat is not monitored, i.e., no admix ampule was used, as this information was not needed for the present study. ATR-FTIR spectroscopy was performed on a Bruker Alpha-P, which uses a diamond ATR crystal. A resolution of 4 cm^{-1} was selected and a measurement considered 32 scans. Before setting, for measurements after 6 h or less, a drop was measured without applying pressure on the paste in the ATR-cell. Because the powder is not pressed against the crystal, a relatively higher intensity will come from the solution, where the changes are anticipated to be the most interesting. For later reaction stages (>6 h), the reported spectrum is the average of 2 measurements on powdered samples (these were pressed against the crystal). The powdering of the samples was performed right before the FTIR (and Mössbauer) measurements, before which the pastes were stored in closed bottles at 21 ± 1°C. The FTIR spectra shown in the plots in the results section are rescaled in the y-axis to show the same maximum absorbance of the Si-O stretching band. ^{57}Fe Mössbauer spectroscopy measurements were performed to investigate the evolution of the state and environment of the Fe atoms during reaction. Gamma rays were emitted from a source using the decay of ^{57}Co in Rh matrix kept at room temperature. The samples were measured in transmission geometry on a constant acceleration spectrometer at 77 K. The reported isomer shift (IS) values are given relative to α-Fe at room temperature. The IMSG software (Douvalis et al., 2010) was used for the fitting of the spectra. Before setting, the samples were prepared by adding a drop of paste in the holder and freezing this in liquid nitrogen to solidify the material and stop the reactions. At later stages of the reaction after hardening, the materials were powdered and pressed in the sample holder before freezing and loading into the spectrometer. The effectiveness of this freezing to stop the reactions was tested by measuring a sample that reacted for 3 h and for 3 h + 14 days in liquid nitrogen. These two measurements resulted in spectra with no experimental difference and led to the conclusions that: (i) the reactions are halting after freezing the samples at 77 K and (ii) the samples do not change through the duration of the measurement, which has a typical length of 24 h.

RESULTS AND DISCUSSION

Isothermal calorimetry measures the heat flow, proportional to the reaction rate, coming from the reactions in the sample. It can thereby provide the time-frame in which the different reaction stages occur. The heat flow, **Figure 1**, shows the exotherm which in geopolymers is often used to indicate the timing of the polymerization reactions (Rahier et al., 2007). The maximum heat flow in **Figure 1** is observed around 4 h, which was also approximately the time of setting; the main part of these polymerization reactions seems to occur between 3 and 24 h after mixing. It should be mentioned that in the Fe-rich IPs the Fe^{2+} in the presented slag is oxidized to Fe^{3+} during and/or after the synthesis (Onisei et al., 2018; Simon et al., 2018). A contribution from this reaction is not distinguished here or in previous studies (Kriskova et al., 2015; Onisei et al., 2015). The oxidation most probably occurs simultaneously with the dissolution or polymerization, or occurs on a longer time-scale and it is not noticed as a separate phenomenon in the calorimetry measurements. Important to note is that no crystalline components are consumed or formed by the reactions; previous work showed that no changes are observed in X-ray diffraction, apart from the appearance of carbonate phases in certain mixtures (Machiels et al., 2014; Iacobescu et al., 2017).

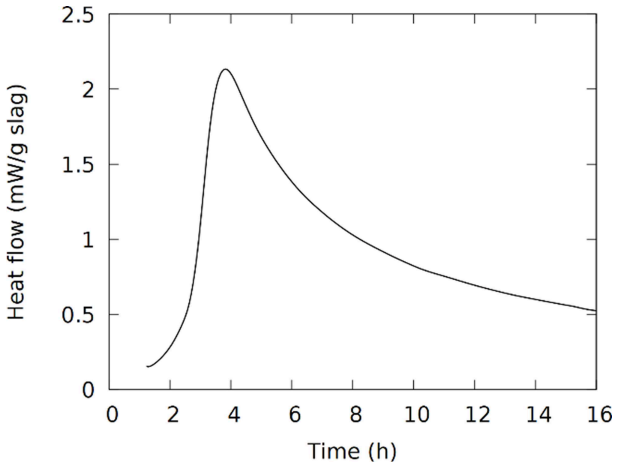

FIGURE 1 | Heat flow in isothermal calorimetry at 20°C from the first 16 h after mixing.

The kinetics of the oxidation of iron are elucidated with ^{57}Fe Mössbauer spectroscopy. **Figure 2** presents the raw spectra of the slag and IPs with curing times up to 28 days. There it can be seen that the slag spectrum is dominated by contributions with IS values of ∼1.0 mm/s and quadrupole splitting (QS) values of ∼2.5 mm/s. This is an indication that the main part of the iron in this sample is of Fe^{2+} character (White et al., 2010; Cuesta et al., 2019), however the asymmetry of the lower and higher velocity resonant line intensities suggests that there must be at least two Fe^{2+} contributions that should have different characteristics, and in particular different QS values. Moreover, a minor peak at ∼1.0 mm/s suggests the presence of an additional minor Fe^{3+} state. Thus, the lowest number of components that could fit the slag spectrum was three, two different Fe^{2+} (S1 and S2) and one Fe^{3+} (S3). The naming of these components is composed of "S" referring to Slag and a number. Similarly, new components in the IPs will be called IP1 and IP2. The fitting result using this model for the slag, in which components S1, S2, and S3 were allowed a Gaussian-type symmetric spreading of their QS values (ΔQS) to simulate the observed broadening of the absorption resonant lines, is given in **Figure 3** and the Mössbauer hyperfine parameters are presented in **Table 2**. The IS and QS values of S1 and S2 correspond to high spin ($S = 2$) Fe^{2+}

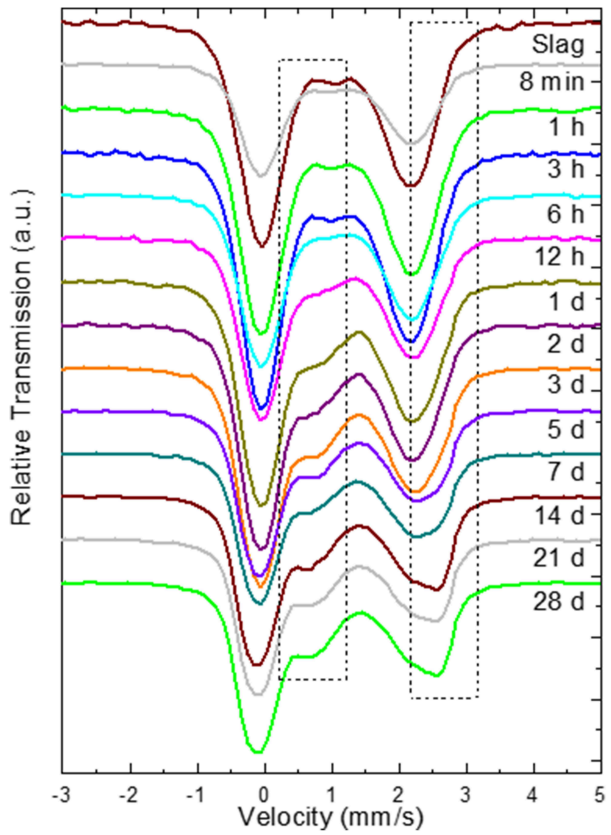

FIGURE 2 | Raw ^{57}Fe Mössbauer spectra during the first 28 days of reaction, where the numbers indicate the reaction time after mixing, in minutes (min), hours (h), or days (d). The dashed rectangles indicate the regions where the high velocity parts of the new Fe^{3+} and Fe^{2+} QS doublet contributions of the binder gradually appear.

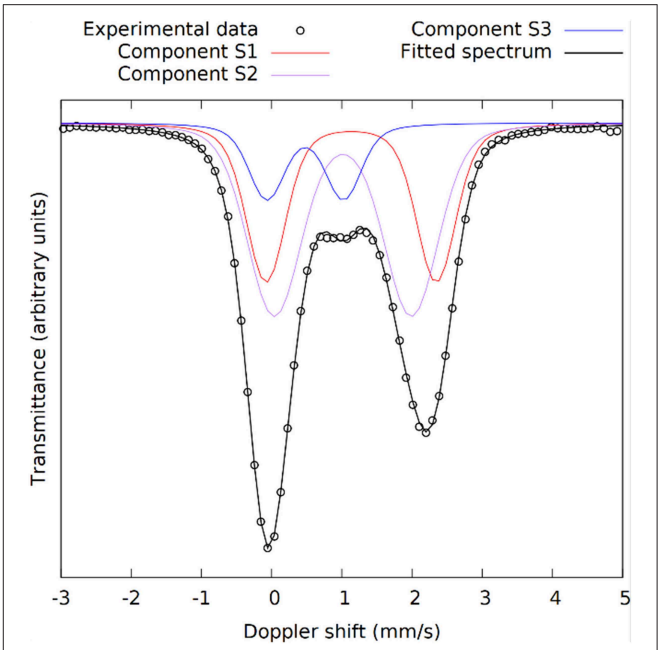

FIGURE 3 | The ^{57}Fe Mössbauer spectrum of the slag with the three components used in the fitting model shown in different colors. S1 and S2 are Fe^{2+} and S3 is Fe^{3+}.

in oxides or silicates (Greenwood and Gibb, 1971; Coey, 1984), while the corresponding values for the minor S3 lie at the upper limit of high spin ($S = 5/2$) Fe^{3+} ions found in such compounds (Greenwood and Gibb, 1971; Coey, 1984). This result shows that the particular slag contains a majority of Fe^{2+} combined with a minority of Fe^{3+} species.

Moving to the IP sample spectra, a more detailed observation of **Figure 2** (insert dashed rectangles) reveals the appearance and increase of the intensity of one additional absorption contribution at ∼0.75 mm/s and a second at ∼2.50 mm/s as the reaction time increases. These are evidences for the appearance of two additional components, one of Fe^{3+} and one of Fe^{2+} character respectively, during the reaction of the slag with the activating solution. Consequently, the fitting of the IP spectra could be performed by keeping the three contributions of the slag (S1, S2, S3) and adding one new Fe^{2+} (IP1) and one new Fe^{3+} (IP2) contribution to the fitting model, which represent the iron ions in the binder part of the newly formed IP. Gaussian spreading of the quadrupole splitting was allowed for components IP1 and IP2, i.e., the ΔQS was refined by the fitting procedure. The parameters of the slag components (S1, S2, and S3) were fixed to the values resulting from fitting the slag spectrum, the intensities and absorption areas (AAs) of components S1 and S3 were made dependent on the major S2 component to result in the same ratio of AAs as in the slag and only the intensity of component S2 was left to vary in the fits. As such, the IP spectra are fitted with a combination of the slag spectrum and the new Fe^{2+} and Fe^{3+} components, IP1 and IP2 respectively. This model thus embeds the idea that the part of the slag that has not reacted with the activating solution to form the binder phase of the IP, is conserved in the configuration it had before the start of the reactions. The described model was used to fit the IP spectra with reaction times equal or longer than 6 h, as for the frozen solutions with reaction times shorter than 6 h the spectra are essentially the same as the slag spectrum within the experimental tolerance limits and according to their fitting results. Example fitting results are shown in **Figure 4**.

The Mössbauer parameters of the two Fe^{2+} sites in the slag, S1 and S2, show similarities with the slag components in our previous work (Onisei et al., 2018). However, the composition of the slag there was found to be close to fayalite, while the IS and QS values here are close to those obtained for pyroxenes toward the ferrosilite composition, in which two sites with varying QS values are observed (Greenwood and Gibb, 1971; Coey, 1984). The spread in the QS values for components S1 and S2 is quite large, showing that this is representing the glassy phase observed with XRD. Component S3 shows relatively large IS and QS values for an Fe^{3+} state as well as a large ΔQS, it is thus another component in the glassy phase of the slag. Based on the absorption areas, the $Fe^{3+}/\Sigma Fe$ ratio of the slag was 0.14.

The Fe^{3+} in the IP binder (component IP2) shows IS and QS values similar to the Fe^{3+} component of the binder in previous

TABLE 2 | Resulting hyperfine parameters values of the components used to fit the ^{57}Fe Mössbauer spectra.

Time (days)	IS (mm/s)	QS (mm/s)	ΔQS (mm/s)	Area (%)	Comp.
0	1.23	2.43	0.43	33	S1
	1.11	1.96	0.64	52	S2
	0.58	1.09	0.38	15	S3
0.25	1.23	2.43	0.43	31	S1
	1.11	1.96	0.64	49	S2
	0.58	1.09	0.38	14	S3
	1.26	2.80	0.40	4	IP1
	0.43	0.56	0.34	2	IP2
0.5	1.23	2.43	0.43	30	S1
	1.11	1.96	0.64	47	S2
	0.58	1.09	0.38	13	S3
	1.23	2.95	0.22	5	IP1
	0.49	0.70	0.32	5	IP2
1	1.23	2.43	0.43	28	S1
	1.11	1.96	0.64	43	S2
	0.58	1.09	0.38	12	S3
	1.25	2.86	0.29	5	IP1
	0.45	0.80	0.38	12	IP2
2	1.23	2.43	0.43	28	S1
	1.11	1.96	0.64	43	S2
	0.58	1.09	0.38	12	S3
	1.25	2.86	0.29	4	IP1
	0.45	0.81	0.38	13	IP2
3	1.23	2.43	0.43	25	S1
	1.11	1.96	0.64	39	S2
	0.58	1.09	0.38	11	S3
	1.25	2.88	0.28	9	IP1
	0.47	0.79	0.36	16	IP2
5	1.23	2.43	0.43	23	S1
	1.11	1.96	0.64	36	S2
	0.58	1.09	0.38	10	S3
	1.25	2.87	0.28	14	IP1
	0.46	0.79	0.37	17	IP2
7	1.23	2.43	0.43	24	S1
	1.11	1.96	0.64	37	S2
	0.58	1.09	0.38	10	S3
	1.28	2.90	0.26	14	IP1
	0.45	0.75	0.34	15	IP2
14	1.23	2.43	0.43	20	S1
	1.11	1.96	0.64	32	S2
	0.58	1.09	0.38	10	S3
	1.27	2.91	0.22	20	IP1
	0.46	0.74	0.33	18	IP2
28	1.23	2.43	0.43	19	S1
	1.11	1.96	0.64	30	S2
	0.58	1.09	0.38	9	S3
	1.27	2.91	0.22	21	IP1
	0.47	0.74	0.33	21	IP2

IS is the isomer shift relative to α-Fe at room temperature, QS is the central value of the quadrupole splitting, ΔQS is the total Gaussian-type spreading of the quadrupole splitting, and AA is the relative absorption area. The half line-width was fixed to Γ/2 = 0.14 mm/s to avoid interference with the ΔQS. Typical errors include ±0.02 mm/s for IS and QS and ±5% for AA.

work on final samples (Onisei et al., 2018) and thus suggest that an average of 5-fold or 4-fold coordination with rather high Fe-O distances is present. The low QS with respect to other glasses (Mysen, 2006) shows, for this high spin Fe^{3+}, that the IP binder contains a higher symmetry of the ligands, i.e., a higher similarity of the species connected to Fe^{3+} or more symmetrically distributed around it (Greenwood and Gibb, 1971; Coey, 1984). This might be an indication of the participation of these Fe^{3+} ions in the silicate network as network formers, charged balanced by Na^{+}, as the network forming character would mean (for the example of a tetrahedron) that Fe^{3+} is surrounded by four bridging oxygen atoms, instead of three bridging and one non-bridging. The new Fe^{2+} site, component IP1, has not been observed in previous measurements (Onisei et al., 2018; Simon et al., 2018), although similar Fe^{3+} sites as component IP2 have been found. This Fe^{2+} state thus seems to have been oxidized in later reaction stages or after milling these samples to a powder. Component IP1 shows larger IS and QS values than the Fe^{2+} components of the slag (S1 and S2), suggesting the presence of distorted, asymmetric octahedra, comparable with fayalite minerals (Coey, 1984; Vandenberghe and De Grave, 2013; Onisei et al., 2018), Fe-rich smectites (Chemtob et al., 2015), micas (Ferrow, 1987), or Fe(II) hydroxides (Génin et al., 1996). The spreading of the quadrupole splitting of IP1 is lower compared to the other components, suggesting a more ordered environment. The presence of crystalline phases has however not been observed in this material with XRD (Machiels et al., 2014; Iacobescu et al., 2017), the IP2 component is thus rather present in a nano-crystalline phase or in very small crystallite clusters.

The evolution of the absorption areas of the new contributions (IP1 and IP2) are illustrated in **Figure 5**. Changes in the Mössbauer spectra do not happen immediately upon dissolution. This is not because of an insignificant extent of dissolution: The immediate start of the dissolution reactions was validated by measuring the concentration of the ions with induced coupled plasma optical emission spectroscopy (Pontikes et al., 2013). No rearrangement of the Fe environment occurs during the first 3 h, there is no oxidation or coordination change. The first changes are observed from 6 h on, meaning reactions have started between 3 and 6 h. This corresponds to the time where according to calorimetry the polymerization reactions start. The Fe^{2+} (IP1) and Fe^{3+} (IP2) components both emerge at this time stage. The largest increase in absorption area of components IP1 and IP2 is observed in the first 24 h, an observation which is analogous to the heat evolution. After the first 24 h, IP1 and IP2 keep increasing in area, although at a slower rate. After 28 days, an AA of 21% is observed for the new Fe^{2+} state (IP1) and 21% for the Fe^{3+} (IP2). At this point it is interesting to check the Na/Fe^{3+} ratio to confirm the possibility of having Fe^{3+} in the silicate network of the binder, like Al^{3+} in geopolymers. This ratio is ∼1 for the mixture presented here, making it possible that Na provides the charge balance for Fe^{3+}. The molar ratio Si/Fe^{3+} provides information on the environment of Si in the network. This ratio is ∼3; the dominant silicate species [using Engelhardt notation (Engelhardt et al., 1982)]

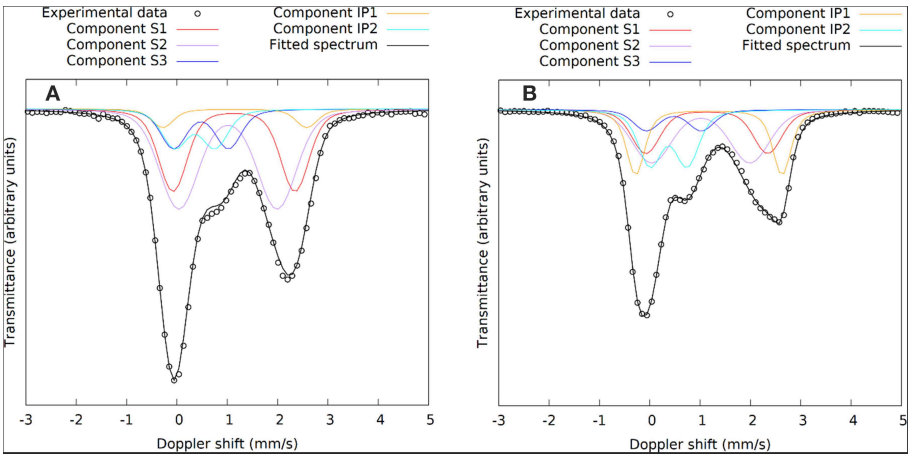

FIGURE 4 | ^{57}Fe Mössbauer spectra of the IPs recorded at **(A)** 1 day and **(B)** 28 days. The slag components (S1, S2, S3) are shown in the same colors as **Figure 3** and the binder components (IP1, IP2) are added in yellow and cyan.

are thus Q^4(1Fe) and Q^4(2Fe). Previous work attempted to provide such compositional information using an electron probe microanalyzer (Kriskova et al., 2015; Iacobescu et al., 2017; Onisei et al., 2018), but because of experimental limitations (e.g., interaction volume, sodium evaporation, etc.) and the inhomogeneity at the nanoscale (see for instance the two different states of Fe), no relevant compositional information could be derived from these experiments. The ratios calculated in the present paper are thus not confirmed by another experimental technique. Future work, for instance considering transmission electron microscopy coupled with electron dispersive X-ray spectroscopy might provide a more accurate and detailed view on the binder phase composition.

The kinetics of the evolution of the AA of components IP1 and IP2 follows an interesting sequence. IP1 seems to form faster initially (**Figure 5A**), which might suggest that the structure associated with IP2 needs IP1 as nucleation site. Between 6 h and 3 days the AA of component IP1 stays approximately constant, while IP2 evolves toward its maximum (**Figure 5B**). Afterwards, also the AA of IP1 gradually goes to its maximum at 28 days. It seems that after the start of formation of IP2, the structure that contains this Fe^{3+} component forms until the Na/Fe^{3+} ratio of 1 is reached, after which the reactions switch again to produce the Fe^{2+} component IP1.

The same time stages and samples are investigated with ATR-FTIR, **Figure 6**. The spectra are focused on the Si-O stretching band (700–1,200 cm^{-1}). The "initial" spectrum, obtained after 8 min, shows two main features. The shoulder at 850 cm^{-1} is associated with the precursor slag, as can be derived from the dotted line representing the spectrum of the slag. The band at 984 cm^{-1} corresponds to the sodium silicate activating solution. The dissolution of the slag is reflected by the decrease in intensity of the shoulder around 850 cm^{-1}. This is not only observed in the initial stages (**Figure 6A**), but extends to days after mixing (**Figure 6B**). The formation of the IP network is seen in the FTIR as the growth of a shoulder around 918 cm^{-1} and the shift of the band that was previously at 984 cm^{-1} (**Figure 6A**, notice the transition from 3 to 6 h). Simultaneously, the shoulder at ∼1,100 cm^{-1} disappears, indicating the consumption of the highly connected silicate species from the activating solution. The difference plot in **Figure 7** shows the changes between the starting point and the spectrum after 6 h more clearly. The emergence of the shoulder at 918 cm^{-1} and the shift of the band at 984 cm^{-1} can both be linked with the emergence of a new band around 950 cm^{-1}. These transitions are associated with the observation from Mössbauer spectroscopy: the incorporation of Fe^{3+} in the silicate network (see the calculations in previous paragraph suggesting the presence of Q^4(1Fe) and Q^4(2Fe) Si) and thus the change from Si-O-Si linkages in the activating solution toward Si-O-Fe linkages in the IP binder results in a lower wavenumber of the Si-O stretching band in the IPs with respect to the activating solution. The position of the maximum of the Si-O stretching band after 28 days is observed at 959 cm^{-1}, which is similar to what is observed for Si-O-Al linkages in aluminosilicate IPs (950–1,000 cm^{-1}) (Rahier et al., 2007; Rees et al., 2007) and in previous work which suggested that Fe has a similar impact on the band (Peys et al., 2017; Onisei et al., 2018). In general, this shift of the stretching band to lower wavenumbers is due to the widening of the Si-O-T distance, compared to Si-O-Si, and is observed in a wide variety of materials (Henderson and Taylor, 1979).

Using the information from the above experiments it is now possible to suggest a reaction scheme for the Fe-rich IPs. A schematic representation of the reactions is shown in **Figure 8**. After dissolution, Fe-silicate species are present in the pregnant activating solution. The concentration of these species rises until polymerization takes place into the partially oxidized binder, which consists of tetrahedral Fe^{3+} and octahedral Fe^{2+} of which at least one should be present in the silicate framework. For the mixture studied in the present paper the starting time of polymerization-oxidation should be between 3 and 6 h at 20°C. The dissolution of the slag and polymerization and oxidation is

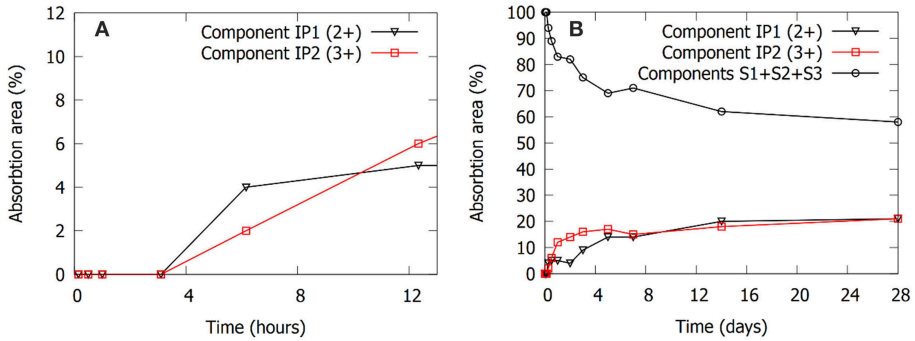

FIGURE 5 | Evolution of the absorption areas of components IP1, IP2, and the sum of absorption areas of components S1, S2, and S3. **(A)** Shows the short term (≤12 h) evolution of the absorption areas of the IP1 and IP2 components. The IP binder components only start forming after 3 h (0.125 days). **(B)** Shows the evolution of the absorption areas up to 28 days of curing.

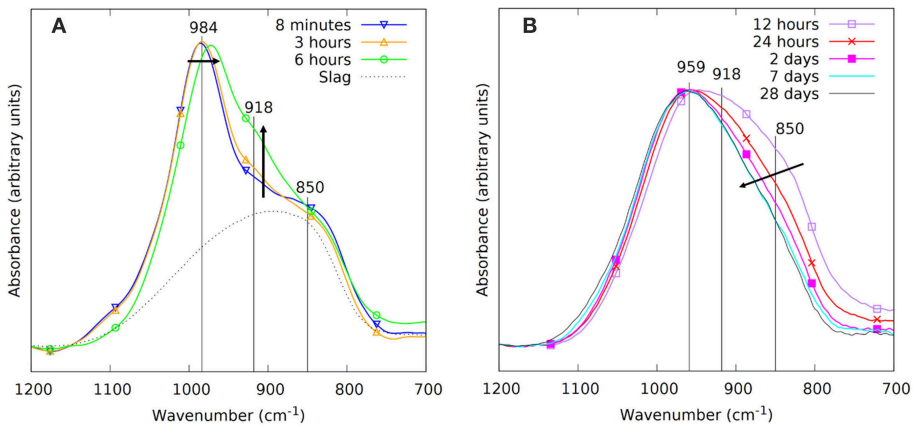

FIGURE 6 | The FTIR spectra during the first 28 days of reaction. The spectra before setting are shown on the left in **(A)**, these thus consider measurements in the liquid state, with the liquid in direct contact with the ATR crystal. The measurements on powdered samples after setting, pressed against the ATR crystal, are shown on the right in **(B)**.

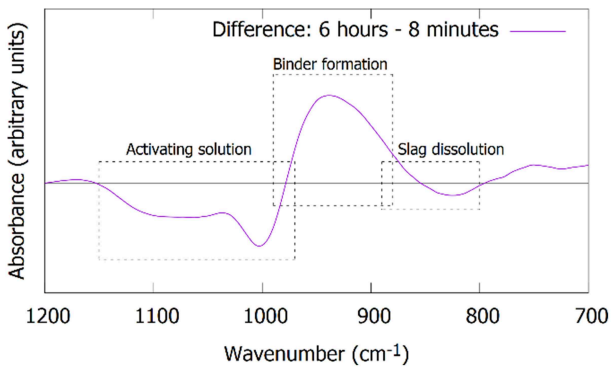

FIGURE 7 | Difference plot of the FTIR spectra after 6 h compared to 8 min, revealing more clearly the changes: (1) transformation of the activating solution, (2) the formation of the binder phase, and (3) the dissolution of the slag.

ongoing until at least 28 days after mixing, however, it is very likely that the time-scale for finalizing the reactions is longer than the 28 days presented here. A comparison with previous work (Onisei et al., 2018; Simon et al., 2018), where the contribution of the Fe^{3+} binder component was much larger and no Fe^{2+} binder component was observed, shows that a more complete oxidation happens in later stages of the reaction or during intensive milling.

Future work will study in detail the transition from the 28 days study presented here, revealing a combination of $^{IV}Fe^{3+}$ and $^{VI}Fe^{2+}$ in the binder, toward the fully oxidized structure observed in previous work (Onisei et al., 2018; Peys et al., 2018b; Simon et al., 2018).

CONCLUSIONS

The evolution of the molecular structure during synthesis of Fe-rich slag based IPs has been monitored with ^{57}Fe Mössbauer spectroscopy and infrared spectroscopy. Fe-rich slags mainly consist of Fe^{2+} (85% absorption area in Mössbauer spectrum), whereas an IP binder was shown to contain both Fe^{2+} and Fe^{3+}. The first appearance of a new Fe^{3+} band in Mössbauer spectroscopy occurs after 6 h of reaction at 20°C, and the

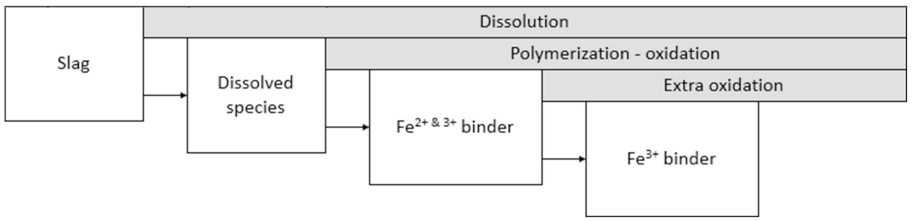

FIGURE 8 | Schematic of the sequence of reaction stages.

main oxidation happened during the first 24 h. It is suggested that this Fe^{3+} is situated in tetrahedral coordination in the silicate framework. At the same time, a novel octahedral Fe^{2+} component is found to form in the binder phase with Mössbauer parameters similar to fayalite or clay minerals and which approximately follows the same kinetics of formation as the Fe^{3+} state. The fact that these new components only develop from 6 h after mixing and are mostly occurring within the first 24 h is in line with the onset of the polymerization exotherm in calorimetry, between 3 and 6 h, and the fact that the largest part of the heat from the reactions evolved in the first 24 h. ATR-FTIR spectroscopy suggested the incorporation of Fe in the silicate network. At 28 days, a total of 42% of the absorption area (AA) in the Mössbauer spectrum was attributed to the binder phase, comprised 21% of Fe^{2+} and 21% of Fe^{3+}, compared to 86% Fe^{2+} and 14% Fe^{3+} in the precursor slag. This results in a Na/Fe^{3+} ratio of ∼1 in the mixture from which the binder phase is formed, revealing an important similarity with geopolymers where a Na/Al^{3+} ratio of 1 is observed. The Fe^{2+} binder state was not observed previously, whereas the Fe^{3+} binder state always had a higher absorption area in previous work. This is probably associated with oxidation at later stages or/and with the milling procedures performed in previous work which increase the surface of the material exposed to air and consequently to oxidation.

DATA AVAILABILITY

The datasets generated for this study are available on request to the corresponding author.

AUTHOR CONTRIBUTIONS

AP lead all parts of the paper making process. AD supported in designing, performing, analyzing, and discussing the ^{57}Fe Mössbauer spectroscopy measurements. VH helped in designing, analyzing and discussing the FTIR, and performed the measurements. HR, BB, and YP are the supervisors of AP and provided feedback, and inspiration in all aspects.

FUNDING

AP is grateful to the Research Foundation–Flanders (FWO) for the Ph.D. grant. VH is thankful to VLAIO for the Baekeland scholarship.

SUPPLEMENTARY MATERIAL

The Supplementary Material for this article can be found online at: https://www.frontiersin.org/articles/10.3389/fmats.2019.00212/full#supplementary-material

REFERENCES

Bae, S., Jee, H., Kanematsu, M., Shiro, A., Machida, A., Watanuki, T., et al. (2018). Pair distribution function analysis of nanostructural deformation of calcium silicate hydrate under compressive stress. *J. Am. Ceram. Soc.* 101, 408–418. doi: 10.1111/jace.15185

Bell, J. L., Sarin, P., Driemeyer, P. E., Haggerty, R. P., Chupas, P. J., and Kriven, W. M. (2008). X-ray pair distribution function analysis of a metakaolin-based, $KAlSi_2O_6.5.5H_2O$ inorganic polymer (geopolymer). *J. Mater. Chem.* 18, 5974–5981. doi: 10.1039/B808157C

Chemtob, S. M., Nickerson, R. D., Morris, R. V., Agresti, D. G., and Catalano, J. G. (2015). Synthesis and structural characterization of ferrous trioctahedral smectites: implications for clay mineral genesis and detectability on Mars. *J. Geophys. Res. Planet.* 120, 1119–1140. doi: 10.1002/2014JE004763

Coey, J. M. D. (1984). "Mössbauer spectroscopy of silicate minerals," in *Mössbauer Spectroscopy Applied to Inorganic Chemistry*, ed G. J. Long (Boston, MA: Springer), 443–509.

Cuesta, A., Zea-Garcia, J. D., De la Torre, A. G., Santacruz, I., and Aranda, M. A. G. (2019). Synchrotron pair distribution function analyses of ye'elimite-based pastes. *Adv. Cem. Res.* 31, 138–146. doi: 10.1680/jadcr.18.00097

Davidovits, J. (2008). *Geopolymer Chemistry and Applications.* Saint-Quentin: Geopolymer Institute.

Douglas, K. T., Howlin, B., and Silver, J. (1984). Solution Chemistry and mössbauer study of iron(II) and iron(III) complexes from gallocyanine. *Inorg. Chim. Acta* 92, 135–140. doi: 10.1016/S0020-1693(00)80010-9

Douvalis, A. P., Polymeros, A., and Bakas, T. (2010). IMSG09: a ^{57}Fe-^{119}Sn Mössbauer spectra computer fitting program with novel interactive user interface. J. Phys. 217:012014. doi: 10.1088/1742-6596/217/1/012014

Engelhardt, G., Hoebbel, D., Tarmak, M., Samoson, A., and Lippmaa, E. (1982). ^{29}Si-NMR-Untersuchungen zur Anionenstruktur von Kristallinen Tetramethylammonium-alumosilicaten und alumosilicatlösungen. *Z. Anorg. Allg. Chem.* 484, 22–32. doi: 10.1002/zaac.19824840103

Ferrow, E. (1987). Mössbauer effect and X-ray diffraction studies of synthetic iron bearing trioctahedral micas. *Phys. Chem. Miner.* 14, 276–280. doi: 10.1007/BF00307994

Garg, N., and White, C. E. (2017). Mechanism of zinc oxide retardation in alkali-activated materials: an *in situ* X-ray pair distribution function investigation. *J. Mater. Chem. A* 5, 11794–11804. doi: 10.1039/C7TA00412E

Geng, G., Myers, R. J., Qomi, M. J. A., and Monteiro, P. J. M. (2017). Densification of the interlayer spacing governs the nanomechanical properties of calcium-silicate-hydrate. *Sci. Rep.* 7:10986. doi: 10.1038/s41598-017-11146-8

Génin, J.-M. R., Olowe, A. A., Refait, P., and Simon, L. (1996). On the stoichiometry and Pourbaix diagram of Fe(II)-Fe(III) hydroxyl-sulphate or sulphate-containing green rust 2: an electrochemical and Mössbauer spectroscopy study. *Corros. Sci.* 38, 1751–1762. doi: 10.1016/S0010-938X(96)00072-8

Grangeon, S., Fernandez-Martinez, A., Baronnet, A., Marty, N., Poulain, A., Elkaïm, E., et al. (2017). Quantitative X-ray pair distribution function analysis of nanocrystalline calcium silicate hydrates: a contribution to the understanding of cement chemistry. *J. Appl. Crystallogr.* 50, 14–21. doi: 10.1107/S1600576716017404

Greenwood, N. N., and Gibb, T. C. (1971). *Mössbauer Spectroscopy*. London: Chapman and Hall.

Hajimohammadi, A., Provis, J. L., and van Deventer, J. S. J. (2010). Effect of alumina release rate on the mechanism of geopolymer gel formation. *Chem. Mater.* 22, 5199–5208. doi: 10.1021/cm101151n

Henderson, C. M. B., and Taylor, D. (1979). Infrared spectra of aluminogermanate- and aluminate-sodalites and a re-examination of the relationship between T-O bond length, T-O-T angle and the position of the main i.r. absorption band for compounds with framework structures. *Spectrochim. Acta A* 35, 929–953. doi: 10.1016/0584-8539(79)80016-1

Iacobescu, R. I., Cappuyns, V., Geens, T., Kriskova, L., Onisei, S., Jones, P. T., et al. (2017). The influence of curing conditions on the mechanical properties and leaching of inorganic polymers made of fayalitic slag. *Front. Chem. Sci. Eng.* 11, 317–327. doi: 10.1007/s11705-017-1622-6

Kamnev, A. A., Dykman, R. L., Kovacs, K., Pankratov, A. N., Tugarova, A. V., Homonnay, Z., et al. (2014). Redox interactions between structurally different alkylresorcinols and iron(III) in aqueous media: frozen-solution ^{57}Fe Mössbauer spectroscopic studies, redox kinetics and quantum chemical evaluation of the alkylresorcinol reactivities. *Struct. Chem.* 25, 649–657. doi: 10.1007/s11224-013-0367-1

Krebs, C., Price, J. C., Baldwin, J., Saleh, L., and Green, M. T., Bollinger, J. M. Jr. (2005). Rapid Freeze-quench ^{57}Fe Mössbauer spectroscopy: monitoring changes of an iron-containing active site during a biochemical reaction. *Inorg. Chem.* 44, 742–757. doi: 10.1021/ic048523l

Kriskova, L., Machiels, L., and Pontikes, Y. (2015). Inorganic polymers from a plasma convertor slag: effect of activating solution on microstructure and properties. *J. Sustainable Metal.* 1, 240–251. doi: 10.1007/s40831-015-0022-8

Kumar, S., Kumar, R., Alex, T. C., Bandopadhyay, A., and Mehrotra, S. P. (2007). Influence of reactivity of fly ash on geopolymerisation. *Adv. Appl. Ceram.* 106, 120–127. doi: 10.1179/174367607X159293

Lemougna, P. N., Chinje Melo, U. F., Delplancke, M.-P., and Rahier, H. (2014). Influence of the chemical and mineralogical composition on the reactivity of volcanic ashes during alkali activation. *Ceram. Int.* 40, 811–820. doi: 10.1016/j.ceramint.2013.06.072

Lemougna, P. N., MacKenzie, K. J. D., Jameson, G. N. L., Rahier, H., and Chinje Melo, U. F. (2013). The role of iron in the formation of inorganic polymers (geopolymers) from volcanic ash: a ^{57}Fe Mössbauer spectroscopy study. *J. Mater. Sci.* 48, 5280–5286. doi: 10.1007/s10853-013-7319-4

Machiels, L., Arnout, L., Jones, P. T., Blanpain, B., and Pontikes, Y. (2014). Inorganic polymer cement from Fe-silicate glasses: varying the activating solution to glass ratio. *Waste Biomass Valori.* 5, 411–428. doi: 10.1007/s12649-014-9296-5

Machiels, L., Arnout, L., Yan, P., Jones, P. T., Blanpain, B., and Pontikes, Y. (2017). Transforming enhanced landfill mining derived gasification/vitrification glass into low-carbon inorganic polymer binders and building products. *J. Sustainable Metall.* 3, 405–415. doi: 10.1007/s40831-016-0105-1

Mysen, B. O. (2006). The structural behavior of ferric and ferrous iron in aluminosilicate glass near meta-aluminosilicate joins. *Geochim. Cosmochim. Acta* 70, 2337–2353. doi: 10.1016/j.gca.2006.01.026

Onisei, S., Douvalis, A. P., Malfliet, A., Peys, A., and Pontikes, Y. (2018). Inorganic polymers made of fayalite slag: on the microstructure and behavior of Fe. *J. Am. Ceram. Soc.* 101, 2245–2257. doi: 10.1111/jace.15420

Onisei, S., Lesage, K., Blanpain, B., and Pontikes, Y. (2015). Early age microstructural transformations of an inorganic polymer made of fayalite slag. *J. Am. Ceram. Soc.* 98, 2269–2277. doi: 10.1111/jace.13548

Peys, A., Arnout, L., Blanpain, B., Rahier, H., Van Acker, K., and Pontikes, Y. (2018a). Mix-design parameters and real-life considerations in the pursuit of lower environmental impact inorganic polymers. *Waste Biomass Valori.* 9, 879–889. doi: 10.1007/s12649-017-9877-1

Peys, A., Arnout, L., Hertel, T., Iacobescu, R. I., Onisei, S., Kriskova, L., et al. (2017). "The use of ATR-FTIR spectroscopy in the analysis of iron-silicate inorganic polymers," in *Proceedings of the 5th International Slag Valorisation Symposium* (Leuven). 385–388.

Peys, A., Rahier, H., and Pontikes, Y. (2016). Potassium-rich biomass ashes as activators in metakaolin-based inorganic polymers. *Appl. Clay Sci.* 119, 401–409. doi: 10.1016/j.clay.2015.11.003

Peys, A., White, C. E., Olds, D., Rahier, H., Blanpain, B., and Pontikes, Y. (2018b). Molecular structure of CaO-FeO_x-SiO_2 glassy slags and resultant inorganic polymer binders. *J. Am. Ceram. Soc.* 101, 5846–5857. doi: 10.1111/jace.15880

Pontikes, Y., Machiels, L., Onisei, S., Pandelaers, L., Geysen, D., Jones, P. T., et al. (2013). Slags with a high Al and Fe content as precursors for inorganic polymers. *Appl. Clay Sci.* 73, 93–102. doi: 10.1016/j.clay.2012.09.020

Provis, J. L., and van Deventer, J. S. J. (2014). *Alkali Activated Materials: State-of-the-Art Report, RILEM TC 224-AAM*. New York, NY: Springer.

Rahier, H., Denayer, J. F., and Van Mele, B. (2003). Low-temperature synthesized aluminosilicate glasses: Part IV Modulated DSC study on the effect of particle size of metakaolinite on the production of inorganic polymer glasses. *J. Mater. Sci.* 38, 3131–3136. doi: 10.1023/A:1024733431657

Rahier, H., Simons, W., Van Mele, B., and Biesemans, M. (1997). Low-temperature synthesized aluminosilicate glasses: part III Influence of the composition of the silicate solution on production, structure and properties. *J. Mater. Sci.* 32, 2237–2247. doi: 10.1023/A:1018563914630

Rahier, H., Wastiels, J., Biesemans, M., Willem, R., Van Assche, G., and Van Mele, B. (2007). Reaction mechanism, kinetics and high temperature transformations of geopolymers. *J. Mater. Sci.* 42, 2982–2996. doi: 10.1007/s10853-006-0568-8

Rees, C. A., Provis, J. L., Lukey, G. C., and van Deventer, J. S. J. (2007). *In situ* ATR-FTIR study of the early stages of fly ash geopolymer gel formation. *Langmuir* 23, 9076–9082. doi: 10.1021/la701185g

Silver, J., Morrison, I. E. G., and Rees, L. V. C. (1979). A Mössbauer spectroscopic study of frozen solutions of FeCl3 – phenols. *Inorg. Nuc. Chem. Lett.* 15, 433–436. doi: 10.1016/0020-1650(79)80103-8

Simon, S., Gluth, G., Peys, A., Onisei, S., and Pontikes, Y. (2018). The fate of iron during the alkali-activation of synthetic (CaO-)FeO_x-SiO_2 slags: an Fe K-edge XANES study. *J. Am. Ceram. Soc.* 101, 2107–2118. doi: 10.1111/jace.15354

Van De Sande, J., Peys, A., Hertel, T., Onisei, S., Blanpain, B., and Pontikes, Y. (2017). "Glass forming ability of slags in the FeO_x-SiO_2-CaO system and properties of the inorganic polymers made thereof," in *Proceedings of the 5th International Slag Valorisation Symposium* (Leuven), 397–400.

Vandenberghe, R. E., and De Grave, E. (2013). "Application of Mössbauer spectroscopy in earth sciences," in *Mössbauer Spectroscopy: Tutorial Book*, eds Y. Yoshida and G. Langouche (Berlin Heidelberg: Springer), 91–185.

White, C. E., Page, K., Henson, N. J., and Provis, J. L. (2013a). *In situ* synchrotron X-ray pair distribution function analysis of the early stages of gel formation in metakaolin-based geopolymers. *Appl. Clay Sci.* 73, 17–25. doi: 10.1016/j.clay.2012.09.009

White, C. E., Provis, J. L., Bloomer, B., Henson, N. J., and Page, K. (2013b). *In situ* X-ray pair distribution function analysis of geopolymer gel nanostructure formation kinetics. *Phys. Chem. Chem. Phys.* 15, 8573–8582. doi: 10.1039/C3CP44342F

White, C. E., Provis, J. L., Llobet, A., Proffen, T., and van Deventer, J. S. J. (2011). Evolution of local structure in geopolymer gels: an *in situ* neutron pair distribution function analysis. *J. Am. Ceram. Soc.* 94, 3532–3539. doi: 10.1111/j.1551-2916.2011.04515.x

White, C. E., Provis, J. L., Proffen, T., Riley, D. P., and van Deventer, J. S. J. (2010). Combining density functional theory (DFT) and pair distribution function (PDF) analysis to solve the structure of metastable materials: the case of metakaolin. *Phys. Chem. Chem. Phys.* 12, 3239–3245. doi: 10.1039/B922993K

Yang, K., and White, C. E. (2016). Modeling the formation of alkali aluminosilicate gels at the mesoscale using coarse-grained Monte Carlo. *Langmuir* 32, 11580–11590. doi: 10.1021/acs.langmuir.6b02592

Zhang, Z., Provis, J. L., Wang, H., Bullen, F., and Reid, A. (2013). Quantitative kinetic and structural analysis of geopolymers. Part 2. Thermodynamics of sodium silicate activation of metakaolin. *Thermochim. Acta* 565, 163–171. doi: 10.1016/j.tca.2013.01.040

Zhou, Y., Huo, D., Manzano, H., Orozco, C. A., Geng, G., Monteiro, P. J. M., et al. (2017). Interfacial connection mechanisms in calcium-silicate-hydrates/polymer nanocomposites: a molecular dynamics study. *ACS Appl. Mater. Inter.* 9, 41014–41025. doi: 10.1021/acsami.7b12795

Conflict of Interest Statement: The authors declare that the research was conducted in the absence of any commercial or financial relationships that could be construed as a potential conflict of interest.

frontiers in Materials

ORIGINAL RESEARCH
published: 28 August 2019
doi: 10.3389/fmats.2019.00211

Microstructure and Composition of Hardened Paste of Soda Residue-Slag-Cement Binding Material System

Rongjie Song[1,2], *Qingxin Zhao*[1,2], *Jinrui Zhang*[3]* and *Jizhong Liu*[1,2]

[1] State Key Laboratory of Metastable Materials Science and Technology, Yanshan University, Qinhuangdao, China, [2] Key Laboratory of Green Construction and Intelligent Maintenance for Civil Engineering of Hebei Province, Yanshan University, Qinhuangdao, China, [3] State Key Laboratory of Hydraulic Engineering Simulation and Safety, Tianjin University, Tianjin, China

In order to utilize industrial waste soda residue, a kind of binding material system based on soda residue-slag-cement has been developed. The microstructure and composition of hardened paste of the binding material system after curing for 28 days was analyzed by means of scanning electron microscope (SEM), energy dispersive X-ray spectroscopy (EDS), X-ray diffraction (XRD), and thermogravimetric-differential scanning calorimetry (DSC-TG). The main hydration products of binding material system after curing for 28 days were C-S-H gel and $3CaO{\cdot}Al_2O_3{\cdot}CaCl_2{\cdot}10H_2O$ crystal (Friedel's salt) with a needle bar and irregular shape. The Ca/Si ratio of C-S-H gel in hydration products varied from 0.7 to 1.4, the ratio of n(Cx-S-Hy)/n($3CaO{\cdot}Al_2O_3{\cdot}CaCl_2{\cdot}10H_2O$) varied in the range of 1.8–6.4. The C-S-H gel and Friedel's salts that densely arranged and closely bonded with pores and cracks constituted the main strength source of the whole soda residue-slag-cement binding material system.

Keywords: soda residue, slag, binding material, hydration products, Friedel's salt

OPEN ACCESS

Edited by:
John L. Provis, University of Sheffield, United Kingdom

Reviewed by:
Ionut Ovidiu Toma, Gheorghe Asachi Technical University of Iaşi, Romania
Marija Nedeljkovic, Delft University of Technology, Netherlands

***Correspondence:**
Jinrui Zhang
jinrui.zhang@tju.edu.cn

Specialty section:
This article was submitted to Structural Materials, a section of the journal Frontiers in Materials

Received: *09 October 2018*
Accepted: *14 August 2019*
Published: *28 August 2019*

Citation:
Song R, Zhao Q, Zhang J and Liu J (2019) Microstructure and Composition of Hardened Paste of Soda Residue-Slag-Cement Binding Material System. Front. Mater. 6:211. doi: 10.3389/fmats.2019.00211

INTRODUCTION

The rapid development of industry has driven the world economy. However, the resulting industrial waste occupied the land and polluted the soil, water and air, which caused pollution to the global environment (Chen, 2018). Researchers around the world have conducted many studies on the reuse of industrial wastes. There are various types of industrial by products, such as calcium carbide slag, blast furnace slag, fly ash, and so on. The technique of using calcium carbide slag as construction materials and alkaline activator has been successfully used by researchers (Bilondi et al., 2018; Hanjitsuwan et al., 2018; Siddiqua and Barreto, 2018). Zhang et al. (2017) used fly ash and high-magnesium nickel slag as solid materials to manufacture geopolymer cement under the room temperature conditions. The results showed that the compressive strengths of the geopolymer cements can achieve 60 MPa, which is comparable to hardened Portland cements and adequate for construction purposes. Wiemes et al. (2017) conducted an experiment with the incorporation of different types of industrial waste in brick manufacturing process. Three types of wastes were mixed with clay: automotive industry waste sludge, glass waste and wood ash. The results showed that brick production can be obtained with different types of industrial waste. Amin et al. (2017) researched chloride resistant cement from industrial waste through geopolymerization, the test showed that the highest compressive strength of cement was 18.85 MPa and resistance to chloride

attack was recorded for geopolymer with silica to alumina ratio of 2.7. Meanwhile, the resistance of geopolymer to magnesium chloride is greater than that of sodium chloride, and the attack of chloride cannot affect the geopolymer network when having optimum silica to alumina ratio. Self-compacting concrete was prepared by El Mir and Nehme (2017) utilizing industrial waste perlite powder, the results indicated that waste perlite powder had a significant pozzolanic effect on the concrete microstructure, resulting in a positive impact on the compressive strength of the concrete.

Soda residue was an industrial waste produced in the process of soda ash production by ammonia-soda process, whose chemical compositions are $CaCO_3$ and soluble salt chloride. The storage and emission of soda residue had caused serious environmental problem (Yan, 2015; Gomes et al., 2016). The accumulation of soda residue will change the acidity and alkalinity of the soil in the region, cause soil salinization and affect the normal growth of vegetation. As time goes by, chloride ions in soda residue will gradually infiltrate into the ground, causing different degrees of pollution to underground water sources and seriously threatening the safety of surrounding residents' drinking water. The soda residue mountain formed by the accumulation of soda residue will occur landslides under the action of earthquake and other external forces, endangering the safety of people's lives and property. How to use soda residue has become the focus of attention in the engineering field. Therefore, a great deal of research work has been carried out by scholars. Uçal et al. (2018) investigated hydration characteristics of alinite cement, which was produced by using soda waste sludge as raw material. It was found that induction period of alinite cement was around 15–20 min and unlike Portland cement, hydration did not practically stop during this period. Up to 12% gypsum addition to alinite cement resulted in increased compressive strength. Zhao et al. (2019) had studied the crucial properties of fly ash-based geopolymers incorporating soda residue. The research showed that the compressive strength of the alkali-activated fly ash-based samples incorporating about 20% soda residue curing for 60 and 180 days was 13.5 and 18.0 MPa, the geopolymers had low shrinkage and good thermal stability. Zhang et al. (2013) had prepared the concrete with some soda residue replacing the cement by mass. The mix proportion of the concrete was 45–49% of stone, 25–29% of sand, 10–14% of cement, 5–10% of soda residue, and 5–8% of water. The research showed that the concrete had good frost resistance and wear resistance. Liu et al. (2017) had researched the property of polymer after mixing soda residue and fly ash. The research showed that when the mass ratio of soda residue and fly ash was <0.36, the flexural strength and compressive strength of the fly ash-NaOH system increased with the proportion of soda residue, the addition of soda residue had a significant modification effect on the development of the system strength. Sun and Gu (2014) prepared a new soda residue curing agent by using soda residue, slag and fly ash as the main raw materials and a proper amount of desulphurization gypsum and compound activator were added to these main materials. The physical and mechanical property of the curing agent basically met the technical parameters of the P.C 32.5 composite cement. Liu et al. (2016) researched the baking-free brick that were prepared with soda residue as the main material. It was found that when soda residue, fly ash, steel slag, and stone powder were prepared according to the mass ratio of 4:3:2:1, the compressive strength of baking-free brick curing for 7 days was 14.0 MPa and was 20.6 MPa curing for 28 days. Sun et al. (2012) improved the expansive soil with soda residue as an additive. The research showed that the relative density, liquid limit, plastic index, free expansion rate, and load expansion of the expansive soil decreased noticeably with the increase of soda residue content, which indicated that the soda residue had obvious improvement effect on expansibility of expansive soil.

However, the consumption of soda residue still cannot meet the needs of society and environment. In order to expand the application scope and further reduce the pressure on the environment, a new kind of binding material system based on soda residue-slag-cement was developed through a series of experiments. The microstructure and composition were analyzed by the scanning electron microscope (SEM), energy dispersive X-ray spectroscopy (EDS), thermogravimetric-differential scanning calorimetry (DSC-TG), and X-ray diffraction (XRD).

EXPERIMENTAL

Raw Materials

The soda residue used in the experiment came from San You group in Tangshan, Hebei, which was dried and crushed into fine powder particles with the maximum diameter of 0.16 mm. The XRD pattern was shown in **Figure 1**. It was apparent that the peak of $CaCO_3$, $CaSO_4$, $CaCl_2$, and NaCl appeared in **Figure 1**, which indicated that $CaCO_3$, $CaSO_4$, $CaCl_2$, and NaCl were contained in the identified phases in the XRD diffractogram of soda residue. The slag in the experiment was S95 grade granulated blast furnace slag powder. The cement used in the soda residue-slag-cement binding material system was Portland cement (P·II 42.5), cement used in preparing cement mortar specimen for strength comparison was ordinary Portland cement (P·O 42.5R). Both slag and cement came from Qinhuangdao municipal construction group co., LTD in Hebei. The chemical components of soda residue, slag and cement were shown in **Tables 1**, **2** respectively. The particle size of nature quartz river sand ranged from 0.16 to 2.36 mm.

Preparation of Mortar Specimens

In the mortar specimen mix design, the water-binder ratio was fixed at 0.5, the sand-binder ratio was fixed as 3:1 and the mix proportions of the binding materials were shown in **Table 3**. The cement mortar was stirred evenly and the specimens of 40 mm $\times$ 40 mm $\times$ 160 mm were prepared. All mortar specimens were cured in the standard curing box of a controlled environment of $(20 \pm 2)^{\circ}C$ and relative humidity $\geq$ 95% for 28 days and then used to test the flexural strength and compressive strength. Each group was molded into six mortar specimens, which were then taken for average calculation.

Methods

SEM and EDS Test of Paste Specimens

According to the test method described in the literature (Aughenbaugh et al., 2016), the paste specimens of 20 mm $\times$

20 mm × 80 mm were prepared according to the mix proportion in **Table 3**, and then removed into containers of a controlled environment of (20 ± 2)°C and relative humidity ≥ 95% to be cured to the ages of 28 days. The microstructure of the hardened pastes curing for 28 days was observed by a Hitachi-3400N SEM after the vacuum and gold spray treatment, and the content of the elements of Ca, Si, and Cl in hydration products was analyzed by the energy dispersive EDS, then the ratio of Ca/Si in the C-S-H gel and the ratio of Si/Cl in the hydration products were calculated.

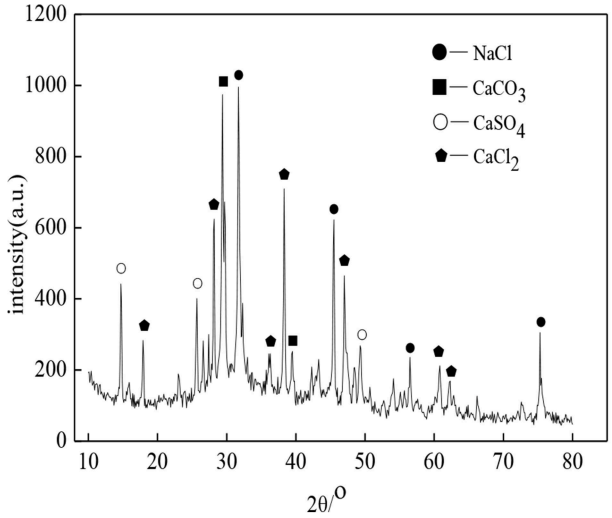

FIGURE 1 | XRD diffractogram of soda residue.

Mineralogical Composition

The component of hydration product was determined by XRD. The paste specimens were taken from the non-carbonated zone. During the testing period, the specimens were processed as following steps. Firstly, the non-carbonated specimens were split into small pieces and put in ethanol and were ground into fine powder particles till they all passed the sieve with the diameter of 0.12 mm. Secondly, the powder was filtered in a vacuum by the suction filter bottle and diluted five times with ethanol and twice with ether. Then, the powder particles were dried in a vacuum drying oven with desiccant at 105°C for 24 h. Finally, the powder particles were placed in the small glass bottles to be used for XRD. The 2θ values ranged from 10° to 80° and the scanning rate applied was 1°/min for all specimens.

DSC-TG Test of Hydration Product Component

Thermogravimetry-differential scanning calorimetries (DSC-TG) of the paste specimens curing for 28 days were carried out by the STA 449F5 integrated thermal analyzer (Zhao et al., 2016). Firstly, the soda residue, slag and cement were dried in an oven at 105°C for 12 h, and the coarse particles over 0.9 mm were removed by a standard sieve. Secondly, the flesh pastes were prepared based on mix proportions in **Table 3,** and the water-binder ratio was 0.5 for all the pastes. Then the flesh pastes were sealed in plastic bags and then cured under the environment of 20 ± 2°C and relative humidity ≥ 95%.

At the age of 28 days, the soda residue-slag-cement paste specimens were processed as per the following steps. Firstly, the specimens were split into small pieces and put in ethanol, and were then crushed into fine powder particles until all passed the sieve with the diameter of 0.12 mm. Secondly, the powder

TABLE 1 | Chemical composition of soda residue w/%.

Cl^-	CaO	Na_2O	SiO_2	MgO	SO_3	Al_2O_3	K_2O	Fe_2O_3
39.11	35.12	13.04	4.17	2.97	2.80	2.06	0.33	0.29

TABLE 2 | Chemical compositions of cement and slag w/%.

Materials	Chemical compositions (by mass)/%										
	CaO	SiO_2	Al_2O_3	Fe_2O_3	MgO	TiO_2	K_2O	SO_3	MnO	Na_2O	P_2O_5
PC	63.70	20.30	4.81	3.24	3.26	0.33	1.25	2.64	0.12	0.03	0.12
OPC	56.50	20.60	6.27	2.79	3.15	0.26	2.34	3.28	0.16	0.05	–
Slag	34.50	28.80	17.10	0.69	11.30	2.79	0.51	2.55	0.31	0.37	–

TABLE 3 | The mix proportion of binders and the strength of mortar specimens.

Sample no.	Mix proportion (by mass)/%			7 days compressive strength/MPa	7 days flexural strength/MPa	28 days compressive strength/MPa	28 days flexural strength/MPa
	Cement	Slag	Soda residue				
D1	20	70	10	13.5	2.1	44.6	6.7
D2	20	60	20	15.3	2.5	45.1	7.4
D3	20	50	30	12.6	1.8	39.6	5.9

was filtered in a vacuum by the suction filter bottle and diluted five times with ethanol and twice with ether. Then the powder samples were dried in a vacuum drying oven with desiccant at 105°C for 24 h. Finally, DSC-TG of the paste specimens curing for 28 days was carried out by the STA 449F5 integrated thermal analyzer. To prevent the carbonization of the specimens during the heating process, the Ar was used as the protective gas and the temperature rising rate was 10°C/min.

RESULTS AND DISCUSSION

Mechanical Properties of Mortar Specimens

Table 3 shows the flexural strength and compressive strength of mortar specimens after curing for 7 days and 28 days, with different percentages of binding materials. It can be seen from **Table 3** that the mechanical property of D2 group curing for 28 days was optimum when the soda residue, slag and cement were prepared as the mass percentage of 2:6:2. **Figure 2** shows the compressive strength of specimens at the age of 7, 28, 60, 90, and 120 days under the ratio of D2 group and the compressive strength of P.O 42.5R cement mortar specimen at the same age. It can be seen from **Figure 2** that the compressive strength of mortar specimen of D2 group curing after 28 days was quite close to the strength of mortar specimens of P.O 42.5R cement.

It was apparent that compressive strength of D2 group curing for 7 days was 15.3 MPa, and the value was much lower than that of P.O 42.5R cement mortar specimens at age of 7 days. Slag is a potentially active cementitious material. The alkaline environment of soda residue makes the slag hydrate slowly. At the beginning, less hydration products are generated, and the system is less dense. With increasing age, the number of hydration products increases and the density increases gradually, and the compressive strength at 28 days increases significantly, reaching 45.1 MPa.

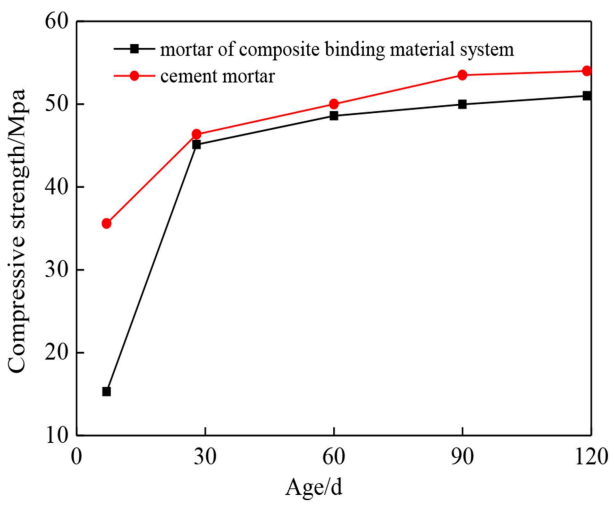

FIGURE 2 | Compressive strength comparison between the soda residue-slag-cement binding system and ordinary Portland cement mortar.

Micro-Morphology Analysis of Hydration Products

Figure 3 shows the SEM photographs of paste specimens of D2 group curing for 28 days. **Figures 3A–D** indicated that the hydration products of D2 group cured to the ages of 28 days were rich, and the microstructure of hardened paste was formed basically. The hydration products were closely bonded with pores and cracks. The crystals were rod-shaped and irregularly shaped, and were distributed on the surface of hydration products. At the same time, a small amount of unreacted binding materials particles were distributed around the hydration products.

Energy Dispersive Spectrum Analysis of Hydration Products

Slices of paste of D2 group curing for 28 days were impregnated and polished to prepare BSE samples as shown in **Figure 3E**. In the SEM-BSE photographs, the detection dots were marked, respectively, in the position of different brightness in the image, and EDS analysis was carried out on every detection dot, respectively. The marked position was shown in **Figure 3F** and the detection results were shown in **Figure 4** and **Table 4**.

It can be seen from **Table 4** that the content of Cl elements at each detection position was far higher than the content of the S elements in the hydration products of D2 group. Therefore, it was inferred that there was a compound containing Cl elements in the hydration products. Meanwhile, it can be seen that the content of Si elements in the detection range was relatively large, because the diameter of the spectrum analysis range was larger than the size of the compound containing Cl elements, thus causing the existence of C-S-H gel in the various measuring regions. In the analysis of elements, it was assumed that all Si elements came from C-S-H gel and the hydration product containing Cl elements was $3CaO{\cdot}Al_2O_3{\cdot}CaCl_2{\cdot}10H_2O$ crystal (Shao et al., 2013). Then the numbers of atoms of the Ca and Cl elements were subtracted from the numbers of atoms of the element in the measured region according to the elemental composition of $3CaO{\cdot}Al_2O_3{\cdot}CaCl_2{\cdot}10H_2O$, subsequently, the numbers of atoms of Ca and Si elements in C-S-H gel were calculated. The result of the atomic weight of Ca and Si elements in C-S-H gel were shown in **Table 5**. It can be seen from **Table 5** that the ratio of Ca/Si in C-S-H gel on the spot 1 was 0.7, the ratio of Ca/Si in C-S-H gel on the spot 2 was 1.2, the ratio of Ca/Si in C-S-H gel on the spot 3 was 1.1, and the ratio of Ca/Si in C-S-H gel on the spot 4 was 1.4 when the hydration product containing Cl element was $3CaO{\cdot}Al_2O_3{\cdot}CaCl_2{\cdot}10H_2O$ crystal. The ratio of Ca/Si of the remaining portion in detection region was within the range of Ca/Si ratio of C-S-H gel, thus, it was proved that the hydration product containing Cl elements was $3CaO{\cdot}Al_2O_3{\cdot}CaCl_2{\cdot}10H_2O$ crystal.

In order to characterize the relative content of C-S-H gel and $3CaO{\cdot}Al_2O_3{\cdot}CaCl_2{\cdot}10H_2O$ crystal in the hydration product of D2 group, the ratio of Si/Cl was introduced, the ratio of which was shown in **Table 5**. It could be seen from **Table 5** that the ratio of Si/Cl was 3.0 on the spot 1, the ratio of Si/Cl was 1.8 on the spot 2, the ratio of Si/Cl was 0.9 on the spot 3, and the ratio of Si/Cl was 3.2 on the spot 4. It was assumed that all the Si elements were

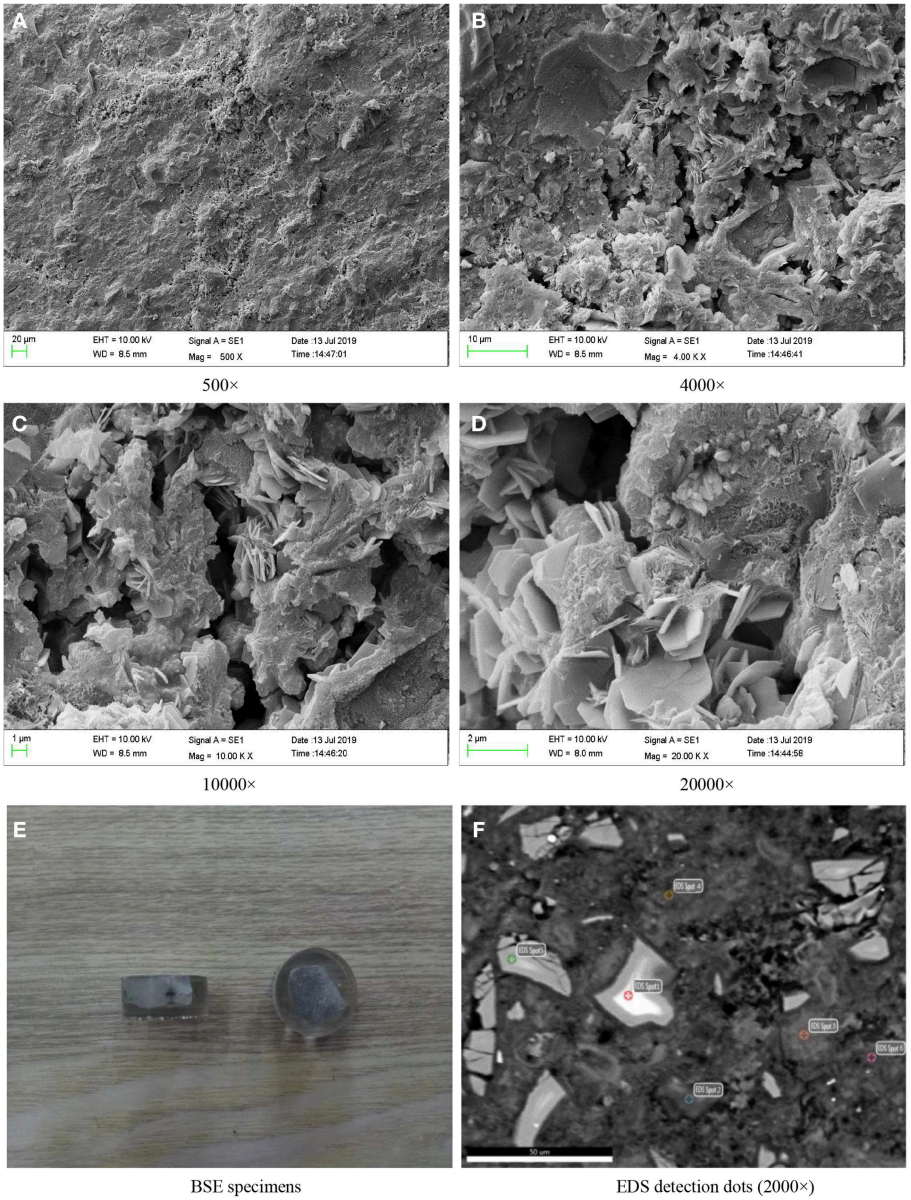

FIGURE 3 | SEM images of the paste specimens of D2 group curing for 28 days and BSE specimens. **(A)** 500×. **(B)** 4000×. **(C)** 10000×. **(D)** 20000×. **(E)** BSE specimens. **(F)** EDS detection dots (2000×).

derived from the C-S-H gel and all the Cl element were derived from the $3CaO{\cdot}Al_2O_3{\cdot}CaCl_2{\cdot}10H_2O$ crystal. Meanwhile, the content of Si element in the C-S-H gel was the benchmark, it was known that the ratio of n(C-S-H)/n($CaO{\cdot}Al_2O_3{\cdot}CaCl_2{\cdot}10H_2O$) on spot 1, spot 2, spot 3, and spot 4 was 6.0, 3.6, 1.8, and 6.4, respectively. Each detection position was representative when the detection marker was made on the position of different brightness in the EDS spectrum analysis, so the data measured at four positions also represent the overall situation of the hydration products. According to the analysis above, the variation range of n(C_x-S-H_y)/n($3CaO{\cdot}Al_2O_3{\cdot}CaCl_2{\cdot}10H_2O$) was 1.8–6.4 in the hydration products. That is, the ratio of molar content of C_x-S-H_y gel to the molar content of $CaO{\cdot}Al_2O_3{\cdot}CaCl_2{\cdot}10H_2O$ crystal was fluctuated in the range of 1.8–6.4. Therefore, C-S-H gel and $CaO{\cdot}Al_2O_3{\cdot}CaCl_2{\cdot}10H_2O$ crystals that densely arranged and closely bonded with pores and cracks were the main contributors to the strength of the whole soda residue-slag-cement binding material system.

To verify the accuracy of the analysis above, the detection points were marked and the energy dispersive spectrum analysis was carried out on different position of brightness. The marked position was shown in **Figure 3F** and the detection results were shown in **Table 4** and **Figures 4E,F**. According to the analysis method above, it can be calculated that the ratio of Ca/Si in C-S-H

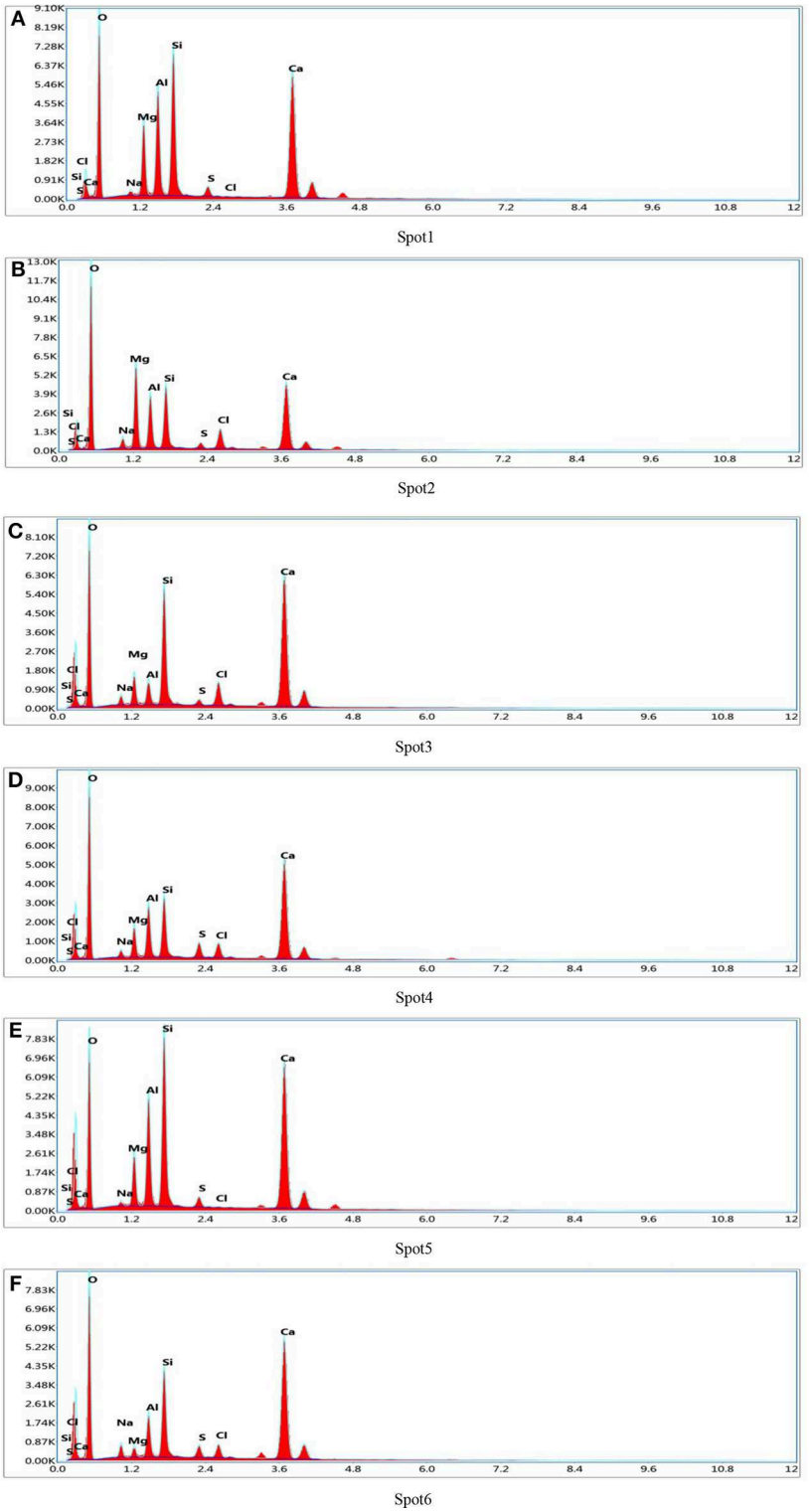

FIGURE 4 | EDS patterns of detection spot. **(A)** Spot 1. **(B)** Spot 2. **(C)** Spot 3. **(D)** Spot 4. **(E)** Spot 5. **(F)** Spot 6.

gel on the spot 5 was 0.75 and the ratio of Ca/Si in C-S-H gel on the spot 6 was 1.3. The ratio of Ca/Si of the remaining portion in detection region was within the range of Ca/Si ratio of C-S-H gel, thus, it supported the conclusion above that the hydration product containing Cl elements was $3CaO{\cdot}Al_2O_3{\cdot}CaCl_2{\cdot}10H_2O$ crystal. It could be seen from **Table 5** that the ratio of Si/Cl on

spot 5 and spot 6 was 2.05 and 2.9, respectively. In other words, the ratio of n(C-S-H)/n($CaO{\cdot}Al_2O_3{\cdot}CaCl_2{\cdot}10H_2O$) on spot 5 and spot 6 was 4.1 and 5.8, respectively. The ratio of n(C-S-H)/n($CaO{\cdot}Al_2O_3{\cdot}CaCl_2{\cdot}10H_2O$) on the two measuring surfaces were within the range of 1.8–6.4, which support the conclusion that the ratio of molar content of C_x-S-H_y gel to the molar content of $CaO{\cdot}Al_2O_3{\cdot}CaCl_2{\cdot}10H_2O$ crystal was fluctuated in the range of 1.8–6.4.

TABLE 4 | Elementary compositions of detection spot.

Location	Elementary compositions (by Atomic)/%							
	O	Na	Al	Si	S	Cl	Ca	Mg
Spot 1	60.13	0.78	6.10	9.18	1.77	3.06	12.55	6.44
Spot 2	61.31	1.93	5.46	5.71	0.53	3.17	13.19	8.69
Spot 3	67.38	1.65	1.95	4.68	0.54	5.20	15.55	3.06
Spot 4	67.02	1.32	4.72	6.62	1.35	2.07	13.41	3.49
Spot 5	58.79	0.73	7.90	8.41	1.08	4.10	14.51	4.50
Spot 6	69.39	2.41	3.62	6.72	1.01	2.32	13.38	1.21

TABLE 5 | Calculation results of Si, Ca, and Cl (by atomic) for spot.

	Item	Si	Cl	Ca
Spot 1	Atomic of element for Si, Ca, and Cl	9.18	3.06	12.55
	Atomic of Ca and Cl in $3CaO{\cdot}Al_2O_3{\cdot}CaCl_2{\cdot}10H_2O$	0	3.06	6.12
	Atomic of remaining elements	9.18	0	6.43
	Ca/Si		0.7	
	Si/Cl		3.0	
Spot 2	Atomic of element for Si, Ca, and Cl	5.71	3.17	13.19
	Atomic of Ca and Cl in $3CaO{\cdot}Al_2O_3{\cdot}CaCl_2{\cdot}10H_2O$	0	3.17	6.34
	Atomic of remaining elements	5.71	0	6.85
	Ca/Si		1.2	
	Si/Cl		1.8	
Spot 3	Atomic of element for Si, Ca, and Cl	4.68	5.20	15.55
	Atomic of Ca and Cl in $3CaO{\cdot}Al_2O_3{\cdot}CaCl_2{\cdot}10H_2O$	0	5.20	10.40
	Atomic of remaining elements	4.68	0	5.15
	Ca/Si		1.1	
	Si/Cl		0.9	
Spot 4	Atomic of element for Si, Ca, and Cl	6.62	2.07	13.41
	Atomic of Ca and Cl in $3CaO{\cdot}Al_2O_3{\cdot}CaCl_2{\cdot}10H_2O$	0	2.07	4.14
	Atomic of remaining elements	6.62	0	9.27
	Ca/Si		1.4	
	Si/Cl		3.2	
Spot 5	Atomic of element for Si, Ca, and Cl	8.41	4.10	14.51
	Atomic of Ca and Cl in $3CaO{\cdot}Al_2O_3{\cdot}CaCl_2{\cdot}10H_2O$	0	4.10	8.20
	Atomic of remaining elements	8.41	0	6.31
	Ca/Si		0.75	
	Si/Cl		2.05	
Spot 6	Atomic of element for Si, Ca, and Cl	6.72	2.32	13.38
	Atomic of Ca and Cl in $3CaO{\cdot}Al_2O_3{\cdot}CaCl_2{\cdot}10H_2O$	0	2.32	4.64
	Atomic of remaining elements	6.72	0	8.74
	Ca/Si		1.3	
	Si/Cl		2.9	

XRD Analysis of Hydration Products

Figure 5 shows the XRD patterns of paste specimens of D2 group cured to the age of 28 days. It was apparent that the peak of paste specimens ($3CaO{\cdot}Al_2O_3{\cdot}CaCl_2{\cdot}10H_2O$) appeared in **Figure 5**. As shown in the reference (Baquerizo et al., 2015), $3CaO{\cdot}Al_2O_3{\cdot}CaCl_2{\cdot}10H_2O$, also known as Friedel's salt, which belongs to a compound of the AFm family. A variety of compounds contained in the AFm family, in which $3CaO{\cdot}Al_2O_3{\cdot}CaSO_4{\cdot}nH_2O$, $3CaO{\cdot}A_2O_3{\cdot}CaCO_3{\cdot}nH_2O$, and $3CaO{\cdot}Al_2O_3{\cdot}CaCl_2{\cdot}nH_2O$ were the typical compounds. A variety of ions will replace each other to produce complex compounds when a large number of mineral admixtures existed. AFm crystal was a six square sheet crystal, but it tended to show tiny needle rod and irregular sheet shape when it grew incompletely. As shown in **Figure 3C**, the crystal in the shape of needle rod and irregular sheet distributed on the surface of hydration products was the $3CaO{\cdot}Al_2O_3{\cdot}CaCl_2{\cdot}10H_2O$ crystal.

It was apparent that the peak of paste specimens ($CaCO_3$) appeared in **Figure 5**. The presence of $CaCO_3$ may be caused by carbonation of the $Ca(OH)_2$ during the sampling and specimens preparation. Although the C-S-H gel belongs to the amorphous state and the spectral line was mainly diffuse peak, but there was a prominent "convex hull" phenomenon at 25–35° in the XRD patterns, indicating that there was the C-S-H gel in the hydration products of the soda residue-slag-cement binding material system curing for 28 days (Wu et al., 2014).

DSC-TG Analysis of Hydration Products

The DSC-TG patterns of paste specimens of D2 group were shown in **Figure 6**. It can be seen from **Figure 6** that there were seven main heat absorption peaks and two main exothermic peaks. The endothermic peaks that located, respectively, at 106.9, 186.4, 299.3, 334.2, 467, 609.9, and 672.6°C were corresponding to the temperature of decomposition of the hydration products. According to the literature (Yang and Xue,

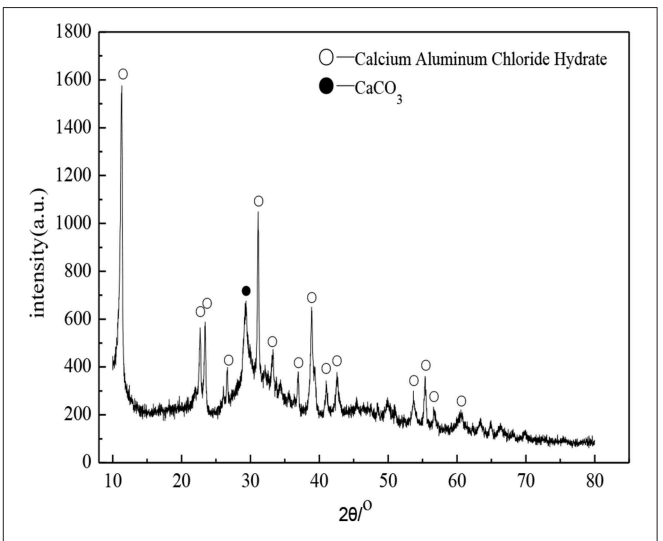

FIGURE 5 | XRD diffractogram of paste specimens of D2 group.

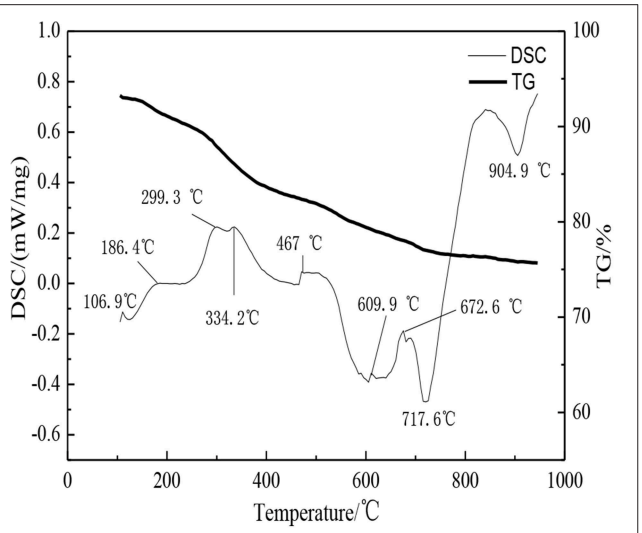

FIGURE 6 | DSC-TG patterns of paste specimens of D2 group.

2000), the endothermic peak at 106.9°C was due to the removal of water molecule in $3CaO{\cdot}Al_2O_3{\cdot}CaCl_2{\cdot}10H_2O$, and forming $3CaO{\cdot}Al_2O_3{\cdot}CaCl_2{\cdot}6H_2O$. The endothermic peak at 299.3°C resulted from $3CaO{\cdot}Al_2O_3{\cdot}CaCl_2{\cdot}6H_2O$ continued taking off 5 crystalline water. The endothermic peak at 186.4, 334.2, and 467°C were caused by dehydration and heat absorption of C-S-H gel. The crest at 609.9°C was due to the continuous hydration and heat absorption of calcium aluminum chloride hydrate. The existence of $CaCO_3$ in the paste specimens was showed in the XRD patterns. Most of the carbonate mineral decomposition temperature are in the range of 600–900°C. It can be seen that there was an endothermic peak at 859.5°C which was due to the decomposition reaction of $CaCO_3$ resulting in releasing CO_2 and generating CaO. The exothermic peaks were at the position of 717.6 and 904.9°C. The exothermic peak at 717.6°C was due to the further crystallization of calcium aluminum chloride hydrate. The exothermic peak at 862.2°C was due to the crystal transformation of the corresponding C-S-H gel and the transformation into the β-wollastonite (Wang and Yan, 2008, 2011). By the analyzation of DSC-TG, the existence of C-S-H gel and $3CaO{\cdot}Al_2O_3{\cdot}CaCl_2{\cdot}10H_2O$ crystal in hydration products was evidenced.

CONCLUSIONS

The icrostructure and composition of hardened paste of the soda residue-slag-cement binding material system were analyzed in this study. Several conclusions could be drawn as follows.

1) As the water-binder ratio was 0.5, sand-binder ratio was 3:1, and soda residue-slag-cement mass ratio was 2:6:2, the compressive strength of the mortar specimen (40 mm × 40 mm × 160 mm) was 45.1 MPa and the flexural strength was 7.4 MPa, which was quite closed to the strength of ordinary Portland cement mortar and can be used in the preparation of non-reinforced building products.
2) Through the microscopic analysis on the paste specimens cured to the ages of 28 days, it was found that the main hydration products were the C-S-H gel and $3CaO{\cdot}Al_2O_3{\cdot}CaCl_2{\cdot}10H_2O$ crystal. The Ca/Si ratio of C-S-H gel in hydration products varied in the range of 0.7–1.4, and the ratio of $n(C_x\text{-}S\text{-}H_y)/n(3CaO{\cdot}Al_2O_3{\cdot}CaCl_2{\cdot}10H_2O)$ varied in the range of 1.8–6.4. The C-S-H gel and Friedel's salts that densely arranged and closely bonded with pores and cracks constituted the main strength source of the whole soda residue-slag-cement binding material system together.

AUTHOR CONTRIBUTIONS

RS: experimental design, investigation, methodology, and writing. QZ: funding acquisition, investigation, methodology, project administration, and writing. JZ: conceptualization, data analysis, supervision, validation, writing, and revising. JL: data analysis, methodology, and writing.

FUNDING

Financial support from the National Natural Science Foundation of China under the grants of 51578477 and 51708403, the Innovative Research Group Science Fund of the National Natural Science Foundation of China under the grant of 51621092, the Key R&D Project of Hebei Province under the grant of 19211505D, and the China Postdoctoral Science Foundation under the grants of 2018T110200 and 2018M640236 was gratefully acknowledged.

REFERENCES

Amin, N., Nawab, L., and Ghani, U. (2017). Synthesis and characterization of chloride resistant cement from industrial waste through geopolymerization. *J. Clean. Prod*. 156, 577–580. doi: 10.1016/j.jclepro.2017.04.079

Aughenbaugh, K. L., Stutzman, P., and Juenger, M. C. G. (2016). Identifying glass compositions in fly ash. *J. Front. Mater*. 3, 1–10. doi: 10.3389/fmats.2016.00001

Baquerizo, L. G., Matschei, T., Scrivener, K. L., Saeidpour, M., and Wadsö, L. (2015). Hydration states of AFm cement phases. *J. Cement Concr. Res*. 73, 143–157. doi: 10.1016/j.cemconres.2015.02.011

Bilondi, M. P., Toufigh, M. M., and Toufigh, V. (2018). Using calcium carbide residue as an alkaline activator for glass powder-clay geopolymer. *J. Constr. Build. Mater*. 183, 417–428. doi: 10.1016/j.conbuildmat.2018.06.190

Chen, Y. C. (2018). Evaluating greenhouse gas emissions and energy recovery from municipal and industrial solid waste using waste-to-energy technology. *J. J. Clean. Prod*. 192, 262–269. doi: 10.1016/j.jclepro.2018.04.260

El Mir, A., and Nehme, S. G. (2017). Utilization of industrial waste perlite powder in self-compacting concrete. *J. Clean. Prod*. 156, 507–517. doi: 10.1016/j.jclepro.2017.04.103

Gomes, H. I., Mayes, W. M., Rogerson, M., Stewart, D. I., and Burke, I. T. (2016). Alkaline residues and the environment: a review of impacts, management practices and opportunities. *J. Clean. Prod.* 112, 3571–3582. doi: 10.1016/j.jclepro.2015.09.111

Hanjitsuwan, S., Phoo-ngernkham, T., Li, L. Y., Damrongwiriyanupap, N., and Chindaprasirt, P. (2018). Strength development and durability of alkali-activated fly ash mortar with calcium carbide residue as additive.

J. Constr. Build. Mater. 162, 714–723. doi: 10.1016/j.conbuildmat.2017.12.034

Liu, C. Y., Zhao, X. H., Zhu, N., Liu, Y. F., and Pang, Y. Z. (2017). Mechanical properties of fly ash-based geopolymers and modification mechanism of soda residue. *J. Bull. Chin. Ceramic Soc.* 36, 679–685. doi: 10.16552/j.cnki.issn1001-1625.2017.02.046

Liu, D. C., Li, Y., Liu, Y. J., Ge, W. Q., Yan, J. H., and Li, S. H. (2016). Preparation of baking-free brick by soda residue. *J. Chin. J. Environ. Eng.* 10, 3249–3254. doi: 10.12030/j.cjee.201511183

Shao, Y., Zhou, M., Wang, W. X., and Hou, H. B. (2013). Identification of chromate binding mechanisms in Friedel's salt. *J. Constr. Build. Mater.* 48, 942–947. doi: 10.1016/j.conbuildmat.2013.07.098

Siddiqua, S., and Barreto, P. N. M. (2018). Chemical stabilization of rammed earth using calcium carbide residue and fly ash. *J. Constr. Build. Mater.* 169, 364–371. doi: 10.1016/j.conbuildmat.2018.02.209

Sun, J. Y., and Gu, X. (2014). Engineering properties of the new non-clinker incorporating soda residue solidified soil. *J. Build. Mater.* 17, 1031–1035. doi: 10.3969/j.issn.1007-9629.2014.06.016

Sun, S. L., Zheng, Q. H., Tang, J., Zhang, G. Y., Zhou, L. G., and Shang, W. T. (2012). Experimental research on expansive soil improved by soda residue. *J. Rock Soil Mech.* 33, 1068–1612. doi: 10.16285/j.rsm.2012.06.045

Uçal, G. O., Mahyar, M., and Tokyay, M. (2018). Hydration of alinite cement produced from soda waste sludge. *J. Constr. Build. Mater.* 164, 178–184. doi: 10.1016/j.conbuildmat.2017.12.196

Wang, Q., and Yan, P. Y. (2008). Early hydration characteristics and paste structure of complex binding material containing high-volume steel slag. *J. Chin. Ceramic Soc.* 36, 1406–1416. doi: 10.14062/j.issn.0454-5648.2008.10.027

Wang, Q., and Yan, P. Y. (2011). The influence of steel slag on the hydration of cement during the hydration process of complex binder. *J. Sci. China Technol. Sci.* 54, 388–394. doi: 10.1007/s11431-010-4204-0

Wiemes, L., Pawlowsky, U., and Mymrin, V. (2017). Incorporation of industrial wastes as raw materials in brick's formulation. *J. Clean. Prod.* 142, 69–77. doi: 10.1016/j.jclepro.2016.06.174

Wu, H., Ni, W., Cui, X. W., and Wang, S. (2014). Preparation of concrete sleeper using hot steaming steel slag with low autogenous shrinkage. *J. Trans. Mater. Heat Treat.* 35, 7–12. doi: 10.13289/j.issn.1009-6264.2014.04.002

Yan, W. J. (2015). *Research on Performance and Mechanism of Mortar and Concrete Using Soda Residue as Mineral Admixture*. Guangzhou: South China University of Technology.

Yang, N. R., and Xue, W. H. (2000). *The Handbook of Inorganic Matalloid Materials Atlas*. Wuhan: Wuhan University of Technology Press.

Zhang, Y., Jiang, H. B., and Wang, Y. L. (2013). *The Concrete and Its Preparation Method With Soda Residue as Admixture*. P. Chinese Patent. Application Number 201310220650.2. 2013-06-05.

Zhang, Z. H., Zhu, Y. C., Yang, T., Li, L. F., Zhu, H. J., and Wang, H. (2017). Conversion of local industrial wastes into greener cement through geopolymer technology: A case study of high-magnesium nickel slag. *J. Clean. Prod.* 141, 463–471. doi: 10.1016/j.jclepro.2016.09.147

Zhao, Q. X., He, X. J., Zhang, J. R., and Jiang, J. Y. (2016). Long-age wet curing effect on performance of carbonation resistance of fly ash concrete. *J. Constr. Build. Mater.* 127, 577–587. doi: 10.1016/j.conbuildmat.2016.10.065

Zhao, X. H., Liu, C. Y., Wang, L., Zuo, L. M., Zhu, Q., and Ma, W. (2019). Physical and mechanical properties and micro characteristics of fly ash-based geopolymers incorporating soda residue. *J. Cement Concr. Comp.* 98, 125–136. doi: 10.1016/j.cemconcomp.2019.02.009

Conflict of Interest Statement: The authors declare that the research was conducted in the absence of any commercial or financial relationships that could be construed as a potential conflict of interest.

Advantages of publishing in Frontiers

OPEN ACCESS
Articles are free to read for greatest visibility and readership

FAST PUBLICATION
Around 90 days from submission to decision

HIGH QUALITY PEER-REVIEW
Rigorous, collaborative, and constructive peer-review

TRANSPARENT PEER-REVIEW
Editors and reviewers acknowledged by name on published articles

Frontiers
Avenue du Tribunal-Fédéral 34
1005 Lausanne | Switzerland

Visit us: www.frontiersin.org
Contact us: info@frontiersin.org | +41 21 510 17 00

REPRODUCIBILITY OF RESEARCH
Support open data and methods to enhance research reproducibility

DIGITAL PUBLISHING
Articles designed for optimal readership across devices

FOLLOW US
@frontiersin

IMPACT METRICS
Advanced article metrics track visibility across digital media

EXTENSIVE PROMOTION
Marketing and promotion of impactful research

LOOP RESEARCH NETWORK
Our network increases your article's readership